

Demonstrating Quantum Speed-Up with a Two-Transmon Quantum Processor.

Andreas Dewes

July 2012

Contents

1	Introduction & Summary	15
1.1	Quantum Computing with Superconducting Circuits	15
1.1.1	Context of this thesis work: 25 years of superconducting quantum circuits	16
1.1.2	This Thesis Work	17
1.2	Realizing a Two-Qubit Quantum Processor	18
1.3	Demonstrating Simultaneous Single-Shot Readout	19
1.4	Generating and Characterizing Entanglement	21
1.5	Realizing a Universal Two-Qubit Quantum Gate	23
1.6	Running a Quantum Search Algorithm	24
1.7	Demonstrating Quantum Speed-Up	26
1.8	Towards a Scalable Multi-Qubit Architecture	27
2	Theoretical Foundations	29
2.1	Classical & Quantum Information Processing	29
2.2	Principles of "Conventional" Quantum Computing	30
2.2.1	Quantum Bits and registers	31
2.2.2	Quantum Gates	32
2.2.3	Quantum Algorithms	33
2.2.4	Quantum Simulation	34
2.2.5	Realization of a Quantum Computer	34
2.3	Superconducting Quantum Circuits	35
2.3.1	The Josephson junction	35
2.3.2	Quantization of Electrical Circuits	36
2.3.3	The LCR Resonator	39
Coplanar Waveguide Resonators	40	
Quantization of the Resonator	42	
2.3.4	The Cooper Pair Box	43
The Transmon Qubit	47	
Decoherence of the Transmon	47	

Relaxation through the Charge Channel	48
Relaxation through the Flux Channel	48
Dephasing through the Charge Channel	49
Dephasing through the Flux Channel	49
2.4 Circuit Quantum Electrodynamics	50
2.4.1 Qubit Driving	51
2.4.2 Dispersive Limit & Qubit Readout	52
2.4.3 The Josephson Bifurcation Amplifier	53
Operation Principle	54
2.4.4 Qubit Decoherence in CQED	56
Relaxation	56
Dephasing	56
2.4.5 Qubit-Qubit Interaction	57
Direct Capacitive Coupling	58
Coupling Bus	58
2.5 Master Equation Formalism	59
3 Realizing a Two-Qubit Processor	61
3.1 Introduction & Motivation	61
3.1.1 Processor Operation	62
3.2 Qubit Design	64
3.2.1 Qubit Frequency & Junction Asymmetry	64
3.2.2 Single-Qubit Driving	64
Charge Driving	65
Flux Driving	66
3.2.3 Qubit-Qubit Coupling	67
3.2.4 Relaxation and Dephasing	68
Qubit Relaxation	69
Relaxation Through the Gate Charge Channel	69
Relaxation Through the Flux Channel	69
Qubit Dephasing	70
Dephasing due to Flux Noise	70
Dephasing due to Charge Noise	70
3.3 Readout Design	70
3.4 Summary: Qubit and Readout Parameters	73
3.5 Processor Layout & Fabrication	73
3.6 Electromagnetic Simulation of the Qubit-Chip	76
3.6.1 Fabrication Recipe	77

<i>CONTENTS</i>	5
-----------------	---

4 Measurement Setup & Techniques	79
4.1 Sample Holder & PCB	79
4.2 Signal Generation & Acquisition	80
4.2.1 Driving and Measurement of the Qubit	80
4.2.2 Microwave Sideband Mixing	82
4.2.3 Fast Magnetic Flux Pulses	83
4.2.4 Pulse Synchronization	85
4.3 Measurement Techniques	86
4.4 Qubit Readout	86
4.5 Qubit Manipulation	87
4.5.1 Spectroscopic Measurements of the Qubit State	88
4.5.2 Rabi Oscillations	89
4.6 Dephasing Time Measurement	89
4.7 Relaxation Time Measurement	90
5 Characterizing the Two-Qubit Processor	93
5.1 Qubit & Readout Characterization	93
Qubit Parameters	94
Readout Parameters	94
Qubit/Readout Coupling	95
Qubit Parameter Survey	95
5.2 Single-Qubit Operations	96
5.2.1 Single-Qubit Drive Errors	97
5.3 Simulation of Processor Operation	97
5.4 Two Qubit Operations	98
5.4.1 Creation of Entanglement	99
5.4.2 Quantum State Tomography	100
Maximum Likelihood Estimation of Quantum States	102
Including Experimental Tomography Errors	103
5.4.3 Creation of Bell states	104
5.4.4 Violation of the Bell Inequality	104
Errors	107
5.4.5 Measuring the Evolution of an Entangled Qubit States	107
5.5 Realizing a Two-Qubit Gate	109
5.5.1 Principle	109
5.5.2 Experimental Implementation	110
5.5.3 Quantum Process Tomography of the Gate	111
Theoretical Description of a Quantum Process	111
Implementation	112

From the χ matrix to the Kraus representation	113
Experimental Results: Input/Output Matrices And χ -Matrix	113
5.5.4 Gate Fidelity	117
5.5.5 Gate Error Analysis	117
Tomographic Errors	117
Unitary and Non-Unitary Gate Errors	118
6 Running the Grover Search Algorithm	119
6.1 Introduction & Motivation	119
6.1.1 Deriving the Grover Algorithm from Schrödinger's Equation	121
Efficiency of Quantum Searching	123
6.1.2 Implementation & Comparability to Classical Algorithms	125
6.1.3 Ancilla-based Implementation of the Algorithm	125
6.2 Comparision to a Classical Algorithm	126
6.3 Experimental Implementation	127
6.3.1 Pulse Sequence	128
6.4 Results	128
6.4.1 State Tomography of the Quantum Register	129
6.4.2 Single Run Results	129
6.5 Algorithm Fidelity	131
6.6 Comparision to a Classical Search Algorithm	132
6.7 Error Analysis	133
6.7.1 Gate Errors & Decoherence	133
Modeling Decoherence	133
Fidelity of the Oracle and diffusion operators	137
6.7.2 Readout Errors	137
6.8 Conclusions	139
7 Designing a Scalable Architecture for Quantum Bits	141
7.1 Definition & Requirements	142
7.2 Qubit Design	142
7.2.1 Qubit Parameters	142
7.2.2 Qubit-Qubit Coupling	142
7.3 Readout Design	142
7.3.1 Readout Parameters	142
7.3.2 Qubit-Readout Coupling	142
7.4 Single-Qubit Manipulation	142
7.4.1 Error Analysis	142
7.5 Multi-Qubit Manipulation	142

7.5.1 Error Analysis	142
7.6 Implementing a Universal Set of Quantum Gates	142
7.7 Realizing A Four-Qubit Architecture	142
7.8 Scaling Up	142
8 Conclusions & Perspective	143
8.1 Future Directions in Superconducting QC	143
8.1.1 3D Circuit Quantum Electrodynamics	143
8.1.2 Hybrid Quantum Systems	143
8.1.3 Quantum Error Correction & Feedback	143
A Modeling of Multi-Qubit Systems	145
A.1 Analytical Approach	145
A.1.1 Multi-Qubit Hamiltonian	145
A.1.2 Energies and Eigenstates	145
A.2 Master Equation Approach	145
Relaxation and Dephasing	146
A.2.1 Direct Integration	147
A.2.2 Monte Carlo Simulation	147
A.2.3 Speeding Up Simulations	147
B Data Acquisition & Management	149
B.1 Data Acquisition Infrastructure	149
B.2 Data Management Requirements	149
B.3 PyView	149
B.3.1 Overview	149
B.3.2 Instrument Management	150
B.3.3 Data Acquisition	150
B.3.4 Data Management	150
B.3.5 Data Analysis	150
C Design & Fabrication	151
C.1 Mask Design	151
C.2 Optical Lithography	151
C.3 Electron Beam Lithography	151
D Bibliography	151

List of Figures

1.1 Blueprint of a “canonical” two-qubit quantum processor	15
1.3 Circuit schematic of the realized two-qubit processor	19
1.4 Switching probabilities of the two qubit readouts as a function of the read-out excitation power	20
1.5 Generating entangled two-qubit states by swapping interaction	22
1.6 Measurement of the CHSH operator of an entangled two-qubit state . . .	23
1.7 Measured χ -matrix of the $\sqrt{i\text{SWAP}}$ gate	24
1.8 Schematic of the Grover search algorithm and measured density matrices when running it	25
1.9 Single-run results of the Grover search algorithm	26
1.10 Schematic of the four-qubit chip realized in this work	27
1.11 Measured $ S_{12} $ transmission coefficient for the input transmission line of our four-qubit chip	28
2.1 The Bloch sphere representation of a qubit state $ \psi\rangle = \cos \frac{\theta}{2} 0\rangle + e^{i\phi} \sin \frac{\theta}{2} 1\rangle$. The state $ \psi\rangle$ is fully characterized by specifying its “latitude” and “azimuth” angles θ and ϕ . Pure quantum states will always lie on the surface of the Bloch sphere, whereas mixed quantum states can also lie anywhere inside the sphere.	30

- 2.3 a) The electric field E and current I inside a $\lambda/2$ resonator. b) The circuit model of an open $\lambda/2$ resonator capacitively coupled to a drive circuit. The (lossless) resonator can be modeled as a series of infinitesimal sections of LC elements, as shown in the inset. c) The schematic of a coplanar waveguide (CPW) resonator, showing the electric field E , magnetic field B and the current I in the resonator. d) The reflected phase $\arg(S_{11})$ and absolute value of the input impedance $|Z_{in}|$ and resonator impedance $|Z_{res}|$ of an LCR resonator with $\omega_r = Z_r = Z_0 = 1$, $R \rightarrow \infty$ and $C_{in} = 0.1$ (dotted lines) as well a $\lambda/2$ resonator with the same effective ω_r and Z_r (solid lines), plotted as a function of the reduced frequency. As can be seen, the resonance frequency of the loaded resonator shifts in respect to that of the uncoupled one. In this case, $\omega_r^{\text{loaded}} \approx 0.969$ 41
- 2.4 a) The circuit schematic of a Cooper Pair Box (CPB). The device consists of a Josephson junction capacitively coupled to a voltage source. The extra capacitance of the Josephson junction is modeled by a capacitor C_J . Charges can accumulate on the island between the voltage source and the Josephson junction. b) A *split Cooper pair box*, where instead of one junction two of them are arranged in a loop. With this geometry it is possible to tune the effective Josephson energy of the circuit by changing the magnetic flux inside the junction loop. c) The schematic of a split CPB capacitively coupled to ground. This schematic corresponds most closely to the experimental CPB circuit that we use in this work. 43
- 2.5 Energies of the first four energy levels of the Cooper pair box for different ratios E_J/E_C , plotted as a function of the gate charge n_g . As can be seen, for $E_J \gg E_C$, the charge-dispersion curve becomes almost completely flat. 46
- 2.6 a) Schematic of a typical CQED circuit, consisting of a Transmon qubit capacitively coupled to a transmission line resonator. c) The equivalent circuit using a lumped-element model of the $\lambda/2$ resonator. 50
- 2.7 a) Circuit schematic of the CJBA, consisting of two parts of transmission line joined by a Josephson junction, forming a non-linear $\lambda/2$ resonator. b) Equivalent lumped elements circuit model of the CJBA. 53
- 2.8 a) Current in the driven non-linear resonator as a function of the drive detuning Ω , plotted for various drive powers P_p . For drive detunings $\Omega > \Omega_c$, the resonator becomes bistable above a certain power threshold $P_p > P_c$. b) Phase diagram of the non-linear resonator, showing the regions of bistability as a function of the drive power P_p and the drive detuning Ω . For $\Omega > \Omega_c$, a bistable region exists that permits to operate the resonator as a CJBA. 54

<i>LIST OF FIGURES</i>	11
3.1 Circuit schematic of the two-qubit processor	61
3.2	63
3.3 Single-qubit π -pulse gate time, gate fidelity and AC stark detuning as a function of drive strength	66
3.9 Optical and electron microscope photos of the two-qubit processor realized in this work. a) shows an optical image of the full processor with the two coupled qubits, fluxlines and readout resonator. b) shows an SEM image of an enlarged part of the central region of the chip with the two qubits and the coupling capacitance. c) Shows an SEM image of a single qubit junction loop.	75
4.2 The measurement setup used for the two-qubit experiments	81
4.3	83
4.5	86
5.1 Spectroscopy of the Two-Qubit Processor	94
5.2 Spectroscopic measurement of the avoided level crossing between the two qubits and their corresponding readout resonator	95
5.3 A qubit parameter survey showing T_1 , readout contrast and Rabi frequency of the two qubits over a large range of qubit frequencies	96
5.4 Demonstration of single-qubit IQ control	97
5.5 Spectroscopic measurement of the avoided level crossing between the two qubits of our processor	99
5.6 Pulse sequence used to create an entangled two-qubit state	99
5.9 Reconstructed density matrices of experimentally created Bell states. Shown are the states $ \Psi_{\pm}\rangle = 1/\sqrt{2}(01\rangle \pm 10\rangle)$ and $ \Phi_{\pm}\rangle = 1/\sqrt{2}(00\rangle \pm 11\rangle)$. The trace fidelities of the density matrices, $F_{tr} = \langle\psi \rho \psi\rangle$ range between 83 % and 87 %.	105
5.13 test	109
5.14 Experimental pulse sequence used for implementing the two-qubit \sqrt{i} SWAP gate. The sequence shown for an exemplary input state $ 10\rangle$ consists in exciting the first qubit to the state $ 1\rangle$, bringing the qubits in resonance for a time $t = 1/8g$, separating them and compensating the acquired dynamical phases by using two single-qubit Z -pulses. Finally, optional tomographic pulses are applied before reading out the qubit state at the optimal readout frequencies of the qubits.	110

5.15 The experimental input-output density matrices of the quantum process tomography of the $\sqrt{i\text{SWAP}}$ gate. Shown are the measured density matrices of 16 different input states and the corresponding output matrices with their state fidelities. The ideal matrices are overlaid in black. (part I/II)	114
5.16 The experimental input-output density matrices of the quantum process tomography of the $\sqrt{i\text{SWAP}}$ gate. Shown are the measured density matrices of 16 different input states and the corresponding output matrices with their state fidelities. The ideal matrices are overlaid in black. (part II/II)	115
5.17 The reconstructed χ matrix of our implementation of the $\sqrt{i\text{SWAP}}$ quantum gate. a) shows the lower half of the Hermitian matrix is shown. b) shows the product $\tilde{\chi} = \chi \cdot \chi_{id}^{-1}$ of the measured χ matrix and the ideal process matrix χ_{id} . The colored arrows connecting different elements of $\tilde{\chi}$ indicate unitary and non-unitary error processes to which the corresponding matrix elements can be associated.	116
6.1 A wavefunction $\psi(x)$ and potential $V(x)$ defined on a grid of points x_1, \dots, x_N	122
6.3 Full version of an ancilla-based implementation of the two-qubit Grover search algorithm	126
6.4 Classical reversible implementation of a search algorithm on a two-bit input register. An exemplary Oracle function can be implemented using two single-bit NOT operations and a Toffoli gate. R designates the generation of a random binary value at the beginning of the algorithm. If the Oracle does not yield the correct answer, the test state is incremented. The average success probability of the algorithm is 50 %.	127
6.5 Schematic of our implementation of the Grover search algorithm	128
6.6 Pulse sequence used for implementing Grovers search algorithm	129
6.7 Quantum state tomographies at different steps during the Grover search algorithm and single-run outcome probabilities	130
6.8 Single-run success probabilities of the Grover search algorithm	131
6.10 Error model used for analyzing gate and decoherence errors for the Grover search algorithm	134
6.11 Comparision of the general error model to our experimental data	136
6.12 Measured single- and two-qubit readout matrices and crosstalk matrix for the Grover search algorithm experiment	138
A.1	147
A.2	148

List of Tables

6.1	Conditional probabilities $p_{ab/ uv\rangle}$ and user fidelities f_{ab} for all possible outcomes ab for our implementation of Grover's algorithm.	131
6.2	Fitted gate error parameters of the Grover algorithm	135
6.3	Measured fidelities of the quantum Oracle and diffusion operators used in the Grover search algorithm	137

Chapter 1

Introduction & Summary

1.1 Quantum Computing with Superconducting Circuits

This thesis presents experiments performed with a superconducting two-qubit quantum processor. The main goal of this work was to demonstrate a possible quantum computing architecture based on superconducting qubits that follows the canonical blueprint of a quantum processor as sketched in fig. 1.1, in accordance with the five criteria formulated by DiVincenzo [29]. By this definition, a universal quantum computer is a register of well-defined quantum bits (1) with long coherence times (2), on which one can implement any unitary evolution using a universal set of quantum gates (3), fitted with individual high fidelity readout of the qubits (4) and with the possibility to reset them to their ground state (5). Implementing this allegedly simple list of requirements in a system of superconducting qubits has been a major research challenge during the last decade, and is part of more general line of research on superconducting quantum circuits briefly summarized below.

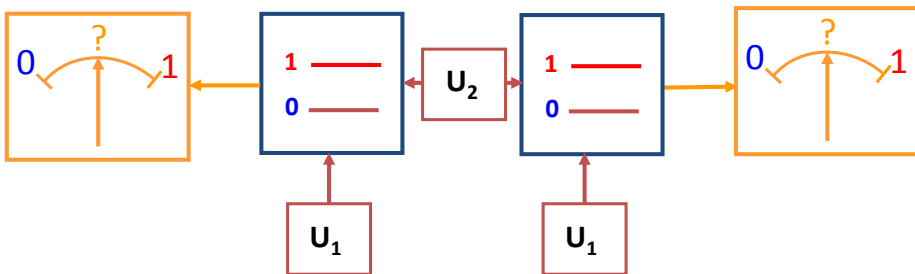


Figure 1.1: The blueprint of a “canonical” two-qubit quantum processor. The two qubits can be individually manipulated (U_1) and a universal two-qubit gate U_2 can be applied to them. Each of the qubits can be read out individually.

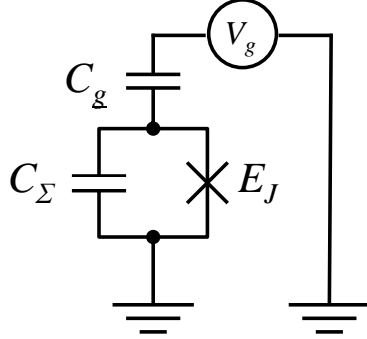


Figure 1.2: The schematic of the simple Cooper pair box (CPB) circuit, consisting of a capacitor in parallel with a Josephson junction capacitively coupled to a voltage source.

1.1.1 Context of this thesis work: 25 years of superconducting quantum circuits

The observation of quantum tunneling in a current-biased Josephson junction switching out of its zero-voltage state by Devoret *et. al.* [26, 59], first demonstrated that a collective electrical variable such as the superconducting phase difference across a Josephson junction (or the conjugated variable, i.e. the number of Cooper pairs that crossed it) can exhibit quantum properties. Then, the observation of microwave induced transitions between the quantum states of the junction by Martinis *et. al.* [59] further confirmed the quantum nature of this degree of freedom (See also [59, 60, 18]). A somewhat simpler quantum electrical circuit called the single Cooper Pair Box (CPB), made of a Josephson junction in series with a gate capacitor and a voltage source as shown in fig. 1.2, was later developed in the Quantronics group during the 1990s [11], and its ground state was characterized. With this electrical circuit, Nakamura *et. al.* [65] performed the first superconducting qubit experiment, demonstrating coherent oscillations between its ground and first excited eigenstates. Although the achieved coherence time was quite short, in the 5-10 ns range, this result attracted a huge interest and triggered the active development of research on superconducting quantum bits.

In the years after, several types of superconducting qubits were proposed using Josephson junctions in different configurations. Different regimes, in which the quantum state of the junctions ranges from almost Cooper pair number states to phase states, were realized. Let us cite here the flux qubit [63, 14] and the phase qubit [61], which were very successful qubits in many aspects. On the side of Cooper Pair Boxes, the Quantronics group contributed to the progress by operating a new circuit called the *Quantronium* (Vion *et. al.* [90]), fitted with a strategy for fighting dephasing due to the noise of the electrical control parameters, and with a single-shot readout (although with limited fidelity). The robustness of the quantronium arises from its operation at a so-called *sweet spot* where the qubit frequency is stationary in respect to variations in charge and phase control parameters. The improved coherence of the quantronium allowed to perform all the basic manipulations possible on spins and more generally on

two level systems [20]. Shortly after, another CPB design, inspired from cavity-QED, was developed at Yale by Wallraff *et. al.* [91]. In this so-called circuit-QED (CQED) design, the CPB, embedded in a microwave resonator, can be thought of as an artificial atom in a resonant cavity. The qubit readout is performed dispersively, i.e. through the cavity pull of the resonator frequency controlled by the qubit state. This small frequency change results in a small phase change of a resonant microwave pulse, which yields –after sufficient repetition– the probability of the two qubit states [10].

Another great bonus of CQED is that the electromagnetic environment in which the qubit relaxes its energy consists of a microwave resonator with a well-controlled impedance. The modern version of the Cooper Pair Box called *Transmon*, follows this design with an extra feature that makes it insensitive to the charge noise which plagues single electron and single Cooper Pair devices. This feature consists in placing the Cooper Pair Box in the phase regime by adding an extra capacitance in parallel with the junction: the qubit frequency is then totally insensitive to the gate charge, and hence to the charge noise to all orders in charge, thus transforming the sweet spot into a “sweet line” in the charge-phase parameter space. This new design, that still leaves sufficient anharmonicity to operate the device as a qubit and allows to drive it, yielded a sizable improvement in coherence times, qubit robustness and usability. The CQED concept was thus rapidly extended to flux and phase qubits [43].

In 2010, a new type of CQED architecture has been developed by Paik *et. al.* [69] that combines Transmon qubits with 3D cavities instead of CPW resonators, resulting again in an impressive increase of qubit coherence times by a large factor, with reported qubit relaxation times approaching $100\ \mu\text{s}$ and dephasing times of the same order. Very recently, these drastically improved coherence times have made possible the realization of elemental quantum feedback and error correction schemes with these systems [89].

The progress achieved during the last decade on the Cooper Pair Box and on the phase qubits has benefited to quantum processors. So far, superconducting CQED processors with up to three qubits have been realized and two- and three-qubit quantum gates [34], multi-qubit entanglement [28, 2] and simple quantum algorithms [27, 57] as well as quantum error correction [75] have recently been demonstrated.

1.1.2 This Thesis Work

At the beginning of this thesis work, CQED processors having demonstrated quantum algorithms did not comply with the rules established by DiVincenzo [29]. In other words, they did not follow the canonical blueprint able to demonstrate quantum speed-up: they were all fitted with a joint readout, which allows to measure the average value of a collective variable of the qubit register, but not each qubit individually. By repeating a given

sequence of gates a large number of times, one can nevertheless determine the quantum state of the qubit register at different steps of the algorithm being run. Since the whole interest of quantum computing is precisely to perform computational tasks more efficiently than with a classical processor, it was essential, in our mind, to demonstrate the quantum speed-up expected from quantum algorithms with a CQED quantum processor fitted with an individual single shot and non-demolishing (QND) readout for each qubit. Such a high fidelity single-shot readout had been developed for a single transmon during a previous thesis in the Quantronics group [56, 70], and it was natural to use it in the present work.

This thesis discusses therefore the realization of a superconducting two-qubit processor based on Transmon qubits, fitted with individual single-shot readouts. In chapter 2, we present the theoretical building blocks of this work. Chapter 3 outlines the design of the two-qubit processor, whereas chapter 4 presents the most relevant measurement techniques used here. With the two-qubit processor, we implement elementary one- and two-qubit quantum operations, as detailed in chapter 5. We use it to run a simple quantum algorithm that demonstrates probabilistic quantum speed-up: the Grover search algorithm, as explained in chapter 6. Finally, we discuss in chapter 7 the realization of a four-qubit quantum processor using a more scalable approach that could possibly be extended to an even larger number of qubits.

Note that during this thesis work, quantum speed-up was also demonstrated for the Deutsch-Josza algorithm with a phase qubit processor using individual single-shot and destructive readouts [92].

1.2 Realizing a Two-Qubit Quantum Processor

The quantum processor implemented in this work is shown in fig. 1.3. It consists of two superconducting quantum bits of the Transmon type, each equipped with its own drive and readout circuit. In order to obtain a high fidelity single-shot readout of the qubit register, we use the Cavity Josephson Bifurcation Amplifier (CJBA) readout method, which is based on the Josephson Bifurcation Amplifier (JBA) readout first developed in the team of Michel Devoret at Yale for the quantronium qubit [82, 88, 81]. This method had indeed already been successfully adapted to the transmon, and yielded a 93 % readout fidelity [56].

Each qubit can be manipulated by driving it with microwave pulses through its readout resonator, allowing robust and fast single-qubit operations. The qubit frequencies can be tuned individually using fast flux lines, allowing us to change the frequency of each qubit over a range of several GHz. The coupling between the two qubits is realized through a fixed capacitance that connects the two top-electrodes of the Transmons

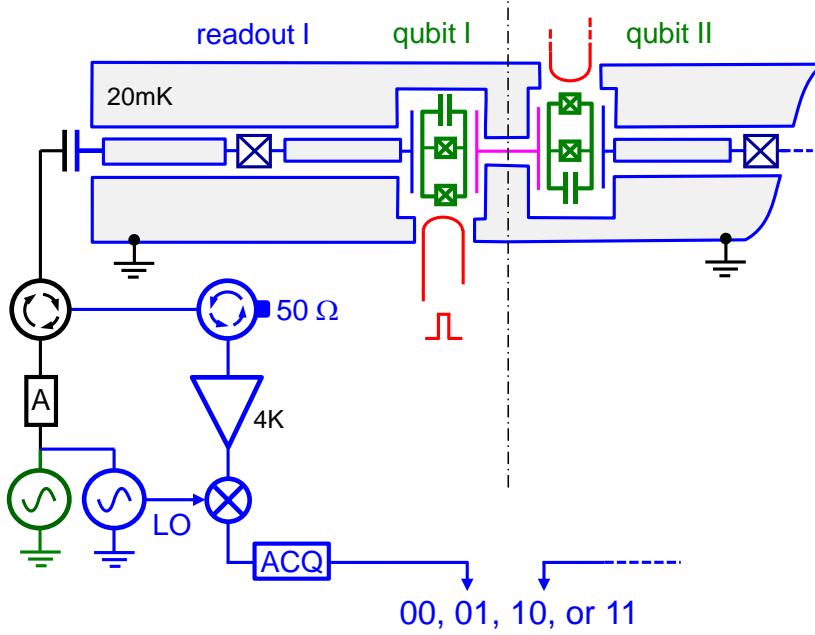


Figure 1.3: Circuit schematic of the two-qubit processor realized in this thesis work, showing the two qubits (in green) coupled by a fixed capacitor (in purple), as well as the fast flux lines (in red) used to tune the qubit frequencies and the qubit readouts (in blue). Each qubit is embedded in its own nonlinear readout resonator and can be driven and read out by microwave reflectometry through an individual microwave line.

and implements a fixed σ_{xx} -type qubit-qubit coupling. This coupling allows us to generate entangled two-qubit states and to implement a two-qubit gate. We use this simple processor to generate entangled two-qubit states, test the Bell inequality, implement a universal two-qubit gate and perform a simple quantum algorithm that demonstrates quantum speed-up, as discussed in the following sections.

1.3 Demonstrating Simultaneous Single-Shot Readout

For readout, each qubit is capacitively coupled to a coplanar waveguide resonator made nonlinear by placing a Josephson junction in its central conductor. We exploit the frequency pull of the bifurcation transition that occurs in this resonator when driven at a suitable frequency and power to map the qubit states on the bifurcated and non bifurcated cavity states, which are then discriminated by reflectometry. Here, the hysteretic character of the bifurcation transition allows to reduce the measuring power, to latch the cavity state, and to measure it without being affected by subsequent qubit relaxation. The state of the resonator can thus be determined reliably without being limited by qubit relaxation, thereby providing a high-fidelity single-shot qubit readout. Contrary to previous CQED processors, our processor is fitted with individual readouts, and a

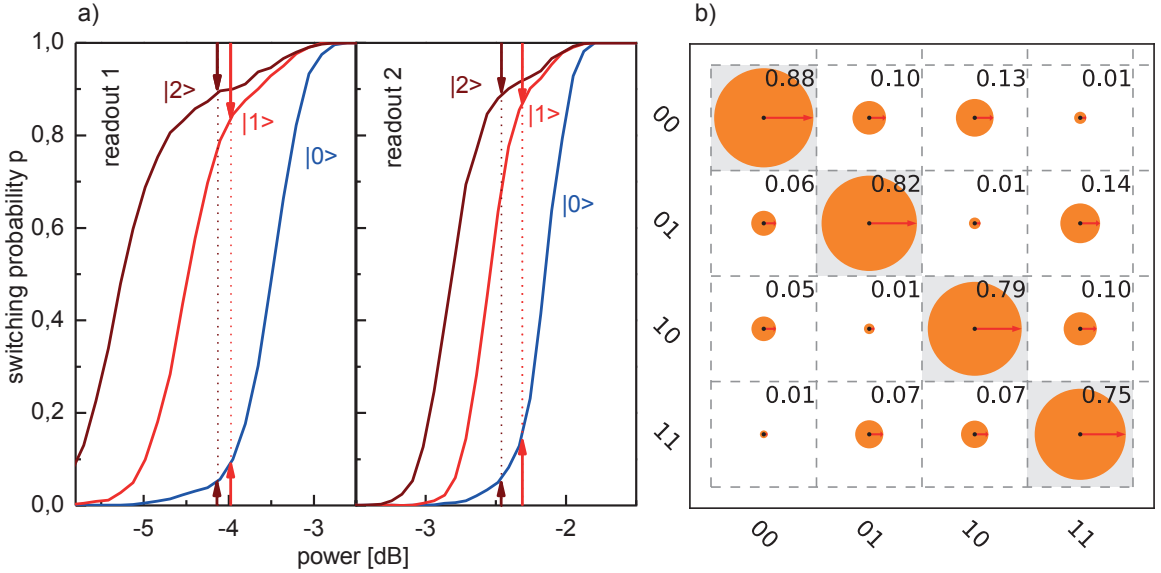


Figure 1.4: a) Switching probabilities of the two readout resonators as a function of the readout drive power at a fixed driving frequency. The measurement is performed after preparing the qubits in the states $|0\rangle$, $|1\rangle$ and $|2\rangle$. The readout contrast is given as the difference in probability between the curves corresponding to the states $|0\rangle$ and $|1\rangle$ or $|2\rangle$, respectively. The highest contrasts of 88 and 89 % are achieved when the qubit is shelved from state $|1\rangle$ to $|2\rangle$. b) Readout matrix of the two-qubit system, giving the probabilities to obtain the different outcomes ij after having prepared the register in the different computational basis states $|kl\rangle$.

simultaneous readout of the full two-qubit register is possible, as requested by the Di-Vincenzo criteria. For a single-qubit CJBA readout, fidelities up to 93 % have been achieved [56] by shelving the first excited state of the transmon $|1\rangle$ to the higher excited state $|2\rangle$. However, due to the higher complexity and design constraints of our system, only 83-89 % fidelity has been achieved for the processor presented here. The full characterization of the readout of our processor is shown in fig. 1.4. Panel a shows the switching probabilities of each individual readout as a function of the drive amplitude, measured at a fixed drive frequency. Individual curves correspond to the qubit being prepared (or shelved) in different states $|0\rangle$, $|1\rangle$ or $|2\rangle$, the difference between either two curves giving the readout contrast between those qubit states. Shelving the qubit from state $|1\rangle$ to state $|2\rangle$ before readout can increase the readout fidelity by more than 10 % and is therefore often used in the experiments presented in this thesis. Panel b shows the full readout matrix of the two-qubit register that relates measured readout switching probabilities with real qubit state occupation probabilities and allows us to correct readout errors when performing quantum state tomography. In chapter 5 we discuss all relevant readout fidelities and errors in detail and analyze different error sources limiting the readout performance in our experiments.

1.4 Generating and Characterizing Entanglement

The capacitive coupling between the two qubits provides a σ_{xx} -type interaction that can be used to generate entangled two-qubit states. Conveniently, this coupling is only effective when the qubit frequencies are near-resonant and can therefore be effectively switched on and off by tuning the qubit frequencies in and out of resonance. For the processor realized in this work, the effective coupling constant g of the two qubits has been measured as $2g/2\pi = 8.2$ MHz. When the two qubits are in resonance, the effective evolution operator of the two-qubit system is:

$$U(t) = \begin{pmatrix} 1 & 0 & 0 & 0 \\ 0 & \cos 2\pi t g & i \sin 2\pi t g & 0 \\ 0 & i \sin 2\pi t g & \cos 2\pi t g & 0 \\ 0 & 0 & 0 & 1 \end{pmatrix}_{\{|00\rangle, |01\rangle, |10\rangle, |11\rangle\}} \quad (1.1)$$

By using fast flux pulses to non-adiabatically tune the qubits in and out of resonance, we can switch on this interaction for a well-defined time. We first characterize the effect of the coupling on the qubit register by preparing the state $|10\rangle$, tuning the qubits in resonance for a given time and measuring the qubit state afterward. The resulting curve is shown in fig. 1.5a and shows swapping oscillations between the two qubits. Analyzing this curve allows us to extract the effective coupling strength between them. Leaving the interaction between the qubits on for a well-defined time allows us to generate entangled Bell states that we characterize by performing quantum state tomography. The experimental reconstruction of the density matrix of such a Bell-state of the type $|\psi\rangle = (|01\rangle + i|10\rangle)/\sqrt{2}$ is shown in fig. 1.5b. The measured fidelity of the prepared state of 91 % and the concurrence of 85 % confirm that entanglement is present in the system. We also characterize the entanglement between the two qubits by measuring the average value of the so-called *Clauser-Horne-Shimony-Holt* operator (CHSH) [19], which combines measurements of the state of the two qubits along different axes on the Bloch sphere and provides a test that can distinguish between classical correlations and quantum entanglement in a two-qubit system.

For classical states, the maximum value of the CHSH operator is bound by 2 but for entangled states it can reach a maximum of $2\sqrt{2}$. Figure 1.6 shows the result of such a CHSH-type measurement performed on a state created by the method described above, showing the value of $\langle \text{CHSH} \rangle$ as a function of the angle ϕ of the measurement basis. We observe a violation of the classical boundary 2 of the operator by 22 standard deviations when correcting the readout errors that are present in our system. The raw, uncorrected data fails to exceed the classical threshold because of readout errors mainly caused by qubit relaxation during the readout. Nevertheless, the observed violation in

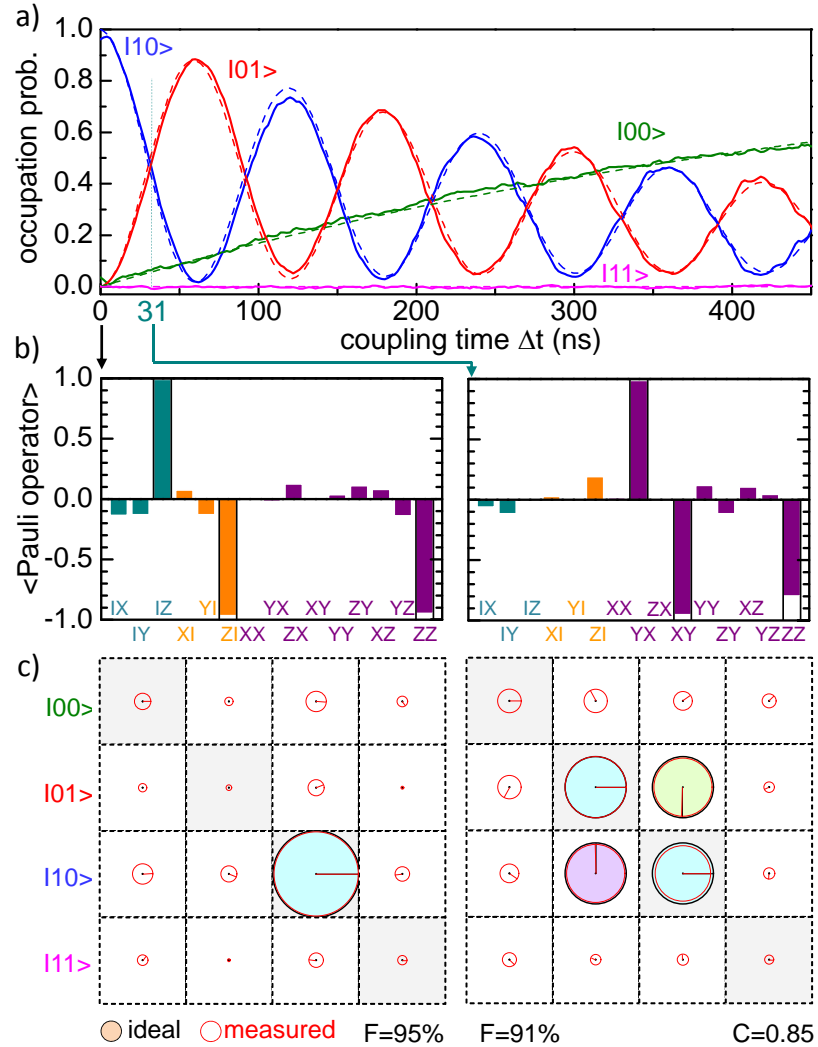


Figure 1.5: Coherent exchange of a single quantum of excitation (swapping oscillations) between the two qubits initially prepared the register state $|10\rangle$, obtained from the resonant interaction between them. a) Register state probabilities as a function of the swapping time Δt . The frequency of the oscillations corresponds to $2g/2\pi = 8.7$ MHz. b) Measured average values of the Pauli operators products $\{I, \sigma_x, \sigma_y, \sigma_z\} \otimes \{I, \sigma_x, \sigma_y, \sigma_z\}$ (Pauli set) for the register states obtained at times 0 ns and 31 ns. c) Corresponding reconstructed density matrices. The area of each circle corresponds to the absolute value of each matrix element and the color and direction of the arrow to the phase of the element. The black circles correspond to the density matrices of the ideal states $|10\rangle$ and $(|10\rangle + i|01\rangle)/\sqrt{2}$, respectively.

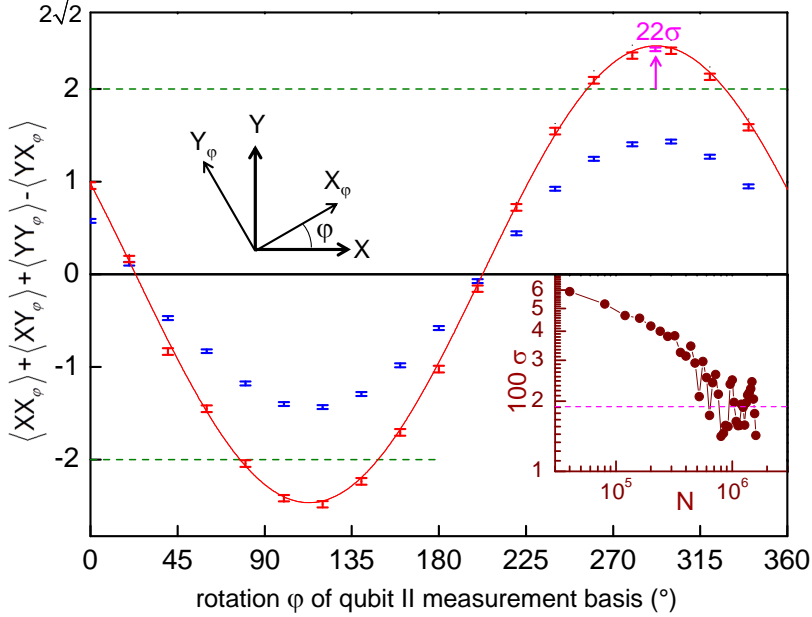


Figure 1.6: Measured average value of CHSH operator for a prepared Bell state. After readout error corrections, the CHSH expectation value (red points) exceeds the classical boundary of 2. The raw measurement data (blue points) lies below this critical threshold. The inset shows the standard deviation σ at the highest point of the curve as a function of the measurement sample size. For the highest sample count, the classical boundary is exceeded by 22 standard deviations.

the calibrated data is a strong indication of entanglement in the system. A more detailed overview of this experiment can be found in chapter 5.

1.5 Realizing a Universal Two-Qubit Quantum Gate

The swapping evolution given by eq. (1.1) allows not only to prepare entangled two-qubit states but also to implement a universal two-qubit gate: When switching on the interaction for a time $t_{\pi/2} = 1/8g$ one realizes the so-called $\sqrt{i\text{SWAP}}$ gate, represented by the evolution operator

$$U(t) = \begin{pmatrix} 1 & 0 & 0 & 0 \\ 0 & 1/\sqrt{2} & i/\sqrt{2} & 0 \\ 0 & i/\sqrt{2} & 1/\sqrt{2} & 0 \\ 0 & 0 & 0 & 1 \end{pmatrix}_{\{|00\rangle, |01\rangle, |10\rangle, |11\rangle\}} \quad (1.2)$$

which forms together with single qubit gates a universal set of gates, on which any algorithm can be decomposed. We characterize the operation and errors of our implementation of this gate by performing quantum process tomography, obtaining a gate fidelity of 90 %. The 10 % error in gate fidelity is caused mainly by qubit relaxation and

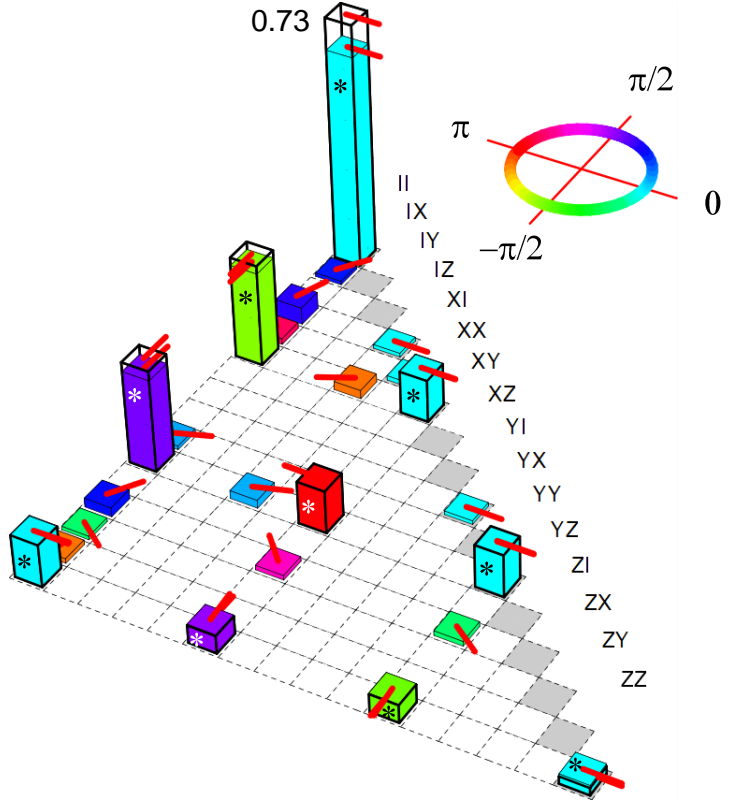


Figure 1.7: Measured χ -matrix of the implemented $\sqrt{i}\text{SWAP}$ gate. The row labels correspond to the indices of the E_i Pauli operators, the height of each bar to the absolute value of the corresponding matrix element, and the color and red arrow direction to the argument of the element. The ideal χ -matrix of the $i\sqrt{\text{SWAP}}$ gate is given by the outlined bars. The upper half of the positive-hermitian matrix is not shown.

dephasing during the gate operation and only marginally by deterministic preparation errors, as will be discussed in chapter 5. Figure 1.7 shows the measured χ matrix of the gate, that describes its effect in the Pauli basis of two-qubit operators. The χ matrix provides the full information on the unitary and non-unitary action of the gate. The achieved fidelity of the gate operation is sufficient to allow the implementation of simple quantum algorithms with our processor.

1.6 Running a Quantum Search Algorithm

Using a two-qubit quantum gate related to the one described above, we run a simple quantum algorithm on our processor, the so called *Grover search algorithm* [40]. The version of this algorithm that we implement operates on the two-qubit basis $x_i \in \{|00\rangle, |01\rangle, |10\rangle, |11\rangle\}$ and can distinguish between four different *Oracle functions* $\mathcal{C}_j(x)$ with $x \in x_i$ that give $\mathcal{C}_j(x = x_j) = 1$ and $\mathcal{C}_j(x \neq x_j) = 0$. In the two-qubit case, this algorithm requires only one evaluation of the Oracle function $\mathcal{C}_j(x)$, implemented as a unitary operator, to determine which state among the four possible ones it tags. This case thus provides a simple benchmark of the operation of the quantum processor, and a simple and illustrative example of quantum speed-up in comparison with classical algorithms, as discussed in chapter 6. The diagram of the Grover search algorithm implemented

in our processor is shown in fig. 1.8a and involves two *i*SWAP gate operations and six single-qubit operations along with a single-shot qubit readout at the end of the algorithm. We measure the success probability of the algorithm from the obtained outcomes, and complete the analysis of its operation by performing the tomography of the quantum state at different steps of the algorithm. We first discuss this evolution that sheds light on how quantum speed-up is achieved.

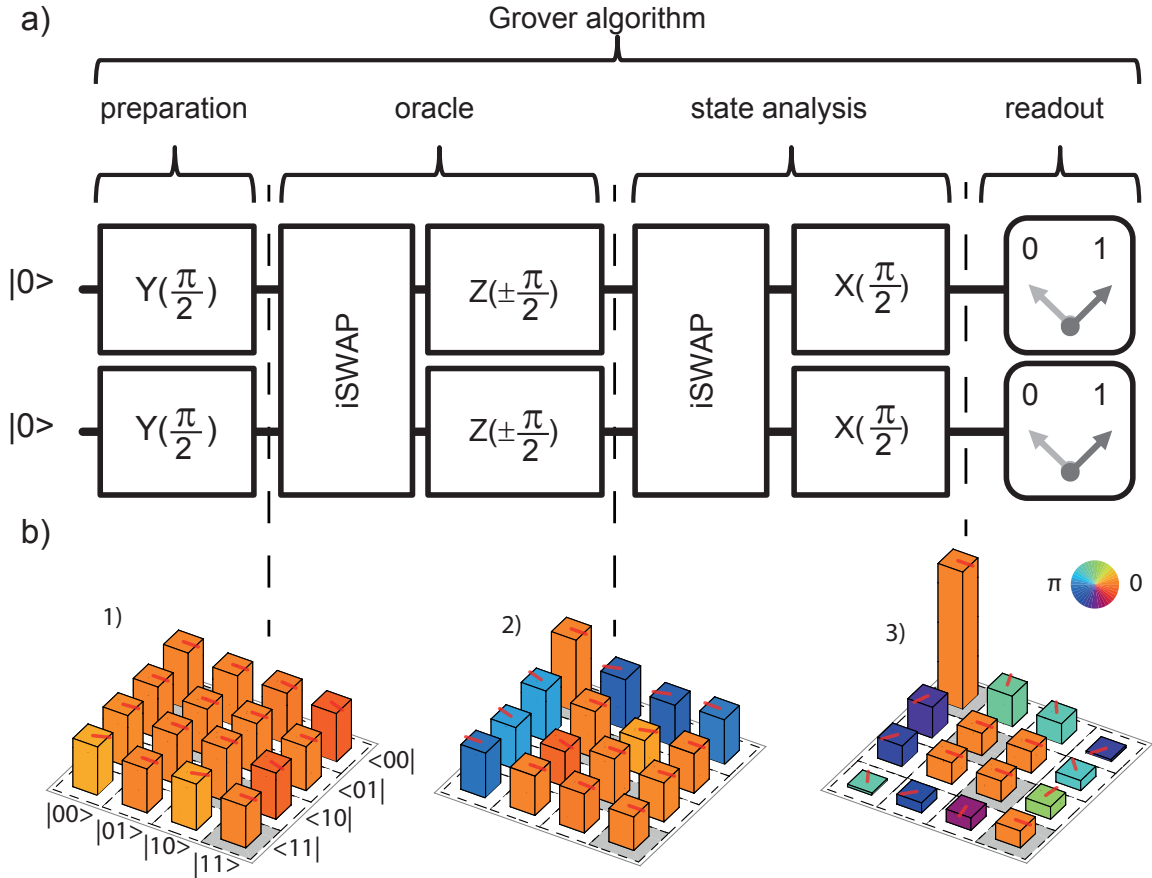


Figure 1.8: a) A two-qubit version of the Grover search algorithm that we implemented on our quantum processor. The algorithm consists in preparing a fully superposed state, applying a given Oracle operator to it only once, and analyzing the resulting output to determine the quantum state tagged by this Oracle operator. b) Measured density matrices when running the Grover search algorithm with a search oracle marking the state $|00\rangle$. 1) shows the state after the generalized Hadamard transform, 2) after applying the quantum oracle and 3) after the final step of the algorithm.

Fig. 1.8b shows the density matrices determined experimentally when running the Grover search algorithm with the Oracle operator tagging the state $|00\rangle$. State tomography is first shown after preparation with a generalized Hadamard transform applied to the initial state $|00\rangle$. It clearly corresponds to a superposition of all the computational basis states. The quantum state after having applied the quantum Oracle is $-|00\rangle + |01\rangle + |10\rangle + |11\rangle$ and the information on the tagged state is encoded in the

phase of the state $|00\rangle$. After extracting this phase information, the tomography displays a large peak on state $|00\rangle$ at the end of the algorithm, just as expected. The fidelity of the final quantum state of the algorithm is 68%, 61%, 64% and 65% for the four different Oracle operators, respectively. These fidelities, corrected for readout errors, do not quantify the quantum speed-up achieved when running the algorithm. For this, it is necessary to analyze the results obtained after a single run, which does not allow for any corrections of the readout outcomes.

1.7 Demonstrating Quantum Speed-Up

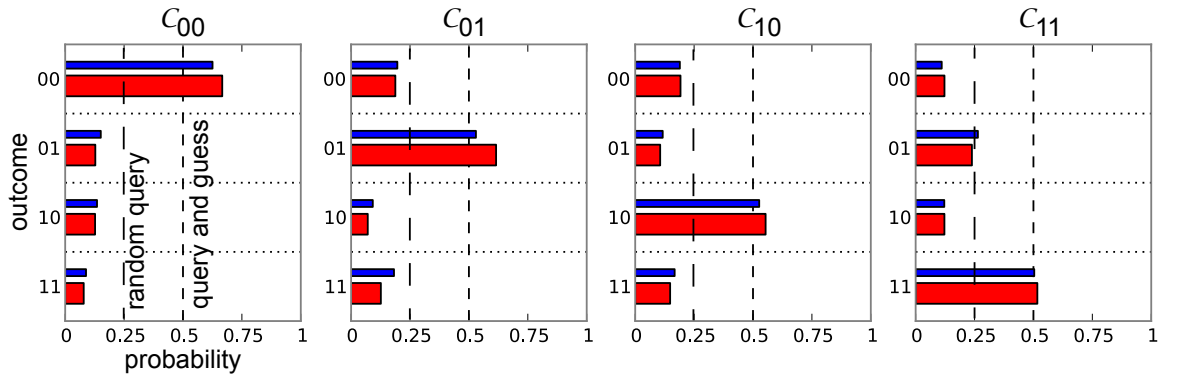


Figure 1.9: Single-run results when running the Grover search algorithm on our two-qubit quantum processor. Shown are the probabilities of measuring the qubit register in state $|i\rangle$ for an Oracle function \mathcal{C}_j marking the state $|j\rangle$ provided to the algorithm. In all four cases, the success probability of the algorithm is $> 50\%$, thus outperforming any classical “random query” or “query and guess” algorithm using a single Oracle call.

The main interest of running a quantum algorithm is to obtain an advantage in the run-time in comparison to a classical algorithm, the so-called *quantum speed-up*. To characterize this speed-up as obtained with our processor, we run the Grover algorithm for all four possible Oracle functions and directly read out the state of the qubit register after the last step of the algorithm instead of performing quantum state tomography, thus not correcting any readout errors. By averaging the outcomes of many such individual runs of the algorithm with different Oracle functions we obtain the so-called *single-run fidelities*, which –for the four different Oracle functions– have been measured as 66%, 55%, 61% and 52%. The full probability distributions for the four possible cases are shown in fig. 1.9. The achieved success probability is always lower than the theoretically possible value of 100 %, mainly because of relaxation and decoherence of the qubit state during the run time of the algorithm and –to a small degree– errors in the pulse sequence. The measured success probabilities are however larger than the 50% success probability of a classical query-and-guess algorithm using the outcome of a sin-

gle query. The algorithm thus demonstrates quantum speed-up, as explained in greater detail in chapter 6.

1.8 Towards a Scalable Multi-Qubit Architecture

The approach to superconducting quantum computing outlined in the previous sections is well suited for the implementation of simple quantum processors with a few qubits. However, due to several design limitations it is not suitable for implementing a large scale quantum computer. As an example, the direct qubit-qubit coupling employed in this thesis work is not suitable for coupling a large number of qubits since it becomes increasingly difficult to deterministically switch on and off the coupling between individual qubits as the number of qubits increases, a problem sometimes referred to as “frequency crowding”. Also, fitting each qubit of the processor with individual drive and readout circuitry –as done in this work– is usually not extensible to a large number of qubits due to topological and space constraints on the chip, as well as financial and practical constraints for a cryogenic experimental setup.

Recently, several research groups have started to address these issues by devising new architectures for superconducting quantum processors that can –in theory– be scaled to a larger number of qubits. Here we will mention only the so-called “Rez-Qu” architecture [37] and the surface-code approach [30] pursued e.g. by IBM. In this thesis work we discuss our own approach towards scalable quantum computing, where we have developed a revised version of our qubit chip that provides a way to implement a system with a larger –albeit still small– number of qubits. Key elements of this architecture are a quantum bus in form of a high-Q microwave resonator that is used for coupling the qubits and a multiplexed drive and readout circuit that allows us to measure

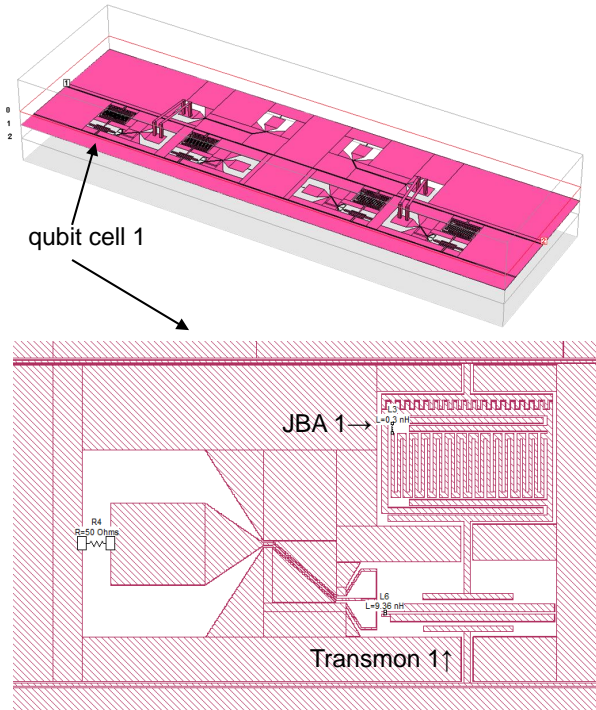


Figure 1.10: Schematic of the four-qubit chip realized in this thesis work. Shown on top is the whole chip with connectors for the drive and readout transmission line and for the four fast flux lines. Below we show a single qubit cell with a Transmon qubit coupled to the quantum bus, a flux line and a JBA readout.

and manipulate all qubits through one single microwave transmission line.

b Figure 1.10 shows the schematic of the first version of this architecture. Our chip contains four Transmon qubits which are capacitively coupled to a distributed high-Q resonator acting as a quantum bus. In addition, each qubit is coupled to a low-Q non-linear lumped element resonator acting as a CJBA, which is used for reading out the qubit state. Each of these resonators is in turn coupled capacitively to the input transmission line. The resonance frequencies of the readout resonators are arranged in ascending order with a frequency spacing of ≈ 50 MHz between adjacent resonators. This frequency spacing allows us to address each resonator individually and to read out the state of the full qubit register in parallel using only one single transmission line. Figure 1.11

shows the measured $|S_{12}|$ matrix element of such a chip with four CJBA resonators at frequencies between 6.78 GHz and 6.95 GHz, plotted as a function of the incident microwave power. The “knee” in each of the four resonance curves appearing between -45 and -40 dBm corresponds to the bifurcation point of the resonators.

Still, this approach suffers from a relatively bad ON/OFF ratio in the qubit-qubit coupling. To alleviate this problem, the Transmon qubit used in the current version of this architecture can be replaced by a qubit with a tunable coupling [85]. Alternatively, it is possible to use a fixed-frequency coupling scheme for the qubits, thereby altogether eliminating the need for frequency tuning of individual qubits and also reducing the number of input transmission lines from $n + 1$ to 1, with n the number of qubits.

A detailed discussion of the scalable architecture and the first preliminary measurements performed with a four-qubit chip are presented in chapter 7 of this thesis.

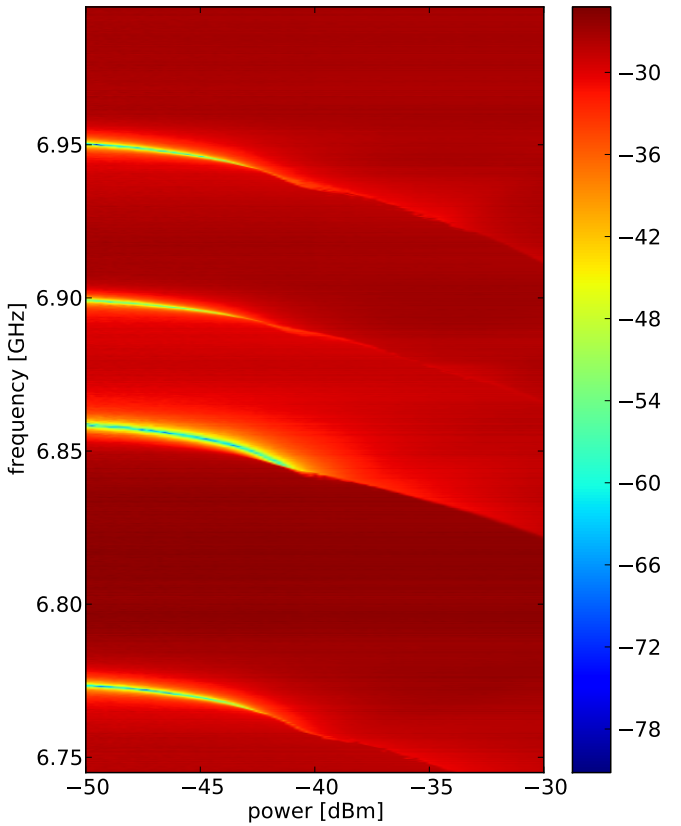


Figure 1.11: The measured $|S_{12}|$ transmission coefficient for the input transmission line of our four-qubit chip. Clearly visible are four resonances of the CJBA resonators and the bifurcation of each resonator at high input power.

Chapter 2

Theoretical Foundations

In this chapter we provide the reader with the minimum conceptual background and theoretical building blocks necessary to understand this thesis work. We begin our discussion with a general overview of classical and quantum information processing with a Turing machine, followed by an introduction to superconducting quantum circuits. We summarize the method to quantize electrical circuits and apply it to Cooper pair box devices, and in particular to the Transmon that will be used to implement the qubit register of our quantum processor. We then present coplanar waveguide resonators, and introduce circuit quantum electrodynamics on the example of a transmon coupled to a such a resonator. Finally, we consider the case of a nonlinear resonator used as a Josephson bifurcation amplifier since we use such a readout device in our processor architecture.

2.1 Classical & Quantum Information Processing

By definition, computing designates the activity of using computer hardware and software to process information, or *data*. Classical information processing can be divided in so-called *analog and digital information processing*, the former being based on continuously changeable physical quantities whereas the latter is based on incrementally changeable quantities. The fundamental unit of digital information processing is the so-called *bit*, which represents a Boolean (true/false) information. The discipline of theoretical computer science has been created to investigate the fundamental limits and properties of classical information processing. One of the main foundational theorems of theoretical computer science is the so-called *Church-Turing thesis* which provides a universal computing model by saying (basically) that everything which is computable can be efficiently computed using a *Turing machine*. Such a Turing machine, in turn, is a simple theoretical device which is able to run programs that operate on a discrete set of data using a well-specified set of operations. The Turing machine is universal in

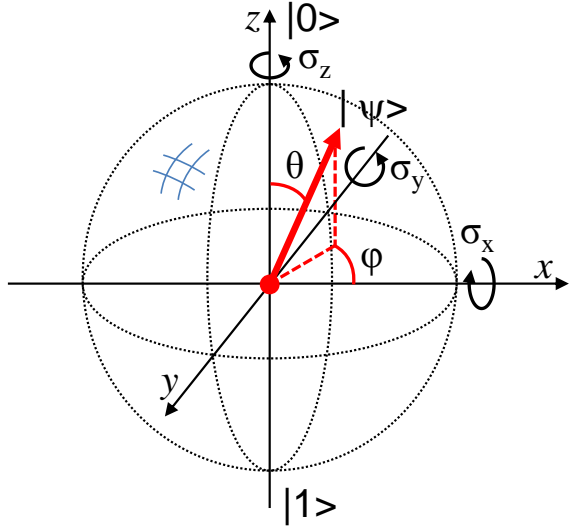


Figure 2.1: The Bloch sphere representation of a qubit state $|\psi\rangle = \cos \frac{\theta}{2} |0\rangle + e^{i\phi} \sin \frac{\theta}{2} |1\rangle$. The state $|\psi\rangle$ is fully characterized by specifying its “latitude” and “azimuth” angles θ and ϕ . Pure quantum states will always lie on the surface of the Bloch sphere, whereas mixed quantum states can also lie anywhere inside the sphere.

the sense that any other classical computing device can be efficiently emulated using a Turing machine with the appropriate program and data.

In the early 1980s, Richard Feynman discovered that a classical Turing machine as described above would be unable to efficiently simulate a quantum-mechanical system [35]. He introduced the concept of a *quantum Turing machine* that would be able to simulate quantum-mechanical systems in an efficient manner. A few years later, David Deutsch took up Feynman’s idea and developed an information processing framework based on quantum mechanics [24], coining the terms *quantum computing* and *quantum information processing*. He showed that by making use of different properties of quantum mechanics, namely, the superposition principle and entanglement, one could solve certain mathematical problems faster than possible with any classical computer [24]. The work by Deutsch created a large interest in the physics community and led to a huge theoretical and experimental effort aimed at realizing an operational quantum computer and developing quantum algorithms for relevant real-world problems.

2.2 Principles of "Conventional" Quantum Computing

The first scheme imagined for quantum information processing is directly inspired from the classical digital Turing machine: information is stored in a set of quantum two level systems, the *quantum bits* or *qubits*, forming a quantum register, which is manipulated by sequentially applying unitary (and possibly non-unitary) operators to subsets of qubits in the register, typically one or two. As for a classical Turing machine, any arbitrary operation of this quantum processor can be decomposed as a sequence of gate operations chosen from a surprisingly small set of gates, said universal. The power of such a machine comes from the gates operating on superposed states, which provides an intrinsic

parallelism in the processing. This *quantum gate* approach is the method relevant to the present thesis work, and we ignore other approaches introduced more recently such as *one-way quantum computing* [74], *adiabatic quantum computing* [33] or *topological quantum computing* [46]. In this section we introduce very briefly quantum bits and quantum gates, as well as some examples of quantum algorithms that are relevant to this work.

2.2.1 Quantum Bits and registers

As in classical computing, one can define in quantum computing a fundamental unit of information: the qubit. Such a qubit is a quantum-mechanical two-level system that can be put in any superposition

$$|\psi\rangle = \cos \frac{\theta}{2} |0\rangle + e^{i\phi} \sin \frac{\theta}{2} |1\rangle \quad (2.1)$$

of its two states $|0\rangle$ and $|1\rangle$. As can be seen, any state can be described by a pair of real numbers θ and ϕ that characterize the amplitude of each of the two basis states and the phase between them. A useful and intuitive representation of such a single-qubit state is the so-called *Bloch sphere representation*, shown in fig. 2.1. The north and south poles of this sphere correspond by convention to the qubit states $|0\rangle$ and $|1\rangle$ (or vice versa). All states lying on the sphere between those two correspond to pure superposition states, which are characterized by their “latitude” and “azimuth” angles θ and ϕ .

Often it is necessary to describe the qubit not as being in one well-defined pure state but rather being in one of several such states $|\psi_i\rangle$. Usually, we can then associate a classical probability p_i with finding the qubit in either of these states. In this case, we can then describe the qubit by a density matrix $\rho = \sum_i p_i \rho_i$, where $\rho_i = |\psi_i\rangle \langle \psi_i|$ is the density matrix of the pure state $|\psi_i\rangle$. All single-qubit density matrices ρ are Hermitian 2×2 matrices with non-negative eigenvalues and can thus be written as

$$\rho = \begin{pmatrix} \rho_{00} & \rho_{01} \\ \rho_{01}^* & \rho_{11} \end{pmatrix} \quad (2.2)$$

in the $|0\rangle, |1\rangle$ basis, with ρ_{00} and ρ_{11} being real numbers and ρ_{01} a complex number. For any state, the matrix has a unity trace $\text{Tr}(\rho) = 1$, for pure states, $\rho = \rho^2$ in addition. The expectation value $\langle A \rangle$ of any operator A acting on the density matrix ρ is given as $\text{Tr}(\rho A)$.

A mixed single-qubit state ρ can also be represented as a 3D vector lying in the so-called *Bloch sphere*. For this, we decompose the density matrix of the state as $\rho = c_i \sigma_I + c_x \sigma_x + c_y \sigma_y + c_z \sigma_z$, where $c_{i,x,y,z}$ are real coefficients and the identity matrix

σ_I and Pauli matrices $\sigma_x, \sigma_y, \sigma_z$ are given as

$$\sigma_I = \begin{pmatrix} 1 & 0 \\ 0 & 1 \end{pmatrix} \quad \sigma_x = \begin{pmatrix} 0 & 1 \\ 1 & 0 \end{pmatrix} \quad \sigma_y = \begin{pmatrix} 0 & -i \\ i & 0 \end{pmatrix} \quad \sigma_z = \begin{pmatrix} 1 & 0 \\ 0 & -1 \end{pmatrix}. \quad (2.3)$$

We can then plot the vector (c_x, c_y, c_z) in a 3D space. The length of it decreases from 1 for a pure state down to 0 for a completely mixed state, hence it will always lie inside a unity sphere.

Quantum states of $n > 1$ qubits cannot be described graphically but can be characterized by a density matrix of dimension $2^n \otimes 2^n$ in the computational basis $|q_1 \dots q_n\rangle = |q_1\rangle \otimes |q_2\rangle \dots \otimes |q_n\rangle$, where $|q_i\rangle$ is the state vector of the i -th qubit. For example, a two-qubit Bell state of the form $|\psi_+\rangle = (|01\rangle + |10\rangle)/\sqrt{2}$ can be written as

$$\rho_{\psi_+} = \frac{1}{2} \begin{pmatrix} 0 & 0 & 0 & 0 \\ 0 & 1 & 1 & 0 \\ 0 & 1 & 1 & 0 \\ 0 & 0 & 0 & 0 \end{pmatrix}_{(|00\rangle, |01\rangle, |10\rangle, |11\rangle)} \quad (2.4)$$

whereas a completely mixed state of 50 % $|01\rangle$ and 50 % $|10\rangle$ is represented by the matrix

$$\rho_{\psi_+} = \frac{1}{2} \begin{pmatrix} 0 & 0 & 0 & 0 \\ 0 & 1 & 0 & 0 \\ 0 & 0 & 1 & 0 \\ 0 & 0 & 0 & 0 \end{pmatrix}_{(|00\rangle, |01\rangle, |10\rangle, |11\rangle)} \quad (2.5)$$

2.2.2 Quantum Gates

Analogously to classical information processing, in quantum computing one defines *quantum gates* that act on individual or multiple qubits and allow us to process information. Such a quantum gate can be described as a unitary operator acting on the state of one or several qubits. Theoretically there is an infinite number of possible quantum gates, however in order to describe all possible quantum operations that can be performed on a qubit register of arbitrary length, it is sufficient to define a so-called *universal set of quantum gates*. Such a set contains a small number of quantum gates that can, by concatenation, produce any arbitrary unitary quantum operator, as shown by the so-called *Solovay-Kitaev theorem* [67, 23]. A universal gate set that will be especially

relevant to this work consists of the three single-qubit rotation operators

$$R_x(\theta) = e^{-i\sigma_x \frac{\theta}{2}} \quad (2.6)$$

$$R_y(\theta) = e^{-i\sigma_y \frac{\theta}{2}} \quad (2.7)$$

$$R_z(\theta) = e^{-i\sigma_z \frac{\theta}{2}} \quad (2.8)$$

that describe rotations of an angle θ around the X , Y and Z axes of the Bloch sphere, together with the so-called $\sqrt{i\text{SWAP}}$ gate

$$\sqrt{i\text{SWAP}} = \begin{pmatrix} 1 & 0 & 0 & 0 \\ 0 & 1/\sqrt{2} & i/\sqrt{2} & 0 \\ 0 & i/\sqrt{2} & 1/\sqrt{2} & 0 \\ 0 & 0 & 0 & 1 \end{pmatrix}_{(|00\rangle, |01\rangle, |10\rangle, |11\rangle)} \quad (2.9)$$

By applying the $\sqrt{i\text{SWAP}}$ operation twice we obtain the $i\text{SWAP}$ quantum gate, which is, by itself, **not** a universal quantum gate but which is nevertheless used in some practical quantum algorithms:

$$i\text{SWAP} = \begin{pmatrix} 1 & 0 & 0 & 0 \\ 0 & 0 & i & 0 \\ 0 & i & 0 & 0 \\ 0 & 0 & 0 & 1 \end{pmatrix}_{(|00\rangle, |01\rangle, |10\rangle, |11\rangle)} \quad (2.10)$$

This universal set is not minimal, since in principle two single-qubit gates with a fixed rotation angle (e.g. $R_x(\pi/4)$ and $R_y(\pi/4)$) together with a universal two-qubit gate would be sufficient to form a universal set of gates [23]. However, it is often advantageous if one can use single-qubit rotations with arbitrary rotation angles around all three axes of the Bloch sphere since it can significantly reduce the number of gates required to implement a given unitary operation.

2.2.3 Quantum Algorithms

The interest in quantum computing is mainly due to the fact that certain problems can be solved faster on a quantum computer than on a classical one. By faster we mean here that the order \mathcal{O} of the run time of the algorithm increases faster on a classical computer than on a quantum computer as a function of the problem size, i.e. the number of bits needed to encode the problem. Up to this day it has not been demonstrated that a quantum computer can perform all tasks faster than a classical computer. However, a small number of real-world problems have been found that can be solved exponentially to polynomially faster on a quantum computer. Here we cite only the two most "famous"

ones:

1. **The Shor Factorization Algorithm** Developed by Peter Shor in 1994 [79, 80]. This algorithm can factorize a binary number of length N into its prime factors in $\mathcal{O}(\log^3 N)$ steps, therefore exponentially outperforming any known classical factorization algorithm. There is large interest in this algorithm since the security of many asymmetrical cryptographic key exchange protocols rely on the assumption that is difficult to factorize large numbers into their prime components, hence realizing a polynomial-time method for number factorization would undermine the security of these algorithms.
2. **The Grover Search Algorithm**: Discovered by Lov Grover in 1996 [39], this search algorithm can find a single well-defined state in an unsorted database of size N in $\mathcal{O}(\sqrt{N})$ steps, being hence \sqrt{N} faster than a classical search algorithm. Recently, similar algorithms using quantum random walks on graphs have been found that provide similar speed-up [78]

2.2.4 Quantum Simulation

Another domain of interest for quantum computers is the so called *quantum simulation* [53]. Here the goal is to simulate the behavior of an arbitrary quantum system using a quantum computer by either engineering the quantum computer in direct analogy with the system being modeled (so called *analog quantum simulation*) or by numerically simulating the Hamiltonian of the quantum system on a general-purpose quantum computer (so-called *digital quantum simulation*). Since no classical computer can simulate a quantum system efficiently, there is a large interest in quantum simulation, especially in the fields of biology & chemistry [5], quantum field theory [38, 36] and many-body physics [84].

2.2.5 Realization of a Quantum Computer

To realize a working quantum computer, it is necessary to implement highly coherent qubits that can be manipulated, read out and coupled with high fidelity. So far, no fully working quantum computer has been experimentally demonstrated. However, larger progress towards its realization has been achieved in the last decade. Promising approaches for its realization include, among others, ions trapped in magnetic and electric fields [62, 16], nuclear magnetic resonance of organic molecules [44, 87], cold atomic gases [12], photonic circuits [47], semiconductor circuits [54] and, last but not least, superconducting circuits. Since this work treats only superconducting qubits, we focus our attention on them. We explain how we can realize a reliable qubit using superconducting

structures and how we can implement circuits to manipulate, couple and read out the qubit state.

2.3 Superconducting Quantum Circuits

In this section we discuss several types of superconducting circuit elements that are most relevant to this work. First, we introduce the reader to the Josephson junction, which is the device we use to realize superconducting qubits and amplifiers. Then, we present a general method for the quantization of arbitrary electrical circuits that we use afterwards to perform canonical quantization of our circuits. We use this method to derive the Hamiltonian of the Cooper pair box and treat the Transmon qubit as a special case. Afterwards, we discuss the properties of transmission lines and transmission line resonators that we use extensively for implementing readout and coupling elements in our qubit design. Then we give a short overview of the field of circuit quantum electrodynamics, which describes the interaction of a superconducting qubit capacitively coupled to a resonator. Finally, we introduce the reader to the Josephson and cavity bifurcation amplifiers that we use for our qubit readout.

2.3.1 The Josephson junction

The core element used to construct superconducting quantum circuits is the *Josephson junction*. A Josephson junction is based on the so-called Josephson effect [45], which states that between two superconductors connected through an insulating barrier, a supercurrent

$$I = I_c \sin \varphi \quad (2.11)$$

will flow, depending on the difference $\varphi = \varphi_2 - \varphi_1$ between the gauge-invariant superconducting phases φ_1 and φ_2 on each side of the link. I_c , the *critical current* of the Josephson junction, is the maximum super-current that it can support. φ is related to the instantaneous voltage between the electrodes of the junction as

$$V = \varphi_0 \frac{\partial \varphi}{\partial t}, \quad (2.12)$$

where $\varphi_0 = \hbar/2e \approx 2.05/2\pi \times 10^{-15}$ Wb. These two simple equations yield a system exhibiting a wealth of interesting physical phenomena which are used today in various applications such as the detection of weak magnetic fields [17], quantum limited amplifiers [88], generation of Terahertz radiation [68] and voltage standards [52]. The energy

associated with the phase difference across the Josephson junction is

$$E = E_J \cdot (1 - \cos \varphi) \quad (2.13)$$

where $E_J = I_c \varphi_0$ is the *Josephson energy*. In addition, the junction usually has an electrostatic energy associated to the capacitance formed by its two electrodes given as $E_C = Q^2/2C$, with $\pm|Q|$ being the charge accumulated on each of the electrodes of the junction.

For currents $I \ll I_c$, the Josephson junction behaves approximately like a nonlinear inductance

$$L_J(\varphi) = \frac{\varphi_0}{I_c \cos \varphi} \approx L_{J0} \left[1 + \frac{\varphi^2}{2} + \mathcal{O}(\varphi^4) \right], \quad (2.14)$$

where $L_{J0} = \varphi_0/I_c$ is the so-called *Josephson inductance*.

Using the potential and capacitive energies of the Josephson junction alone, we can formulate the quantum Hamiltonian of the junction, which is

$$\hat{H} = \frac{1}{2C} \hat{Q}^2 + E_J(1 - \cos \hat{\varphi}), \quad (2.15)$$

where $\hat{\varphi}$ and \hat{Q} are now conjugate quantum operators that, in analogy to a classical pendulum, play the role of position and momentum for the Josephson junction. In the limit of small angles φ , the Hamiltonian becomes that of a quantum harmonic LC oscillator. The nonlinearity present in the system is a key ingredient for realizing a Josephson qubit since it makes it possible to drive transitions between the first two quantum states of the device without also exciting higher quantum states, as would be the case when driving a harmonic oscillator.

2.3.2 Quantization of Electrical Circuits

In this section we outline a general method to treat arbitrary electrical circuits as the ones discussed before within the framework of quantum-mechanics, hence *quantizing* them. This introduction on circuit quantization presented in this chapter is based on a seminal article by B. Yurke [93] and an article by M. Devoret [25]. A more specific example of circuit quantization can be found in [13].

An electrical circuit is fully characterized by the parameters of its elements and its topology. The latter can be described as a set of nodes j connected by a number of branches i that are formed by dipolar circuit elements. In classical circuit theory, each branch is described by a voltage V_i between its ends and a current I_i flowing through it. The Kirchhoff laws demand that the sum of the branch voltages V_i along any closed path in the circuit must be zero and that the sum of currents flowing in and out of each

node must be zero. For quantization it is usually more convenient to replace voltages and currents with branch charges and fluxes that are defined as

$$\Phi_i(t) = \int_{t_{ref}}^t V_i(t') dt'; \quad (2.16)$$

$$Q_i(t) = \int_{t_{ref}}^t I_i(t') dt', \quad (2.17)$$

where t_{ref} is an arbitrarily chosen reference time. The Kirchhoff laws now write

$$\sum_i Q_i = Q_c , \quad \sum_i \Phi_i = \Phi_c \quad (2.18)$$

with Q_c and Φ_c constants, where the first sum is over charges Q_i of all elements connected to a certain node c and the second one is over all branches forming a closed loop in the circuit. We can obtain a complete set of node and branch equations for any given circuit by constructing the so-called *spanning tree* of the circuit, which is a tree in which all nodes are connected to an arbitrarily chosen *ground node* by one unique path [25]. From the spanning tree we can obtain a complete set of branches and the corresponding Kirchoff equations for the fluxes Φ_i around them. Together with the set of Kirchhoff equations for the charges at each node, we can use this system of equations to eliminate unnecessary circuit variables and obtain a description of the circuit using a minimal set of degrees of freedom. Now, to quantize a circuit made up of non-dissipative elements we can follow the method given in [93], writing the Lagrangian (using the reduced set of variables) as

$$\mathcal{L}(\Phi_1, \dots, \Phi_n, \dot{\Phi}_1, \dots, \dot{\Phi}_n) = \sum_i \mathcal{V}_i - \sum_i \mathcal{T}_i, \quad (2.19)$$

where the sum i runs over all circuit elements and \mathcal{V}_i and \mathcal{T}_i are the potential and kinetic energies associated to the i -th element. Here, linear inductances contribute only to the potential energy as $\mathcal{V}_{L_i} = \Phi_i^2 / 2L_i$, whereas linear capacitances contribute only to the kinetic energy as $\mathcal{T}_{C_i} = C_i \dot{\Phi}_i^2 / 2$. Resistors can be described within the Lagrangian formalism by modeling them as semi-infinite transmission lines with a characteristic impedance matching their resistance [93]. We can also include general nonlinear capacitances and inductances that obey the relations $\dot{\Phi} = f_C(Q)$ and $\dot{Q} = g_L(\Phi)$ between their node flux

and charge, and whose energies are given as

$$E_C = \int_0^Q f_C(Q)dQ, \quad (2.20)$$

$$E_L = \int_0^\Phi g_L(\Phi)d\Phi. \quad (2.21)$$

A Josephson junction, for example, can be described as a nonlinear inductance with $g_L^{JJ}(\Phi) = I_c \sin(\Phi/\varphi_0)$, having an associated energy

$$E_L^{JJ} = \int_0^\Phi I_c \sin(\Phi/\varphi_0) d\Phi = E_J(1 - \cos\left[\frac{\Phi}{\varphi_0}\right]). \quad (2.22)$$

Transmission lines can be quantized by a similar approach, as shown e.g. in [93]. Externally imposed charges and fluxes can be modeled as “pre-charged” capacitors and inductors with infinite charge or flux and infinite capacitance or inductance that get renormalized at the end of the quantization process [25]. Externally imposed voltages and currents can be treated like this as well by converting them to corresponding fluxes or charges. From the Lagrangian as given by eq. (2.19) we can obtain the classical equations of motion of the system by variation of the action

$$\frac{\partial}{\partial t} \left(\frac{\partial \mathcal{L}}{\partial \dot{\Phi}_i} \right) - \frac{\partial \mathcal{L}}{\partial \Phi_i} = 0. \quad (2.23)$$

For each flux Φ_i we obtain its canonically conjugate momentum Q_i by the equation

$$Q_i = \frac{\partial \mathcal{L}}{\partial (\dot{\Phi}_i)}, \quad (2.24)$$

where $\dot{\Phi}_i = d\Phi_i/dt$. Having obtained Φ_i and Q_i , we can calculate the Hamiltonian \mathcal{H} of the system by applying the transformation

$$\mathcal{H}(\Phi_1, \dots, \Phi_n, Q_1, \dots, Q_n) = \sum_j \dot{\Phi}_i Q_i - \mathcal{L}(\Phi_1, \dots, \Phi_n, \dot{\Phi}_1, \dots, \dot{\Phi}_n). \quad (2.25)$$

This Hamiltonian, written in generalized coordinates, yields the full set of equations of motion of the electrical circuit and depends only on the canonically conjugate variables Φ_1, \dots, Φ_n and Q_1, \dots, Q_n . First Quantization of the circuit can then be done by simply replacing the classical variables by quantum observables such that $\Phi_i \rightarrow \hat{\Phi}_i$ and $Q_i \rightarrow$

\hat{Q}_i and imposing commutation relations between them:

$$[\hat{Q}_i, \hat{Q}_j] = 0, \quad (2.26)$$

$$[\hat{\Phi}_i, \hat{\Phi}_j] = 0, \quad (2.27)$$

$$[\hat{\Phi}_i, \hat{Q}_i] = i\hbar\delta_{ij}. \quad (2.28)$$

In the following sections we apply this quantization method to the Cooper pair box circuit that we use to implement a superconducting qubit and to the simple LCR resonator circuit that we use as a qubit readout and coupling bus.

2.3.3 The LCR Resonator

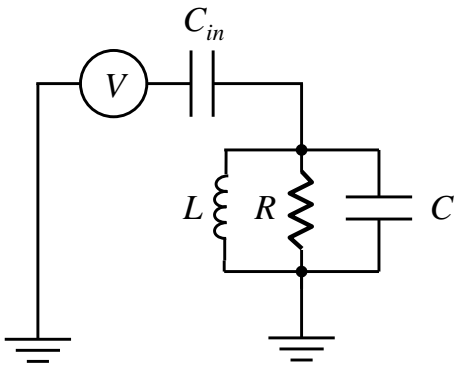


Figure 2.2: An *LCR* resonator coupled to a voltage source through an input capacitance C_{in} .

The *LCR* resonator is the circuit element that forms the basis of our qubit readout. The schematic of a *LCR* resonator coupled to a voltage source through an input capacitance C_{in} is shown in fig. 2.2. The impedance of the resonator alone is

$$Z_{LCR} = \frac{1}{\frac{1}{R} + i\omega C - \frac{i}{\omega L}}, \quad (2.29)$$

yielding a resonance frequency $\omega_r = 1/\sqrt{LC}$ and an *internal quality factor* $Q_{int} = \omega_r RC$. To probe the resonator we couple it through a gate capacitance C_{in} to an input transmission line with characteristic impedance Z_0 . We can model the resulting circuit as a LCR resonator with a frequency-dependent, effective resistance

$$R' = \left(\frac{1}{R} + \frac{C_{in}^2 Z_0 \omega^2}{1 + C_{in}^2 Z_0^2 \omega^2} \right)^{-1}. \quad (2.30)$$

The quality factor of this *loaded resonator* changes according to

$$Q_r^{-1} = Q_{int}^{-1} + Q_{ext}^{-1}, \quad (2.31)$$

where $Q_{ext} \approx \omega_r C (1 + C_{in}^2 Z_0^2 \omega_r^2) / C_{in}^2 Z_0 \omega_r^2 \approx \omega_r C Z_{in} / (C_{in} Z_0 \omega_r)^2$. As can be seen, the external quality factor increases $\propto 1/C_{in}^2$. We can define a coupling or decay rate $\kappa = \omega_r / Q_r$, which corresponds to the rate at which energy leaks out of the resonator. Due to the coupling to the input line, the resonance frequency of the loaded resonator is changed as well and is given as $\omega_r^{\text{loaded}} = 1/\sqrt{LC_{eff}}$, where $C_{eff} \approx C + C_{in}\omega_r/(1 + (C_{in}\omega_r Z_0)^2)$. For frequencies close to the resonance frequency of the resonator, we can write its impedance as

$$Z_{LCR}(\Delta) = \frac{\omega_r Z_r}{\kappa + 2i\Delta} \quad (2.32)$$

where $\Delta = \omega_r - \omega$ and $Z_r = \sqrt{L/C}$ is the characteristic impedance of the resonator. This approximation is useful when e.g. experimentally fitting resonance data to obtain the quality factor of the resonator.

Coplanar Waveguide Resonators

Due to practical reasons we use so-called *coplanar waveguide resonators* instead of simple LCR resonators in our experiments. We will therefore briefly discuss them and show how we can map them to the simple LCR resonator model. A coplanar waveguide is a flat structure with a central conductor that is separated by a gap from a ground plane on either side, as shown in fig. 2.3c. In general, it can be treated as a so-called *transmission line*. A detailed treatment of the physics of transmission lines can be found e.g. in [72]. If we regard a transmission line of finite length l , the voltages and currents at both ends are related through [72]

$$\begin{pmatrix} V_1 \\ I_1 \end{pmatrix} = \begin{pmatrix} \cos \gamma l & iZ_r \cos \gamma l \\ iY_r \sin \gamma l & \cos \gamma l \end{pmatrix} \cdot \begin{pmatrix} V_2 \\ I_2 \end{pmatrix}, \quad (2.33)$$

where $\gamma = \alpha + i\beta = \sqrt{(R + i\omega L)(G + i\omega C)}$ is the *propagation constant* which describes the dispersion and damping of electromagnetic waves along the waveguide, ω is the angular frequency of the electromagnetic wave, L , C , R and G are the characteristic inductance, capacitance, resistance and conductance of the transmission line per unit length (for a lossless line $G = R = 0$), $Z_r = \sqrt{L/C}$ is the characteristic impedance of the waveguide and $Y_r = 1/Z_r$ the corresponding admittance.

Let us now consider the open-ended $\lambda/2$ CPW resonator that we use in our experiments to realize the qubit readout resonator, as shown in fig. 2.3b-c. To realize the resonator, we terminate the transmission line at one end by an open gap and connect the other end to a drive line through an input capacitance C_{in} . We can then make use of eq. (2.33) to calculate the end voltages and currents of the resonator, demanding that $I_2 = 0$ (since the resonator is open-ended). We obtain for the voltage V_1 and current I_2

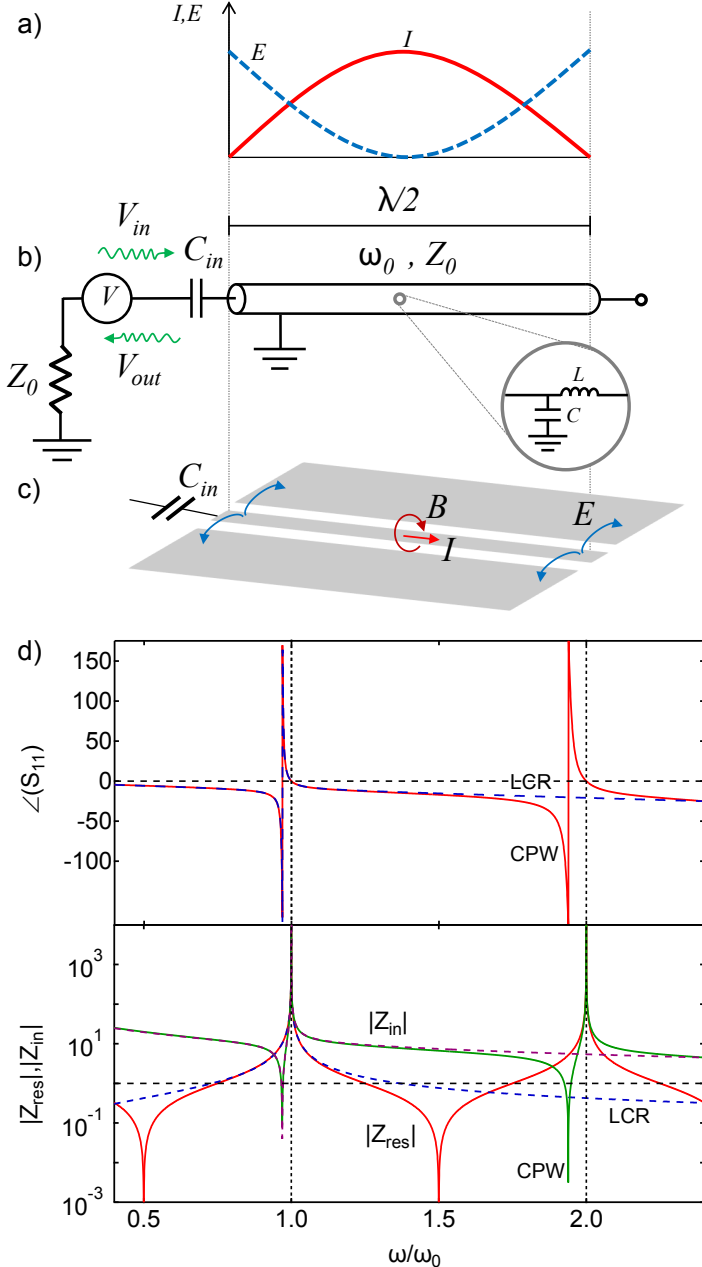


Figure 2.3: a) The electric field E and current I inside a $\lambda/2$ resonator. b) The circuit model of an open $\lambda/2$ resonator capacitively coupled to a drive circuit. The (lossless) resonator can be modeled as a series of infinitesimal sections of LC elements, as shown in the inset. c) The schematic of a coplanar waveguide (CPW) resonator, showing the electric field E , magnetic field B and the current I in the resonator. d) The reflected phase $\arg(S_{11})$ and absolute value of the input impedance $|Z_{in}|$ and resonator impedance $|Z_{res}|$ of an LCR resonator with $\omega_r = Z_r = Z_0 = 1$, $R \rightarrow \infty$ and $C_{in} = 0.1$ (dotted lines) as well a $\lambda/2$ resonator with the same effective ω_r and Z_r (solid lines), plotted as a function of the reduced frequency. As can be seen, the resonance frequency of the loaded resonator shifts in respect to that of the uncoupled one. In this case, $\omega_r^{\text{loaded}} \approx 0.969$.

the relation

$$V_1 = \cos \gamma l V_2, \quad (2.34)$$

$$I_1 = i Y_r \sin \gamma l V_2. \quad (2.35)$$

The impedance of the resonator is thus given as $V_1/I_1 = -i Z_r \cot \gamma l$. We can approximately model this distributed CPW resonator as a lumped element parallel LCR resonator by equating their impedances close to their resonance frequency ω_r . This

yields an effective inductance, capacitance and resistance for the CPW resonator of

$$L_r = \frac{2Z_r}{\omega_r \pi} \quad (2.36)$$

$$C_r = \frac{\pi}{2\omega_r Z_r} \quad (2.37)$$

$$R_r = \frac{2Z_r Q}{\pi} \quad (2.38)$$

Using this mapping, we can calculate all relevant resonator properties using the more simple theory of the lumped element LCR resonator, disregarding however the internal multi-mode structure of the resonator.

Quantization of the Resonator

We can quantize the LCR resonator by following the procedure outlined in the last section. The circuit in fig. 2.2 contains two active nodes. If we disregard for now the input voltage source V , the input capacitance C_{in} and the resistance R , we can directly obtain the Hamiltonian of the non-dissipative part of the LCR resonator as

$$H = \frac{1}{2C}Q^2 + \frac{1}{2L}\Phi^2, \quad (2.39)$$

where Q is the charge accumulated on the capacitor and Φ the flux in the inductance of the resonator. This Hamiltonian corresponds to that of a harmonic oscillator given as

$$\hat{H} = \omega_r \hbar \left(\hat{a}^\dagger \hat{a} + \frac{1}{2} \right). \quad (2.40)$$

with \hat{a}^\dagger and \hat{a} the *creation and annihilation operators* given as

$$\hat{a}^\dagger = \sqrt{\frac{1}{2\hbar L\omega_r}} (\hat{\Phi} + iL\omega_r \hat{Q}), \quad (2.41)$$

$$\hat{a} = \sqrt{\frac{1}{2\hbar L\omega_r}} (\hat{\Phi} - iL\omega_r \hat{Q}). \quad (2.42)$$

By inverting these relations we obtain the flux and charge operators $\hat{\Phi}$ and \hat{Q} . Calculating their time derivatives gives us the voltage and current operators $\hat{V} = i[\hat{H}, \hat{\Phi}]/\hbar$ and

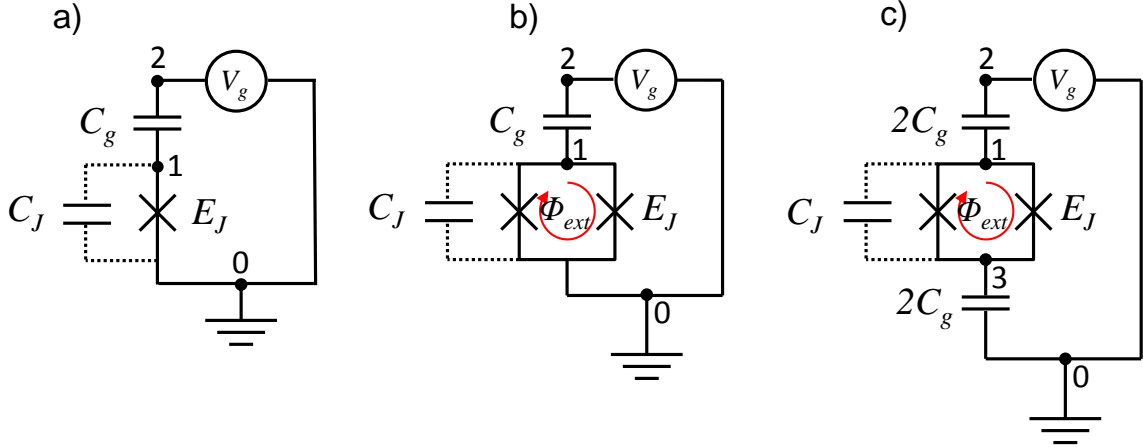


Figure 2.4: a) The circuit schematic of a Cooper Pair Box (CPB). The device consists of a Josephson junction capacitively coupled to a voltage source. The extra capacitance of the Josephson junction is modeled by a capacitor C_J . Charges can accumulate on the island between the voltage source and the Josephson junction. b) A *split Cooper pair box*, where instead of one junction two of them are arranged in a loop. With this geometry it is possible to tune the effective Josephson energy of the circuit by changing the magnetic flux inside the junction loop. c) The schematic of a split CPB capacitively coupled to ground. This schematic corresponds most closely to the experimental CPB circuit that we use in this work.

$$\hat{I} = i[\hat{H}, \hat{Q}]/\hbar:$$

$$\hat{V} = V_{rms} (\hat{a}^\dagger + \hat{a}), \quad (2.43)$$

$$\hat{\Phi} = \frac{V_{rms}}{\omega_r} (\hat{a}^\dagger + \hat{a}), \quad (2.44)$$

$$\hat{I} = i\omega_r C V_{rms} (\hat{a}^\dagger - \hat{a}), \quad (2.45)$$

$$\hat{Q} = iC V_{rms} (\hat{a}^\dagger - \hat{a}), \quad (2.46)$$

where $V_{rms} = \sqrt{\hbar\omega_r/2C}$ is the root-mean-square voltage corresponding to one photon in the resonator.

2.3.4 The Cooper Pair Box

The LC resonator discussed in the last section is one of the key elements for building quantum circuits. However, it is not possible to implement a superconducting qubit using such a linear resonator since the transition frequencies between all adjacent energy levels are equal, which makes it impossible to drive e.g. the $|0\rangle \rightarrow |1\rangle$ transition of the system without also exciting higher energy states. Therefore, to realize a qubit we need to introduce a non-linear element in the circuit. One way of doing this is to replace the linear inductance of the LC resonator by a non-linear one. A Josephson junction

conveniently provides such a non-linear inductance. The resulting circuit, called a *Cooper pair box (CPB)* contains thus a Josephson junction in parallel with a capacitance and is coupled to an input voltage source through a gate capacitance C_g , as shown in fig. 2.4a. Often one also uses two junctions in a loop instead of a single one, as shown in fig. 2.4b, which allows one to tune the effective Josephson energy of the system by changing the flux inside the junction loop. Finally, in our experimental setup, we can separate the bottom electrode of the CPB capacitively from the ground, as shown in fig. 2.4c. In this section we discuss only the circuit a), since b) can be mapped to the simpler version a) and the topology of c) is mathematically equivalent to that of b). The simple CPB circuit 2.4a consists of three nodes (including ground) and two branches. The flux Φ_2 is not independent since it is set by the voltage source V_g , so we can directly eliminate it from the equations. This leaves us with only one remaining active node Φ_1 . Using these specifications, the Lagrangian of the circuit is given as

$$\mathcal{L} = \frac{1}{2}C_J\dot{\Phi}_1^2 + \frac{1}{2}C_g(\dot{\Phi}_1 + V_g)^2 - E_J(1 - \cos\phi_1), \quad (2.47)$$

where $\phi_1 = \Phi_1/\varphi_0$. The canonical momentum Q_1 associated to the flux Φ_1 is given as

$$Q_1 = \frac{\partial \mathcal{L}}{\partial \dot{\Phi}_1} = C_J\dot{\Phi}_1 + C_g(V_g + \dot{\Phi}_1). \quad (2.48)$$

From this, we can directly calculate the Hamiltonian by using eq. (2.25) and substituting Q_1 as given by eq. (2.48) for $\dot{\Phi}_1$, which yields

$$\mathcal{H} = E_J(1 - \cos\phi_1) + \frac{(Q_1 - C_gV_g)^2}{2(C_J + C_g)} - \frac{1}{2}C_gV_g^2. \quad (2.49)$$

Quantization of the Hamiltonian is completed by replacing $Q_i \rightarrow \hat{Q}_i$ and $\phi_1 \rightarrow \hat{\phi}_1$ and imposing the commutation relations given by eqs. (2.28). If, in addition we introduce reduced operators for the charge $\hat{n} = \hat{Q}/2e$ and discard the energy stored in the voltage source (which is irrelevant), we obtain the Hamiltonian of the Cooper pair box, as formulated e.g. in the thesis of V. Bouchiat [11],

$$\hat{H} = E_C(\hat{n} - n_g)^2 - E_J \cos \hat{\theta}, \quad (2.50)$$

with $\hat{\theta} = \hat{\phi}_1$, $E_C = (2e)^2/(C_J + C_g)$ the charging energy of the Cooper pair box and $n_g = C_gV_g/2e$ the reduced gate charge.

For the split Cooper pair box as shown in fig. 2.4b, the treatment is slightly modified [21]. First of all, we write the Josephson energies of the two junctions as $E_{J1} = (1 + d)E_J/2$ and $E_{J2} = (1 - d)E_J/2$, where $d \in [0, 1]$ is the energy asymmetry between the junctions. When imposing an external phase $\phi_{ext} = \Phi_{ext}/\varphi_0$ in the loop, the potential

energy of the two junctions can be written as

$$\mathcal{V}_J = -\frac{E_J}{2} [(1+d) \cos(\phi_1 - \phi_{ext}/2) + (1-d) \cos(\phi_2 + \phi_{ext}/2)] \quad (2.51)$$

$$= -E_J \left[\cos \phi_1 \cos \frac{\phi_{ext}}{2} + d \sin \phi_1 \sin \frac{\phi_{ext}}{2} \right]. \quad (2.52)$$

The remaining part of the quantization process proceeds as above, yielding a Hamiltonian of the split Cooper pair box of the form

$$\hat{H}_{split} = E_C(\hat{n} - n_g)^2 - E_J \left[\cos \hat{\phi}_1 \cos \frac{\phi_{ext}}{2} + d \sin \hat{\phi}_1 \sin \frac{\phi_{ext}}{2} \right]. \quad (2.53)$$

This Hamiltonian can be recast in the form [21]

$$\hat{H}_{split} = E_C(\hat{n} - n_g)^2 - E'_J(d, \phi_{ext}) \cos [\hat{\phi}_1 + \gamma(\phi_{ext})], \quad (2.54)$$

with

$$E'_J(d, \phi_{ext}) = E_J \sqrt{\frac{1 + d^2 + (1 - d^2) \cos \phi_{ext}}{2}}, \quad (2.55)$$

$$\tan \gamma(\phi_{ext}) = -d \tan \frac{\phi_{ext}}{2}. \quad (2.56)$$

It is therefore possible to map the Hamiltonian of the split CPB to that of the single-junction one by defining $\hat{\theta} \rightarrow \hat{\phi}_1 + \gamma(\phi_{ext})$ and $E_J \rightarrow E'_J(d, \phi_{ext})$.

Using the Hamiltonian defined in eq. (2.50), we can calculate the eigen-wavefunctions of the simple Cooper pair box. The variables \hat{n} and $\hat{\theta}$ are conjugate such that $[\hat{\theta}, \hat{n}] = i\hbar$, the corresponding wave function $\Psi_k(\theta) = \langle \theta, k \rangle$ will therefore satisfy a Schrödinger equation of the form

$$E_k \Psi_k(\theta) = E_C \left(\frac{1}{i} \frac{\partial}{\partial \theta} - n_g \right)^2 \Psi_k(\theta) - E_J \cos(\theta) \Psi_k(\theta). \quad (2.57)$$

Since the potential $-E_J \cos(\theta)$ is 2π periodic, the solution will be of the form

$$\Psi_k(\theta) = \Psi_k(\theta + 2\pi), \quad (2.58)$$

which allows us to map eq. (2.57) to the so-called *Mathieu equation*

$$\frac{d^2 y}{dx^2} + [a - 2q \cos(2x)] y = 0. \quad (2.59)$$

The *Floquet theorem* states that all solutions to this equation can be written in the form

$$F(a, q, x) = \exp(i\mu x)P(a, q, x), \quad (2.60)$$

and the most general solutions are [21]

$$\Psi_k(r, q, \theta) = C_1 \exp(in_g \theta) \mathcal{M}_C \left(\frac{4E_k}{E_C}, -\frac{2E_J}{E_C}, \frac{\theta}{2} \right) + C_2 \exp(in_g \theta) \mathcal{M}_S \left(\frac{4E_k}{E_C}, -\frac{2E_J}{E_C}, \frac{\theta}{2} \right), \quad (2.61)$$

with

$$E_k = \frac{E_C}{4} \mathcal{M}_A \left(r_k, -\frac{2E_J}{E_C} \right). \quad (2.62)$$

Here, \mathcal{M}_C , \mathcal{M}_S are the cosine and since *Mathieu functions* and \mathcal{M}_A corresponds to the Mathieu characteristic value of each solution. Following the convention in [21] we order the E_k such that the energy increases with increasing k , yielding [48]

$$\begin{aligned} r_k(n_g) &= \sum_{l \pm 1} [\text{int}(n_g + l/2) \bmod 2] \\ &\times \left\{ \text{int}(n_g/2) + l(-1)^k [(k+1) \bmod 2] \right\} \end{aligned} \quad (2.63)$$

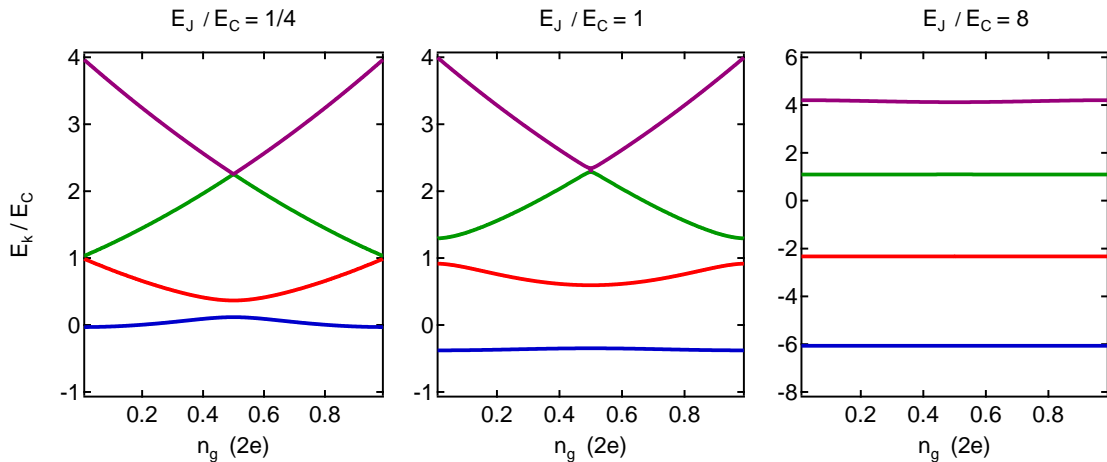


Figure 2.5: Energies of the first four energy levels of the Cooper pair box for different ratios E_J/E_C , plotted as a function of the gate charge n_g . As can be seen, for $E_J \gg E_C$, the charge-dispersion curve becomes almost completely flat.

We denote the energy differences between individual energy levels i, j by $E_{ij} = E_j - E_i$. We also define the absolute and relative anharmonicities of the first two energy levels as $\alpha \equiv E_{12} - E_{01}$ and $\alpha_r \equiv \alpha/E_{01}$. An in-depth treatment of the Cooper pair box can be found in [21]. Using the basis states $|i\rangle$ of the CPB, we can rewrite its Hamiltonian in the form

$$\hat{H} = \hbar \sum_{i=0} \omega_i |i\rangle \langle i|, \quad (2.64)$$

where $\hbar\omega_i$ is the energy associated to the i -th CPB state. Disregarding CPB levels $i \geq 2$, we can also formulate an approximate qubit Hamiltonian of the CPB of the form

$$\hat{H} = -\frac{\hbar\omega_{01}}{2}\hat{\sigma}_z, \quad (2.65)$$

where $\omega_{01} = \omega_1 - \omega_0$ is the frequency of the transition $|0\rangle \rightarrow |1\rangle$.

The Transmon Qubit

The Transmon qubit as developed in the Schoelkopf lab [48, 91] is a Cooper pair box whose charging energy is strongly reduced by putting a large capacitance in parallel to the Josephson junction, such that the device is in the regime $E_J \gg E_C$. As shown in fig. 2.5, in this regime the charge dispersion of the energy levels of the Cooper pair box becomes extremely weak, thus rendering the transition frequency E_{01} practically insensitive to the value of the gate charge n_g . This reduced sensitivity to charge noise is highly advantageous in experiments since it increases the coherence time of the qubit. However, when increasing the ratio E_J/E_C , we also reduce the anharmonicity α_r of the qubit, therefore limiting the speed of gate operations that can be realized with this system (driving errors related to weak anharmonicity will be discussed more thoroughly chapter 5). In the limit $E_J \gg E_C$ these qubit anharmonicities are well approximated by $\alpha \simeq -E_C/4$ and $\alpha_r \simeq -(2E_J/E_C)^{-1/2}$. α_r decreases only geometrically with E_J/E_C , whereas the sensitivity of the qubit to charge noise decreases exponentially with the ratio of Josephson and charging energy.

Decoherence of the Transmon

An in-depth derivation of the decoherence of the CPB and the Transmon can be found e.g. in [21, 48]. Here, we give the relevant expressions that we use to estimate the coherence of the Transmon qubits in our quantum processor. Fundamentally, *relaxation* and *dephasing* are the relevant decoherence mechanisms of the qubit, each one characterized by relaxation and dephasing rates Γ_1 and Γ_ϕ and corresponding coherence times $T_1 = \Gamma_1^{-1}$ and $T_\phi = \Gamma_\phi^{-1}$. Following the treatment by Cottet *et. al.* [21], a perturbation of the CPB Hamiltonian can be written as $\delta\hat{H}_\lambda = -\hbar/2(\hat{\mathbf{D}}_\lambda \cdot \boldsymbol{\sigma})\delta\lambda$, where $\hat{\mathbf{D}}_\lambda = 1/\hbar \cdot \partial\hat{H}/\partial\lambda$ describes the sensitivity of the Hamiltonian to a noise source λ . In the operator \mathbf{D} we can distinguish between transversal parts $\hat{\mathbf{D}}_{\lambda,\perp}$ that describe relaxation processes and longitudinal parts $\hat{\mathbf{D}}_{\lambda,z}$ that describe dephasing processes. For the relaxation processes, we can calculate the relaxation rate from the sensitivity $\hat{\mathbf{D}}_{\lambda,\perp}$ and spectral density of the noise channel $S_\lambda(\omega_{01})$ using Fermi's golden rule:

$$\Gamma_{S,\lambda}^{rel} = \frac{\pi}{2}|D_{\lambda,\perp}|^2 S_\lambda(\omega_{01}) \quad (2.66)$$

Similarly, for the dephasing processes $\hat{D}_{\lambda,z}$ we can calculate the dephasing rates using the corresponding sensitivities and spectral densities as

$$\Gamma_{S,\lambda}^\phi = \pi |D_{\lambda,z}|^2 S_\lambda(\omega = 0). \quad (2.67)$$

Here, the spectral density of the noise is evaluated at $\omega = 0$. If the noise is not regular at low frequencies $S_\lambda(\omega = 0)$ can diverge, hence it is often necessary to choose a cut-off frequency in order to renormalize the spectral density [21].

The most relevant couplings for relaxation and dephasing through the charge and current/phase channels of the CPB are

$$D_{n_g,z} = 2 \frac{E_C}{\hbar} (\langle 0 | \hat{n} | 0 \rangle - \langle 1 | \hat{n} | 1 \rangle) \quad (2.68)$$

$$D_{\phi_{ext}/2\pi,z} = \frac{2\pi\Phi_0}{\hbar} (\langle 1 | \hat{I} | 1 \rangle - \langle 0 | \hat{I} | 0 \rangle) \quad (2.69)$$

$$D_{n_g,\perp} = 4 \frac{E_C}{\hbar} |\langle 0 | \hat{n} | 1 \rangle| \quad (2.70)$$

$$D_{\phi_{ext}/2\pi,\perp} = \frac{4\pi\Phi_0}{\hbar} |\langle 0 | \hat{I} | 1 \rangle|. \quad (2.71)$$

Using these sensitivities and the spectral density of the corresponding noise parameter, we can calculate the relevant dephasing or relaxation rate. In the following paragraph we calculate the most relevant sensitivities for the CPB and give analytical expressions for the corresponding spectral noise densities and relaxation or dephasing rates.

Relaxation through the Charge Channel The spectral density of the charge noise seen by the qubit through its gate capacitance is given as

$$S_{V_g}(\omega) = \frac{\hbar\omega}{2\pi} \left[\coth\left(\frac{\hbar\omega}{2k_B T}\right) + 1 \right] \text{Re}[Z_g(\omega)]. \quad (2.72)$$

At low temperatures $k_B T \ll \hbar\omega$, $\coth(\hbar\omega/2k_B T) \approx 1$, so the resulting relaxation rate as given by eq. (2.66) simply becomes

$$\Gamma_1^{gate} = 16\pi\beta^2\omega_{01} \frac{\text{Re}[Z_g(\omega_{01})]}{R_K} |\langle 0 | \hat{n} | 1 \rangle|^2, \quad (2.73)$$

where $R_K = h/e^2$ and $\beta = C_g/C_\Sigma$ and $C_\Sigma = C_g + C_J$.

Relaxation through the Flux Channel The spectral density of magnetic flux fluctuations is given as

$$S_{\phi_{ext}}(\omega) = \left(\frac{M}{\Phi_0}\right)^2 S_I(\omega) = \left(\frac{M}{\Phi_0}\right)^2 \frac{\hbar\omega}{2\pi} \text{Re}\left(\frac{1}{Z_{fl}(\omega)}\right) \left[\coth\left(\frac{\hbar\omega}{2k_B T}\right) + 1 \right], \quad (2.74)$$

where $Z_{fl}(\omega)$ is the impedance of the flux line coupled to the qubit. The sensitivity of the qubit to flux noise is given as

$$D_{\phi_{ext},\perp} = \frac{E_J}{2\hbar} \left(\langle 0 | \cos \hat{\theta} | 1 \rangle \sin \frac{\phi_{ext}}{2} - d \langle 0 | \sin \hat{\theta} | 1 \rangle \cos \frac{\phi_{ext}}{2} \right). \quad (2.75)$$

Due to parity, the first term in eq. (2.75) is usually small compared to the second one and can be disregarded, yielding a sensitivity to relaxation through the flux channel $\propto d \cos(\phi_{ext}/2)$.

Dephasing through the Charge Channel Noise in the gate charge n_g randomly changes the transition frequency of the CPB and induces dephasing. The corresponding dephasing rate in the case of $1/f$ gate charge noise can be written as [21, 86]

$$\Gamma_{\phi}^{\delta n_g} \simeq 3.7A \left| \frac{\partial \omega_{01}}{\partial n_g} \right|, \quad (2.76)$$

where $A \approx 10^{-5}$ is an heuristic parameter that describes the amplitude of the gate charge fluctuations. In the limit $E_J \gg E_C$ this rate can be written analytically as

$$\Gamma_{\phi}^{\delta N_g} \simeq 3.7 \frac{A\pi}{\hbar} |(\epsilon_1 - \epsilon_0) \sin(2\pi N_g)| \leq 3.7 \frac{A\pi}{\hbar} |\epsilon_1|, \quad (2.77)$$

where ϵ_i is the energy modulation amplitude of the i -th CPB level, given as [48]

$$\epsilon_m \simeq (-1)^m E_C \frac{2^{4m+3}}{m!} \sqrt{\frac{2}{\pi}} \left(\frac{2E_J}{E_C} \right)^{\frac{m}{2} + \frac{3}{4}} \exp \left(-\sqrt{\frac{32E_J}{E_C}} \right). \quad (2.78)$$

As can be seen, the sensitivity of the CPB to charge noise decreases exponentially with the ratio E_J/E_C for $E_J \gg E_C$.

Dephasing through the Flux Channel Analogously to charge-induced dephasing, one can consider dephasing due to $1/f$ -type flux noise seen by the CPB, which has an associated dephasing rate

$$\Gamma_{\phi}^{\delta \phi_{ext}} \simeq 3.7A \left| \frac{\partial \omega_{01}}{\partial \phi_{ext}} \right| \quad (2.79)$$

with a typical noise amplitude $A = 10^{-5}$ [48]. For the general, asymmetric CPB in the limit $E_J \gg E_C$ we obtain a dephasing rate

$$\Gamma_{\phi}^{\delta \phi_{ext}} \approx \frac{1}{2} A \omega_{01}^{\max} \left| \sin(\phi_{ext})(1-d^2) \left(\frac{1+d^2+(1-d^2)\cos(\phi_{ext})}{2} \right)^{-3/4} \right| \quad (2.80)$$

where $\omega_{01}^{\max} = \sqrt{2E_C E_J}/\hbar$ is the maximum transition frequency of the qubit.

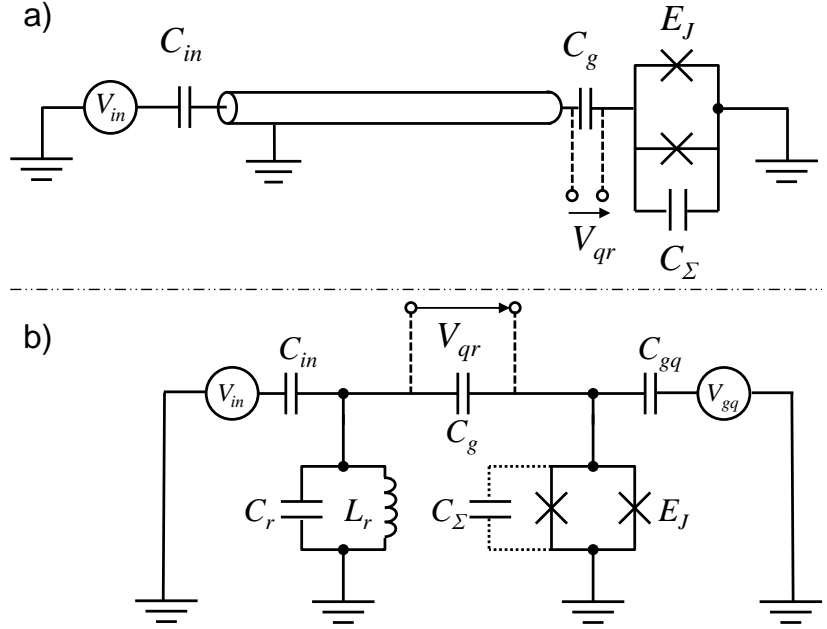


Figure 2.6: a) Schematic of a typical CQED circuit, consisting of a Transmon qubit capacitively coupled to a transmission line resonator. c) The equivalent circuit using a lumped-element model of the $\lambda/2$ resonator.

2.4 Circuit Quantum Electrodynamics

In this section, we discuss the physics of a Transmon qubit that is coupled to a harmonic oscillator. The corresponding research field is today referred to as *circuit quantum electrodynamics* (CQED). This term was coined in reference to *cavity quantum electrodynamics*, a research field that investigates the physics of Rydberg atoms interacting with a microwave cavity. In circuit QED, qubits that act as “artificial atoms” interact with coplanar or lumped elements resonators on a chip, where the qubit-resonator system can be represented as in fig. 2.6. There, a Transmon qubit is capacitively coupled to a $\lambda/2$ resonator which itself is capacitively coupled to an input transmission line. The Hamiltonian of the resonator and the qubit are given by eqs. (2.40) and (2.65). Due to the capacitance between the qubit and the resonator, a coupling energy between the two arises. The full Hamiltonian of the qubit-resonator system can therefore be written as

$$\hat{H}_{cqed} = \hat{H}_r + \hat{H}_q + \hat{H}_{qr}, \quad (2.81)$$

where \hat{H}_r and \hat{H}_q are the Hamiltonians of the resonator and the qubit as given by eqs. (2.40) and (2.50), respectively, and \hat{H}_{qr} is the interaction Hamiltonian between them. For small couplings $C_g \ll C_{in}, C_r, C_\Sigma$, we can estimate the coupling energy between the qubit and the resonator simply as

$$\hat{H}_{qr} = \frac{1}{2} C_g \hat{V}_{qr}^2 = \frac{1}{2} C_g \left(V_{rms}^0 (a^\dagger + a) - \hat{V} \right)^2, \quad (2.82)$$

where \hat{V}_{qr} is the voltage across the coupling capacitance C_g and $\hat{V} = 2e/C_\Sigma \cdot (n_g - \hat{n})$ is the voltage across the Transmon electrodes. A rigorous treatment of the coupling energy, which is necessary for large coupling capacitances $C_{qr} \simeq C_r, C_\Sigma$, would require a full quantization of the coupled qubit-resonator circuit, as performed e.g. in [66]. The coupling energy in eq. (2.83) can be rewritten as

$$\begin{aligned}\hat{H}_{qr} &= \frac{1}{2}C_g \left[V_{rms}^0(a^\dagger + a) - \frac{2e}{C_\Sigma}(n_g - \hat{n}) \right]^2 \\ &= 2e\beta V_{rms}^0 \hat{n}(a^\dagger + a) + \dots\end{aligned}\quad (2.83)$$

in the limit $\beta = C_g/C_\Sigma \ll C_\Sigma$. The terms omitted in eq. (2.83) correspond to energy shifts of the qubit and the resonator which are not directly relevant for the coupling between them. In the limit where the resonator capacity $C_r \gg C_\Sigma$, we can write the effective Hamiltonian of the qubit-resonator system using the uncoupled basis states $|i\rangle$ of the Transmon as

$$\hat{H} = \hbar \sum_{j=0} \omega_j |j\rangle \langle j| + \hbar \omega_r \hat{a}^\dagger \hat{a} + \hbar \sum_{i \neq j} g_{ij} |i\rangle \langle j| (\hat{a} + \hat{a}^\dagger), \quad (2.84)$$

where the coupling energies g_{ij} are given as

$$\hbar g_{ij} = 2\beta e V_{rms}^0 \langle i | \hat{n} | j \rangle = \hbar g_{ji}^* \quad (2.85)$$

When the coupling between the resonator and the Transmon is weak, such that $g_{ij} \ll \omega_r, E_{01}/\hbar$, we can ignore the terms in eq. (2.84) that describe simultaneous excitation or de-excitation of the Transmon and the resonator and obtain the so-called *rotating wave approximation*, yielding the Hamiltonian

$$\hat{H} = \hbar \sum_{j=0} \omega_j |j\rangle \langle j| + \hbar \omega_r \hat{a}^\dagger \hat{a} + \hbar \sum_{i=0} g_{i,i+1} (|i\rangle \langle i+1| \hat{a}^\dagger + |i+1\rangle \langle i| \hat{a}) \quad (2.86)$$

The term $|i\rangle \langle i+1| \hat{a}^\dagger$ describes the creation of a photon in the resonator accompanied by the de-excitation of the n-level system by one energy level and the term $|i+1\rangle \langle i| \hat{a}$ describes the opposite process.

2.4.1 Qubit Driving

When driving the qubit with a large signal we can model the drive as a classical parameter $V_d(t)$. The coupling Hamiltonian in this case is given as

$$\hat{H}_d = 2\beta e V_d(t) \hat{n} \quad (2.87)$$

In the reduced $\{|0\rangle, |1\rangle\}$ basis, this Hamiltonian can be written as

$$\hat{H}_d = 2\beta e V_d(t) \begin{pmatrix} 0 & n_{01}^* \\ n_{01} & 0 \end{pmatrix} \quad (2.88)$$

where $n_{01} = \langle 0 | \hat{n} | 1 \rangle$. Usually, we apply the drive voltage through the resonator coupled to the qubit. That resonator acts then as a band-pass filter which filters the voltage seen by the qubit. For an input drive signal at a fixed frequency ω , $V_{in}(t) = V_{in} \cdot \cos \omega t$, the voltage $V_d(t) = V_d \cdot \cos \omega t$ seen by the qubit at its gate capacitance is given as

$$V_d = V_{in} \cdot \frac{C_{in} L_r \omega^2}{(C_{in} + C_r) L_r \omega^2 - 1} \quad (2.89)$$

At resonance where $\omega = \omega_0 = 1/\sqrt{C_r L_r}$, we have $V_d = V_{in}$.

2.4.2 Dispersive Limit & Qubit Readout

When the qubit frequency is far detuned from the resonator frequency such that $|\omega_{ij} - \omega_r| \gg g_{ij}$, direct energy exchange between the qubit and the resonator is completely suppressed and only a dispersive shift of the transition frequency of both systems remains as an effect of the coupling between them. This effect has been discussed e.g. in [10, 48] and yields the effective Hamiltonian

$$\hat{H}_{eff} = \frac{\hbar \omega'_{01}}{2} \hat{\sigma}_z + (\hbar \omega'_r + \hbar \chi \hat{\sigma}_z) \hat{a}^\dagger \hat{a}, \quad (2.90)$$

where we have used the two-level qubit Hamiltonian as given by eq. (2.65). Here, the resonance frequencies of the qubit and the resonator are shifted as $\omega'_{01} = \omega_{01} + \chi_{01}$ and $\omega'_r = \omega_r - \chi_{12}/2$ and the dispersive shift is given as $\chi = \chi_{01} - \chi_{12}/2$, where $\chi_{ij} = g_{ij}^2 / (\omega_{ij} - \omega_r)$. As can be seen, for a state with n photons the qubit transition frequency ω_{01} is given as

$$\omega_{01}^n = \omega'_{01} + 2\chi n. \quad (2.91)$$

Thus, there is a dispersive shift of the qubit transition frequency that is proportional to the number of photons in the resonator. Likewise, the resonance frequency of the resonator gets also shifted by $\pm \chi$ depending on the state of the qubit. The latter effect is very useful since it allows us to read out the state of the qubit by measuring the state-dependent frequency displacement of the resonator, as will be explained now.

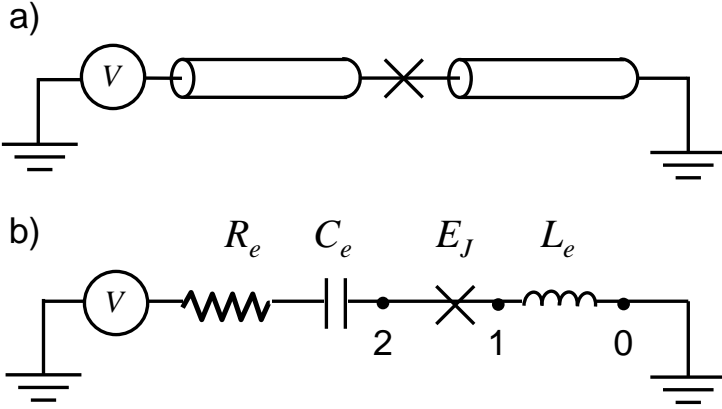


Figure 2.7: a) Circuit schematic of the CJBA, consisting of two parts of transmission line joined by a Josephson junction, forming a non-linear $\lambda/2$ resonator. b) Equivalent lumped elements circuit model of the CJBA.

2.4.3 The Josephson Bifurcation Amplifier

In this section we discuss the physics of superconducting nonlinear bifurcation amplifiers, which we use to realize a single-shot readout scheme for our qubits. Most notably, we discuss the so-called *cavity Josephson bifurcation amplifier (CJBA)*, as shown in fig. 2.7a. A detailed discussion of the CJBA can be found e.g. in [70]. The device consists of a transmission line resonator with a Josephson junction embedded in its central conductor. We can model the whole circuit as a lumped elements resonator, as shown in fig. 2.7b. The Hamiltonian of the resonator, disregarding the resistor and the voltage source, is

$$H = \frac{\Phi_1^2}{2L_e} - E_J \cos\left(\frac{\Phi_2 - \Phi_1}{\varphi_0}\right) + \frac{Q_2^2}{2C_e}. \quad (2.92)$$

By using the current-phase relation of the Josephson junction we obtain the current

$$I = \frac{\Phi_1}{L_e} = I_0 \sin\left(\frac{\Phi_2 - \Phi_1}{\varphi_0}\right). \quad (2.93)$$

We can hence write $\Phi_1 = g(\Phi_2)$. When we develop this equation to second order in Φ_2 and insert in eq. (2.92), we obtain

$$H = \frac{\phi_2^2}{2L_t} + \frac{Q_2^2}{2C_e} - \frac{1}{24} p^3 \frac{\Phi_2^4}{L_t \varphi_0^2}, \quad (2.94)$$

where $L_t = L_J + L_e$ and $p = L_J/L_t$ is the so-called *participation ratio*. Quantizing this Hamiltonian and writing Φ_2 and Q_2 in terms of creation and annihilation operators yields, up to second order, the Hamiltonian

$$H_{NL} = \hbar \omega_r \left(\hat{a}^\dagger \hat{a} + \frac{K}{2} \hat{a}^{\dagger 2} \hat{a}^2 \right), \quad (2.95)$$

where $\omega_r = 1/\sqrt{L_t C_e}$, $R_K = h/e^2$ and $K = -\pi p^3 Z_e / R_K$ is the so-called *reduced Kerr constant*. When subjecting the resonator to a classical drive signal

$$H_p/\hbar = \epsilon_p e^{-i\omega_p t} \hat{a}^\dagger + \text{h.c.}, \quad (2.96)$$

the complex amplitude of the intra-resonator field α will satisfy the equation

$$i \left(\Omega \frac{\kappa}{2} \alpha + K |\alpha|^2 \alpha \right) + \frac{\kappa}{2} \alpha = -i \epsilon_p, \quad (2.97)$$

where $\Omega = 2Q(1 - \omega_p/\omega_r)$. For certain drive parameters, this equation has one or two stable solutions for α . Fig. 2.8a shows the current in the resonator as a function of Ω , plotted for several values of the drive power $P_p \propto |\epsilon_p|^2$. Fig. 2.8b shows the different regimes of the resonator as a function of the input power and the detuning Ω . For drive frequencies with $\Omega > \Omega_c = \sqrt{3}$, a bistable region exists in the phase diagram, in which we typically operate the resonator when using it as a CJBA readout of our qubit. For this, we make use of the dispersive shift of the resonance frequency ω_r caused by the qubit, which allows us to map the qubit state to one of the bistable resonator states.

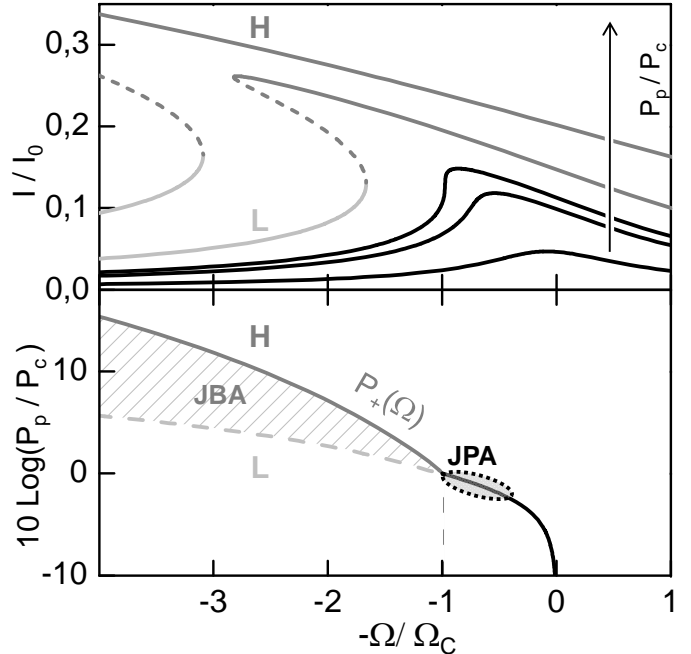


Figure 2.8: a) Current in the driven non-linear resonator as a function of the drive detuning Ω , plotted for various drive powers P_p . For drive detunings $\Omega > \Omega_c$, the resonator becomes bistable above a certain power threshold $P_p > P_c$. b) Phase diagram of the non-linear resonator, showing the regions of bistability as a function of the drive power P_p and the drive detuning Ω . For $\Omega > \Omega_c$, a bistable region exists that permits to operate the resonator as a CJBA.

Operation Principle

We can use the CJBA to read out the qubit state using the dispersive interaction between the qubit and the resonator as given by eq. (2.90). Due to this interaction, the frequency of the resonator gets shifted depending on the qubit state by $\pm\chi \simeq g_{01}^2/\Delta$ (neglecting the effect of higher Transmon levels), where $\Delta = \omega_r - \omega_{01}$ is the frequency difference

between qubit and resonator. Fig. 2.9b shows again the phase diagram of the CJBA, indicating the stability regions of the different solutions L (low-amplitude) and H (high-amplitude) of the driven system for two different qubit states. If we drive the resonator at a frequency ω_m and ramp the drive power up to point A as indicated in the diagram, the resonator will remain in the low-amplitude state L if the qubit is in state $|0\rangle$, whereas it will switch to the high-amplitude state H if it is in $|1\rangle$. We can thus map the state of the qubit to one of the two states of the resonator, and since these two states can be easily distinguished by measuring the phase of the reflected resonator drive signal, we can obtain a single-shot readout of the qubit state. The measurement of the phase of the reflected drive signal has to be carried out during a long time interval (typically $1 - 2 \mu\text{s}$) to distinguish between the two oscillator states with certainty. To avoid further switching processes during the measurement of the reflected phase, we reduce the drive power of the resonator down to point B in fig. 2.9b. There, the switching probability of the resonator regardless of the qubit state is very small, thus virtually no switching events will occur and we can hence measure the reflected phase of the drive signal for an arbitrarily long time without being limited by spurious switching events. This phase of the readout is usually referred to as *latching*.

In theory, the CJBA readout method is able to achieve perfect readout fidelity. However, in reality several factors can degrade its performance:

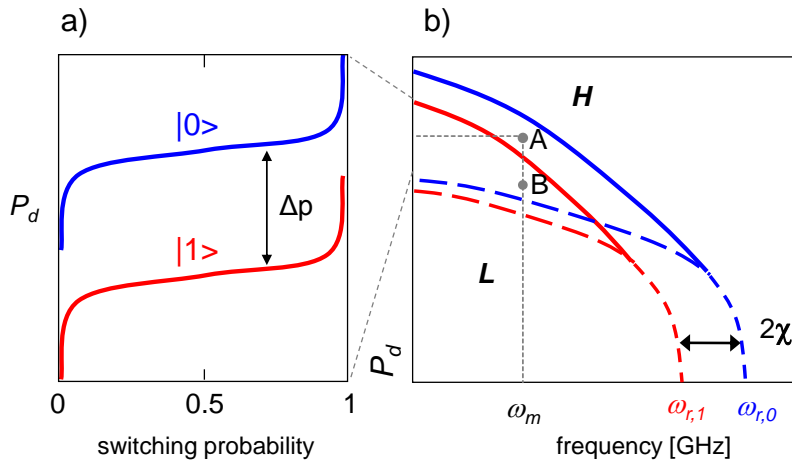


Figure 2.9: a) The switching probability of the CJBA as a function of the input drive power, shown for the qubit in the states $|0\rangle$ and $|1\rangle$. b) The bifurcation diagram of the CJBA, shown for the qubit in the states $|0\rangle$ and $|1\rangle$. L and H indicate solutions with low and high amplitude, respectively.

- Since the switching of the resonator is a stochastic process, the associated switching probability will exhibit a sigmoidal dependence on the drive power, as shown in fig. 2.9. Now, if the shift of this distribution along the power axis which is induced by the shift of the resonator frequency that depends itself on the state of the qubit is less than the width of the distribution, erroneous switching will occur and reduce the fidelity of the readout.
- If the qubit state changes during the measurement phase, e.g. due to qubit relaxation or excitation, the resonator state will, with high probability, also fall to

the state corresponding to the new qubit state, thereby producing a wrong readout signal.

- The resonator state can switch back from H to L during the latching phase of the readout (so-called *retrapping*), producing a wrong readout value.

With the CJBA, a single-shot readout contrast of 93 % has been achieved in past experiments [56].

2.4.4 Qubit Decoherence in CQED

In this section we discuss the relaxation and dephasing mechanisms specific to the CQED architecture.

Relaxation In CQED, the qubit is coupled capacitively to a resonator, which itself is coupled to a low-Q input transmission line. The qubit can relax into this transmission line through the gate circuit. The resulting relaxation rate is given by eq. (2.73). If we assume that the Transmon sees only the impedance of the readout resonator through its gate capacitance, as given by eq. (2.32), we can insert the impedance of the resonator in the equation and obtain the resulting relaxation rate:

$$\begin{aligned}\Gamma_1^{Purcell} &= 2\pi \frac{\omega_{01}}{Z_0 \omega_r^2} g_{01}^2 \operatorname{Re}[Z(\omega_{01})] \\ &= \kappa \cdot \frac{g_{01}^2}{\Delta^2 + \kappa^2/4}\end{aligned}\quad (2.98)$$

As can be seen, the rate is proportional to $(\Delta^2 + \kappa^2/4)^{-1}$ ($\approx \Delta^{-2}$ for $\Delta \gg \kappa$). The relaxation (or emission) rate of the Transmon compared to the relaxation rate of a qubit get thus modified by the presence of the resonator, which is the so-called *Purcell effect* [73]. For our processor, this effect is advantageous since it shields the qubit from the low impedance environment presented by the input transmission line and increases thus its relaxation time compared to a direct gate coupling to the input line. For a real-world qubit chip, we have to take into account further capacitive couplings of the qubit to e.g. the fast flux line, which will also contribute to the relaxation rate.

Dephasing Besides the usual dephasing mechanisms due to the presence of gate charge noise, dephasing can occur due to photon-number fluctuations in the resonator which affects the qubit frequency through the induced AC-Stark shift of its frequency [7, 8, 76].

The sensitivity of the qubit to fluctuations of the photon number n can be derived in the dispersive limit from the Hamiltonian (2.90) as

$$\delta\hat{H}_{\bar{n}} = \hbar\delta\bar{n}\chi\hat{\sigma}_z = -\frac{\hbar}{2}(\hat{D}_{\bar{n}} \cdot \hat{\sigma}_z) \cdot \delta\bar{n}, \quad (2.99)$$

where $\hat{D}_{\bar{n}} = -2\chi$. When driving the resonator, shot-noise induced photon number fluctuations δn will randomly change the transition frequency of the qubit through the AC Stark effect and cause the qubit phase $\phi(t)$ to dephase. In the limit where the fluctuations of n are slow compared to the qubit frequency(??), we can model the dephasing according to the equation

$$\delta\phi(t) = 2\chi \int_0^t d\tau \delta n(\tau) \quad (2.100)$$

The dephasing rate of the qubit induced by this noise can be calculated from the correlator

$$\langle \hat{\sigma}_-(t)\hat{\sigma}_+(0) \rangle = \langle e^{-i\delta\phi(t)} \rangle. \quad (2.101)$$

Here, for a linear resonator with a loss rate κ , the correlator of the photon-number noise $\delta n(t)$ is given as

$$\langle \delta n(t_1)\delta n(t_2) \rangle = \bar{n}e^{-\frac{\kappa}{2}|t_1-t_2|} \quad (2.102)$$

Inserting this in eq. (2.101) yields a relaxation rate in the limit $t \gg \kappa$ of

$$\Gamma_{\phi}^{\bar{n}} = \frac{8\chi^2}{\kappa}\bar{n} \quad (2.103)$$

As expected, the dephasing rate depends on the dispersive shift χ and the resonator photon loss-rate κ .

2.4.5 Qubit-Qubit Interaction

In this section we discuss possible qubit-qubit coupling schemes. We regard a direct coupling scheme involving a capacitive coupling between two qubits and an indirect scheme involving the coupling of multiple qubits to a resonator which acts as a *quantum bus*.

Direct Capacitive Coupling

A direct capacitive coupling C_{qq} between two qubits yields a coupling Hamiltonian of the form

$$\hat{H}_{qq} = \frac{1}{2}C_{qq}\hat{V}_{qq}^2 = \frac{1}{2}C_{qq}\left[\frac{2e}{C_{\Sigma 1}}(n_{g1} - \hat{n}_1) - \frac{2e}{C_{\Sigma 2}}(n_{g2} - \hat{n}_2)\right]^2 \quad (2.104)$$

$$= \frac{4e^2C_{qq}}{C_{\Sigma 1}C_{\Sigma 2}}\hat{n}_1\hat{n}_2 + \dots \quad (2.105)$$

Again, this equation is valid in the limit where $C_{qq} \ll C_{\Sigma 1}, C_{\Sigma 2}$. For larger capacitances C_{qq} the coupling gets renormalized by a factor $\alpha = 1/(1 - C_{qq}^2/[C_{\Sigma 1}C_{\Sigma 2}])$ [66]. Rewriting this coupling in the basis of uncoupled qubit states yields the effective Hamiltonian

$$\hat{H}_{qq} = \hbar g_{qq}(\sigma_1^+ \sigma_2^- + \sigma_1^- \sigma_2^+), \quad (2.106)$$

where $\sigma^+ = |1\rangle\langle 0|$ and $\sigma^- = |0\rangle\langle 1|$ and $\sigma_1^\pm = \sigma^\pm \otimes I$, $\sigma_2^\pm = I \otimes \sigma^\pm$ and where we have defined the effective qubit-qubit coupling as $\hbar g_{qq} = 4e^2C_{qq}/C_{\Sigma 1}C_{\Sigma 2}$. Full energy exchange between the qubits is achieved when the qubit frequencies are on resonance. For the more general case of two coupled n-level Transmons, the coupling Hamiltonian takes a slightly more complicated form, as discussed in the Appendix. The time evolution operator of the Hamiltonian in eq. (2.106) yields a swapping interaction of the form

$$i\text{SWAP}(t, \Delta) = \begin{pmatrix} 1 & 0 & 0 & 0 \\ 0 & \cos t g_e - i \frac{\Delta}{g_e} \sin t g_e & i \frac{g_{qq}}{g_e} \sin t g_e & 0 \\ 0 & i \frac{g_{qq}}{g_e} \sin t g_e & \cos t g_e + i \frac{\Delta}{g_e} \sin t g_e & 0 \\ 0 & 0 & 0 & 1 \end{pmatrix} \quad (2.107)$$

where $\Delta = \omega_{01}^2 - \omega_{01}^1$ is the detuning between the qubits and $g_e = \sqrt{4g_{qq}^2 + \Delta^2}$ is the effective swapping frequency. Using this interaction, it is straightforward to implement e.g. an $\sqrt{i\text{SWAP}}$ or $i\text{SWAP}$ quantum gate by tuning the qubits non-adiabatically from an off-resonant condition $\Delta \gg g_{qq}$ to a resonance-condition $\Delta = 0$ and letting them interact there for a well-defined amount of time before re-establishing the large detuning ($t = \pi/4g_e$ for the $\sqrt{i\text{SWAP}}$ gate and $t = \pi/2g_e$ for the $i\text{SWAP}$ gate).

Coupling Bus

For this particular coupling scheme, we consider two (or more) Transmon qubits coupled to the same resonator. Blais *et. al.* [9] showed that extending the single-qubit rotating-wave Hamiltonian as given in eq. (2.86) to the case of two qubits coupled to a resonator

yields an effective qubit-qubit coupling Hamiltonian of the form

$$\hat{H}_{2q} = \hbar \frac{g_1 g_2 (\Delta_1 + \Delta_2)}{2\Delta_1 \Delta_2} (\sigma_1^+ \sigma_2^- + \sigma_1^- \sigma_2^+) \quad (2.108)$$

This approximation is valid in the limit of large qubit-resonator detuning where $\Delta_1 \gg g_1, \Delta_2 \gg g_2$ with $\Delta_{1,2} = \omega_{01}^{1,2} - \omega_r$ the detuning of the $|0\rangle \rightarrow |1\rangle$ transition frequency of each qubit to the bus resonator. Full energy-exchange between the qubits is achieved when the qubit frequencies are on resonance. By detuning the qubits from the resonator, the effective coupling constant can be varied, which is often advantageous. The time evolution operator resulting from eq. (2.108) is identical to eq. (6.20) when taking into account the modified coupling constant $g_{qq,r} = g_1 g_2 (\Delta_1 + \Delta_2) / 2\Delta_1 \Delta_2$.

2.5 Master Equation Formalism

As we have explained, the qubits that we use in this work are subjected to decoherence. This means that their quantum state will at least partially evolve in a non-unitary way, making it impossible to model their evolution using a Schrödinger equation approach alone. In this work we will therefore employ the *master equation approach*, which is a more powerful formalism that can treat the qubit register as an *open quantum system* which interacts with its environment.

A detailed introduction to the master equation formalism can be found e.g. in [42]. Here we give only a brief overview of the most relevant concepts. The formalism describes the interaction of a quantum system A , described by its density matrix ρ_A defined in a Hilbert space \mathcal{H}_A , with an environment E that interacts with A and induces a non-unitary evolution of the density operator ρ_A .

In general, any evolution of the quantum system ρ_A between two points in time can be described by a so-called *quantum map*. Such a quantum map transforms ρ_A into a new matrix $\mathcal{L}_A(\rho_A)$. It can be described as a linear *super-operator* acting in the space of operators defined in \mathcal{H}_A . To be a valid quantum operator, \mathcal{L}_A must fulfill the following conditions:

- **Linearity:** The operator \mathcal{L}_A must be linear, i.e. $\mathcal{L}_A(p\rho_A + q\rho'_A) = p\mathcal{L}_A(\rho_A) + q\mathcal{L}_A(\rho'_A)$ with $p + q = 1$.
- **Preservation of $\text{Tr}(\rho_A)$:** The operator \mathcal{L}_A must preserve the unity trace of ρ_A , i.e. $\text{Tr}(\mathcal{L}_A(\rho_A)) = 1$.
- **Complete Positivity:** $\mathcal{L}_A(\rho_A)$ must be positive, i.e. $\langle \phi^{(A)} | \mathcal{L}_A(\rho_A) | \phi^{(A)} \rangle \geq 0$ for all $|\phi^{(A)}\rangle$ in \mathcal{H}_A . In addition, for any composite quantum system $A \otimes B$, the quantum

map $\mathcal{L}_A \otimes 1_B$ (where 1_B is the identity super-operator acting in \mathcal{H}_B) must be positive, i.e.

$$\langle \phi^{(AB)} | \mathcal{L}_A \otimes 1_B(\rho_{AB}) | \phi^{(AB)} \rangle \geq 0$$

for all $|\phi^{(AB)}\rangle$ in \mathcal{H}_{AB} .

Under these conditions it can be shown that any quantum map \mathcal{L}_A can be expressed as a sum of operators [49]

$$\mathcal{L}_A(\rho_A) = \sum_{\mu=0}^{N_k} M_{\mu} \rho_A M_{\mu}^{\dagger} \quad (2.109)$$

where $N_k \leq N_A^2$ and N_A is the dimension of the Hilbert space \mathcal{H}_A and M_{μ} are the *Kraus operators* of the quantum map. These operators satisfy the normalization condition

$$\sum_{\mu=0}^{N_k} M_{\mu}^{\dagger} M_{\mu} = 1. \quad (2.110)$$

Now, we can also use a quantum map \mathcal{L}_{τ} to describe the evolution of a density matrix $\rho_A(t)$ during an infinitesimal time τ . In this case, we can approximatively write the time derivative of $\rho(t)$ as

$$\frac{d\rho_A(t)}{dt} = \frac{\mathcal{L}_{\tau}[\rho_A(t)] - \rho_A(t)}{\tau}. \quad (2.111)$$

In order for this approximation to be valid, τ needs to be longer than the “memory time” of correlations between the system A and its environment and smaller than the characteristic evolution time of system A [42]. In general, since $\mathcal{L}_{\tau} \rightarrow \mathbb{1}$ for $\tau \rightarrow 0$, the Kraus operators M_{μ} of the process \mathcal{L}_{τ} will depend on τ and can be usually written as $M_{\mu} = \sqrt{\tau} L_{\mu}$, where the L_{μ} are the time-independent *Lindblad operators*. By developing eq. (2.111) up to first order in τ , we obtain the so-called *Lindblad master equation*

$$\frac{d\rho_A}{dt} = -\frac{i}{\hbar}[H_A, \rho] + \sum_{\mu=1} \left(L_{\mu} \rho_A L_{\mu}^{\dagger} - \frac{1}{2} L_{\mu}^{\dagger} L_{\mu} \rho_A - \frac{1}{2} \rho_A L_{\mu}^{\dagger} L_{\mu} \right), \quad (2.112)$$

This equation describes the evolution of quantum system under a Hamiltonian H_A and coupled to an environment that is simulated by the non-unitary action of the operators L_{μ} . Often these operators can be guessed or derived from the relevant decoherence mechanism present in the quantum system. We will make extensive use of eq. (2.112) in this work to simulate the dynamics of the qubit register of our quantum processor and fit experimental data to a master equation model of our system.

Chapter 3

Realizing a Two-Qubit Processor

This chapter discusses the design process for the realization of the two-qubit processor used in this thesis work. We start by introducing the general constraints we face when designing a two-qubit processor, followed by a component-wise discussion of the individual parts of the processor and the associated parameters we need to choose for them.

3.1 Introduction & Motivation

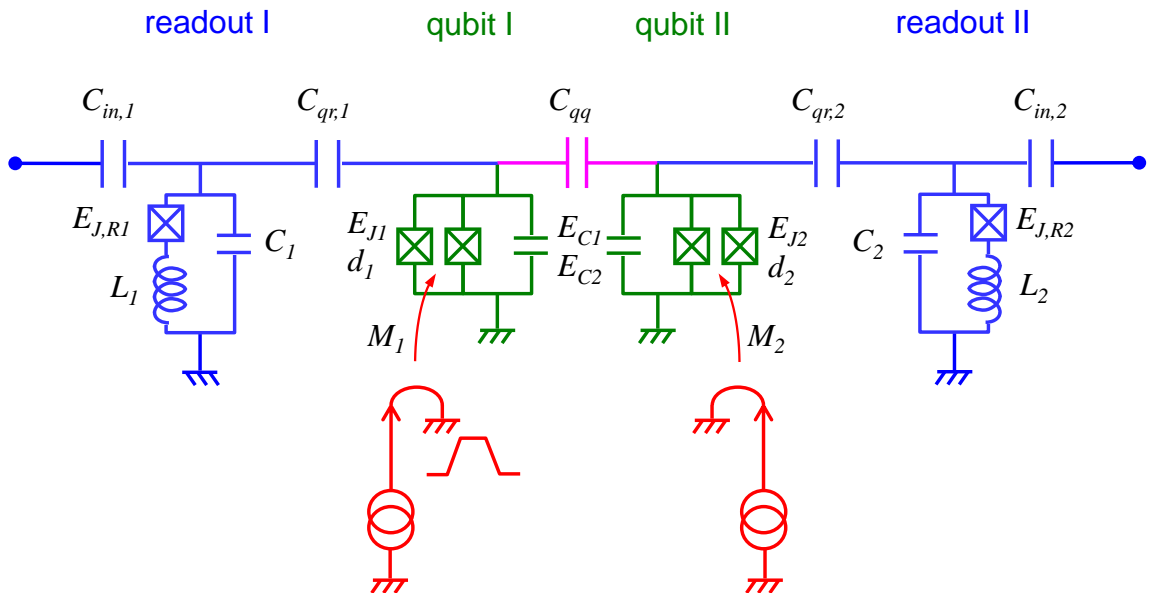


Figure 3.1: The circuit schematic of the two-qubit processor used in this work, together with all parameters that have to be chosen. Shown are the two Transmon qubits in green, the drive and readout circuit in blue, the fast flux lines in red and the coupling capacitance in magenta.

As discussed in the introduction, the most simple imaginable quantum processor

consists of two qubits that can be manipulated and read out individually, and between which one can realize a universal two-qubit gate. We implement such a two-qubit processor using two Transmon qubits that are coupled by a fixed capacitor and that can be read out individually by a pair of cavity Josephson bifurcation amplifiers (CJBAs). Figure 3.1 shows the circuit diagram of our processor with all relevant design parameters. Shown are the two qubits in green, the drive and readout circuit in red, the coupling capacitance between them in magenta, and in red fast flux lines required to tune the qubit frequencies (as we show below).

3.1.1 Processor Operation

We want to perform three basic operations with the quantum processor:

- **Single-qubit gates:** Manipulating a single qubit by rotating its Bloch vector around the X , Y or Z axis of the Bloch sphere.
- **Two-qubit gate:** Performing a (universal) two-qubit gate, in this work in particular the $\sqrt{i\text{SWAP}}$ and $i\text{SWAP}$ gates.
- **Qubit readout:** Performing single-shot readout of the state of each qubit, possibly simultaneously for both of them.

The parameter requirements for each of these operations are usually conflicting: For single-qubit manipulation, no interaction between the qubits must be present, hence the qubit frequencies need to be strongly detuned. However, to implement the two-qubit gates, strong resonant interaction between the qubits is required, hence the two qubit frequencies should be resonant. Furthermore, during qubit manipulation the relaxation of the qubit state through the readout resonator should be negligible, hence the frequency detuning between each qubit and its readout resonator should be large, as discussed in section . On the other hand, to obtain a high state fidelity during the readout of the qubit state, the interaction between the qubit and its readout resonator should be large, which requires a small frequency detuning between the two.

We solve these conflicting requirements by dynamically changing the qubit frequencies during the operation of the processor using fast on-chip flux lines. Fig. 3.2 illustrates this basic operating principle of the two-qubit processor: For each of the three basic operations (single-qubit manipulation, two-qubit gate and readout), we choose a different set of qubit frequencies $f_{01}^{I,II}$. For the single-qubit gates, the two frequencies $f_{01}^{m,I}$ and $f_{01}^{m,II}$ are detuned by $\Delta f_m = f_{01}^{m,II} - f_{01}^{m,I}$. This tuning is chosen such that only negligible qubit-qubit interaction is present when performing single-qubit manipulations or no operation. Furthermore, at this working point the detuning between each qubit and its readout resonator is such that the qubit lifetime is not limited by relaxation through the gate circuit. To realize a two qubit gate, the two

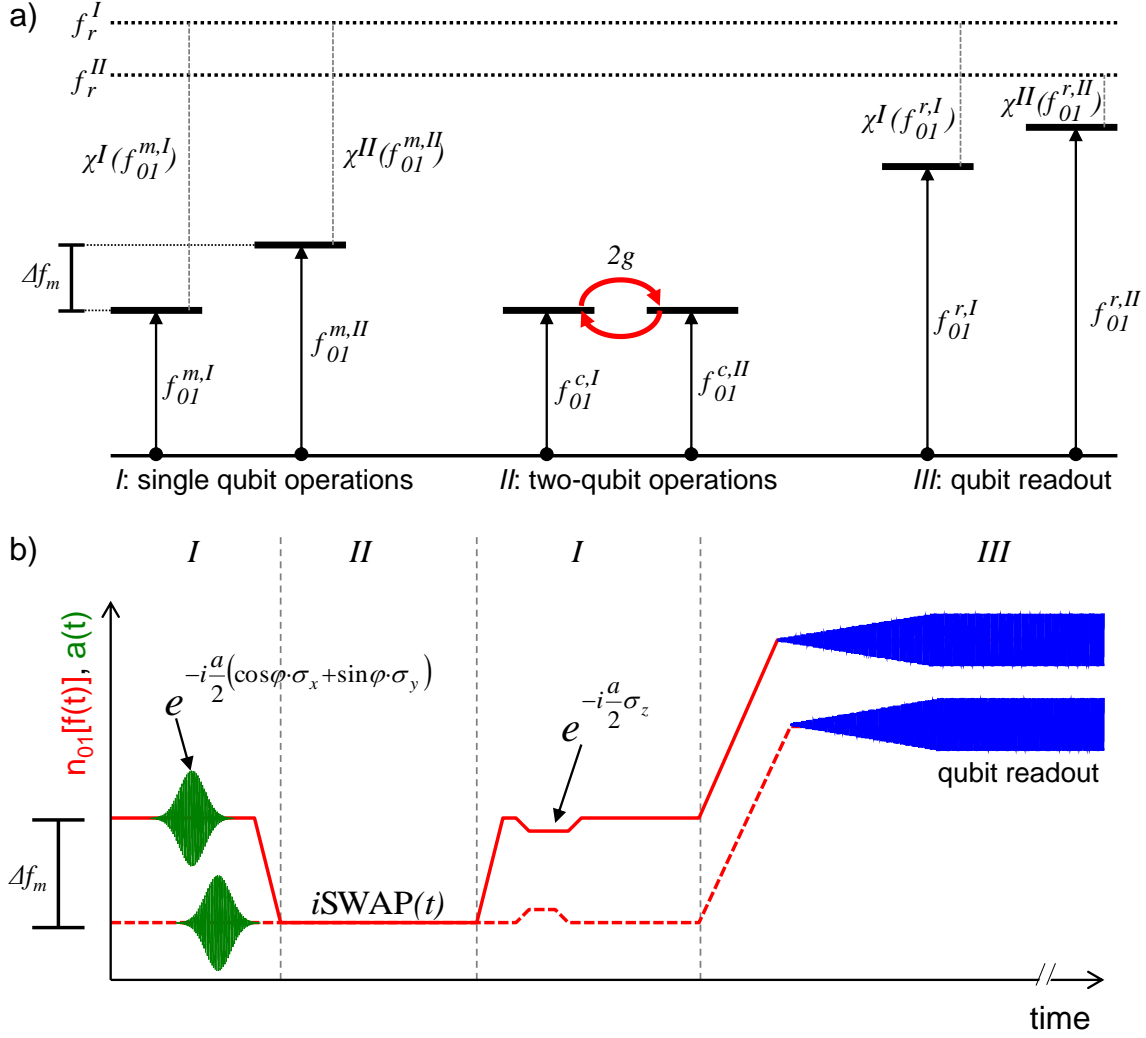


Figure 3.2: Operation principle of the two-qubit processor. a) The qubit frequencies for different operations. I: Single-qubit manipulation and parking. II: Two-qubit coupling. III: Qubit readout. For each operation, different qubit frequencies are chosen, resulting in different qubit-qubit coupling and qubit-readout couplings $\chi_r^{I,II}(f_{01}^{I,II})$. b) Typical gate sequence illustrating the different operations. The sequence consists of two single-qubit XY-gates, a two-qubit $i\text{SWAP}(t)$ gate, two single-qubit Z-gates and ends with the qubit readout.

qubits get tuned in resonance such that $f_{01}^{c,I} = f_{01}^{c,II}$. At this point, the qubits experience a swapping interaction as given by eq. (2.106) with an effective swapping frequency $2g$. For the readout, we change the qubit frequencies to $f_{01}^{r,I}$, $f_{01}^{r,II}$, reducing the qubit-resonator detuning such that the corresponding dispersive shift $\chi^I(f_{01}^{r,I})$ and $\chi^{II}(f_{01}^{r,II})$ of the resonator during readout assures an optimal readout fidelity. The displacement of the qubit frequency between the different working points has to be performed on a time scale faster than all relevant qubit manipulation and coupling frequencies but not as a fast as to induce transitions of the qubit state.

We discuss now the parameters of each component of the processor in greater detail, explaining each time the relevant design goals and possible conflicts and presenting the parameter choice or compromises we arrive at.

3.2 Qubit Design

The main design goals for the qubits are large coherence times, good frequency tunability and the possibility of fast single-qubit driving. Good frequency tunability is important since we need to move the qubits to different frequency working points for single-qubit and two-qubit manipulation as well as qubit readout. The maximum qubit drive frequency should be large compared to the decoherences times of the qubit, so that we are able to perform a large number of gate operations on the qubit before its coherence is destroyed, which is crucial when running quantum algorithms.

3.2.1 Qubit Frequency & Junction Asymmetry

The choice of the maximum qubit frequency is influenced by several requirements:

- The density of thermal photons at the qubit frequency should be sufficiently low at the operating temperature of the circuit (typically 20-100 mK) such that the thermal excitation of the qubit into higher energy levels is negligible.
- Robust equipment for signal generation and measurement in the frequency range of the qubit should be available. This includes microwave sources needed to generate the charge drive pulses as well as room-temperature and cryogenic microwave components such as mixers, splitters and circulators.
- The design of microwave circuits is all the more easy, the lower the required frequency range involved is.

In addition, the choice of the qubit frequency also influences the choice of the readout resonator frequency. For our qubits, we choose a minimum transition frequency of $\omega_{01}^{1,2}/2\pi = 4 \text{ GHz}$, which ideally yields a negligible excited state occupation probability of $p(|1\rangle) = 1/[1 + \exp(\hbar\omega/k_B T)] = 2.1 \times 10^{-2}$ at $T = 50 \text{ mK}$. In addition, in the frequency range 2 – 18 GHz, commercial microwave equipment and components are available for both room-temperature as well as cryogenic applications.

As described in chapter 2, we use a split Josephson junction geometry as shown in fig. 2.4b to make the Josephson energy of the qubit tunable by an external flux Φ_{ext} . The modulation depth of $E_J(\Phi_{ext})$ is given by eq. (2.56): The higher the junction asymmetry d , the smaller the modulation depth of the Josephson energy $\simeq 1 - d$. In general, it can be advantageous to operate the qubit at a working point where $\partial E_J(\Phi)/\partial\Phi = 0$ since at that point the qubit will be insensitive to flux noise at first order. For our processor, we choose therefore a minimum qubit frequency of $\omega_{01}^{min} = 2\pi \cdot 4 \text{ GHz}$, which corresponds to an asymmetry $d \approx 0.35$.

3.2.2 Single-Qubit Driving

We distinguish between single-qubit rotations around the X and Y axes and around the Z axis of the Bloch sphere. The latter are implemented by changing the qubit frequency using a fast

on-chip flux line, whereas the former are implemented by driving the qubit with an oscillatory electrical drive signal at its resonance frequency. For the X/Y gates, it is necessary to capacitively couple the qubit to an external charge driving circuit.

Charge Driving The maximum drive frequency of the qubit is limited by its anharmonicity: Since the Transmon qubit is only a weakly anharmonic system, when driving the qubit at a frequency comparable to the qubit anharmonicity, transitions to higher Transmon levels will be induced, therefore producing a leakage of the qubit state out of the computational basis and hence unitary drive errors. This effect can be partially alleviated by increasing the anharmonicity of the qubit. However, by increasing the anharmonicity, one also increases the sensitivity of the qubit to charge noise. Hence it is necessary to find a compromise for the value of the qubit anharmonicity which allows sufficiently fast qubit driving but which does not incur too much dephasing.

To estimate the drive error arising due to the finite anharmonicity of the driven Transmon, we model the qubit driving using a simple three-level Hamiltonian in the rotating-frame, as used e.g. in [64]:

$$\hat{H} = \alpha \begin{pmatrix} 0 & \epsilon^*(t)/\alpha & 0 \\ \epsilon(t)/\alpha & \delta/\alpha & \sqrt{2}\epsilon^*(t)/\alpha \\ 0 & \sqrt{2}\epsilon(t)/\alpha & 2\delta/\alpha + 1 \end{pmatrix} \quad (3.1)$$

Here, $\epsilon(t) = \epsilon_x(t) + i\epsilon_y(t)$ is the complex drive IQ amplitude in the rotating qubit frame, δ is the detuning of the microwave drive from the Transmon ω_{01} transition frequency and α is the Transmon anharmonicity. Due to the presence of the third energy level, the effective $|0\rangle \rightarrow |1\rangle$ transition frequency will get shifted in respect to the bare frequency ω_{10} when driving the qubit. For $\delta = \alpha = 0$, the characteristic polynomial of \hat{H} is given as $E(E^2 - 3|\epsilon|^2/4) = 0$ with the two eigenvalues $E = \pm|\epsilon|\sqrt{3}/2$. Thus, for weak anharmonicities this frequency shift is given approximatively as $\Delta_{ac} = \sqrt{3}|\epsilon|/2$. To estimate the leakage to the Transmon level $|2\rangle$ when driving the system, we calculate the eigenvalues and eigenvectors of the Hamiltonian given in eq. (3.1). We then decompose an initial state $|0\rangle$ in the basis of eigenstates of \hat{H} and calculate its evolution operator $U_d(t, \delta, \epsilon_0)$ under a constant drive amplitude ϵ_0 . By numerically maximizing the occupation probability of the state $|1\rangle$ as a function of the evolution time t and the drive detuning δ we obtain the ideal gate time, gate error and frequency shift for a π -pulse at a given drive frequency/anharmonicity ratio. In fig. 3.3 we show these quantities as a function of ϵ/α . As can be seen, the gate error due to leakage into the level $|2\rangle$ increases with the drive frequency. For very large drive frequencies, the gate fidelity saturates at a value of $F \approx 0.86$ (the numerically obtained maximum π -pulse fidelity for ultra-strong driving of the three-level system is $F_{max} \approx 0.895$). We can make use of fig. 3.3 to estimate the minimum required qubit anharmonicity given the desired gate fidelity and gate time. If we demand a maximum Rabi frequency $\epsilon/2 = \Omega_{Rabi}^{max} = 2\pi \cdot 100$ MHz, which corresponds to a gate time for a single-qubit π -pulse of $T_\pi = 5$ ns that is small compared to the targeted relaxation and dephasing times of the qubit of $T_1, T_\phi \simeq 1$ μ s, and a maximum π -gate error of $1 - F_\pi = 0.04$, we need an absolute anharmonicity $\alpha > 250$ MHz.

It is possible to correct leakage errors using optimized DRAG drive pulses [55, 15], thereby eliminating leakage to the third qubit level. In this work, we did not use such techniques but we will include possible errors arising due to this leakage to higher Transmon levels in our error models when discussing our experimental data.

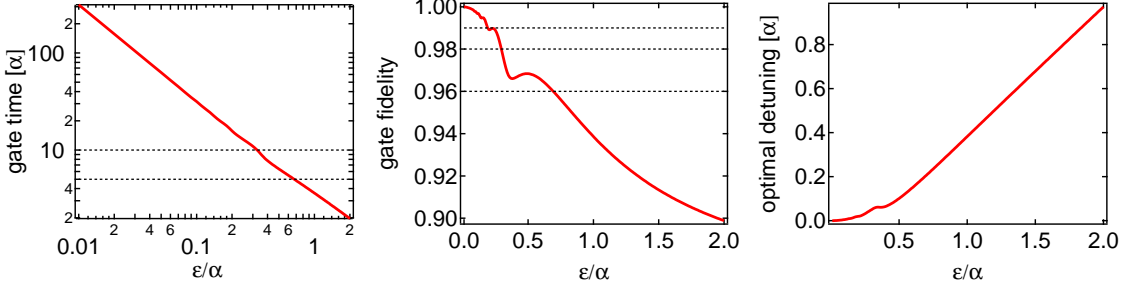


Figure 3.3: The single-qubit π -pulse gate time, gate fidelity and AC Stark detuning, plotted as a function of the reduced drive strength ϵ/α applied to the three-level Transmon. As the drive strength increases, the gate time decreases as α/ϵ whereas the gate fidelity decreases non-monotonously.

Futhermore, on the chip charge driving of the qubit is done through the readout resonator, as shown in fig. 3.1. The Rabi frequency of the qubit in eq. (2.88) is given as $\Omega_{Rabi} = 2\beta eV_d \langle 0 | \hat{n} | 1 \rangle$, where the drive voltage V_d seen at the qubit gate capacitance depends on the input voltage V_{in} at the input capacitance of the resonator as given by eq. (2.89). Since the resonator acts as a band-pass filter for the input drive signal, the more the drive frequency ω_d is detuned from the resonator frequency ω_r , the smaller the gate voltage seen by the qubit is. A Rabi frequency of $\Omega_{Rabi}^{max}/2\pi = 100$ MHz at $\omega_{01}/2\pi = 4$ GHz corresponds to $V_{in} = 0.4$ mV for the resonator parameters that we choose below, $\omega_r/2\pi = 6.7$ GHz, $g_{01}/2\pi = 50$ MHz and $Q = 800$. With 70 dB attenuation inside the cryostat this corresponds to an input power of $P \approx 15$ dBm at room temperature, which is compatible with our microwave setup.

Flux Driving To rapidly change the flux in the qubit loop, we couple each qubit inductively to a fast flux line. The flux induced in the qubit loop by this line is given as $\Phi_{ext} = MI_{fl}$, where I_{fl} is the current in the line and M is the mutual inductance between the flux line and the qubit loop, which can be estimated as $M = \mu_0 l \ln [(d + w)/d]/2\pi$, where l is the length of the qubit loop parallel to the flux line, d the distance of the loop to the line and w the width of the qubit loop perpendicular to the flux line. In order to avoid sample heating through the flux line, we demand a maximum current for inducing one flux quantum Φ_0 in the loop not in excess of $I_{\Phi_0}^{max} = 10$ mA, corresponding to an electrical power of $P^{max} = 500$ μ W on a 50Ω transmission line, which can be easily dissipated on the 1 K stage of the cryostat. This yields a minimum value of the mutual inductance $M \geq 0.23$ pH, which can easily be achieved with a qubit loop of $l = w = 4 \mu\text{m}$ at a distance $d = 12 \mu\text{m}$ to the flux line. The coupling of the qubit to the flux line also induces decoherence that we will take into account later when confirming our choice of M .

3.2.3 Qubit-Qubit Coupling

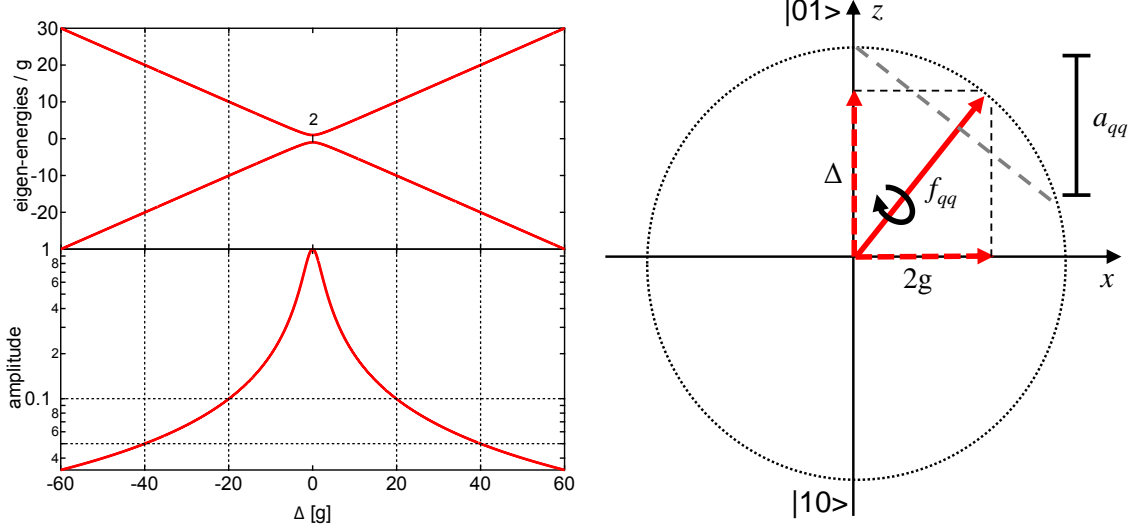


Figure 3.4: a) The two-qubit eigen-energies E_{\pm} and swapping amplitude a_{qq} as given by eqs. (3.2). For $\Delta \gg g$, the amplitude of the swap decreases $\propto 1/\Delta$ and the frequency increases $\propto \Delta$. To effectively switch off the swapping interaction to $a_{qq} = 0.1$, a detuning of $\Delta = 20g$ is required. b) Illustration of the swapping amplitude and frequency on the $|01\rangle, |10\rangle$ Bloch sphere: The rotation axis depends on the ratio Δ/g , for $\Delta = 0$ it coincides with the x axis whereas for $\Delta \gg g$ it asymptotically approaches the z axis. At the same time, the frequency of rotation around this axis increases $\propto \Delta$.

We use a direct capacitive coupling between our qubits to create an interaction between them that we use to implement a two-qubit gate. The full interaction Hamiltonian is given by eq. (6.20), and the coupling strength g_{qq} between the two qubits can be calculated with eq. (2.105). This coupling strength must be chosen such that the interaction between the qubits is sufficiently fast to realize two-qubit gate operations with adequate fidelity but not too strong in order to still allow us to suppress the coupling sufficiently by detuning the qubit frequencies, if needed. By diagonalizing the Hamiltonian given in eq. (2.106) we find for the eigen-energies E_{qq}^{\pm} , the swapping frequency f_{qq} and the swap amplitude a_{qq} of the two coupled qubits as a function of the qubit-qubit detuning $\Delta/2\pi = f_{01}^I - f_{01}^{II}$ the values

$$\begin{aligned} E_{qq}^{\pm} &= \pm \frac{1}{2} \sqrt{4g_{qq}^2 + \Delta^2} \\ f_{qq} &= \sqrt{4g_{qq}^2 + \Delta^2} \\ a_{qq} &= \frac{2g_{qq}}{\sqrt{4g_{qq}^2 + \Delta^2}} \end{aligned} \tag{3.2}$$

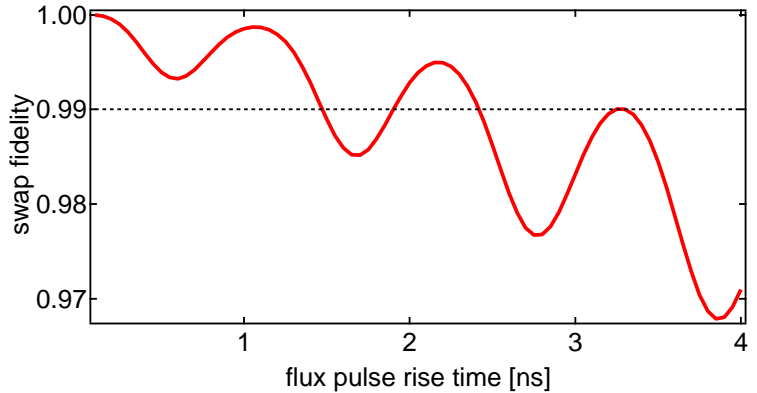
Fig. 3.4 shows the swap amplitude and the eigen energies / swapping frequency as a function of the normalized qubit-qubit detuning Δ/g . As can be seen, for $\Delta \gg g$ the swap amplitude decreases $\propto 1/\Delta$ whereas the swap frequency increases $\propto \Delta$. For our processor, we demand that the residual swapping amplitude $a \leq 0.1$ when the qubits are “parked” for single-qubit gates

and readout, hence it is necessary to detune the qubits by $\Delta \approx 20g$. At this detuning, the swapping frequency is given as $f_{qq}(20g) \approx 20g$. For our processor, we choose $2g/2\pi = 10$ MHz, corresponding to a qubit-qubit detuning of 200 MHz at $a_{qq} = 0.1$ and an associated swapping frequency $f_{qq} = 100$ MHz = $(10\text{ ns})^{-1}$. The required frequency displacement is easily achievable with the on-chip fast flux lines. On resonance, the swap frequency of 10 MHz allows us to realize an $\sqrt{i}\text{SWAP}$ gate in 25 ns and an $i\text{SWAP}$ gate in 50 ns, which is sufficiently fast compared to the estimated relaxation and dephasing times of the qubits. The residual swapping between the qubits at their parking position is usually small enough to be irrelevant for most experiments performed in this work. However, when executing long gate sequences, as required for certain algorithms, the induced error may be too large, hence a larger detuning has to be chosen for these cases.

To estimate the error due to finite rise times for the flux pulse before the $i\text{SWAP}$ gate, we numerically solve the Schrödinger equation of the 2-qubit system in the $|01\rangle, |10\rangle$ basis, which is given as

$$i\hbar \begin{pmatrix} \dot{\psi}_{01} \\ \dot{\psi}_{10} \end{pmatrix} = \begin{pmatrix} -\frac{\Delta(t)}{2} & g \\ g & \frac{\Delta(t)}{2} \end{pmatrix} \cdot \begin{pmatrix} \psi_{01} \\ \psi_{10} \end{pmatrix} \quad (3.3)$$

Figure 3.5: Numerically obtained maximum fidelity of a two-qubit $i\text{SWAP}$ gate realized by changing the detuning Δ in eq. (3.3) from $\Delta = 20g$ to $\Delta = 0$ using a Gaussian pulse of width δt .



To estimate the error, we go from a detuning $\Delta = 20g$ at $t = 0$ to a detuning $\Delta = 0$ at $t = \delta t$ using a Gaussian waveform. We then numerically determine the maximum SWAP amplitude between the qubits and plot the resulting value against δt . The result of this simulation is shown in fig. 3.5. As can be seen, the fidelity of the gate decreases in a non-monotonous way as a function of the flux pulse rise time. In order to obtain $F > 0.99$, a flux pulse rise time of $\delta t \leq 1.5$ ns is required.

3.2.4 Relaxation and Dephasing

In this section we discuss the relaxation and dephasing channels of the Transmon qubit which are most relevant to our experiment. We analyze the relaxation and dephasing rates as a function of the Transmon parameters and optimize these parameters to achieve maximum qubit coherence times.

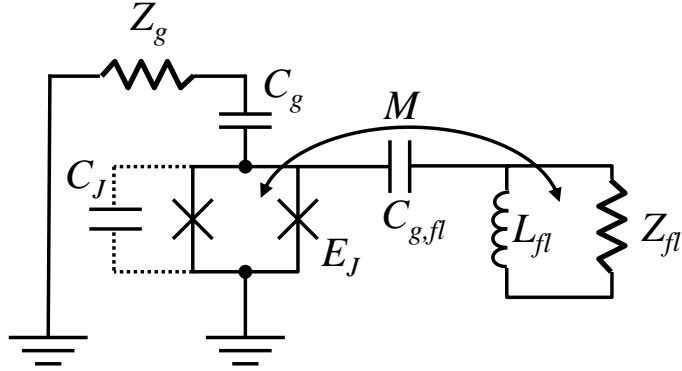


Figure 3.6: A schematic model showing the coupling of the qubit to its environment, modeled by impedances Z_g and Z_{fl} , through capacitive and inductive couplings C_g and M .

Qubit Relaxation

Relaxation of the qubit can occur either through the charge channel or the flux channel. The qubit has a capacitive coupling to both the flux line and the readout resonator, hence charge relaxation through both of them is possible. On the other hand, the only relevant relaxation channel through the flux channel is through the inductive coupling to the external flux line.

Relaxation Through the Gate Charge Channel Since the CPB is coupled to an external impedance (in this case the readout resonator that is coupled to a lossy input transmission line) through a gate capacitance C_g , as shown in fig. 3.6, relaxation into modes of the input impedance seen by the qubit can occur. The relaxation time of the Transmon qubit used in this work is limited by intrinsic loss mechanisms [83, 58] to $T_1^{int} \approx 1 - 4 \mu\text{s}$, hence we require the relaxation time associated to charge relaxation through the gate circuit to be significantly longer than this intrinsic relaxation time, i.e. $\Gamma_1^{Purcell} \ll 1 \text{ MHz}$. This requirement influences the choice of the coupling of the qubit to the readout resonator g_{01} , the quality factor and associated loss rate κ of this resonator and the qubit-resonator detuning Δ for the different processor operations. The relaxation rate due to the coupling of the qubit to the input resonator is given by eq. (2.98). For the qubit parameters chosen above, a resonator quality factor $Q = 800$ and a resonator-qubit coupling of $g_{01}/2\pi = 50 \text{ MHz}$ chosen below, the relaxation rate is $\Gamma_1^{Purcell} \approx 0.25 \text{ MHz}$ at $\Delta/2\pi = 2 \text{ GHz}$ (for qubit manipulation) and $\Gamma_1^{Purcell} \approx 1 \text{ MHz}$ at $\Delta/2\pi = 1 \text{ GHz}$ (for qubit readout). This rate is comparable or larger than the typical intrinsic relaxation rate of the qubit and thus compatible with our design goals.

In addition to the capacitive coupling to the input impedance Z_g , the qubit is also coupled to its flux line by $C_{g,fl}$. Assuming that the flux line is terminated by a 50Ω load and that $C_{g,fl} \leq 10 \text{ fF}$, this capacitive coupling yields a relaxation rate $\Gamma_1^{\text{fl},n_g} \leq 260 \text{ kHz}$ for the qubit parameters discussed above, which is lower than the maximum demanded relaxation rate and thus compatible with our design requirements.

Relaxation Through the Flux Channel On the two-qubit chip, each Transmon is equipped with a fast magnetic flux line that is used to perform flux biasing and fast frequency displacements. The flux lines are coupled to the qubits through a mutual inductance M , as shown in

fig. 3.6. The sensitivity of the qubit to relaxation through the flux channel via the mutual inductance M is given by eq. (2.75). For the mutual inductance discussed above, $M \approx 0.23$ pH, a characteristic impedance of the flux line of $Z_{fl} = 50 \Omega$, a qubit frequency $\omega_{01}/2\pi = 7$ GHz and anharmonicity $\alpha = -250$ MHz and an asymmetry $d = 0.35$, we obtain a maximum relaxation rate of $\Gamma_1^{fl} = xxx$ Hz (ask Mathematica or Denis to calculate matrix element), which is absolutely negligible compared to all other relevant relaxation channels. We confirm therefore our choice of the mutual inductance $M = 0.25$ pH for the flux coupling of the qubit.

Qubit Dephasing

Dephasing of the qubit can occur due to coupling to external charge or flux noise. Here we will calculate the associated rates for both cases for our designed qubit parameters.

Dephasing due to Flux Noise For the qubit parameters discussed in the last paragraph, using eq. (2.79) we obtain a maximum dephasing rate $\Gamma_\phi^{\delta\phi_{ext}} = 0.3$ MHz in the relevant frequency interval $\omega_{01}/2\pi = 4 - 7$ GHz. This rate is thus smaller than the relaxation-limited dephasing rate of the qubit at all relevant working frequencies of our processor. Our choice of qubit parameters is thus compatible with the demanded dephasing time.

Dephasing due to Charge Noise We can use eq. (2.78) to calculate the charge-induced dephasing rate of our Transmon qubit. This rate depends exponentially on the ratio E_J/E_C . The highest dephasing rate occurs thus at the smallest qubit frequency that we operate our qubit at, in our case $\omega_{01}/2\pi = 4$ GHz. The chosen maximum tolerable dephasing rate of $(\Gamma_\phi^{\delta N_g})^{-1} \approx 1 \mu\text{s}$ at $\omega_{01}/2\pi = 4$ GHz is obtained for a qubit anharmonicity of $\alpha \approx -500$ MHz, which is thus the upper bound for the anharmonicity. However, for this work we choose $\alpha = -250$ MHz, since it allows already for sufficiently fast driving of the qubit, as discussed in section 3.2.2. For this parameter choice, we obtain a negligible maximum dephasing rate $(\Gamma_\phi^{\delta N_g})^{-1} \approx 1 \text{ ms}$ at $\omega_{01}/2\pi = 4$ GHz.

As mentioned in section 3.1.1, the coupling of the qubit to the readout resonator can induce dephasing through the AC-Stark shift of the qubit induced by photon-number fluctuations in the resonator. The resulting relaxation rate is given by eq. (2.103). For the qubit parameters discussed above and a qubit-resonator coupling $g_{01}/2\pi = 50$ MHz, the dephasing rate is $\Gamma_\phi^{\bar{n}} = 0.95 \cdot \bar{n}$ MHz at the minimum chosen qubit-resonator detuning $\Delta = 1$ GHz. The average number of photons in a resonator with $\omega_r/2\pi = 6.7$ GHz at $T = 100$ mK is given as $\bar{n} = [\exp(\hbar\omega_r/k_B T) - 1]^{-1} \approx 0.05$, yielding an effective dephasing rate $\Gamma_\phi^{\bar{n}} \approx 38$ kHz, which is small compared to the flux-induced dephasing rate at all working points of the qubit.

3.3 Readout Design

As explained in section 2.4.3 of chapter 2, the readout fidelity is influenced by three sources of error: Finite overlap between the switching probability distributions for different qubit states,

relaxation of the qubit during the measurement phase of the readout and retrapping of the resonator state during the latching phase of the readout. In order to minimize these errors, the following constraints should be met for the readout resonator:

1. The state-dependent dispersive shift of the resonator frequency should be large enough such that the switching probability distributions of the resonator corresponding to the qubit states $|0\rangle$ and $|1\rangle$ do not overlap.
2. The measurement phase of the readout should be completed in a time T_{meas} which is short compared to the relaxation time of the qubit, i.e. $T_{meas} \ll T_1$.
3. There should be no retrapping of the resonator state during the latching period of the readout.

In order to maximize the dispersive shift, we can either increase the coupling g_{01} between the resonator and the qubit or reduce the frequency detuning Δ between them. However, increasing g_{01} or decreasing Δ will also increase the relaxation rate of the qubit through the Purcell effect, thereby reducing the readout fidelity. There is an optimum choice for g_{01} and Δ [56]. To counteract the qubit relaxation through the cavity, we can simply increase the quality factor of the resonator. However, usually the maximum relaxation time of the Transmon qubit used in this work is limited to $T_1 \approx 1 - 4 \mu\text{s}$ due to intrinsic relaxation processes. Therefore, increasing the quality factor of the resonator does not necessarily increase the readout fidelity because a higher quality factor also increases the time required to excite the readout resonator by the drive pulse and hence the measurement time of the qubit state. Therefore, if the qubit relaxation time is intrinsically limited, a longer measurement time at a constant relaxation rate implies a higher probability for the qubit to relax during the measurement, hence actually reducing the readout fidelity. We therefore need to find a compromise for the values of g_{01} , χ and Δ that will maximize the readout fidelity under the given constraints.

To illustrate the effect of g_{01} and Δ on the relaxation time T_1 and the dispersive shift χ , fig. 3.7 shows both quantities as a function of g_{01} , plotted for several choices of Δ . Now, criterion 1 above demands that the dispersive shift be large enough to completely separate the switching probability distributions for different qubit states. The width of these probability curves can be calculated theoretically, however for this discussion we rely on experimentally measured values and assume that a dispersive shift of $\Delta\chi \approx 5 \text{ MHz}$ suffices to fully separate the two distributions. This assumption limits the range of possible values for g_{01} and Δ to the region above the horizontal line in fig. 3.7a. On the other hand, criterion 2 demands that the time required to map the qubit state to the oscillator state should be small compared to the relaxation time of the qubit. For the CJBA parameters relevant to this work, this time is given as $T_{meas} \approx 50 - 100 \text{ ns}$. In order to have negligible qubit relaxation during the readout, we therefore demand that $T_1 \geq 1 \mu\text{s}$, which corresponds to a 5 % relaxation probability during the measurement interval. This again limits the choice of possible values of g_{01} and Δ .

Another important design parameter of the CJBA is the Kerr constant K . This constant defines the non-linearity of the resonator and determines the power at which the resonator be-

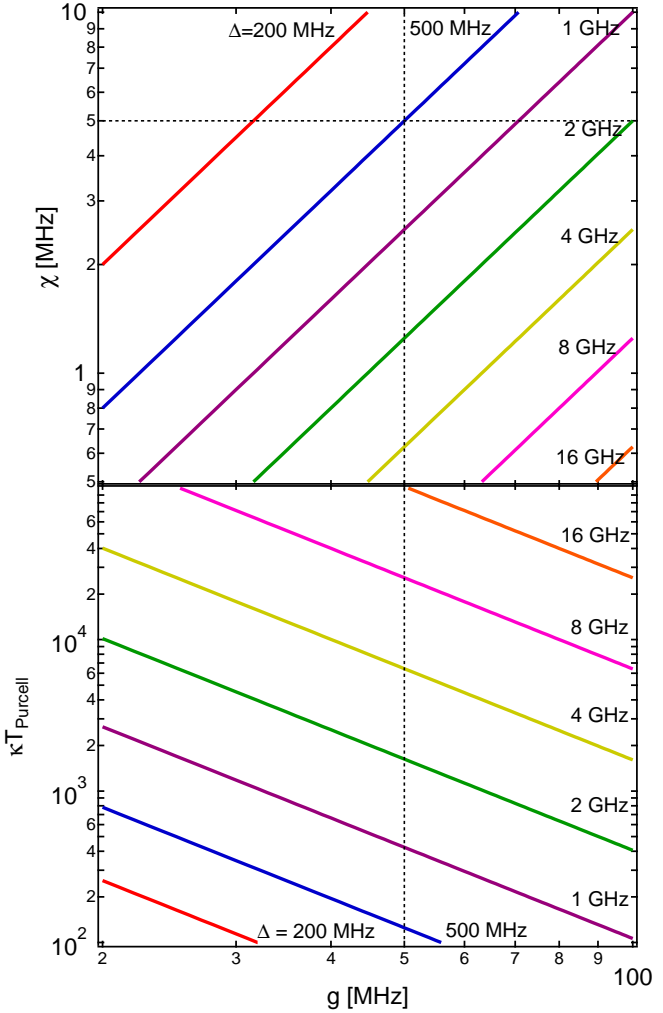


Figure 3.7: The dispersive shift χ of the resonator and the relaxation time $\kappa \cdot T_{\text{Purcell}}$ (normalized to the decay rate $\kappa = \omega_r/Q$ of the resonator) of the qubit for a qubit dispersively coupled to a resonator, plotted as a function of the coupling strength g_{01} and shown for different values of the qubit-resonator detuning $\Delta = \omega_r - \omega_{01}$.

comes bistable. Also, the number of photons in the low- and high-amplitude solution of the resonator increases with increasing K . Since the dispersive shift of the qubit frequency caused by the resonator is proportional to the number of these photons, choosing a too high K should be avoided since it can induce large displacements of the qubit frequency, thereby e.g. recoupling the two qubits of the processor during the readout operation. In addition, as shown before the photons in the readout resonator can lead to additional dephasing in the computational basis of the qubit.

Taking these constraints into account, for the final choice of parameter values we rely on a set of optimized CJBA parameters that have been obtained in an earlier experiment by Mallet *et al.* [56]. For our processor we choose therefore readout resonator frequencies $\omega_r^1/2\pi = 6.7$ GHz and $\omega_r^2/2\pi = 6.85$ GHz, quality factors $Q^{1,2} = 800$, Kerr constants $2\pi K^{1,2}/\omega_r^{1,2} = -2.5 \times 10^{-5}$ and qubit-resonator couplings $g_{01}^{1,2}/2\pi = 50$ MHz. In addition, we choose a detuning $\Delta/2\pi = 500$ MHz for reading out the qubits, yielding a relaxation rate $\Gamma_1^{\text{Purcell}} \approx 500$ kHz during readout.

Parameter	Value	Related Parameters
E_J	$h \cdot 28.4 \text{ GHz}$	$f_{01} = 7 \text{ GHz}, \alpha = -250 \text{ MHz}$
E_C	$h \cdot 0.92 \text{ GHz}$	$C_q = 83.8 \text{ fF}, I_c = 57.4 \text{ nA}$
d	0.35	
$M_{1,2}$	0.25 pH	
$g_{qq}/2\pi$	10 MHz	$C_{qq} = 0.45 \text{ fF}$
$g_{01}/2\pi$	50 MHz	$C_{qr} \approx 62.8 \text{ fF}$
$\omega_r^1/2\pi$	6.7 GHz	$L_r^1 = 756 \text{ pH}, C_r^1 = 497 \text{ fF}$
$\omega_r^2/2\pi$	6.85 GHz	$L_r^2 = 739 \text{ pH}, C_r^2 = 486 \text{ pF}$
$Q_r^{1,2}$	800	$C_{in}^{1,2} \approx 17 \text{ fF}$
$K_r^{1,2}$	-2.5×10^{-5}	$I_{J,r} \approx 2.3 \mu\text{A}$

Table 3.1: The sample parameters chosen for the two-qubit processor. The table contains all independent parameters of the processor as well as the dependent parameters derived from them.

3.4 Summary: Qubit and Readout Parameters

Having discussed the relevant properties of all building blocks of our processor and their dependence on the sample parameters, we choose a full set of these parameters, summarized in table 3.1.

3.5 Processor Layout & Fabrication

After having chosen a set of sample parameters, it remains to find a physical implementation of the design that we can realize. In this section we discuss therefore the layout design of the qubit processor. From the beginning, we will restrict our discussion to lithographically fabricated circuits on a chip, disregarding e.g. recent approaches to the realization of superconducting qubits and resonators using 3D microwave cavities [69].

The readout resonator can be realized e.g. as a lumped-elements LC resonator or as a transmission line resonator. In the original approach to CQED [91], a coplanar waveguide (CPW) resonator was used. Distributed microwave resonators such as CPW resonators are often advantageous since they can be fabricated with a high intrinsic quality factors []. Also, the isolation between the input port of the distributed resonator and the qubit electrode to which the open end of the resonator is coupled is usually absolutely negligible, whereas for a discrete LC resonator a significant capacitive coupling between the input port of the resonator and the qubit can exist, which is usually unwanted since it will cause additional relaxation. For this work, we

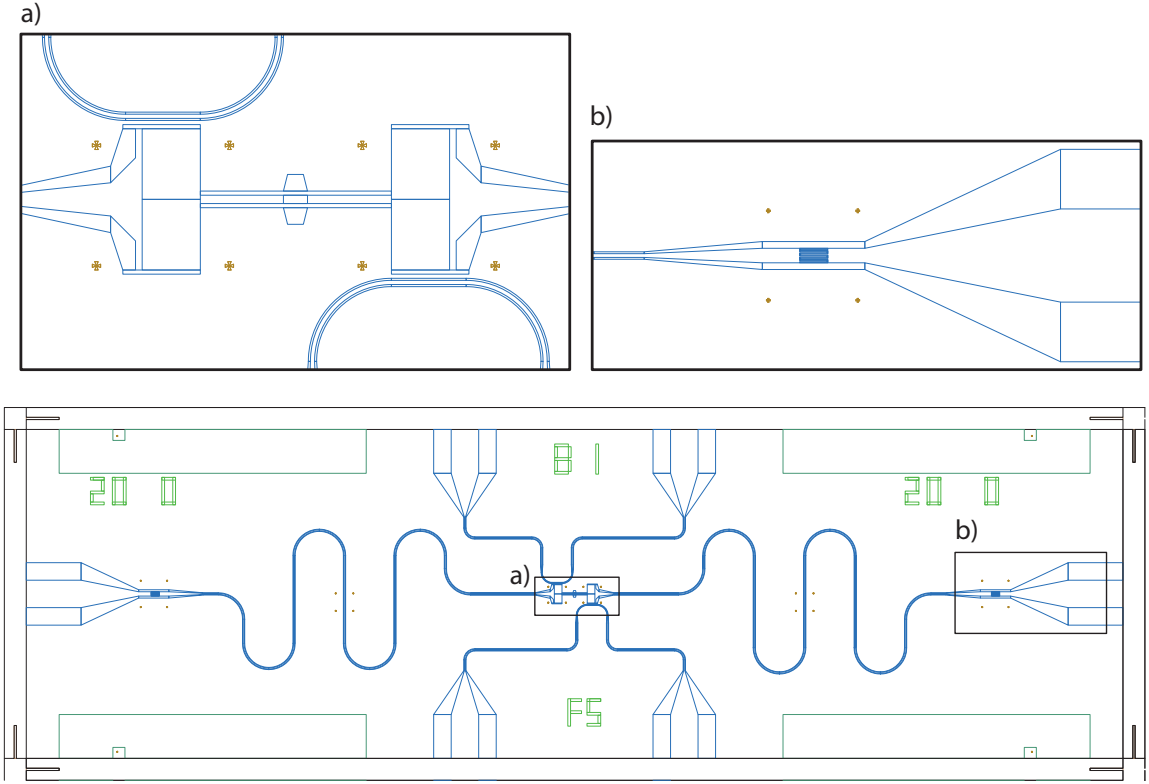


Figure 3.8: CAD layout schematic of the two-qubit processor, showing the two CPW readout resonators and the two qubits with their adjacent fast flux lines. Subfigure a) gives a magnified view of the two qubits and their capacitive coupling element, subfigure b) shows the input coupling capacitance of the CPW resonator to the input transmission line.

therefore chose a distributed design using a $\lambda/2$ CPW resonator. The open port of the resonator is capacitively coupled to one of the qubit electrodes to achieve the desired coupling factor g_{01} .

The flux lines can be realized in several ways. For our processor, we choose a simple 50Ω CPW transmission line that is passing nearby the qubit SQUID at a distance of $d \approx 12 \mu\text{m}$. Since we use the flux line for DC biasing of the qubits as well, shielding currents will flow in the ground planes on either side of the line when a DC current gets applied. These currents can create an unwanted flux bias in the qubit loop and should therefore be eliminated. We achieve this by removing the ground plane between the qubit and the central conductor of the flux line. However, by doing this, we also increase the capacitive coupling between the line and the qubit electrodes, thereby increasing the charge relaxation rate through the flux line. However, as discussed in section 3.2.4, for our sample parameters this effect is usually negligible. The flux line can be terminated either directly at the 20 mK stage by wire-bonding it to the ground plane of the chip, or by connecting it to a matched impedance at the 1 K stage of the cryostat. Alternatively, we can also feed back the flux signal to room temperature, which is useful for e.g. measuring the response function of the flux line.

For the Transmon qubit itself, we need to fabricate a large shunt capacitance C_J in order to achieve the desired charging energy. We implement this capacitance as an interdigitated planar

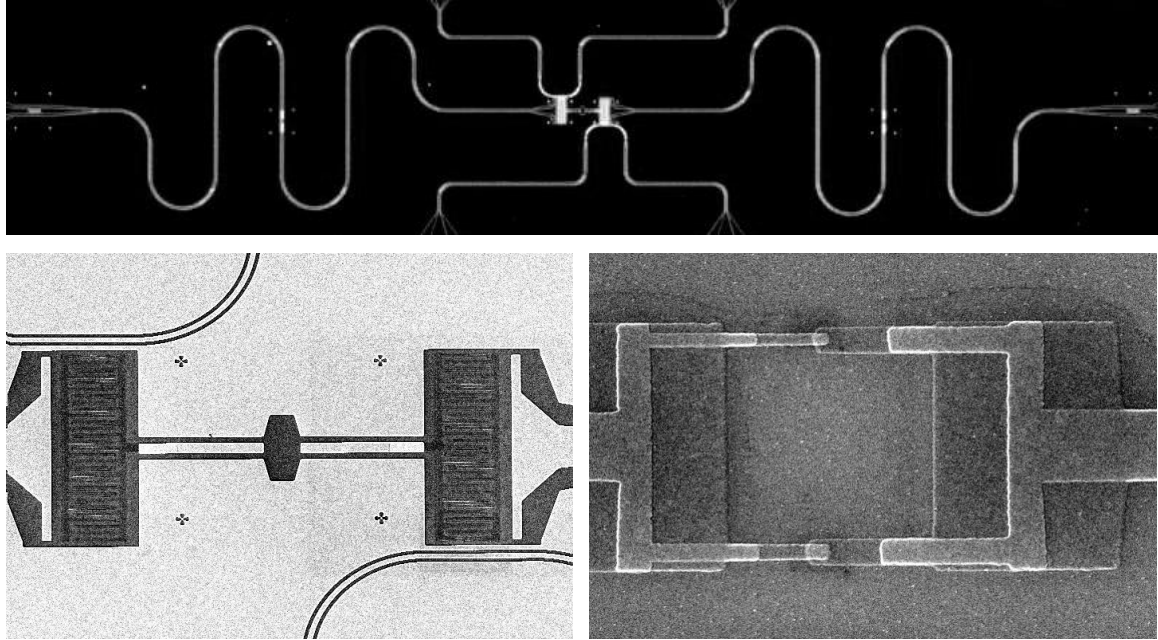


Figure 3.9: Optical and electron microscope photos of the two-qubit processor realized in this work. a) shows an optical image of the full processor with the two coupled qubits, fluxlines and readout resonator. b) shows an SEM image of an enlarged part of the central region of the chip with the two qubits and the coupling capacitance. c) Shows an SEM image of a single qubit junction loop.

capacitor that we pattern together with the qubit junctions using electron-beam lithography. The Josephson junctions of the qubit are realized in a SQUID geometry with a loop area of $A \approx 16 \mu\text{m}^2$ and are fabricated using double-angle shadow-evaporation of Aluminium.

We fabricate the processor on a silicon substrate with a 50 nm thermal oxide layer. First, we deposit 150 nm of Niobium by magnetron sputtering. Afterwards, we spin a photoresist and define an etch mask through optical lithography. Then we dry-etch in a SF₆ plasma, defining the readout resonators, transmission lines and qubit flux lines on the chip. This optical patterning is performed for the wafer as a whole. Afterwards, we spin a bilayer of MAA/PMMA electron beam resist (with typically 1050 nm of MMA and 115 nm of PMMA thickness). Then the wafer gets diced and the qubits and JBA junctions are patterned per chip using electron beam lithography, using a double-angle shadow evaporation technique to define the Josephson junctions and capacitances on the chip. The e-beam resist is then lifted off chemically in an Acetone bath. We characterize the chip optically afterwards. In addition, we place “twin” structures of the Transmon qubits and the JBAs on each chip whose normal state resistance we measure at room temperature. Giving the normal-state resistance of a Josephson junction we can calculate the Josephson energy by using the Ambegaokar-Baratoff relation

$$E_J = \frac{2\pi^2 \Delta}{R_n h}, \quad (3.4)$$

where $E_J = hI_c/4\pi e$. When measuring R_n at room temperature, a corrective factor of $\approx 10\%$

has to be applied to the resulting value of E_J to account for variations in R_n with temperature. Furthermore, we perform numerical microwave simulations to extract the values of all relevant capacitances and inductances on the chip, which allows us to calculate all relevant parameters of our qubit chip.

3.6 Electromagnetic Simulation of the Qubit-Chip

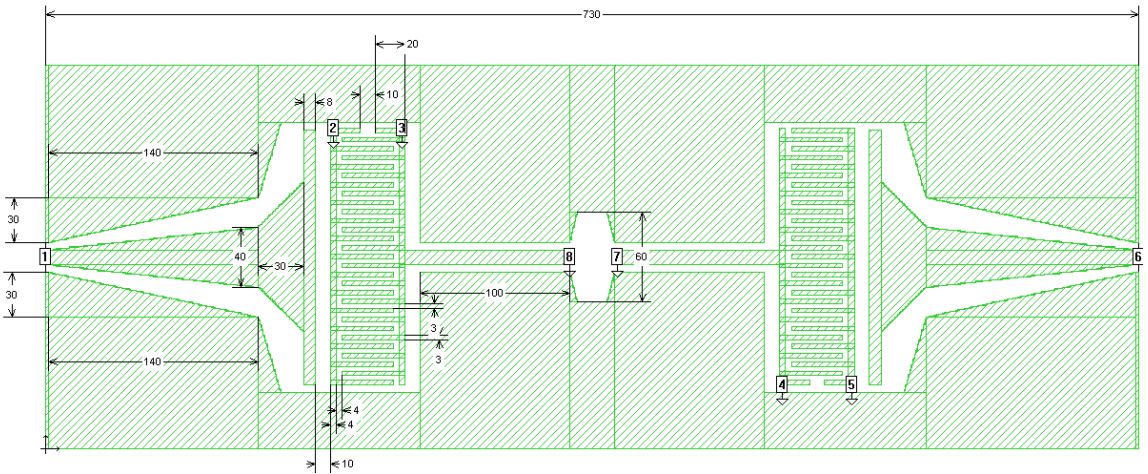


Figure 3.10: 2D Electromagnetic model of the processor chip, generated using Sonnet microwave simulator [1]. Shown are the two Transmon qubit capacitances that are capacitively coupled to each other and to their readout resonator (not shown). Numerical simulation of the circuit yields the capacitances and inductances between all ports of the circuit (1-8).

We use a software package for electromagnetic simulation [1] to simulate individual parts of the chip and obtain the transmission coefficients between all relevant circuit components and an equivalent lumped-element model of the circuit. Using this equivalent model we calculate all relevant capacitances and inductances of the circuit. We can then iteratively adapt the geometry of individual circuit elements in order for them to match the designed parameter values.

We can also simulate the Transmon qubits as harmonic oscillators by modeling their Josephson junction as an inductance that matches the Josephson inductance of the junction, as given by eq. (2.14). By simulating the resonance curve of this harmonic resonator and calculating the corresponding quality factor Q , we can estimate the relaxation rate of the qubit through the gate circuit. We can also obtain an estimate of the coupling strength between the two qubits by simulating them as two coupled, linear resonators. We can obtain the impedance seen by the qubit through the gate circuit by this method as well, thereby being able to calculate the corresponding qubit relaxation rate.

3.6.1 Fabrication Recipe

Here we give the detailed procedure followed for fabrication of the two-qubit processor chip. The fabrication is performed on a 2 " Si-wafer thermally oxidized with 50 nm oxide.

1. **Niobium Sputtering:** Deposit 150 nm Niobium at an argon pressure of 1.25 mbar and a power of 500 W with a 5 minute pre-deposition and ≈ 2 min 20 sec deposition time.
2. **Spinning of Photo-Resist:** Spin S1813 + Shipley Primer at 6000 RPM for 60 sec, bake at 115 °C for 1 min 15 sec.
3. **Photo Lithography:** Expose the wafer through a contact mask at $5 \text{ mW} / \text{cm}^2$ for 30 sec.
4. **Development:** Develop in pure MF 319 for 50 s.
5. **Reactive Ion Etching:** Pump the RIE chamber to $P \leq 4 \times 10^{-5}$ mbar. Etch using 20 cc of SF₆, 10 cc Ar and 2 cc O₂ at a pressure of ≈ 0.013 mbar at a power of 50 W and a voltage of 150 V. The total etch time should be ≈ 60 sec + 10 sec for the finish. Remove the resists in heated Acetone (40 °C) for at least 10 min, possibly clean further in an ultrasonic bath.
6. **Surface Regeneration:** Pump the RIE chamber to $P \leq 4 \times 10^{-5}$ mbar, etch using 20 cc of SF₆, 10 cc Ar at ≈ 0.0133 mbar, 50 W and 150 V for 8 sec.
7. **Electron Resist Spinning:** Spin twice an MAA EL 10 layer at 2000 RPM for 60 sec, 6000 RPM for 2 sec. Bake after each step at 170 °C for 60 sec. Spin PMMA 950k A3 (AFM / STM) at 4000 RPM for 60 sec, 6000 RPM for 2 sec. Bake at 170 °C for 20 min. This should yield ≈ 1050 nm of MAA and 110 nm of PMMA (verify using interferometer).
8. **Dicing:** Dice the wafer using either a diamond cutter or wafer saw.
9. **Electron Beam Lithography:** Clean the chip in iso-propanol (possibly in ultrasound) for less than 2 minutes. Perform electron beam lithography at a dose of $\approx 350 \mu\text{C}/\text{cm}^2$ (correct units???). Develop the chip in a 1:3 Acetone/Iso-Propanol solution for 50 sec.
10. **Metal Deposition:** Put the sample in the evaporation chamber and pump to $P < 10^{-6}$ mbar. Ion mill the sample at the evaporation angles for 1 sec (power, current, voltage?). Deposit Aluminium at a rate of 1 nm / sec. Oxidize the Aluminium film at an adequate Oxygen pressure (typically 15 - 25 mbar) for 10 min. Deposit the second Aluminium sheet at 1 nm / sec.
11. **Lift-Off:** Put the chip in a heated Acetone bath at 65 °C for at least 5 min. Rinse in Iso-Propanol. Thermally activate the chip at 65 °C for 1 min.

Chapter 4

Measurement Setup & Techniques

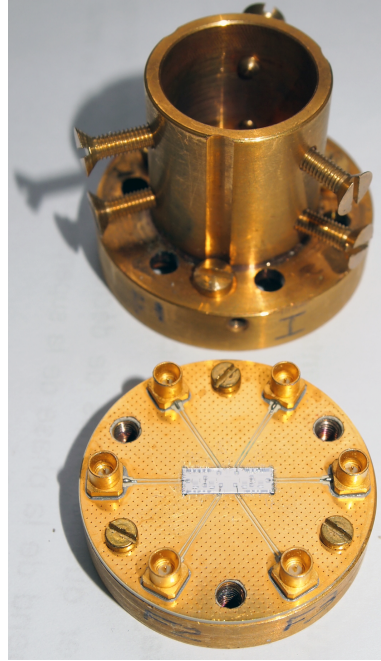
In this chapter we discuss the measurement setup and techniques that we use in this thesis work. We present all individual parts of our signal generation and measurement chain, putting emphasis on the generation and measurement of high-frequency signals. Afterwards we briefly discuss the calibration and compensation techniques that we use to correct signal imperfections when generating qubit drive and flux signals. Finally we introduce the different measurement techniques that we use in this work, including qubit readout and driving as well as more advanced methods used to obtain all relevant qubit parameters such as frequency, anharmonicity as well as relaxation and dephasing times.

Our experimental setup consists of the qubit chip discussed in chapter 3, which is put at the 20 mK stage of a He_3/He_4 dilution cryostat and connected to a room temperature signal generation and measurement chain via cryogenic microwave components and 50Ω coaxial transmission lines. At room temperature, we generate microwave pulses as well as DC and high-frequency flux bias pulses using heterodyne mixing and/or high-frequency arbitrary signal generators. We use a cryogenic amplifier chain and homodyne demodulation at room temperature to perform reflectometric measurements of the phase of our microwave readout signal.

4.1 Sample Holder & PCB

For mounting the qubit chip as shown in fig. ?? in the sample holder, it is first glued to a custom-designed high-frequency PCB, as shown in fig. 4.1 (bottom). On this PCB, six 50Ω CPW waveguides terminated by Mini-SMP connectors are bond-wired to the drive/readout and fast flux lines of the qubit chip. For each qubit, one readout/drive line and two flux lines are present on the chip. In addition, bond wires are used to connect the ground plane of the chip to that of the PCB. On-chip bond wires are used to connect separated parts of the on-chip ground plane which are isolated from each other due to the circuit topology, which is important to avoid spurious on-chip resonances in the relevant frequency range 4 – 7 GHz [77]. The PCB with the mounted chip is then screwed to a sample holder machined in copper that fully encloses the PCB, as shown in fig. 4.1 (top and bottom) and that consists of a bottom part on which the PCB

Figure 4.1: The sample holder with the mounted PCB carrying the qubit chip. Bond wires are used to connect the on-chip transmission lines to the PCB, which in turn uses a Mini-SMP connector to connect the bond-wire to a set of external coaxial SMP cables. The top part of the sample holder is screwed to the bottom part, forming a closed box with cavities only for the transmission lines and the qubit chip. The whole sample holder is screwed to the 20 mK stage of the dilution cryostat.



is screwed and that is itself screwed to the top part of the sample holder. The top part provides holes for the SMP connectors and is pressed against the surface of the PCB. Machined grooves in the top part provide the necessary open space above the qubit chip and the transmission lines on the PCB. The function of the sample holder is to thermally anchor the PCB and the qubit chip to the cryostat and, more importantly, to shield the qubit chip from spurious electromagnetic signals and enclose it in a conducting cavity that is small enough to suppress box resonances at all relevant working frequencies.

4.2 Signal Generation & Acquisition

Fig. 4.2 shows the wiring of our experiment from room temperature down to the 20 mK state of the dilution cryostat. Superconducting cables are used where adequate to minimize signal attenuation, in addition lossy cables made from special alloys such as CuNi are used to minimize heat transfer into the cryostat, which is especially critical between the 300 mK and 20 mK stages. Pairs of bifilar cables are used to provide DC biasing of one or several superconducting coils.

4.2.1 Driving and Measurement of the Qubit

Each of the qubits together with the corresponding readout resonator on our chip is fitted with an individual drive and readout circuit. At room temperature we generate qubit and resonator drive waveforms using phase-locked single-tone microwave sources whose continuous output is mixed with fast control pulses generated by two arbitrary waveform generators (the details of this microwave mixing will be discussed in the following paragraph). The drive and readout signals are then combined and sent to the qubit chip through a series of (cryogenic) attenuators

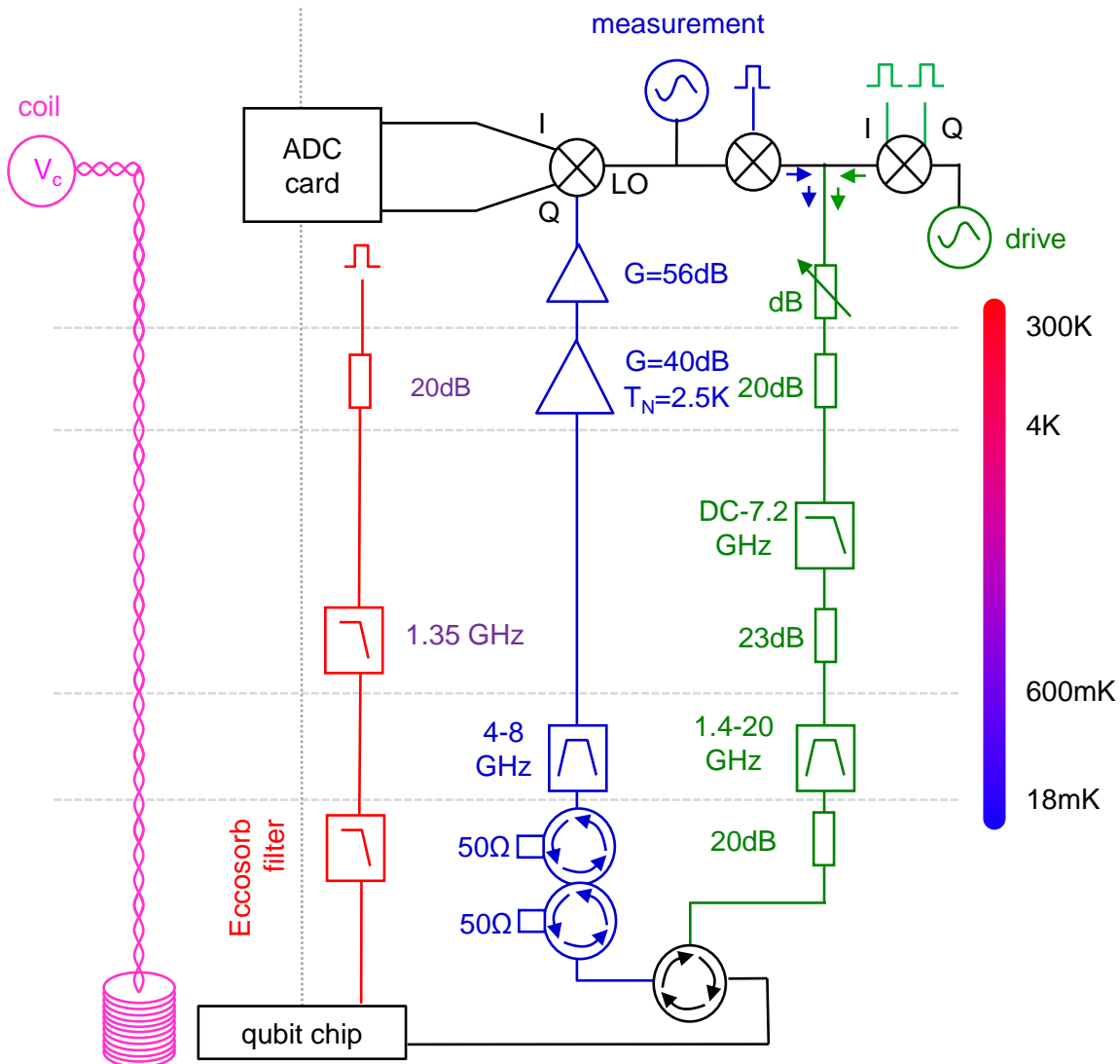


Figure 4.2: The measurement setup used for the two-qubit experiments. Exactly the same drive and readout scheme is used for both qubits with phase-locked microwave sources and arbitrary waveform generators.

and filters. A cryogenic circulator at the 20 mK sample stage of the dilution cryostat routes the incoming pulses to the qubit chip where they are sent to the qubit readout resonator and finally reflected by it. The reflected signal passes again through the input microwave circulator and gets routed through a double isolator and a band-pass filter to a cryogenic HEMT amplifier with a gain of 40 dB. The amplified signal gets transmitted to the room temperature electronics, where it gets filtered and amplified further. Finally, the signal is demodulated with a continuous microwave reference tone and fed to an ADC board through a pair of low-noise amplifiers.

In addition to this, each qubit is equipped with a pair of fast flux lines. High-frequency and DC flux pulses are generated using an arbitrary waveform generator at room temperature. The flux signal is then sent to the qubit chip through 20 dB of attenuation, a conventional Microtronics low-pass filter as well as a custom-made high-frequency powder filter that uses an absorptive

material (Eccosorb) to attenuate high-frequency noise. After passing through the transmission line on the qubit chip, the outgoing flux signal gets routed to room temperature through a transmission line identical to the input line. There, the signal can be measured, which is useful for correcting possible signal imperfections caused by the non-ideal character of the transmission line (we will detail in one of the following sections how to numerically compensate the imperfect frequency response of the flux line).

4.2.2 Microwave Sideband Mixing

To generate the qubit drive pulses we use single-sideband mixing techniques. We use a pair of IQ mixers that we drive with a continuous single-frequency microwave tone and two synchronized fast control signals generated by an arbitrary waveform generator (Tektronix AWG5014b). In general, when feeding a signal $LO(t) = i_0 \cos(\omega_{rft})$ to the LO port of an IQ mixer and two signals $I(t)$, $Q(t)$ to the I and Q ports of the mixer, we obtain a signal

$$RF(t) = I(t) \cos(\omega_{rft}) + Q(t) \sin(\omega_{rft}) \quad (4.1)$$

at the RF port of the mixer. Since the IQ mixer that we use is a passive, reciprocal device one can as well feed two input signals to the LO and RF ports and obtain the demodulated signal quadratures at the I and Q ports, a technique that we make use in our qubit readout scheme, as will be detailed later in this chapter.

Typically we use sideband mixing to generate drive pulses that are displaced in frequency in respect to the original LO (carrier) waveform. This is often advantageous since it eliminates microwave leakage at the signal frequency for zero voltage on the IQ inputs, which is often a big problem for commercially available IQ mixer, as we will discuss below.

Commercially available IQ mixers often deviate from the ideal behavior as given by eq. (4.1). Typical imperfections include large insertion losses –i.e. loss of signal power between the different ports of the mixer–, RF signal leakage at zero IQ-input and frequency-dependent phase and amplitude errors of the mixed sideband signals. In order to achieve reliable single-qubit operations we need to correct the signal leakage and quadrature-specific amplitude and phase errors. The signal leakage causes a small part of the LO signal to leak through to the RF port even when the IQ inputs are zeroed. This leakage can be compensated by adding center-frequency ω_c dependent DC offset voltages to the IQ ports. The appropriate offset voltages can be determined by applying a continuous input signal at a frequency ω_c to the LO port of the mixer and minimizing the measured signal power at the RF port by varying the IQ offset voltages. To correct the sideband amplitude and phase errors we apply another correction procedure that we outline here. First, for the signals at the IQ inputs of the mixer we introduce the notation

$$A(t) = I(t) + iQ(t) = a(t) \exp(-i\phi(t)) \quad (4.2)$$

We consider an IQ signal at a single sideband frequency ω_{IF} and at fixed complex amplitude $a(t) = a = a_0 \exp(i\phi_0)$ such that $A(t) = a \exp(-i\omega_{IFT})$. The effect of the gain and phase

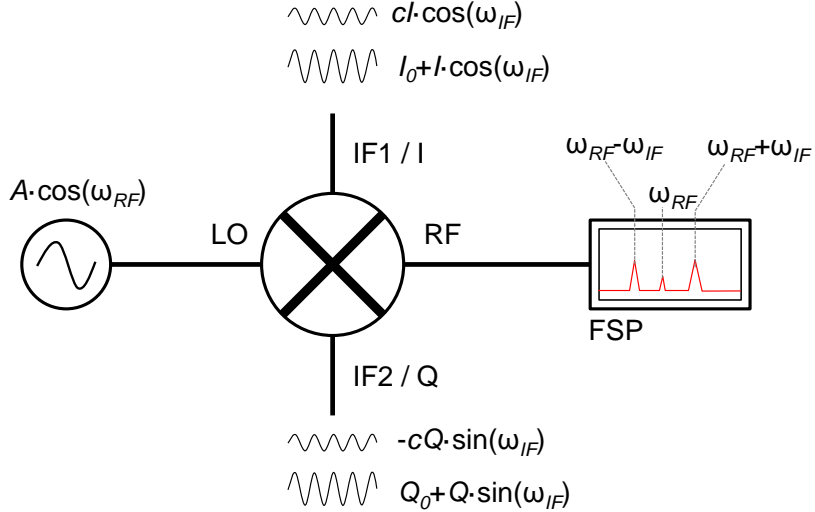


Figure 4.3: Illustration of the method used to measure and correct the imperfect signal behavior of the IQ mixer used in our experiments: To minimize the leakage of the LO signal to the RF port, we apply a continuous input signal at frequency ω_{rf} to the LO port and minimize the power at ω_{rf} the RF port by tuning the two offset voltages I_0 and Q_0 at the IF1/I and IF2/Q ports. To correct phase and amplitude errors during heterodyne mixing, we apply the same signal as before to the LO port and in addition two sideband signals to the IF ports. We then minimize the measured power at the RF port at $\omega_{rf} + \omega_{IF}$ by adding a correction waveform at the IF ports.

imperfections of the IQ mixers can then be modeled by assuming that the mixer adds another IQ signal $\epsilon(\omega_{IF}, \omega_{RF})A^*(t)$ at the mirrored sideband frequency $-\omega_{IF}$. We can correct this unwanted signal by adding a small correction $c(\omega_{IF}, \omega_{RF})A^*(t)$ to our IQ input signal. The complex-valued correction coefficient $c(\omega_{IF}, \omega_{RF}) = |c| \exp(i\angle c)$ usually depends both on the carrier frequency ω_{RF} and the sideband frequency ω_{IF} . We determine the correction coefficients by generating a continuous waveform at a given center and sideband frequency, measuring the amplitude of the unwanted sideband signal with a fast spectrum analyzer and minimizing its amplitude by varying the correction coefficient $c(\omega_{IF}, \omega_{RF})$.

Both the offset and the sideband-amplitude and -phase corrections have been automated using our data acquisition software. By using the optimization techniques described above we can achieve ≤ -80 dBm residual leakage power at the RF port of the mixer when no input IQ signal is present and a suppression of the unwanted mirror sideband during heterodyne modulation by > 70 dB.

4.2.3 Fast Magnetic Flux Pulses

We use a pair of superconducting coaxial cables to realize the qubit flux lines. Each qubit is connected to an on-chip transmission line, whose ends are connected to two fully symmetric transmission lines through the PCB. These two lines lead back to the room-temperature stage and can be used to send signals down the flux line and measure the transmitted signal. Between room temperature and the 20 mK stage of the cryostat, we apply 20 dB attenuation to each

line and low-pass filter all signals both at the 4K and 20 mK stages of the cryostat. The low-pass filters at the 20 mK stage consist of custom-built powder filters made from a commercially available, highly absorptive and lossy material (Eccosorb, [1]). Appendix ?? contains details on the fabrication and frequency attenuation characteristic of these filters. The heavy filtering of the flux line is necessary since it reduces the high-frequency noise seen by the qubit. On the other hand, it also distorts all deterministic input signals that we send through the flux line, which is an unwanted effect and has to be corrected. For this, we measure and compensate the frequency response of the flux line by sending a well-defined test signal down the line and measuring the transmitted signal at the other end of the line. This allows us to obtain the response function of the input line. Fig. 4.4a shows the model of the qubit flux line that we use to model the response function of the line. We assume that the response of the line is given by

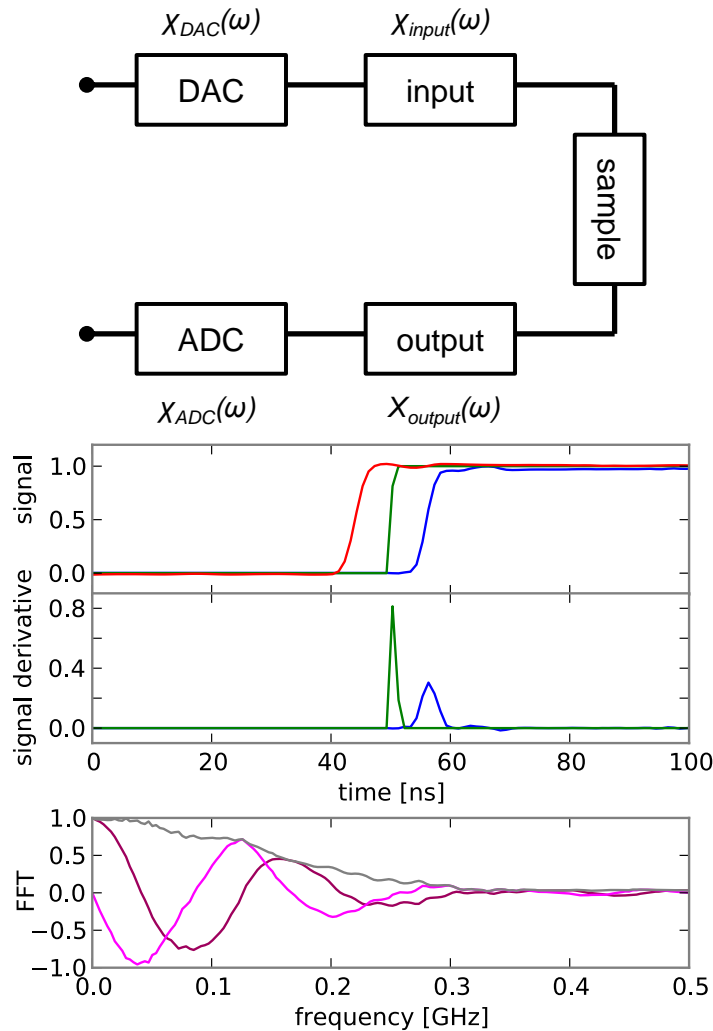


Figure 4.4: (response function filtered with a Gaussian filter with a cut-off at 0.4 GHz)

$$\chi_{\text{fl}}(\omega) = \chi_{\text{signal}}(\omega) \cdot \chi_{\text{DAC}} \cdot \chi_{\text{input}} \cdot \chi_{\text{output}} \cdot \chi_{\text{ADC}} \quad (4.3)$$

Here, χ_{signal} is the Fourier transform of the ideal input signal, χ_{ADC} and χ_{DAC} describe the response functions of the DAC and ADC, χ_{input} and χ_{output} corresponds to the response function of the input and output transmission lines. We can assume that $\chi_{\text{input}} \approx \chi_{\text{output}}$ since the input and output lines are symmetrical. By measuring χ_{fl} and correcting the measured Fourier spectrum for the response function of the ADC χ_{ADC} (which can be measured separately) we obtain the input line response $\chi_{\text{DAC}}\chi_{\text{input}}$ including the DAC response that we can then correct by applying

$$\chi_{\text{signal}}^{\text{corr}} = \chi_{\text{signal}} \cdot (\chi_{\text{DAC}} \cdot \chi_{\text{input}})^{-1} \cdot G(f_0). \quad (4.4)$$

Here, $G(f_0)$ is a Gaussian filter function that we apply to the measured response function to renormalize the signal distortion at high frequencies that is caused by the fact that we are not able to accurately measure the response function of the flux line above a certain frequency threshold due to the limited bandwidth of our measurement equipment. Usually, we set this cutoff frequency to $f_0 = 300$ MHz which allows us to correct most signal distortion in the frequency band up to $f = 1$ GHz that is relevant to this work.

After having corrected the response of the flux line by this technique, we can further reduce signal distortion by directly probing the flux seen by the qubit at a given time by measuring the qubit frequency as a function of the time while applying a flux test signal to it. The measurement of the qubit frequency is done by driving it with a calibrated X_π Rabi pulse and maximizing the measured $|1\rangle$ occupation probability after the pulse by tuning the qubit drive frequency. Using this technique, we can achieve a time resolution that is comparable to the length of the Rabi pulse that we use and which, for this work, is about 3 – 4 ns. After having reconstructed the flux signal seen by the qubit, we can calculate the response function of the flux line and again correct it by changing the input signal. Fig. 4.4b shows the measured flux signal seen by the qubit, the corresponding response function and the corrected input waveform for one of our qubits.

4.2.4 Pulse Synchronization

In our experiment, each qubit possesses two microwave sources that generate the drive and readout signals for it. The fast drive pulses for each qubit are generated by a single arbitrary waveform generator (AWG). A second AWG generates the flux pulses for the two qubits. The measurement of the reflected and demodulated readout signal of both qubits is done by a single ADC card. All these different signal generators and measurement devices need to be synchronized in order to maintain the relative phases and time differences between them between individual runs of our experiment. For this, we use a 10 MHz frequency reference chain, whose master clock is generated by the AWG that is responsible for generating the qubit drive pulses. The reference signal is then passed on to all microwave sources and signal generators as well as oscilloscopes, spectrum analyzers and ADC cards in our setup. In addition, to avoid random phase-jitter between the signals of the two microwave sources that generate the drive pulses of the two qubits, their drive frequencies need to be chosen such that they correspond a multiple of the repetition frequency of the master AWG, which is typically 50 kHz. If this condition is met, the relative phases between the two microwave signals is conserved between individual runs of

the experiment, which is crucial when performing measurements that are sensitive to this phase such as quantum state tomography of entangled two-qubit states. In addition, a 1 GHz phase synchronization chain is used to phase-lock the two microwave generators and reduce phase drift between them.

4.3 Measurement Techniques

In this section, we discuss the techniques used to characterize and manipulate our two-qubit processor. We will cover the qubit readout and manipulation and will describe how we can determine all relevant qubit parameters using microwave reflectometry measurements.

4.4 Qubit Readout

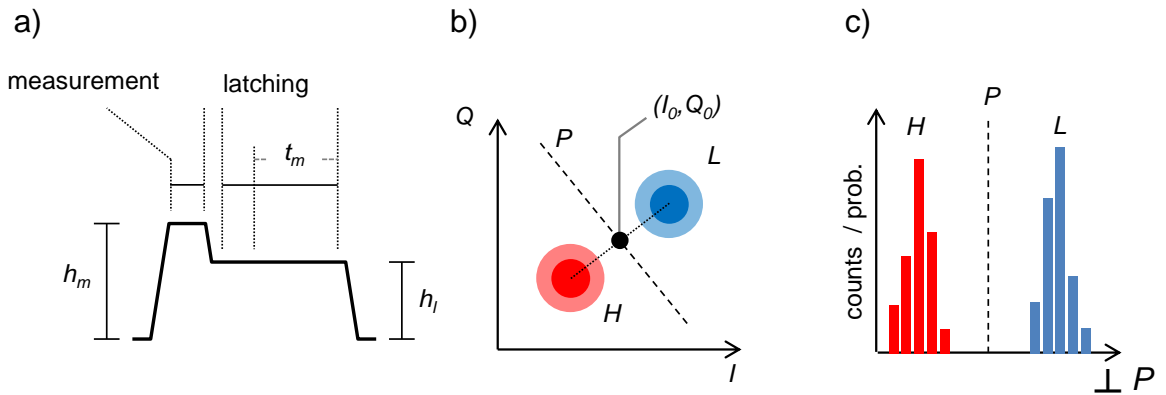


Figure 4.5: ...

The general readout principle of the CJBA readout that we use in this work is described in section 2.4.3. Here we explain how we choose the frequency and drive amplitude working point for the readout. For all measurements described in this paragraph, the qubit is assumed to be in the $|0\rangle$ state all the time. To bring up the readout, we first determine the resonance frequency f_r of the CJBA by reflectometry. We then choose a relative drive detuning $\Omega > \sqrt{3}$ at which the bistable regime is accessible. We mix the continuous drive signal with a drive pulse as shown in fig. 4.5a. We attenuate the resulting drive signal using a tunable attenuator at room temperature and send it to the sample. The reflected and amplified signal is then demodulated with the continuous input drive signal using an IQ demodulator. The resulting I/Q quadrature signals get then again amplified and digitized by an ADC card at a sample rate of 1 GHz, where we measure the signal only in the time window t_m indicated in fig. 4.5a. We average the digitized I/Q signals over the whole measurement window to obtain a single measurement point in the IQ plane and repeat this sequence a large number of times (typically 10^4). We repeat this sequence while ramping the attenuation, each time calculating the variance $\sigma_{IQ}^2 = \text{var}(Q) + \text{var}(I)$ of the obtained set of points. When reducing the attenuation, at some point the input power sent to the

CJBA will be sufficient to make it switch from the L to the H state, thereby changing the phase and consequently the I/Q values of the obtained signal. σ_{IQ}^2 will be biggest at a power where approximately 50 % of switching occurs, as shown in fig. 4.5b. By subtracting the average (I,Q) values at this point and performing a principal axis transformation that diagonalizes the covariance matrix

$$\text{var}_{IQ} = \begin{pmatrix} \text{var}(I) & \text{cov}(I, Q) \\ \text{cov}(I, Q) & \text{var}(Q) \end{pmatrix}. \quad (4.5)$$

We can project the measured (I,Q) data points on the axis P in fig. 4.5 and obtain a 1D probability distribution. The obtained offsets I_0 , Q_0 and principal axis rotation angle α_{IQ} gives us then the discrimination criterion $Q_L < Q_0 + \tan \alpha_{IQ}(I - I_0)$ that we use to classify new data points as belonging either to a L or H state. If measurement window is large enough and no retrapping occurs during the measurement, the distributions corresponding to the L and H states will not overlap, yielding perfect discrimination between them.

After having determined the I_0 , Q_0 and α_{IQ} we tune the attenuation such that we obtain $\approx 20\%$ switching, which usually gives us sufficient readout contrast to perform a qubit spectroscopy, as described in section ?? and calibrate a X_π Rabi pulse, as described in section ?? . We can then measure the switching probability of the CJBA readout as a function of the input power for the qubit in the state $|0\rangle$ and $|1\rangle$. Fig. ?? shows an example of such an s-curve measurement. The difference between the two curves corresponding to the $|1\rangle$ and $|0\rangle$ corresponds to the readout contrast and allows us to choose the optimum drive power that yields the highest readout contrast. If desired, we can also perform a X_π^{12} pulse on the qubit to put it in the state $|2\rangle$. In this state, the dispersive shift of the resonator frequency is larger than in the state $|1\rangle$, usually yielding a comparatively higher readout contrast, as shown in fig. ?? . This is advantageous when performing e.g. single-run quantum algorithms on the processor, as described in chapter 6.

4.5 Qubit Manipulation

To drive the qubits, we need to generate fast microwave pulses with a well defined frequency and phase. As described in one of the previous paragraphs we can use IQ sideband mixing to shape arbitrary drive pulses of the form

$$u(t) = I(t) \cos \omega_{rf} t + Q(t) \sin \omega_{rf} t \quad (4.6)$$

We can rewrite this as a product of two complex quantities

$$u(t) = \Re [A(t) \cdot \exp(-i\omega_{rf}t)] \quad (4.7)$$

where we defined, as before, $A(t) = I(t) + iQ(t)$. The reference phase defining an x-pulse can be chosen arbitrarily but must be conserved during one single experimental run. Thus, to realize a rotation of the qubit state in the xy-plane of the bloch sphere around an axis defined through

an angle ϕ we can use a Gaussian-shaped pulse of the form

$$A(t) = A_0 \cdot \exp\left(-\frac{(t - t_0)^2}{2\sigma_t^2}\right) \cdot \exp(-i\phi) \quad (4.8)$$

In the following chapter we will discuss more in detail the calibration of these drive pulses and possible errors induced when driving the qubit at frequencies comparable to its anharmonicity.

4.5.1 Spectroscopic Measurements of the Qubit State

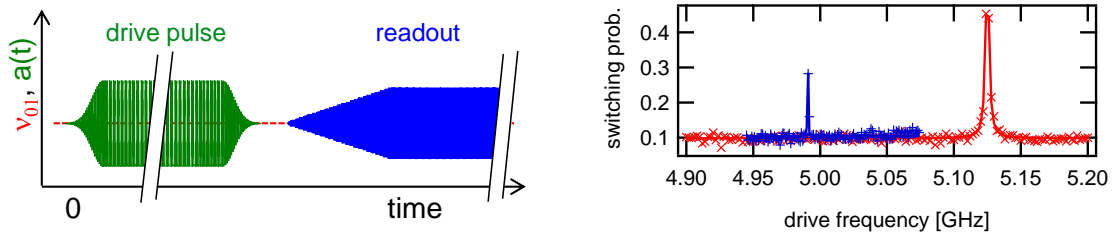


Figure 4.6: Example of a measured qubit spectroscopy. Shown is the switching probability of the qubit readout when driving the qubit with a very long drive pulse (typically $1 \mu\text{s}$) at a given drive frequency. The resonance to the right corresponds to the $|0\rangle \rightarrow |1\rangle$ (at frequency f_{01}) transition of the qubit, the resonance on the left to the 2-photon $|0\rangle \rightarrow |2\rangle$ (at frequency $f_{02}/2$) transition. We perform a Lorentzian fit of the two resonances to obtain the $|0\rangle \rightarrow |1\rangle$ and $|0\rangle \rightarrow |2\rangle/2$ resonance frequencies, from which we can calculate all other qubit transition frequencies.

In order to characterize the transition frequency and anharmonicity of the qubit it is useful to perform spectroscopic measurements of the qubit state. For this we drive the qubit with a very long Rabi pulse (usually $> 500 \text{ ns}$ at a well-defined frequency f_r). When the drive frequency f_r corresponds to the f_{01} frequency of the qubit the drive pulse will induce a strong Rabi oscillation of the quantum state of the qubit. Since the decoherence time of the qubit is of the order of the length of the drive pulse, the qubit state will decay and dephase during the driven evolution, effectively yielding an equal probability to measure the qubit in either of the states $|0\rangle$ or $|1\rangle$ at the end. When the drive frequency is detuned from the qubit transition frequency, no oscillation will be induced and hence the qubit will remain in the state $|0\rangle$. The width of the resonance in frequency space is inversely proportional to the dephasing time of the qubit, following the equation

$$\dots \quad (4.9)$$

Fig. 4.6 shown an exemplary qubit spectroscopy. Plotted is the probability of measuring the qubit in state $|1\rangle$ after applying a $1 \mu\text{s}$ rabi pulse at a given drive frequency to it. The blue curve has been measured at 10 dB higher power than the red curve and shows the $|0\rangle \rightarrow |2\rangle$ transition of the qubit. By fitting the resonance curves with a Lorentzian model we obtain the qubit frequencies f_{01} and $f_{02}/2$, which allow us to calculate the effective Josephson and charging energies at the given working point.

4.5.2 Rabi Oscillations

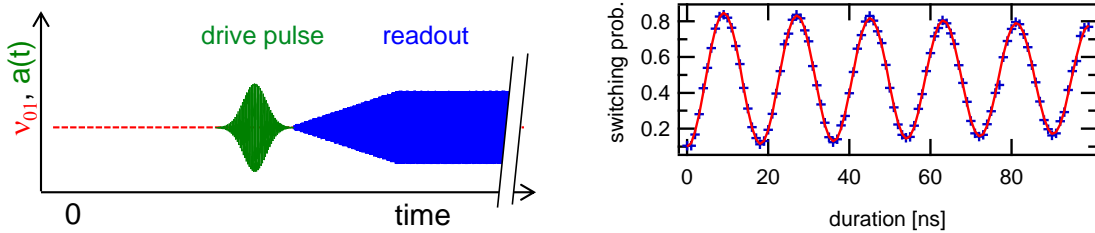


Figure 4.7: Example of a measured qubit Rabi experiment. Shown is the switching probability of the qubit readout when driving the qubit at f_{01} with a Gaussian drive pulse of varying duration. The measurement results are not corrected for readout errors.

After having obtained the proper qubit transition frequency f_{01} using the technique described above, we can perform a Rabi oscillation experiment by driving the qubit for a well-defined time with a drive pulse at the f_{01} transition frequency and measuring the state of the qubit directly afterwards. Fig. 4.7 shows an exemplary Rabi measurement. The blue dots correspond to measured data points whereas the continuous red line corresponds to a fit of a model of the form $p(t) = p_0 + a \cos \Omega t \exp -\Gamma_1 t$ to the experimental data. As can be seen, the amplitude of the Rabi oscillations gets damped the longer the drive pulse becomes, which is due to relaxation and dephasing during the driven evolution of the qubit. The maximum probability contrast is limited due to readout errors, as we will explain in more detail in the following chapter. From the fit of the Rabi data we obtain the Rabi frequency Ω , which we can then use to perform precise single-qubit rotations, as will be explained later. Due to the finite anharmonicity of the qubit, there will always be a leakage to the second excited state $|2\rangle$ of the qubit which gets stronger, the faster we drive the system. This leakage mechanism is an important source of errors and very relevant to the experiments that will be discussed later, so we will quantify it in detail in the following chapter as well.

4.6 Dephasing Time Measurement

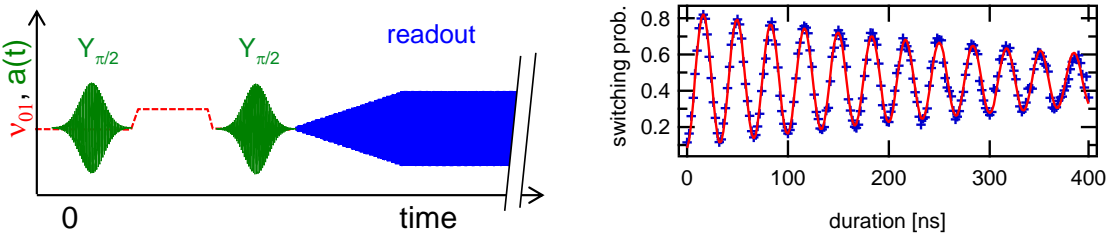


Figure 4.8: Example of a measured qubit Ramsey experiment. Shown is the switching probability of the qubit readout after performing a $X_{\pi/2}$ -wait- $X_{\pi/2}$ drive sequence at a frequency $f_{01} - \delta f$. Fitting the resulting curve with an attenuated sine-wave model allows us to determine the f_{01} frequency of the Qubit with high accuracy.

After having obtained the transition frequency f_{01} of the qubit and the Rabi frequency Ω , we can characterize the dephasing of the qubit by performing a so-called *Ramsey fringe experiment*[1]. In this experiment, we perform a $Y_{\pi/2}$ rotation of the qubit from the state $|0\rangle$, obtaining thus a superposed qubit state of the form $1/\sqrt{2}(|0\rangle + |1\rangle)$. Then we displace the qubit frequency by an amount Δf by using e.g. a fast magnetic flux pulse and let the qubit state evolve freely during a certain amount of time Δt . Finally, we apply another $Y_{\pi/2}$ pulse to the qubit and measure the state of the qubit directly afterwards. Since the qubit frequency has been displaced during the free evolution, the qubit will acquire a phase $\Delta\phi = 2\pi\Delta f\Delta t$. The final state of the qubit after applying the second $Y_{\pi/2}$ pulse will therefore be given as

$$|\phi_f\rangle = \begin{pmatrix} 1 & -1 \\ 1 & 1 \end{pmatrix} \cdot \begin{pmatrix} 1 \\ e^{i\Delta\phi} \end{pmatrix} = \begin{pmatrix} i \sin \Delta\phi/2 \\ -\cos \Delta\phi/2 \end{pmatrix} \quad (4.10)$$

Hence, the resulting state $|\phi_f\rangle$ will oscillate between the state $|0\rangle$ and $|1\rangle$ with a frequency $\Delta f/2$. As before, due to dephasing and relaxation during the free evolution of the qubit state, the amplitude of these oscillations will decay. If the system dephasing time is limited by qubit relaxation, the decay will follow a Gaussian decay of the form $\exp(-\Gamma t^2)$, otherwise it will also exhibit an exponential decay $\simeq \exp(-\Gamma t)$ [2]. In the Ramsey sequence, instead of detuning the qubit frequency during the free evolution phase we can also detune the qubit drive frequency instead. If this detuning is small in comparison to the Rabi frequency Ω , we will induce only a negligible error when applying the first $Y_{\pi/2}$ pulse. But since the drive frequency is detuned, the qubit will also acquire a phase $\Delta f\Delta t$ during the free evolution phase. Fitting the experimental data obtained for such an experiment to a model of the form $p(|1\rangle) = p_0 + a \cos(\Delta f\Delta t + \phi_0) \exp -\Gamma_2 t^2 / 2$ we can obtain an estimate of Δf . Since we know the frequency detuning of the drive during the free evolution of the qubit we can subtract it from the fitted value in order to obtain the remaining detuning of the qubit from the drive frequency at zero drive detuning. This method allows us thus to make a precise fit of the qubit frequency and to correct drive frequency errors with an accuracy of typically 100 kHz.

4.7 Relaxation Time Measurement

We can characterize the relaxation time of the qubit by performing a simple experiment where we put the qubit in state $|1\rangle$ by applying a X_π pulse and let the qubit evolve freely for a given time before measuring its state. The resulting curve when performing such an experiment is shown in fig. 4.9. It shows the probability of measuring the qubit in state $|1\rangle$, plotted as a function of the delay between the initial state preparation and measurement. As can be seen, this probability decreases exponentially as a function of time. As before, in the curve the blue markers correspond to experimental data and the red line corresponds to a fit of this data to a model of the form $p(|1\rangle) = p_0 + p_a \exp(-\Gamma_1 t)$. From this fit we can then easily extract the relaxation rate Γ_1 of the qubit at the given working point. In the following chapter we will look more in detail at the relaxation time of both qubits as a function of their transition frequency and

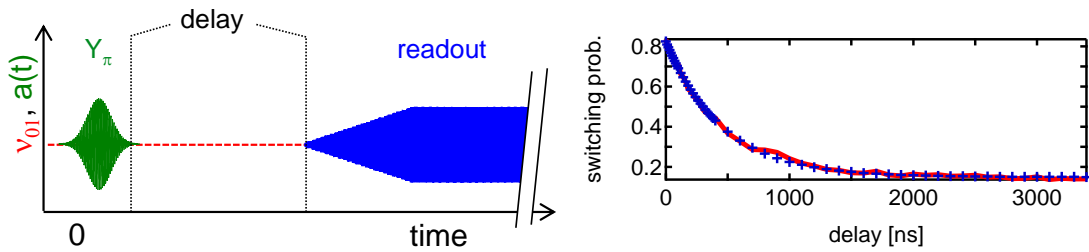


Figure 4.9: Example of a qubit relaxation time measurement. Shown is the probability of measuring the qubit in state $|1\rangle$ as a function of the delay time between the preparation of the state $|1\rangle$ and the actual measurement of the qubit state. The decay of this probability follows an exponential law of the form $p(|1\rangle) \simeq \exp(-\Gamma_1 t)$

their detuning from the readout resonator.

Chapter 5

Characterizing the Two-Qubit Processor

After having detailed the design of the processor and the measurement techniques employed in this work, we will now show how we can “test drive” it to show the basic functionality that we need to run meaningful quantum algorithms. In particular we show how we can implement a robust two-qubit quantum gate that we will use in the following chapter to run a real-world quantum algorithm on our processor.

We begin the chapter by discussing the measurement of the basic qubit and readout parameters. We will then give a detailed overview of the relevant decoherence times and readout fidelities of our processor at different working points and discuss our strategy for optimizing these parameters during the operation of the processor. Afterward we will explain the realization of single-qubit gates together with possible error sources that we need to take into account. We also discuss in detail the generation and characterization of entanglement. Finally, we discuss the implementation of a universal two-qubit gate and its characterization through quantum process tomography.

5.1 Qubit & Readout Characterization

The first step in the characterization of the processor consists in obtaining all the relevant qubit and readout parameters. For this, we perform a set of measurements from which we obtain the qubit frequencies, anharmonicities, junction asymmetries, the inter-qubit coupling, the coupling to the microwave drive lines, the coupling of each qubit to its readout and the relaxation and dephasing times of the qubits. Most of these parameters, such as the drive and readout couplings as well as the relaxation and dephasing times are measured for a range of qubit frequencies, which will allow us later to pick an ideal working point for our two-qubit experiments. A detailed account of the spectroscopic techniques employed here can be found in chapter 4. The qubit parameters that we obtain from our measurements are as follows:

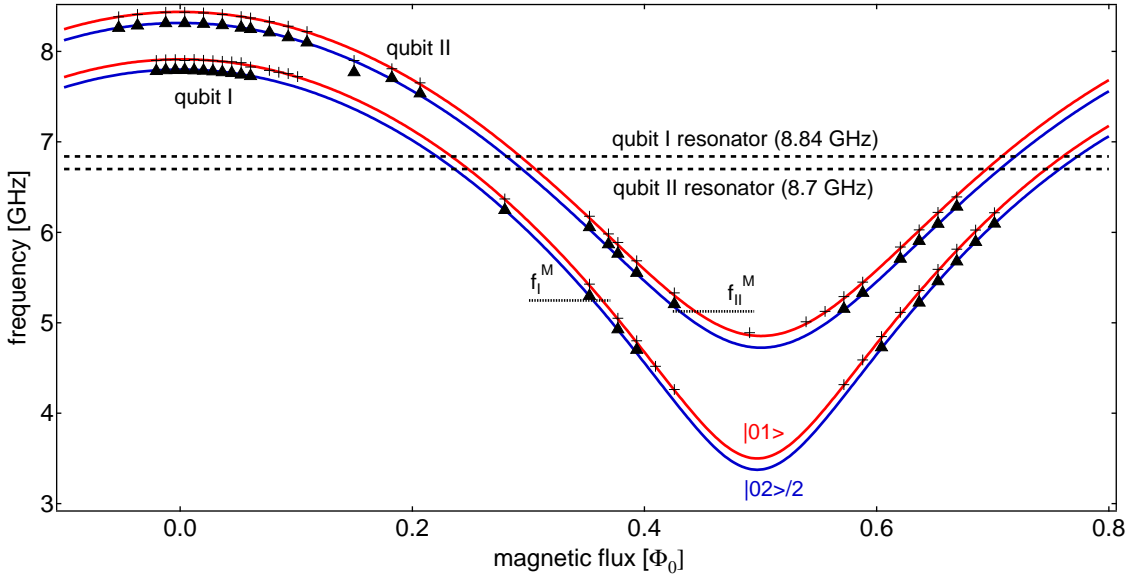


Figure 5.1: Spectroscopy of our two-qubit processor. Shown are the $|0\rangle \rightarrow |1\rangle$ (ω_{01}) and $(|0\rangle \rightarrow |2\rangle)/2$ ($\omega_{02}/2$) transition frequencies of the two qubits, together with a fitted analytical model of the qubit parameters. We also show the frequencies of the two readout resonators. The frequencies f_M^I and f_M^{II} indicate the working points of the qubits for single-qubit manipulation

Figure Comment 2: add more information to the figure and correct the notation of the manipulation working point

Qubit Parameters

To obtain the Josephson and charging energies as well as the junction asymmetries of the qubits we perform spectroscopic measurements of the single-photo $n|0\rangle \rightarrow |1\rangle$ and the two-photon $|0\rangle \rightarrow |2\rangle$ qubit transitions at different values of the magnetic flux Φ . Fitting the resulting values $\omega_{01}(\Phi)$ and $\omega_{02}(\Phi)$ to a theoretical model we obtain all relevant qubit parameters. For our processor, these are $E_J^I/h = 36.2$ GHz, $E_c^I/h = 0.98$ GHz and $E_J^{II}/h = 43.1$ GHz, $E_C^{II}/h = 0.87$ GHz for the Josephson and charging energies of the two qubits and $d^I = 0.2$, $d^{II} = 0.35$ for the qubit junction asymmetries.

Readout Parameters

To obtain the resonance frequencies and quality factors of the readout resonators we perform a simple reflectometric measurement of the S_{11} transmission coefficient of the resonators. The resulting frequencies are $\nu_R^I = 6.84$ GHz and $\nu_R^{II} = 6.70$ GHz with quality factors $Q^I \simeq Q^{II} = 730$. We measure the Kerr nonlinearity K of the resonators by following the procedure given in [70, p. 166] and obtain $K^I/\nu_R^I \simeq K^{II}/\nu_R^{II} = -2.3 \pm 0.5 \times 10^{-5}$

Qubit/Readout Coupling

The coupling of the qubits to the readout resonators can be determined by spectroscopically measuring the avoided level crossing between the two systems. For this, we perform a series of spectroscopic measurements of the resonator for a range of qubit frequencies ranging from below the resonator frequency to above it. The results of these measurements are shown in fig. 5.2 and clearly show an avoided level crossing between the two systems. From the width of this crossing we can obtain the qubit-resonator coupling coefficients, which are $g_0^I \simeq g_0^{II} = 50$ MHz.

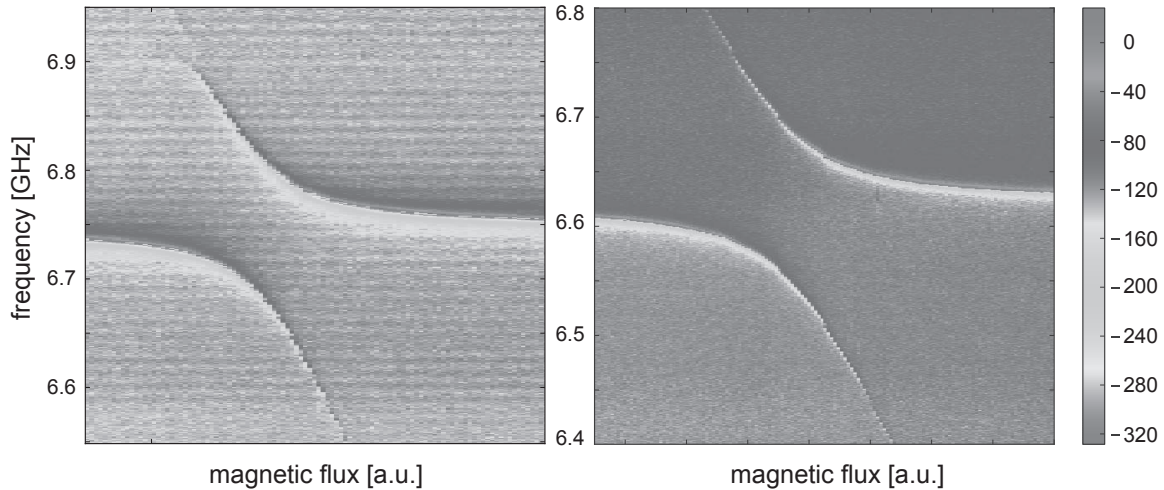


Figure 5.2: Spectroscopic measurement of the avoided level crossing between the two qubits and their corresponding readout resonator, corresponding to an effective qubit-resonator coupling strength $2g \approx 50$ MHz.

Qubit Parameter Survey

In order to determine the optimal working point for our processor we need to characterize the properties of the qubits at many different frequencies. For this, we perform an automated survey where we measure the transition frequencies ω_{01} and ω_{20} , the readout contrast c and the relaxation and dephasing times T_1 and T_2 of each qubit at different values of the magnetic flux Φ . The results of such a parameter survey are summarized in fig 5.3, where we show the relaxation time T_1 , the readout contrast c_{10} and the Rabi frequency f_{Rabi} at fixed drive amplitude for the two qubits within a frequency range between 5.2 and 6.5 GHz. As can be seen, the relaxation time of the qubits tends to increase the farther detuned each qubit is from its readout resonator. Not surprisingly, the drive frequency of the qubit also decreases when the qubit-resonator detuning increases, as expected from the so-called *Purcell effect*, which filters incoming microwave signals that are far-detuned from the resonator frequency. The inverse is true for the readout contrast, which increases nearly linear when reducing the qubit-resonator detuning. This can be explained by the increase of the dispersive resonator frequency shift χ induced by the qubit, which decreases with the detuning Δ roughly as $1/\Delta$ (???)

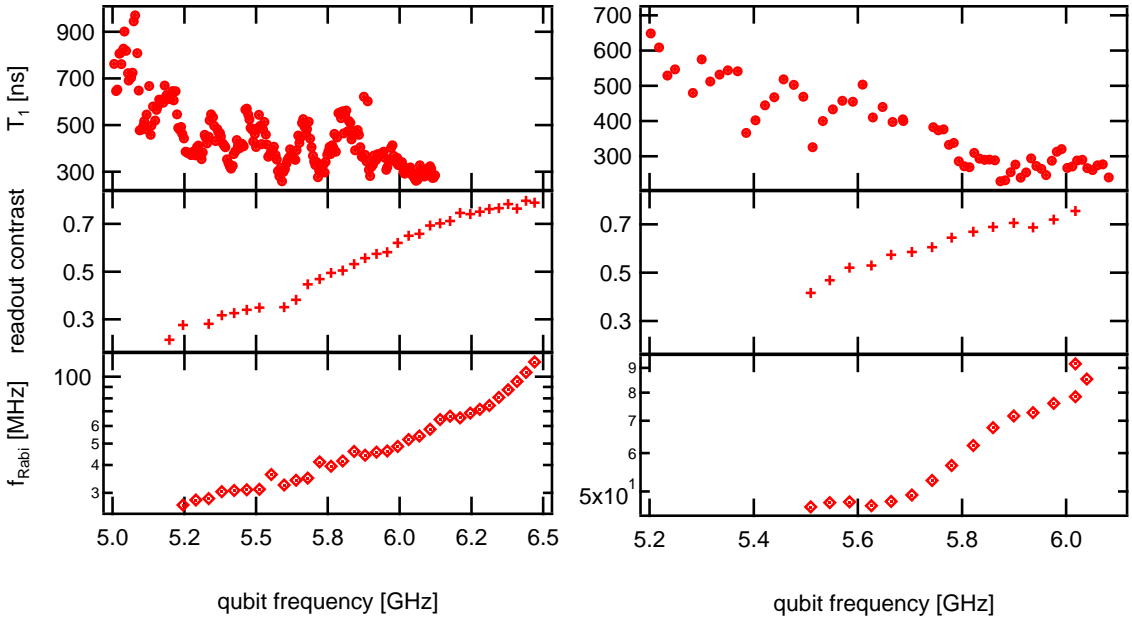


Figure 5.3: A qubit parameter survey showing the relaxation time T_1 , the readout contrast and the Rabi frequency at a fixed drive amplitude for the two qubits over a large range of qubit frequencies.

It is interesting to note the non-monotonous characteristic of the qubit relaxation time T_1 shown in fig. 5.3, which cannot be explained by Purcell-filtering through the readout resonator and hints thus at a different qubit relaxation process present in the system. A possible explanation would be the coupling of the qubit to spurious low-Q resonances in the environment. For example, the coupling of the qubit to volumetric resonance modes of the sample holder or to non-CPW resonance modes of the readout resonator could be possible explanations for the data. Also, the overall dependency of the relaxation time T_1 on the qubit-resonator detuning –ignoring the “fine-structure” present in the system– is not quadratic as would be expected from the Purcell theory but rather linear. Also, by comparing the qubit relaxation time to the Rabi drive frequency reveals that the increase in T_1 is clearly not proportional to the Purcell factor, that determines both the qubit relaxation rate through the readout resonator and the Rabi drive frequency. However, the observed T_1 dependency can be partially explained by taking into account the qubit relaxation through the fast fluxline, which might be too strongly coupled to the qubit, hence inducing additional qubit relaxation beyond the Purcell and intrinsic qubit relaxation rates.

5.2 Single-Qubit Operations

To perform arbitrary single-qubit operations – as needed e.g. for implementing a quantum algorithm or performing quantum state tomography – we need to implement a universal set of X , Y and Z qubit gates on our processor. Qubit rotations in the XY -plane are implemented through microwave drive pulses, where the phase of the drive pulse in reference to an arbitrary

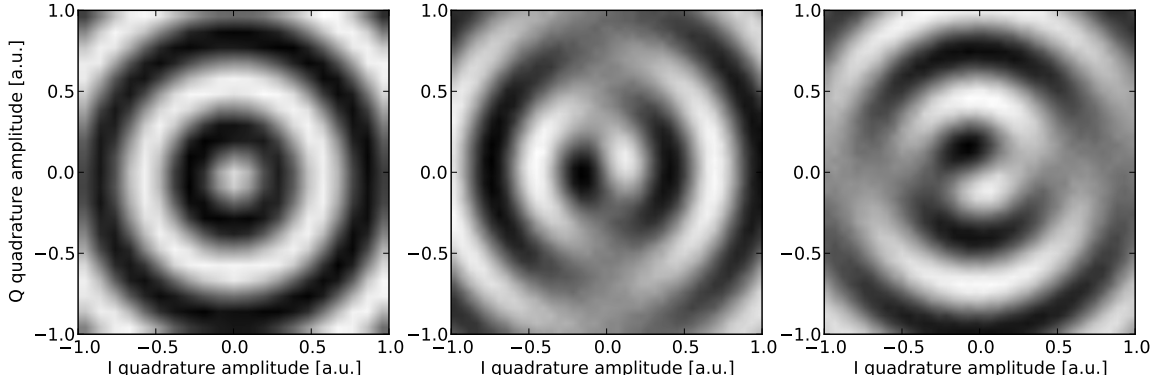


Figure 5.4: Demonstration of single-qubit IQ control. The figures show the state probability of a single qubit when preparing it in one of the states $|1\rangle$, $1/\sqrt{2}(|0\rangle+|1\rangle)$ or $1/\sqrt{2}(|0\rangle+i|1\rangle)$ and subjecting the qubit to a microwave drive pulse of the form $a(t) = V_I \cdot \cos \omega_{rf}t + V_Q \cdot \sin \omega_{rf}t$ of varying amplitudes V_I and V_Q and constant duration.

reference determines the rotation axis and the amplitude of the drive pulse the Rabi frequency of the gate. To characterize the drive pulses, we perform an experiment where we initialize a single-qubit in the states $|1\rangle$, $1/\sqrt{2}(|0\rangle+|1\rangle)$ and $1/\sqrt{2}(|0\rangle+i|1\rangle)$ and subject it afterward to a single microwave pulse of the form $a(t) = V_I \cdot \cos \omega_{rf}t + V_Q \cdot \sin \omega_{rf}t$, which we tune by changing the input voltages V_I and V_Q to the IQ -mixer that generates the pulse from a continuous input microwave-tone at frequency ω_{rf} . We measure the qubit state at different values of V_I , V_Q , obtaining the graph shown in fig. 5.4. The qubit which was prepared in state $|1\rangle$ shows a perfectly cylinder-symmetric switching probability pattern when subjecting it to an IQ-pulse of a given phase, which is what one would expect for a qubit being prepared in either the $|0\rangle$ or $|1\rangle$ state. On the contrary, the switching probability distributions of the measured qubits prepared in the states $1/\sqrt{2}(|0\rangle+|1\rangle)$ and $1/\sqrt{2}(|0\rangle+i|1\rangle)$ are mirror-symmetric, where the switching probability does not vary at all along the drive axis that corresponds to the axis along which the qubit has been prepared. These measurements demonstrate therefore our ability to prepare and drive the qubit along arbitrary axes of the Bloch sphere. In the following sections we will analyze more in detail the drive errors inherent to our system and quantitatively analyze different error sources.

5.2.1 Single-Qubit Drive Errors

5.3 Simulation of Processor Operation

In order to obtain estimates of the experimental fidelities of the processor operation we perform numerical simulations of the full two-qubit processor. For this, we use the master equation approach discussed in section 2.5. In most cases we will use a simplified model that takes into account only the levels $|0\rangle$ and $|1\rangle$ of the qubit. However, in order to quantify the effect of the finite qubit anharmonicity we are forced to take into account the state $|2\rangle$ of the Transmon as

well, which leads to a slightly more complicated Hamiltonian, as discussed in section A.2. Here, we discuss only the simple two-qubit variant: The Hamiltonian of the two-qubit system can be written as

$$\hat{H} = \hat{H}_1^d \otimes \mathbf{I} + \mathbf{I} \otimes \hat{H}_2^d + \hat{H}_{qq} \quad (5.1)$$

where \hat{H}_1^d and \hat{H}_2^d are the drive Hamiltonians of the first and second qubit, respectively, and are given as

$$\hat{H}_{1,2}^d = \alpha_{1,2}(t)\hat{\sigma}_x + \beta_{1,2}(t)\hat{\sigma}_y + \gamma_{1,2}(t)\hat{\sigma}_z, \quad (5.2)$$

where $\alpha_{1,2}(t)$ and $\beta_{1,2}(t)$ are complex functions and $\gamma_{1,2}(t)$ are real-valued functions. The interaction Hamiltonian in the frame rotating at the average qubit-frequency $(\omega_{01}^1 + \omega_{01}^2)/2$ is given as

$$\hat{H}_{qq} = \begin{pmatrix} 0 & 0 & 0 & 0 \\ 0 & -\frac{\Delta(t)}{2} & g & 0 \\ 0 & g & +\frac{\Delta(t)}{2} & 0 \\ 0 & 0 & 0 & 0 \end{pmatrix}, \quad (5.3)$$

where $\Delta(t) = \omega_{01}^2(t) - \omega_{01}^1(t)$ is the time-dependent frequency detuning between the two qubits. Inserting the Hamiltonian in eq. (5.1) into eq. (2.112) we can simulate the operation of the two qubit Hamiltonian. To model qubit relaxation and decoherence, we use for each qubit two Lindblad operators of the form $L_{01}^{r,i} = \sqrt{\Gamma_{01}^{r,i}}\hat{\sigma}_{01}^-$ and $L_{01}^{\phi,i} = \sqrt{\Gamma_{01}^{\phi,i}/2}\hat{\sigma}_{01}^z$, where $i \in \{1, 2\}$ and $\Gamma_{01}^{r,i}$ and $\Gamma_{01}^{\phi,i}$ are the effective relaxation and dephasing rates of each qubit, respectively, and where $\hat{\sigma}_{01}^-$ and $\hat{\sigma}_{01}^z$ are matrices

$$\hat{\sigma}_{01}^- = \begin{pmatrix} 0 & 1 \\ 0 & 0 \end{pmatrix} \quad \hat{\sigma}_{01}^z = \begin{pmatrix} 1 & 0 \\ 0 & -1 \end{pmatrix} \quad (5.4)$$

that describe a relaxation or dephasing process, respectively. The relaxation and dephasing rates depend on the qubit frequency and can be adapted in the simulation according to the chosen qubit frequency working point. Single-qubit gate sequences are fully described by the three functions $\alpha_{1,2}(t)$, $\beta_{1,2}(t)$ and $\gamma_{1,2}(t)$, a two-qubit swap gate can be modeled by changing the parameter $\Delta(t)$.

5.4 Two Qubit Operations

We use the capacitive coupling between the qubits to implement two-qubit gates and create entangled states between the two qubits. To characterize the qubit-qubit interaction, we first perform a spectroscopic measurement of the system. For this, we measure a spectroscopy of one of the qubits for a range of qubit frequencies such that the frequency of qubit I, ω_{01}^I gets tuned through the frequency of qubit II, ω_{01}^{II} . When these two frequencies are sufficiently close we observe an avoided level crossing between the qubits. At resonance, the gap between the two spectroscopic lines that appear corresponds to the qubit-qubit coupling strength $2g$. Fig 5.5 shows the results of such a measurement, qubit II was positioned at a 5.125 GHz and the

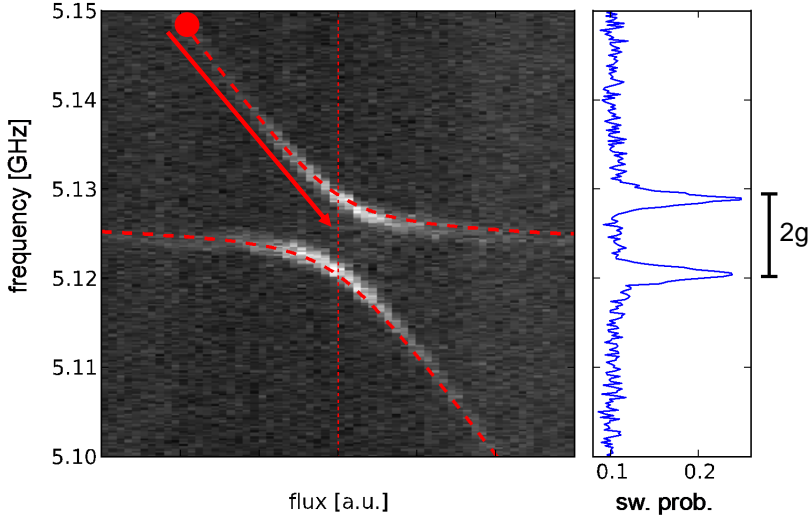


Figure 5.5: a) Spectroscopy measurement of the avoided level crossing between the two qubits of our processor. b) Single spectroscopy of qubit I when in resonance with qubit II. From this spectroscopic measurement, a qubit-qubit strength of $2g = 8.9$ MHz can be deduced.

frequency of qubit II was tuned from 5.1 – 5.15 GHz. At resonance we measure a coupling strength of $2g = 8.3$ MHz.

If the two qubit frequencies $\omega_{01}^I, \omega_{01}^{II}$ are far detuned such that $|\omega_{01}^I - \omega_{01}^{II}| \gg 2g$, the eigenstates of the coupled two-qubit Hamiltonian correspond to a very good accuracy to the independent qubit states $|01\rangle$ and $|10\rangle$. Therefore, far from the resonance we observe only one spectroscopic line corresponding to the transition $|00\rangle \rightarrow |10\rangle$ (since we drive only the first qubit). However, close to resonance the eigenstates approach the Bell states $|\Psi_{\pm}\rangle = 1/\sqrt{2}(|10\rangle \pm |01\rangle)$, which can both be excited by driving qubit I. Hence we observe two spectroscopic lines corresponding to the two transitions $|00\rangle \rightarrow 1/\sqrt{2}(|01\rangle + |10\rangle)$ and $|00\rangle \rightarrow 1/\sqrt{2}(|01\rangle - |10\rangle)$.

5.4.1 Creation of Entanglement

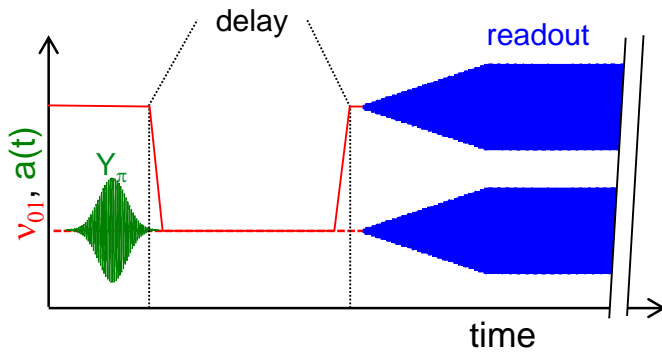


Figure 5.6: Pulse sequence used to create an entangled two-qubit state using a non-adiabatic transfer from an off-resonant to a resonant two-qubit state.

After having characterized the qubit-qubit interaction using a spectroscopic measurement we perform a coherent swapping operation between the qubits. We implement this operation by

non-adiabatically changing the resonance frequency of the qubits from an off-resonance to an on-resonance condition. When doing this after preparing the qubits in one of the states $|01\rangle$ or $|10\rangle$ we induce a coherent energy swap between the qubits. We then terminate the interaction after a well-defined time and measure the state of the two-qubit register directly afterward. When the qubits are in resonance, the time evolution operator of their quantum state is given as

$$U(t) = \begin{pmatrix} 1 & 0 & 0 & 0 \\ 0 & \cos 2\pi t g & i \sin 2\pi t g & 0 \\ 0 & i \sin 2\pi t g & \cos 2\pi t g & 0 \\ 0 & 0 & 0 & 1 \end{pmatrix}_{\{|00\rangle, |01\rangle, |10\rangle, |11\rangle\}} \quad (5.5)$$

As can be seen, the two basis states $|01\rangle$ and $|10\rangle$ oscillate back and forth between each other with frequency g . The states $|00\rangle$ and $|11\rangle$ are not affected by the interaction.

Fig. 5.6 summarizes the frequency, drive and measurement pulse sequence that we use for this experiment. When varying the time during which the qubits are in resonance we can observe the coherent swapping of energy between them. Figure 5.7 presents the results of such a measurement. Shown are the measured qubit state probabilities $p(|00\rangle)$, $p(|01\rangle)$, $p(|10\rangle)$ and $p(|11\rangle)$ as a function of the swap duration Δt . Subfigure a) shows the raw, uncorrected readout data, subfigure b) shows the probabilities corrected for limited readout visibility and subfigure c) shows the probabilities corrected for both limited readout visibility and inter-readout crosstalk. The oscillatory behavior between the states $|01\rangle$ and $|10\rangle$ is well-visible in the data. Also, the frequency of the energy swap $2g = 8.3$ MHz agrees well with the value obtained from the spectroscopic measurement. Fig. 5.7c shows, in addition to the measured state occupation probabilities, a master equation simulation of the experiment. This simulation takes into account relaxation and dephasing of the qubits. The relaxation rates used in the simulation correspond to the experimentally measured relaxation rates at the operating frequencies of the qubits, whereas the dephasing rates were free fitting parameters. We do not use the measured single-qubit dephasing times in our simulation since they do not correspond to the effective dephasing rate of the two-qubit system at resonance, which cannot be described within the master equation formalism. The reason for this is that the transition frequency of the two eigenstates $|\phi_{\pm}\rangle = 1/\sqrt{2}(|01\rangle \pm |10\rangle)$ at resonance $\omega_{01}^{\pm} = \omega_{01}^{I,II} \pm \sqrt{4g^2 + \Delta^2}/2 \approx \omega_{01}^{I,II} \pm g + \Delta^2/8g$ is insensitive to variations of Δ to first order. Hence, the effective dephasing rate of the two-qubit system will be much higher than the single-qubit dephasing rates. To reproduce the experimentally observed dephasing we therefore use effective dephasing rates $\Gamma_{\phi}^{I,II} = 2 \mu\text{s}$ in our simulation. As can be seen, using these rates and the measured relaxation rates and coupling parameter the simulation agrees very well with the experimental data.

5.4.2 Quantum State Tomography

The experiments that we describe in the following sections often require us to determine the density matrix of an experimental two-qubit state. The method that we use for this purpose is called *quantum state tomography* (QST) (see e.g. [67] for an overview of this method). In this

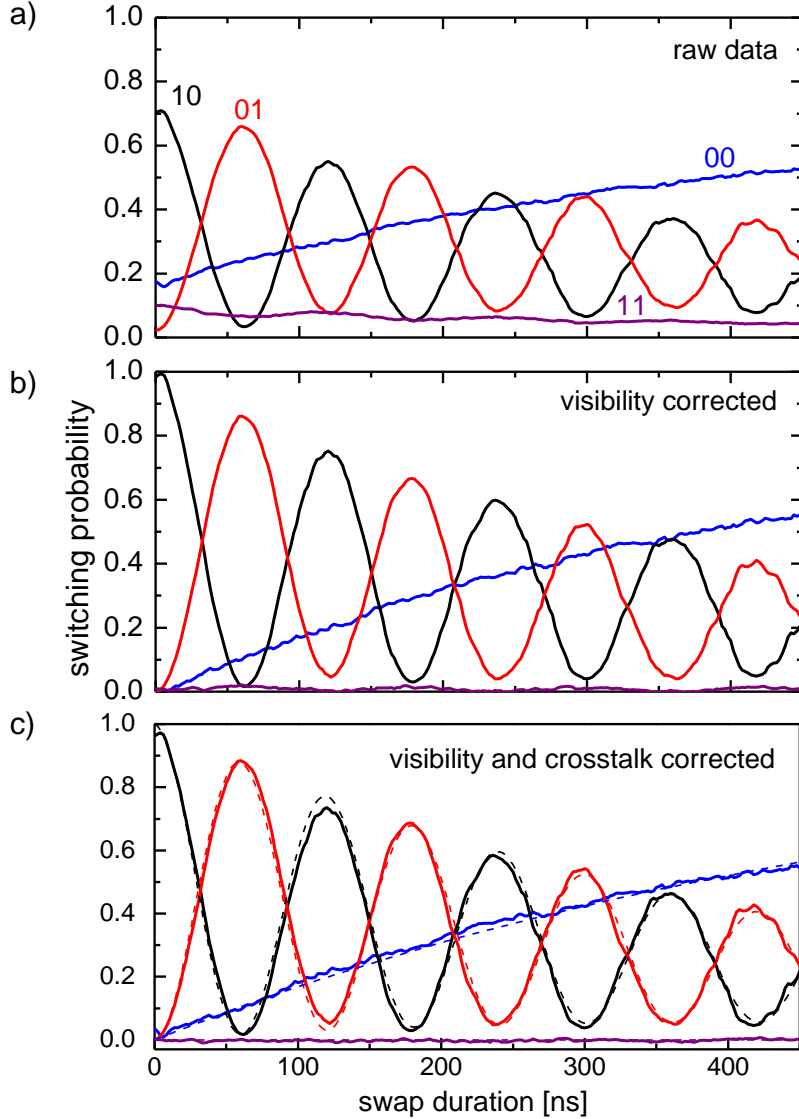


Figure 5.7: State occupation probabilities for the two-qubit register during a coherent energy swap. a) Shows the raw state probabilities corresponding to the states $|00\rangle$, $|01\rangle$, $|10\rangle$ and $|11\rangle$, b) shows the same data corrected for the limited visibility of each qubit readout and c) shows the fully corrected readout data where we account for both visibility and inter-qubit readout crosstalk errors.

section, we therefore explain in detail the procedure that we use to perform QST. Furthermore, we also discuss several sources of errors occurring in standard QST and how we can estimate their effect on our results.

The density matrix of an n -qubit system can be written as

$$\rho = \sum_{v_1, v_2 \dots v_n} \frac{c_{v_1, v_2 \dots v_n} \sigma_{v_1} \otimes \sigma_{v_2} \dots \otimes \sigma_{v_n}}{2^n} \quad (5.6)$$

$$c_{v_1, v_2 \dots v_n} = \text{Tr} \{ \sigma_{v_1} \otimes \sigma_{v_2} \dots \otimes \sigma_{v_n} \rho \} \quad (5.7)$$

where $v_i \in \{X, Y, Z, I\}$ and n gives the number of qubits in the system and where the c_{v_1, v_2, \dots, v_n} are real-valued coefficients that describe the given density matrix. To reconstruct the density matrix of an experimental quantum system in a well-prepared state it is thus sufficient to measure the expectation values of these $n^2 - 1$ coefficients on an ensemble of identically prepared states. For our two qubit system, this means measuring all possible combinations of the operators $\{I, \sigma_x^I, \sigma_y^I, \sigma_z^I\} \otimes \{I, \sigma_x^{II}, \sigma_y^{II}, \sigma_z^{II}\}$. However, in our experiments, rather than measuring σ_x and σ_z operators directly, we rotate the quantum state of each qubit around such that the state vector along the desired measurement axis coincides with the z-axis of the Bloch sphere and measure σ_z afterward.

When using this direct measurement method, statistical and systematic measurement errors can yield a set of coefficients v_i that corresponds to a *non-physical* density matrix, which violates either the positivity $\langle \psi | \rho | \psi \rangle > 0$ (for all valid states $|\psi\rangle$) or the unity-trace condition $\text{Tr}(\rho) = 1$. To alleviate this problem, several techniques can be employed. In the following section we discuss an estimation technique which is able to overcome the problem of non-physical density matrices, the so-called *maximum likelihood estimation*. When using this direct measurement method, statistical and systematic measurement errors can yield a set of coefficients v_i that corresponds to a *non-physical* density matrix, which violates either the positivity $\langle \psi | \rho | \psi \rangle > 0$ (for all valid states $|\psi\rangle$) or the unity-trace condition $\text{Tr}(\rho) = 1$. To alleviate this problem, several techniques can be employed. In the following section we discuss an estimation technique which is able to overcome the problem of non-physical density matrices, the so-called *maximum likelihood estimation*.

Maximum Likelihood Estimation of Quantum States

Maximum likelihood estimation is a method that numerically or analytically maximizes a likelihood function that is based on a number of measured outcomes and a set of parameters that need to be estimated. The set of parameters that corresponds to the maximum of the probability function can then be interpreted as the one with the highest probability of generating the observed outcomes. When estimating the parameters of a density matrix with this method, the probability function to be maximized is the joint probability of obtaining the measured values $\{c_{X,X,\dots,X}, c_{Y,X,\dots,X}, \dots, c_{I,I,\dots,I}\}$ for a given density matrix $\hat{\rho}$. By numerically or analytically maximizing this joint probability over the set of possible density matrices we obtain the density matrix which is most likely to have produced the set of measurement outcomes that we have observed.

The joint measurement operators $\Sigma_j = \sigma_{v_1} \otimes \sigma_{v_2} \dots \otimes \sigma_{v_n}$ have the eigenvalues ± 1 and can thus be written as

$$\sigma_{v_1} \otimes \sigma_{v_2} \dots \otimes \sigma_{v_n} = |+_j\rangle \langle +_j| - |-_j\rangle \langle -_j| \quad (5.8)$$

where $|+_j\rangle$ and $|-_j\rangle$ are the eigenstates corresponding to the eigenvalues ± 1 of Σ_j . When

performing l measurements of the operator Σ_j , the expectation value $\langle \Sigma_j \rangle$ can be calculated as

$$\widehat{\langle \Sigma_j \rangle}_\rho = \frac{1}{l} \sum_{i=1}^l M_i(\Sigma_j, \rho) \quad (5.9)$$

where $M_i(\Sigma, \rho)$ denotes the outcome of the i -th measurement of the operator Σ on the state described by the density matrix ρ . Since each outcome $M_i(\Sigma_j, \rho)$ is Bernoulli distributed, the sum $\widehat{\langle \Sigma_j \rangle}_\rho$ of them is binomially distributed with an expectation value $E(\widehat{\langle \Sigma_j \rangle}_\rho) = \langle \Sigma_j \rangle_\rho$ and the variance $\sigma^2(\widehat{\langle \Sigma_j \rangle}_\rho) = 1/l \cdot (1 - \langle \Sigma_j \rangle_\rho^2)$. For large sample sizes l , the binomial distribution can be well approximated by a normal distribution with the same expectation value and variance. The joint probability of obtaining a set of measurement values $\{s_1, \dots, s_{n^2-1}\}$ for the set of operators $\{\widehat{\langle \Sigma_1 \rangle}_\rho, \dots, \widehat{\langle \Sigma_{n^2-1} \rangle}_\rho\}$ is thus given as

$$P\left(\widehat{\langle \Sigma_1 \rangle}_\rho = s_1; \dots; \widehat{\langle \Sigma_{n^2-1} \rangle}_\rho = s_{n^2-1}\right) = \prod_{i=1}^{n^2-1} \exp\left(-\frac{l}{2} \frac{(s_i - \langle \Sigma_i \rangle_\rho)^2}{1 - \langle \Sigma_i \rangle_\rho^2}\right) \quad (5.10)$$

By maximizing this probability (or the logarithm of it) we obtain an estimate of the parameters of the density matrix ρ of the quantum state.

Including Experimental Tomography Errors

This technique also allows us to include further optimization parameters when calculating the joint probability. This is useful for modeling e.g. systematic errors of the measurement or preparation process, which can be described by modifying the operators contained in the probability sum. A common source of errors in our tomography measurements are shifts in the amplitude and phase of the microwave pulses used to drive the qubit. We are obliged to rotate the qubit state when performing state tomography since our measurement apparatus permits us only to measure the σ_z operator of each qubit. We can therefore replace the operators σ_x and σ_y in eq. (5.8) with an effective measurement of σ_z preceded by a rotation R_{ν_i} given as

$$R_X = \exp(-i\sigma_y\pi/4) \quad (5.11)$$

$$R_Y = \exp(+i\sigma_x\pi/4) \quad (5.12)$$

Within this model, phase and amplitude errors can be modeled by including additional phase factors in the exponential of these expression, such that we obtain new operators

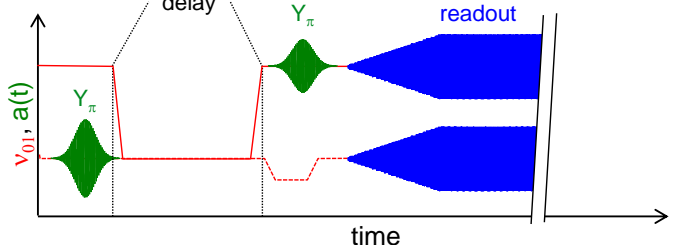
$$R'_X = \exp(-i[+\sigma_y \cos \alpha + \sigma_x \sin \alpha] [\pi/4 + \gamma]) \quad (5.13)$$

$$R'_Y = \exp(+i[-\sigma_y \sin \beta + \sigma_x \cos \beta] [\pi/4 + \delta]) \quad (5.14)$$

Here, α and β represent phase errors whereas γ and δ represent amplitude errors in the drive pulses. An detailed discussion of how we fit these parameters in our experiment will be given in section 5.5.5.

5.4.3 Creation of Bell states

Figure 5.8: Pulse sequence used to experimentally generate entangled Bell states. The sequence consists in exciting one of the qubits to the state $|1\rangle$, creating an entangled state using the swapping interaction and correcting the acquired phase of the state. For the $|\Phi_{\pm}\rangle$ states, we use an additional $Y(\pi)$ pulse at the end of the sequence.



We can use the ML method presented above to perform state tomography of entangled Bell states that we create by using the swapping interaction between the qubits. In general, the four Bell states are

$$|\Psi_+\rangle = \frac{1}{\sqrt{2}} (|01\rangle + |10\rangle) \quad (5.15)$$

$$|\Psi_-\rangle = \frac{1}{\sqrt{2}} (|01\rangle - |10\rangle) \quad (5.16)$$

$$|\Phi_+\rangle = \frac{1}{\sqrt{2}} (|00\rangle + |11\rangle) \quad (5.17)$$

$$|\Phi_-\rangle = \frac{1}{\sqrt{2}} (|00\rangle - |11\rangle) \quad (5.18)$$

The experimental protocol for generating a Bell state is shown in fig. 5.8. In essence, we use the swapping interaction between the qubits to create an entangled state and compensate the acquired dynamic phase of that state by a short z-pulse. To create the Φ_+ and Φ_- states we use a $X(\pi)$ pulse at the end of the sequence in addition. Finally we perform quantum state tomography on the created state to reconstruct its density matrix. In fig. 5.9 we show the reconstructed density matrices of the four created Bell states. The trace fidelity $\langle \psi | \rho | \psi \rangle$ between the experimentally created and ideal state is shown on top of the density matrix and ranges between 83% and 87%.

5.4.4 Violation of the Bell Inequality

After having showed that we can create superposition states of the two qubits using the swapping interaction, we proceed to demonstrate that we have actually created entangled qubit states by performing a so called *Bell test* on our two-qubit system. In this section, we will give an introduction to this test and explain how we implement it on our two-qubit processor.

In a famous 1935 paper [32], A. Einstein, B. Podolsky and N. Rosen (EPR) pointed out that quantum mechanics can be considered “incomplete” if one assumes that a set of simple physical principles holds true. These two principles are *locality* and *realism*, together often referred to as *local realism*. The principle of locality states that an object is influenced directly only by

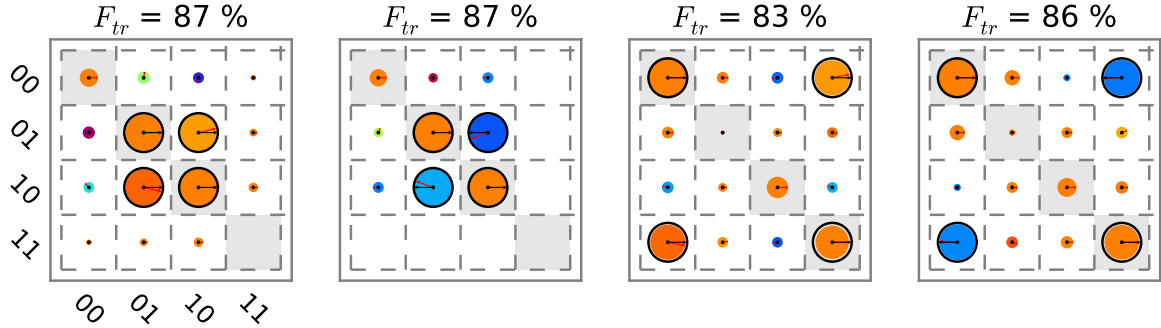


Figure 5.9: Reconstructed density matrices of experimentally created Bell states. Shown are the states $|\Psi_{\pm}\rangle = 1/\sqrt{2}(|01\rangle \pm |10\rangle)$ and $|\Phi_{\pm}\rangle = 1/\sqrt{2}(|00\rangle \pm |11\rangle)$. The trace fidelities of the density matrices, $F_{tr} = \langle \psi | \rho | \psi \rangle$ range between 83 % and 87 %.

its immediate surroundings, or stated differently, that no interaction between any two objects may propagate faster than the speed of light. The principle of realism states that any physical observable has, at all times, a pre-existing measurement value which exists independent of any actual measurement of the observable. In their paper, Einstein, Podolsky and Rosen showed that within standard quantum mechanics it is possible to write down quantum states that, when performing certain measurements on them, clearly violate at least one of the principles of locality or realism. As an example, take the state

$$|\psi\rangle = \frac{1}{\sqrt{2}} (|\uparrow\downarrow\rangle + |\downarrow\uparrow\rangle) \quad (5.19)$$

which describes a system of two spin 1/2 particles that is in a superposition between the $|\uparrow\downarrow\rangle$ and $|\downarrow\uparrow\rangle$ states. Now, when separating the two particles by a large distance and measuring the value of one of the spins –such that by the assumption of locality, no information exchange can take place between the two systems–, the wave function of the system will collapse in either of the two states $|\uparrow\downarrow\rangle$ or $|\downarrow\uparrow\rangle$. Hence, a measurement of one of the particles will instantaneously change the spin state of the other particle, seeming violating the principle of locality by which no instantaneous information exchange can take place between two distant systems. In their paper, Einstein, Podolsky and Rosen called this effect *spooky action at a distance*.

However, the violation of locality can be resolved by assuming that the state of the quantum system does possess a well-defined value before actually measuring it. This would imply that our description of the quantum-mechanical state as given by eq. (5.19) is just missing some additional, *hidden variables* that contain the information on the spin of each particle and which are not accessible by us. A hypothetical theory that contains these hidden variables and could thus complete the quantum mechanical description of the particle is usually referred to as a *hidden variable theory*.

In 1964, J. Bell provided a mathematicalal description of locality and realism and devised an experimental test of the hypothesis formulated by Einstein *et. al.* [6]. Building on his work, J. Clauser, M. Horne, A. Shimony and R. Holt proposed an actual experiment to test the hypotheses of quantum mechanics against hidden-variable or non-local theories as formulated in the Bell and

EPR papers [19]. The first successful realization of this proposed experiment was achieved by A. Aspect *et. al.* [3] and confirmed the validity of quantum mechanics, showing that either the assumption of realism or that of locality must be false. In the following decades, several more experiments have been performed to test the Bell hypothesis, trying to close several so-called *loopholes* that can put in doubt the results obtained in a Bell experiment. Such a loophole is a problem of the experimental setup or design that affects the validity of the experimental findings. Typical loopholes affecting Bell-type experiments are the *detection efficiency* or *fair sampling*, the *communication* or *locality* and the *rotational invariance* loophole. We will discuss the loopholes most relevant to our own experiment in the following paragraph.

To test the Bell inequality with our two-qubit setup, we follow the experimental procedure proposed by Clauser *et. al.* [19]. According to this procedure, we first prepare an entangled two-qubit state of the form

$$|\phi\rangle = \frac{1}{\sqrt{2}} (|01\rangle + e^{-i\varphi} |10\rangle) \quad (5.20)$$

On this quantum state we measure then the expectation value of the operator

$$\text{CHSH} = \langle Q\text{S} + R\text{S} + RT - QT \rangle \quad (5.21)$$

where the individual operators Q, R, S, T are given as

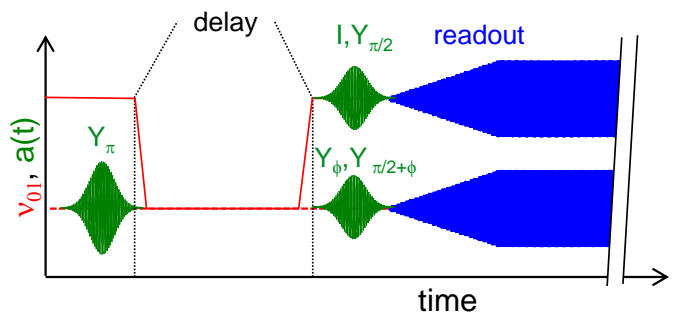
$$\begin{aligned} Q &= \sigma_z^1 & S &= \sigma_z^2 \cdot \cos \phi + \sigma_x^2 \cdot \sin \phi \\ R &= \sigma_x^1 & T &= -\sigma_z^2 \cdot \sin \phi + \sigma_x^2 \cdot \cos \phi \end{aligned} \quad (5.22)$$

Here, the angle ϕ is a parameter that gives the rotation of the measurement basis in respect to the z axis and should be chosen in accordance to the phase φ of the entangled qubit state to which the operator is applied. To obtain the value of $\langle \text{CHSH} \rangle$, we measure $\langle Q\text{S} \rangle$, $\langle R\text{S} \rangle$, $\langle RT \rangle$ and $\langle QT \rangle$ on an ensemble of identically prepared quantum states. For a classical state without entanglement, the operator $\langle \text{CHSH} \rangle$ is bound by

$$|\langle \text{CHSH} \rangle| \leq 2. \quad (5.23)$$

However, for an entangled quantum state, the maximum value of the operator is given as $2\sqrt{2}$.

Figure 5.10: Experimental pulse sequence used in the CHSH experiment. It consists in exciting one of the qubits to the state $|1\rangle$, bringing it in resonance with the other qubit for a well-defined duration, performing single-qubit rotations to align the qubit state with the desired measurement basis and finally measuring the $\langle \sigma_z^I \cdot \sigma_z^{II} \rangle$ operator of the two-qubit register.



The pulse sequence used for generating an entangled two-qubit state and measuring the CHSH operator on it is shown in fig. 5.10. As before, we generate the state by exciting one of the qubits to the state $|1\rangle$ and bringing it in resonance with the other qubit for a well-defined duration. Afterward, we apply single-qubit rotations to align the qubit state with the axis along which we want to perform the measurement. Finally we measure the $\langle \sigma_z^I \cdot \sigma_z^{II} \rangle$ operator of the rotated qubit state. We then repeat this procedure on an ensemble of identically prepared input states for all of the four individual operators of CHSH operator. Figure 5.11 shows the results of such a measurement. As can be seen, the operator $\langle \text{CHSH} \rangle$ varies sinusoidally as a function of the rotation ϕ of the measurement basis. The maximum and minimum of the raw value of $\langle \text{CHSH} \rangle$ reaches ≈ 1.4 , thereby failing to violate the boundary for non-classical states as given by eq. (5.23). However, when accounting for the readout errors in our experiment, the corrected CHSH data reaches a maximum value ≈ 2.52 , thereby violating the classical boundary of the CHSH equation. We can hence violate the Bell inequality with our two-qubit processor, however we are not able to close the detector efficiency loophole. In addition, due to the measurement time required to determine the state of each qubit and the close proximity of the two qubits we are not able to close the communication or locality loophole either. However, when accepting the general validity of quantum mechanics, the violation of the Bell inequality with the generated two-qubit states can serve as an entanglement witness and confirms that we are able to generate a highly entangled quantum states with our processor.

Errors

Besides obvious readout errors, the main source of errors in our experiment is drift of the measurement equipment. Most importantly, the phase of the arbitrary waveform generator (AWG) can drift in respect to the phases of the microwave sources, thereby changing the effective phase of the measurement basis of the CHSH operator. Fig. 5.12 illustrates the effect of this drift on the phase of the generated Bell state. Shown is the phase of the state $|\phi\rangle$ as given by eq. (5.20) extracted from a full CHSH data set as shown in fig. 5.11. When repeating this measurement over a long time period, oscillations of the phase φ with an amplitude of $\approx 40^\circ$ can be observed. This amplitude can be explained by a time shift of the AWG waveform driving the microwave sources of the order of 200 ps, which has indeed been observed experimentally.

5.4.5 Measuring the Evolution of an Entangled Qubit States

Using quantum state tomography, we can repeat the swapping experiment described in section 5.4.1 and reconstruct the full experimental density matrix of our system at many different times during the swap sequence. Like this we can follow the evolution of the quantum state during the course of the swap. Fig. 5.13 shows the result of such an experiment. We plot the measured values of all Pauli operators as a function of the swapping time between the qubits. The red and green curves correspond to the single-qubit Pauli operators $\sigma_{X,Y,Z}^I \otimes I$ and $I \otimes \sigma_{X,Y,Z}^{II}$, the blue curves to the two-qubit Pauli operators $\sigma_{X,Y,Z}^I \otimes \sigma_{X,Y,Z}^{II}$. The dashed line corresponds to a master equation simulation of the swapping experiment, where the qubit coupling, relaxation

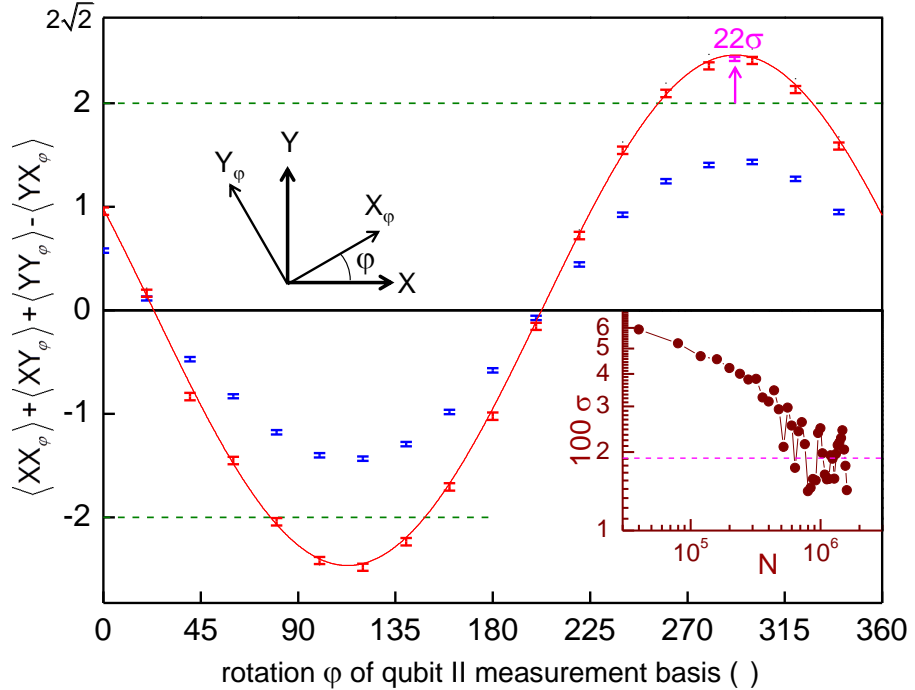


Figure 5.11: Value of the $\langle \text{CHSH} \rangle$ operator measured for an ensemble of identically prepared Bell states $1/\sqrt{2}(|01\rangle + e^{-i\varphi}|10\rangle)$, plotted as a function of the rotation ϕ of the measurement basis. Blue markers correspond to raw measurement data, red markers to data corrected for readout errors. The solid line represents the best fit to the theory. The inset shows the standard deviation σ of the maximum value of the $\langle \text{CHSH} \rangle$ operator as a function of the sample size. For large samples, σ is limited by experimental drift of the measurement basis.

and dephasing parameters are chosen in accordance with experimental values. As can be seen, the simulation agrees well with the experimental data. Deviation between data and simulation can be seen in the $\sigma_{X,Y}^I \otimes \sigma_{X,Y}^{II}$ operators and is caused by an additional phase acquired by the qubits during the swap. This phase appears due to the fact that we have to shift the frequency of the qubits to bring them in resonance, hence we acquire a dynamical phase in the frame rotating at the uncoupled qubit frequencies. In addition, experimental drift of our measurement equipment may induce an additional phase factor during the measurement, which takes several

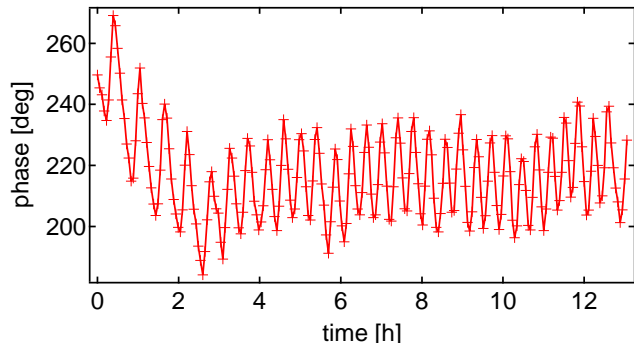


Figure 5.12: Phase φ of an experimentally generated Bell state as a function of time. The phase exhibits oscillatory drift of the order of $\approx 40^\circ$ being caused by a time offset drift of the AWG.

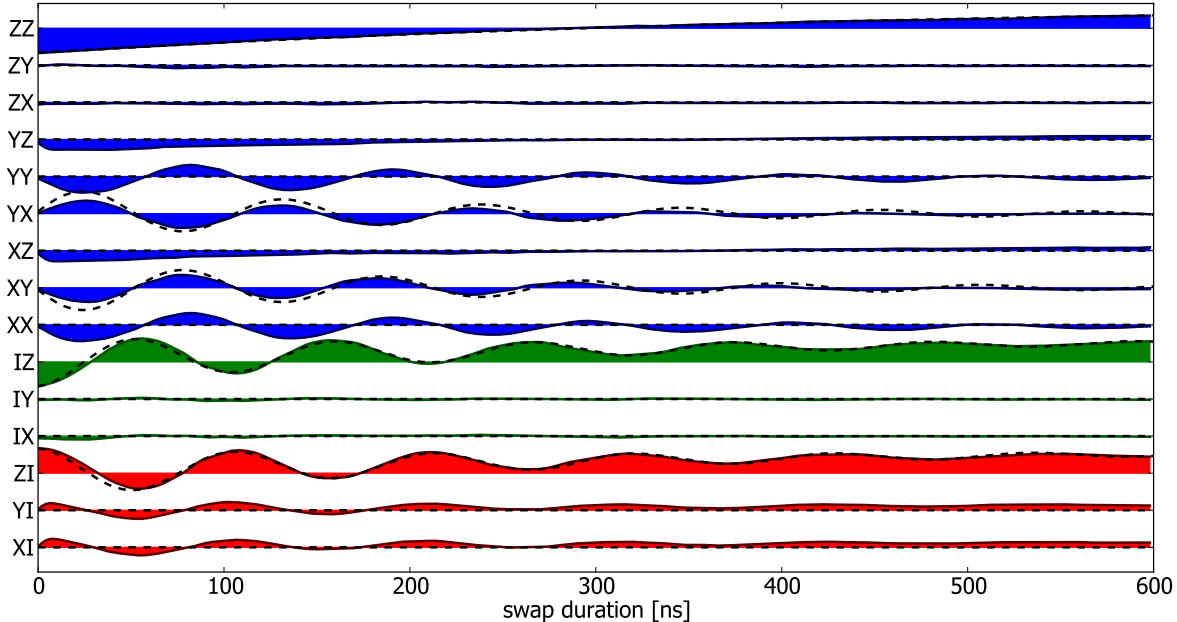


Figure 5.13: Measured Pauli operators $\sigma_i \otimes \sigma_j$ with $i, j \in \{X, Y, Z, I\}$ as a function of the interaction time. Shown are the 6 single-qubit operators as well as the 9 two-qubit correlation operators. The dashed line represents a master-equation simulation of the experiment.

hours to complete.

From the measured Pauli set, we can reconstruct the density matrix of the two-qubit system at any point during the swap. This density matrices are (will be soon :) shown in the margins of this thesis book. When following the evolution of the quantum state as a function of time (by flipping the pages of the book) it can be seen that the coherence between the two qubits decreases steadily during the swapping sequence, due to relaxation and dephasing.

5.5 Realizing a Two-Qubit Gate

We have demonstrated that it is possible to create highly entangled qubit states with our processor by preparing Bell states, performing quantum state tomography and violating the Bell inequality. However, to realize a universal two-qubit quantum processor, it is necessary to implement a so-called *universal two-qubit gate* on our processor. In the following sections we discuss how we can realize and characterize such a gate.

5.5.1 Principle

By definition, a universal two-qubit gate together with a set of universal one-qubit gates, allows us to create any possible two-qubit quantum state [4]. In principle, there are (infinitely) many choices for possible universal two-qubit gates. In this work, we are interested mainly in the

so-called $\sqrt{i\text{SWAP}}$ gate, which has the representation

$$U(t) = \begin{pmatrix} 1 & 0 & 0 & 0 \\ 0 & 1/\sqrt{2} & i/\sqrt{2} & 0 \\ 0 & i/\sqrt{2} & 1/\sqrt{2} & 0 \\ 0 & 0 & 0 & 1 \end{pmatrix}_{\{|00\rangle, |01\rangle, |10\rangle, |11\rangle\}} \quad (5.24)$$

We can implement this gate naturally using the swapping interaction as given by eq. (5.5) when letting the qubits evolve in resonance for a time $t_{\sqrt{i\text{SWAP}}} = 1/8g$, which, for our experimental value of $2g = 8.3$ MHz corresponds to $t_{\sqrt{i\text{SWAP}}} = 30$ ns.

5.5.2 Experimental Implementation

Figure 5.14 shows the pulse sequence that we use to realize the $\sqrt{i\text{SWAP}}$ gate with our processor for an exemplary input state. In the case shown, we excite the first qubit to the state $|1\rangle$, creating an input state $|10\rangle$. We then tune in resonance the two qubits for a time $t_{\sqrt{i\text{SWAP}}}$. After tuning the qubits out of resonance again, we apply two single-qubit Z -gates to compensate the dynamical phases acquired during the swap. Then, we optionally apply single-qubit tomography gates and finally read out the qubit state at the optimal readout working point. Using this technique we can reconstruct the density matrix of the quantum state after applying the two-qubit gate to it. Similarly, we can perform quantum state tomography on the input state to obtain its density matrix. Reconstructing the input and output density matrices for a range of different input state will then allow us to fully characterize the gate operation, as will be discussed in the next section.

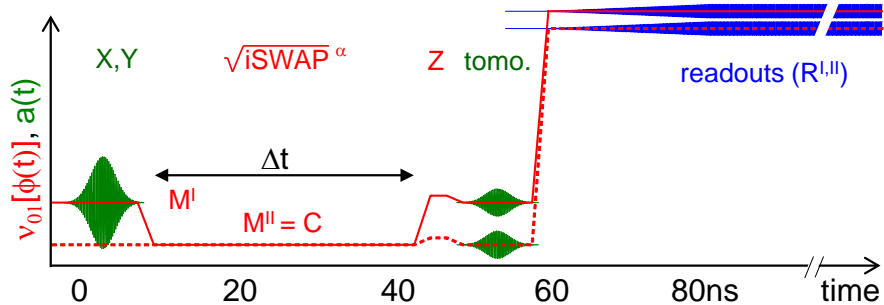


Figure 5.14: Experimental pulse sequence used for implementing the two-qubit $\sqrt{i\text{SWAP}}$ gate. The sequence shown for an exemplary input state $|10\rangle$ consists in exciting the first qubit to the state $|1\rangle$, bringing the qubits in resonance for a time $t = 1/8g$, separating them and compensating the acquired dynamical phases by using two single-qubit Z -pulses. Finally, optional tomographic pulses are applied before reading out the qubit state at the optimal readout frequencies of the qubits.

5.5.3 Quantum Process Tomography of the Gate

To characterize the fidelity of our quantum gate, we perform so-called *quantum process tomography* [71]. This procedure allows us to fully characterize a quantum process in an open quantum system. The approach that we use in this work is called *standard quantum process tomography* (SQPT), however, there exist other common methods such as ancilla-assisted quantum process tomography [31, 22, 1], that we will not discuss since they are not relevant to this work.

In the following section, we will introduce the concept of a quantum process, explain possible parametrizations of such a process and discuss the experimental implementation of standard quantum process tomography on our two-qubit processor.

Theoretical Description of a Quantum Process

A quantum process can be described as a function $\mathcal{E} : \rho_{\mathcal{H}} \rightarrow \rho_{\mathcal{H}}$ that maps a density matrix ρ defined in a Hilbert space Q_1 to another density matrix $\mathcal{E}(\rho)$ defined in a target Hilbert space Q_2 and that fulfills three axiomatic properties [67, 42]:

Axiom 5.0.1. $\text{tr} [\mathcal{E}(\rho)]$ is the probability that the process represented by \mathcal{E} occurs, when ρ is the initial state.

Axiom 5.0.2. \mathcal{E} is a *convex-linear map* on the set of density matrices, that is, for probabilities $\{p_i\}$,

$$\mathcal{E} \left(\sum_i p_i \rho_i \right) = \sum_i p_i \mathcal{E}(\rho_i) \quad (5.25)$$

Axiom 5.0.3. \mathcal{E} is a *completely-positive* map. That is, if \mathcal{E} maps density operators of system Q_1 to density operators of system Q_2 , then $\mathcal{E}(A)$ must be positive for any positive operator A . Furthermore, if we introduce an extra system R of arbitrary dimensionality, it must be true that $(\mathcal{I} \otimes \mathcal{E})(A)$ is positive for any positive operator A on the combined system $R \otimes Q_1$, where \mathcal{I} denotes the identity map on system R .

As shown in [67], any quantum process fulfilling these criteria can be written in the form

$$\mathcal{E}(\rho) = \sum_i E_i \rho E_i^\dagger \quad (5.26)$$

for some set of operators $\{E_i\}$ which map the input Hilbert space to the output Hilbert space, and for which $\sum_i E_i^\dagger E_i \leq I$. Here, the operators E_i are called the *Kraus operators* of the quantum process. They contain the full information of the quantum process acting on ρ .

If we express the operators E_i in a different operator basis \tilde{E}_j such that $E_i = \sum_j a_{ij} \tilde{E}_j$ and insert into eq. (5.26), we obtain

$$\mathcal{E}(\rho) = \sum_i \sum_j a_{ij} \tilde{E}_j \rho \sum_k a_{ik}^* \tilde{E}_k^\dagger \quad (5.27)$$

$$= \sum_{j,k} \tilde{E}_j \rho \tilde{E}_k^\dagger \sum_i a_{ij} a_{ik}^* \quad (5.28)$$

$$= \sum_{j,k} \tilde{E}_j \rho \tilde{E}_k^\dagger \chi_{jk} \quad (5.29)$$

where we defined $\chi_{jk} = \sum_i a_{ij} a_{ik}^*$. This is the so-called χ -matrix representation of the quantum process. Here, all the information on the process is contained in the matrix χ , which controls the action of the now process-independent operators \tilde{E}_i on the initial density matrix ρ .

Implementation

As said before, the goal of QPT is to obtain the coefficients of the χ -matrix – or any other complete parametrization of the process – from a set of experimentally measured density matrices $\{\rho_i\}$ and $\{\mathcal{E}(\rho_i)\}$. Standard process tomography [67, 71] can be implemented for our two-qubit gate by using the following procedure:

1. Choose a set of operators E_i that forms a full basis of $\mathcal{M} : Q_1 \rightarrow Q_2$. For n-qubit process tomography we usually choose $E_{i_1, i_2, \dots, i_n} = \sigma_{i_1} \otimes \sigma_{i_2} \dots \otimes \sigma_{i_n}$, where σ_i are the single-qubit Pauli operators and $i \in \{I, X, Y, Z\}$. For a Hilbert space of dimension n , this yields $4^n - 1$ operators (excluding the trivial operator $I^{\otimes n}$).
2. Choose 4^n pure quantum states $|\phi_i\rangle$ such that the basis $\{|\phi_1\rangle\langle\phi_1|, \dots, |\phi_{4^n}\rangle\langle\phi_{4^n}|\}$ spans the whole space of input density matrices ρ . Usually, for a n-qubit system we choose $\phi = \{|0\rangle, |1\rangle, (|0\rangle + |1\rangle)/\sqrt{2}, (|0\rangle + i|1\rangle)/\sqrt{2}\}^{\otimes n}$, where $\otimes n$ denotes the n-dimensional Kronecker product of all possible permutations.
3. For each of the $|\phi_i\rangle$, determine $\mathcal{E}(|\phi_i\rangle\langle\phi_i|)$ by quantum state tomography. Usually we also determine $|\phi_i\rangle\langle\phi_i|$ experimentally since the preparation of this state already entails small preparation errors that should be taken into account when performing quantum process tomography.

After having obtained the ρ_i and $\mathcal{E}(\rho_i)$ one obtains the χ -matrix by writing $\mathcal{E}(\rho_i) = \sum_j \lambda_{ij} \tilde{\rho}_j$, with some arbitrary basis $\tilde{\rho}_j$ and letting $\tilde{E}_m \tilde{\rho}_j \tilde{E}_n^\dagger = \sum_k \beta_{jk}^{mn} \tilde{\rho}_k$. We can then insert into eq. (5.29) and obtain

$$\sum_k \lambda_{ik} \tilde{\rho}_k = \sum_{m,n} \chi_{mn} \sum_k \beta_{ik}^{mn} \tilde{\rho}_k \quad (5.30)$$

This directly yields $\lambda_{ik} = \sum_{m,n} \beta_{ik}^{mn} \chi_{mn}$, which, by linear inversion, gives χ . Hence, we can fully characterize a quantum process acting on an n -dimensional Hilbert space by measuring $2 \cdot 4^n$ experimental density matrices (or 4^n when assuming that no errors occur during the preparation of the input states, which thereby are known).

Similar to quantum state tomography, experimental errors occurring during quantum process tomography can produce a set of process parameters χ that are *non-physical* in the sense that the resulting quantum process does not obey the three axioms stated above. We can resolve this problem by rendering the obtained χ matrix physical by a standard mathematical procedure. When doing this, we usually choose the physical χ_{ph} matrix that has the smallest distance $d = \|\chi - \chi_{ph}\|$.

From the χ matrix to the Kraus representation

To go back from the χ -matrix representation of the quantum process to the Kraus form we write each process-independent operator \tilde{E}_i as a sum of all the Kraus operators E_l , such that

$$\tilde{E}_i = \sum_l a_{il} E_l \quad (5.31)$$

Inserting this into eq. (5.29) we obtain

$$\mathcal{E}(\rho) = \sum_{j,k} \chi_{jk} \sum_{l,m} a_{jl} a_{km}^* E_l \rho E_m^\dagger \quad (5.32)$$

$$= \sum_i E_i \rho E_i^\dagger \quad (5.33)$$

We find hence that $\sum_{j,k} \chi_{jk} a_{jl} a_{km}^* = \delta_l^m$, or, written in matrix form $A\chi A^\dagger = I$. This identity is true for A being the matrix of eigenvectors of χ , multiplied by the square root of the corresponding matrix of eigenvalues. It is thus easy to obtain the Kraus representation of the quantum process by diagonalizing the Hermitian matrix χ .

The Kraus operator form of the quantum process is useful since it allows us to easily visualize the different operators acting on the density matrix ρ . By ordering the Kraus operators in function of their associated eigenvalues we can easily visualize the different unitary and non-unitary processes acting together on the density matrix ρ .

Experimental Results: Input/Output Matrices And χ -Matrix

We perform standard process tomography of our two-qubit gate by following the procedure outlined in the last sections. Figs. 5.16 and 5.16 summarize the experimentally determined input-output density matrices, measured for our two-qubit \sqrt{iSWAP} quantum gate. We show pairs of corresponding input and output states together, containing both the reconstructed experimental density matrices as well as the ideal density matrices. The ideal input states are annotated below the corresponding density matrices. Above each matrix we show the trace fidelity between it and the ideal quantum state. A total of 16 input/output pairs has been measured, corresponding to a complete set of states necessary to fully characterize the quantum process of our gate operation.

From these input/output matrices, we can easily calculate the χ matrix of the quantum process by the method described above. The resulting matrix is shown in fig. 5.17. There, we show

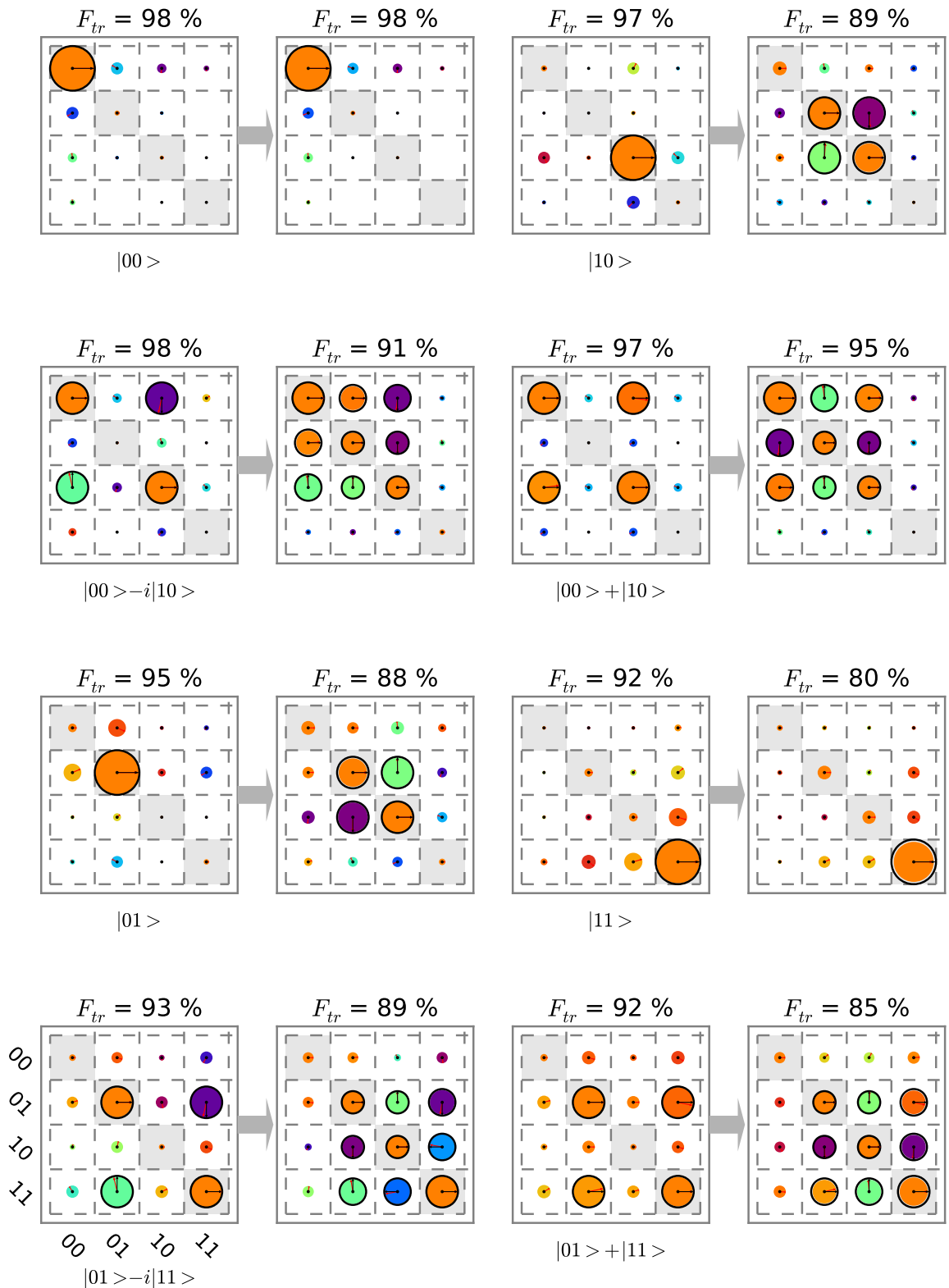


Figure 5.15: The experimental input-output density matrices of the quantum process tomography of the $\sqrt{i\text{SWAP}}$ gate. Shown are the measured density matrices of 16 different input states and the corresponding output matrices with their state fidelities. The ideal matrices are overlaid in black. (part I/II)

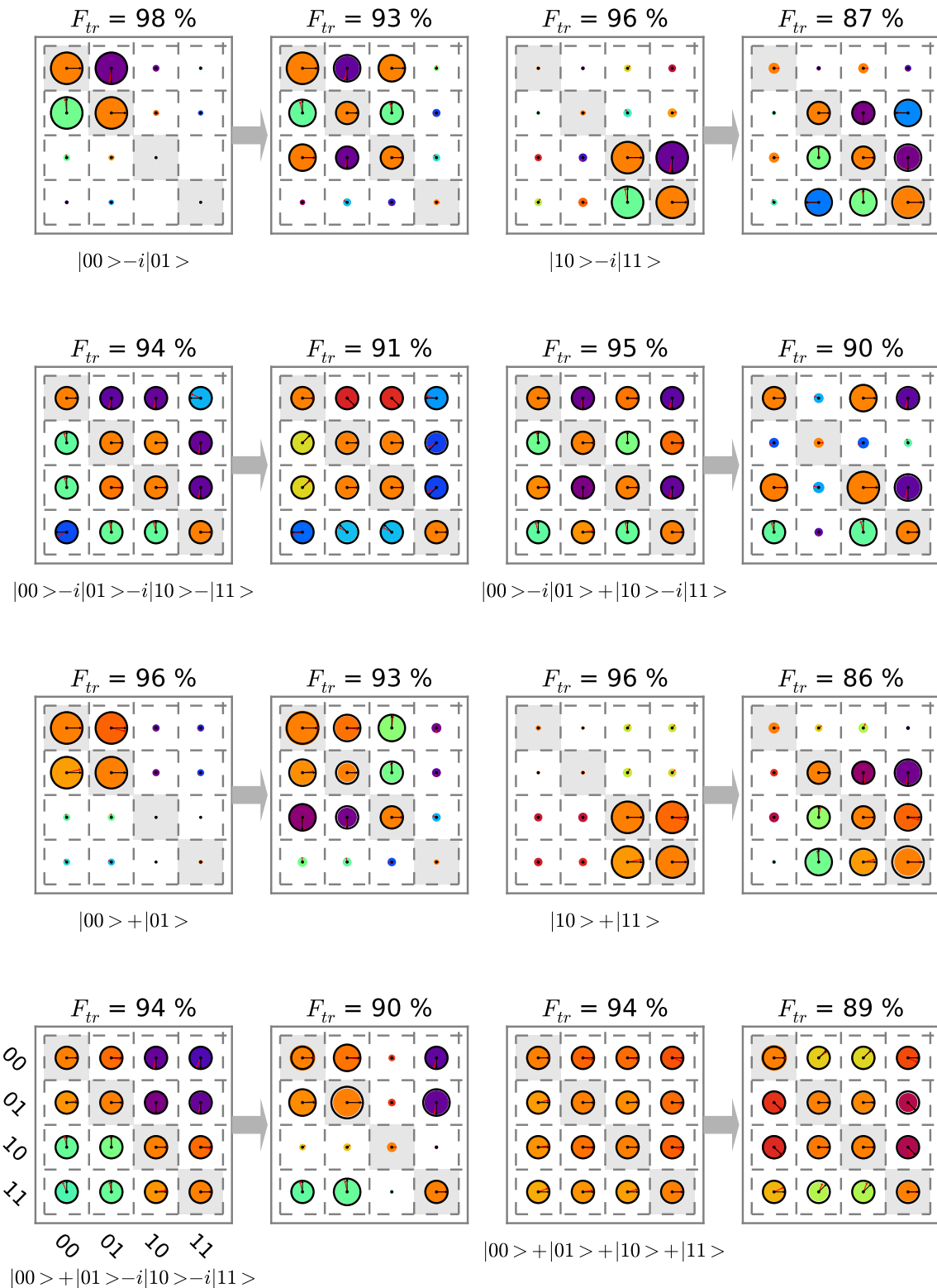


Figure 5.16: The experimental input-output density matrices of the quantum process tomography of the $\sqrt{i\text{SWAP}}$ gate. Shown are the measured density matrices of 16 different input states and the corresponding output matrices with their state fidelities. The ideal matrices are overlaid in black. (part II/II)

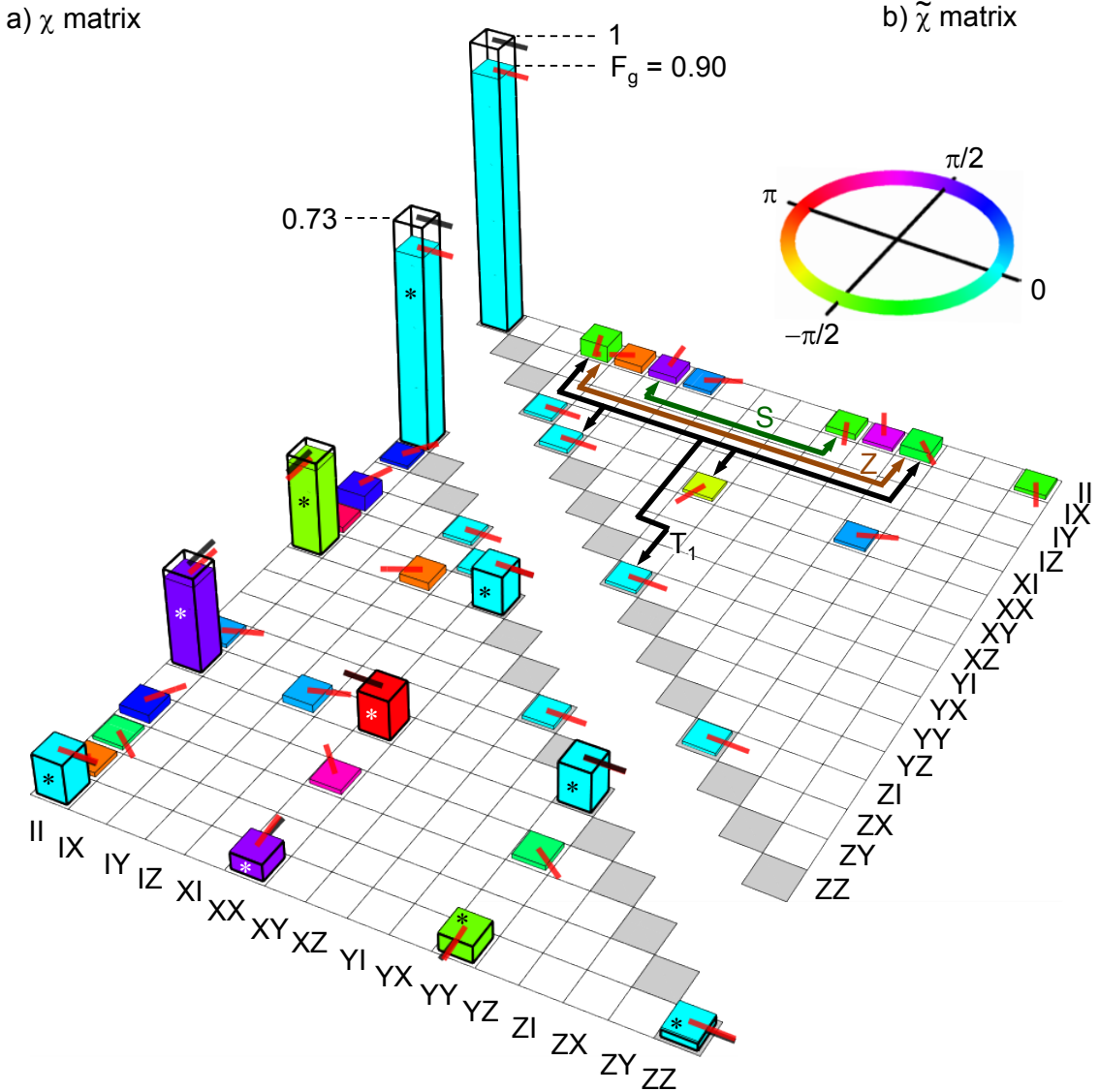


Figure 5.17: The reconstructed χ matrix of our implementation of the $\sqrt{i\text{SWAP}}$ quantum gate. a) shows the lower half of the Hermitian matrix is shown. b) shows the product $\tilde{\chi} = \chi \cdot \chi_{id}^{-1}$ of the measured χ matrix and the ideal process matrix χ_{id} . The colored arrows connecting different elements of $\tilde{\chi}$ indicate unitary and non-unitary error processes to which the corresponding matrix elements can be attributed.

the experimentally obtained χ matrix of our $\sqrt{i\text{SWAP}}$ gate as well as the error process defined as $\tilde{\chi} = \chi \cdot \chi_{id}$, where χ_{id} corresponds to the ideal gate process. χ_{id} is as well shown as black outlines overlaid to the measured χ matrix. The arrows connecting different parts of the $\tilde{\chi}$ matrix group several unitary and non-unitary error processes that can be attributed to the individual elements.

5.5.4 Gate Fidelity

After having obtained the experimental χ matrix, it is trivial to calculate the process fidelity, which is defined as $F = \text{Tr}\{\chi_{id} \cdot \chi\}$, where χ_{id} corresponds to the ideal quantum process. For our experimental process matrix, it is given as $F = 0.9$. The fidelity can be roughly compared to the output state fidelity averaged over the whole set of possible input density matrices.

5.5.5 Gate Error Analysis

We treat two classes of errors in our analysis: Unitary and non-unitary gate errors as well as tomography errors. The former are associated to errors in the quantum process itself, whereas the latter are caused by unitary and non-unitary errors during quantum state tomography.

Tomographic Errors

Tomographic errors are removed from the process map of our \sqrt{iSWAP} gate using the following method: The measured Pauli sets corresponding to the sixteen input states are first fitted by a model including errors both in the preparation of the state (index *prep*) and in the tomographic pulses (index *tomo*). The errors included are angular errors $\varepsilon_{I,II}^{\text{prep}}$ on the nominal π rotations around $X_{I,II}$, $\eta_{I,II}^{\text{prep,tomo}}$ and $\delta_{I,II}^{\text{prep,tomo}}$ on the nominal $\pi/2$ rotations around $X_{I,II}$ and $Y_{I,II}$, a possible departure $\xi_{I,II}$ from orthogonality of (\vec{X}_I, \vec{Y}_I) and $(\vec{X}_{II}, \vec{Y}_{II})$, and a possible rotation $\mu_{I,II}$ of the tomographic XY frame with respect to the preparation one. The rotation operators used for preparing the states and doing their tomography are thus given by

$$\begin{aligned} X_{I,II}^{\text{prep}}(\pi) &= e^{-i(\pi+\varepsilon_{I,II}^{\text{prep}})\sigma_x^{I,II}/2}, \\ X_{I,II}^{\text{prep}}(-\pi/2) &= e^{+i(\pi/2+\eta_{I,II}^{\text{prep}})\sigma_x^{I,II}/2}, \\ Y_{I,II}^{\text{prep}}(\pi/2) &= e^{-i(\pi/2+\delta_{I,II}^{\text{prep}})[\cos(\xi_{I,II})\sigma_y^{I,II}-\sin(\xi_{I,II})\sigma_x^{I,II}]/2}, \\ X_{I,II}^{\text{tomo}}(\pi/2) &= e^{-i(\pi/2+\eta_{I,II}^{\text{tomo}})[\sin(\mu_{I,II})\sigma_y^{I,II}+\cos(\mu_{I,II})\sigma_x^{I,II}]/2}, \\ Y_{I,II}^{\text{tomo}}(-\pi/2) &= e^{+i(\pi/2+\delta_{I,II}^{\text{tomo}})[\cos(\mu_{I,II}+\xi_{I,II})\sigma_y^{I,II}-\sin(\mu_{I,II}+\xi_{I,II})\sigma_x^{I,II}]/2}. \end{aligned}$$

The sixteen input states are then $\{\rho_{in}^e = U |0\rangle\langle 0| U^\dagger\}$ with

$$\{U\} = \{I_I, X_I^{\text{prep}}(\pi), Y_I^{\text{prep}}(\pi/2), X_I^{\text{prep}}(-\pi/2)\} \otimes \{I_{II}, X_{II}^{\text{prep}}(\pi), Y_{II}^{\text{prep}}(\pi/2), X_{II}^{\text{prep}}(-\pi/2)\}, \quad (5.34)$$

and each input state yields a Pauli set $\{\langle P_k^e \rangle = \text{Tr}(\rho_{in}^e P_k^e)\}$ with $\{P_k^e\} = \{I_I, X_I^e, Y_I^e, Z_I\} \otimes \{I_{II}, X_{II}^e, Y_{II}^e, Z_{II}\}$, $X^e = Y^{\text{tomo}}(-\pi/2)^\dagger \sigma_z Y^{\text{tomo}}(-\pi/2)$, and $Y^e = X^{\text{tomo}}(\pi/2)^\dagger \sigma_z X^{\text{tomo}}(\pi/2)$. The best fit to the modeled $\{\langle P_k^e \rangle\}$ set to the measured input Pauli sets yields $\varepsilon_I^{\text{prep}} = -1^\circ$, $\varepsilon_{II}^{\text{prep}} = -3^\circ$, $\eta_I^{\text{prep}} = 3^\circ$, $\eta_{II}^{\text{prep}} = 4^\circ$, $\delta_I^{\text{prep}} = -6^\circ$, $\delta_{II}^{\text{prep}} = -3^\circ$, $\eta_I^{\text{tomo}} = -6^\circ$, $\eta_{II}^{\text{tomo}} = -4^\circ$, $\lambda_I^{\text{tomo}} = 12^\circ$, $\lambda_{II}^{\text{tomo}} = 5^\circ$, $\xi_I = 1^\circ$, $\xi_{II} = -2^\circ$, and $\mu_I = \mu_{II} = -11^\circ$.

Knowing the tomographic errors and thus $\{\langle P_k^e \rangle\}$, we then invert the linear relation $\{\langle P_k^e \rangle = \text{Tr}(\rho P_k^e)\}$ to find the 16×16 matrix B that links the vector $\overrightarrow{\langle P_k^e \rangle}$ to the columnized density matrix $\overrightarrow{\rho}$, i.e. $\overrightarrow{\rho} = B \cdot \overrightarrow{\langle P_k^e \rangle}$. The matrix B is finally applied to the measured sixteen input and sixteen output

Pauli sets to find the sixteen $(\rho_{in}, \rho_{out})_k$ couples to be used for calculating the gate map.

Unitary and Non-Unitary Gate Errors

After having eliminated the tomography errors, only gate errors remain. These can be unitary or non-unitary errors occurring during the quantum process. We characterize both of these errors by fitting the experimental χ matrix to a master equation model of the quantum process which includes unitary (a frequency offset when performing the swapping interaction and phase errors in the compensating Z pulses applied after the swap) and non-unitary (qubit relaxation and dephasing during the whole process). Typically, the relaxation and dephasing rates employed in the simulation are chosen in accordance with experimentally measured T_1 and T_2 times (taking into account possible renormalizations of these coefficients). On the other side, the unitary error parameters are used as fitting parameters to maximize the fidelity between the experimentally measured process matrix χ and the simulated one χ_{sim} . Using this technique, we can calculate an error budget of the quantum process that quantifies the contributions of individual error sources. For our process, we find a total gate error of 10%, where we can attribute 8% of the errors to relaxation and decoherence during the process and 2% to unitary gate errors. In principle, after having characterized the unitary gate errors occurring during the process we could, in theory, compensate them in our experiment. However, due to fast drift of the qubit parameters during the experiment we usually do not perform this kind of optimal qubit control to our gate. Under certain circumstances, the effect of non-unitary errors can also be compensated or alleviated by adding or modifying the unitary gate sequence during the quantum process (see e.g. [50]). However, this procedure is in general not applicable to arbitrary quantum processes and is not applicable to this work.

Chapter 6

Running the Grover Search Algorithm

This chapter describes an experimental implementation of the so-called *Grover search algorithm* with our two-qubit quantum processor. The first section provides a short introduction of the algorithm and motivate the interest in realizing it. The following sections then discuss the details of the experimental realization of the algorithm. We will discuss the results that we obtained and compare the algorithm fidelity and runtime to that of an equivalent, classical algorithm. Finally, we will analyze all relevant unitary and non-unitary error sources relevant to our experiment and provide a quantitative error model of our implementation of the Grover algorithm.

6.1 Introduction & Motivation

Search algorithms are of great importance in many domains of mathematics and computer science. One such search problem that often arises and which will be discussed in the following sections can be formulated in simple terms as follows:

Theorem 6.1. Assume that we have a search space \mathcal{S} that consists of a finite number N of states $s \in \mathcal{S}$. The solution to our search problem corresponds to a subset of M states of the search space $\mathcal{T} \subset \mathcal{S}$. We can then define a search function $\mathcal{C}(s) : \mathcal{S} \rightarrow \{0, 1\}$ that discriminates between states that solve the search problem and states that don't, such that $\mathcal{C}(s) = 1$ for $s \in \mathcal{T}$ and $\mathcal{C}(s) = 0$ otherwise. In accordance with the general convention in the research literature on the Grover search algorithm we will often refer to this search function as the *Oracle function* or (in a quantum-mechanical context) as the *Oracle operator* in the following sections.

Using this definition of the search problem, the goal of a search algorithm is to find all states $t \in \mathcal{S}$ for which $\mathcal{C}(t) = 1$. In the following sections, for the sake of simplicity we assume that the solution set \mathcal{T} contains only one single state t . This special case can be generalized to cases where more than one solution to the search problem exists (see e.g. [67] for a detailed review of the general-case Grover search algorithm)

The first step in order to solve a search problem of the kind described above using classical or quantum computation is to map the problem to a form suitable for solution by a digital (quantum)

computer. For this, we first number and encode the N input states $i \in \mathcal{S}$ in binary form as $i = (b_l^i, \dots, b_0^i)_B$, where l is the length of the binary register able to hold all N input states. With this definition, it is then trivial to find a mathematical representation of \mathcal{C} that operates on a binary input register.

Using these assumptions and definitions, it can then be shown that the most efficient classical search algorithm for solving the search problem above will use $\mathcal{O}(N)$ calls of the function \mathcal{C} to find all solutions t of the search problem. Assuming that the time to evaluate the function \mathcal{C} is far superior to the time needed to perform any other operation during the search algorithm, the time needed for calling n -times the function \mathcal{C} corresponds approximately to the runtime of the whole search algorithm.

Amazingly, in 1997, Lov Grover found a quantum algorithm that could solve this search problem with only $\mathcal{O}(\sqrt{N})$ calls to the function \mathcal{C} [40]. His algorithm achieves this by repeatedly calling a quantum-mechanical implementation of the function \mathcal{C} starting from a highly superposed qubit register $\sum_i^N |i\rangle$ and applying a special operator to the output state afterwards. The individual steps of his algorithm are straightforward and are given as follows:

1. Initialize a qubit register to the state $|\psi\rangle = |0\rangle$ (corresponding to a binary input state $|0000\dots 0_B\rangle$)
2. Apply the generalized Hadamard operation to the qubit register, producing a fully superposed quantum state
$$|\psi\rangle = \frac{1}{\sqrt{N}} \sum_{i=0}^{N-1} |i\rangle$$
3. Repeat the following sequence $\mathcal{O}(\sqrt{N})$ times:
 - a) Apply the *Oracle operator* $|i\rangle \rightarrow (-1)^{\mathcal{C}(i)} |i\rangle$ to the state $|\psi\rangle$
 - b) Apply the so-called *diffusion operator* $|i\rangle \rightarrow -|i\rangle + \frac{2}{N} \sum_{j=0}^{N-1} |j\rangle$ to $|\psi\rangle$
4. Measure the state of the quantum register in the computational basis $|i\rangle$.

For the description above we have enumerated the states of the qubit register from $|0\rangle$ to $|N-1\rangle$. Basically, the Grover algorithm makes use of quantum parallelism to solve the search problem $\mathcal{O}(\sqrt{N})$ times faster than the most efficient classical algorithm. To understand better the strategy it uses to solve the search problem, the different steps of the algorithm can be rephrased in the following more intuitive way:

- First, the algorithm creates a fully superposed quantum state which contains all possible solutions to the search problem at once. The amplitudes and phases of each individual state are all equal in the beginning.
- Then, it applies the Oracle operator to this superposed state. The effect of the Oracle is to turn the phase of the states t by an angle π for which $\mathcal{C}(t) = 1$. As will be shown later,

such an Oracle operator can be implemented in a straightforward way for any classical search function.

- In the next step, it applies a diffusion operator to the quantum state which transfers a fraction of the amplitude from states with zero phase to the states with π phase, increasing thus the amplitude of the latter. In this process, the phases of all states gets also turned back to zero, allowing the algorithm to repeat the sequence above.
- Repeating these two operations increases each time the amplitude of the states that correspond to a solution of the search problem until the amplitudes of all the other states vanish. After that point, the process reverses and the amplitude is transferred back to the original states. It is therefore crucial to stop the repetition sequence given above after the right number of iterations.

By implementing the search function as a quantum operator, the Grover algorithm is able to evaluate it in one single call for all possible input states. This so-called *quantum parallelism* provides the basis for the speed-up of the search in comparison to a classical algorithm. However, being able to encode the result of the search function in the phase of a multi-qubit state does not directly translate to a speed advantage since it is usually very hard to extract this phase information from the quantum state. Indeed, to extract the values of all phases from an N -qubit state, it would be necessary to perform $\mathcal{O}(2^N)$ measurements on an ensemble of identically prepared quantum states. However, extracting the state amplitudes from such a state takes only $\mathcal{O}(N)$ measurements, which in addition can usually be carried out in parallel. It is for this that the Grover algorithm uses an operator that transforms the information encoded in the phases of the qubits to an information encoded in their amplitude. However, since the conversion between phase to amplitude information through the application of an unitary operator is limited by certain physical constraints, the algorithm needs to repeat the encode-and-transfer sequence described above $\mathcal{O}(\sqrt{N})$ times.

To analyze further the constraints and principles of the algorithm, we will discuss a more detailed derivation of it starting from the Schrödinger equation and we will also explain what limits the efficiency of the phase-to-amplitude conversion in the algorithm.

6.1.1 Deriving the Grover Algorithm from Schrödinger's Equation

An interesting derivation of the Grover algorithm starting from Schrödinger's equation has been detailed by Grover himself in a seminal paper [41] and shall be briefly rediscussed here since it sheds light on the basic principles on which the algorithm is based. The derivation begins by considering a quantum system governed by Schrödinger's equation, which can be written as (setting $\hbar = 1$ for clarity)

$$-i\frac{\partial}{\partial t}\psi(x, t) = \frac{\partial^2}{\partial x^2}\psi(x, t) - V(x)\psi(x, t) \quad (6.1)$$

Here $\psi(x, t)$ describes the wave-function and V is a time-independent potential. Let us assume that the potential $V(x)$ is shaped as in fig. 6.1, i.e. possessing a global minimum of energy. When one initializes the system to a state $\psi_0(x, t_0)$ and lets it evolve for a given time, $\psi(x, t)$ will be attracted by the minimum of potential energy and “fall into it” much like a classical particle in such a potential would¹. We might thus ask if we can encode the solution to a search problem as a point of minimum energy x_0 of a potential $V(x)$, take an initial state $\psi_0(x, t_0)$ and let it evolve into a state that has a high probability around x_0 , thereby solving the search problem. To answer this question, it is first necessary to discretize the wavefunction $\psi(x, t)$ such that it can represent the search problem stated in the last section, which is defined over a finite number of states. In the most simple case, we can use a regular grid of points x_i with a spacing Δx for this, as shown in fig. 6.1b. Discretizing the time evolution of eq. 6.1 in steps Δt as well and defining $\epsilon = \Delta t / \Delta x^2$, we obtain a new equation of the form

$$-\frac{\psi_i^{t+\Delta t} - \psi_i^t}{\Delta t} = \frac{\psi_{i+1}^t + \psi_{i-1}^t - 2\psi_i^t}{\Delta x^2} - V(x_i)\psi_i^t \quad (6.2)$$

where we have written $\psi(x_i, t) = \psi_i^t$. For a circular grid with N points we can write this equation in matrix form as

$$\vec{\psi}^{t+\Delta t} = S^{\Delta t} \cdot \vec{\psi}^t \quad (6.3)$$

with S being a state transition matrix of the form

$$S^{\Delta t} = \begin{pmatrix} 1 - 2i\epsilon - iV(x_1)\Delta t & i\epsilon & 0 & \dots & i\epsilon \\ i\epsilon & 1 - 2i\epsilon - iV(x_2)\Delta t & i\epsilon & \dots & 0 \\ 0 & i\epsilon & \ddots & & \vdots \\ \vdots & & \ddots & & \vdots \\ i\epsilon & 0 & \dots & i\epsilon & 1 - 2i\epsilon - iV(x_N)\Delta t \end{pmatrix} \quad (6.4)$$

For infinitesimal times Δt we can separate the effect of the potential $V(x)$ on the wavefunction from the spatial dispersion by writing $S^{\Delta t} \approx D \cdot R$ with

$$D = \begin{pmatrix} 1 - 2i\epsilon & i\epsilon & 0 & 0 & \dots & i\epsilon \\ i\epsilon & 1 - 2i\epsilon & i\epsilon & 0 & \dots & 0 \\ \dots & \ddots & & & & \vdots \\ i\epsilon & 0 & 0 & \dots & i\epsilon & 1 - 2i\epsilon \end{pmatrix} \quad (6.5)$$

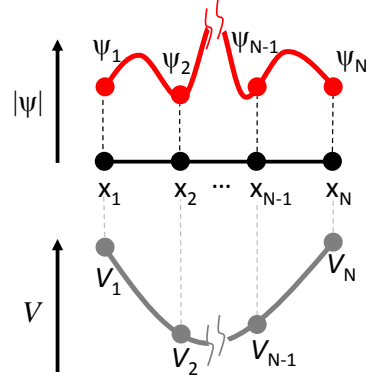


Figure 6.1: A wavefunction $\psi(x)$ and potential $V(x)$ defined on a grid of points x_1, \dots, x_N .

¹of course, since there is no dissipation, the state will not come to rest at the minimum point of energy but rather oscillate around it conserving its total potential and kinetic energy

and

$$R = \begin{pmatrix} e^{-iV(x_1)\Delta t} & 0 & \dots & 0 \\ 0 & e^{-iV(x_2)\Delta t} & \dots & 0 \\ 0 & \dots & 0 & e^{-iV(x_N)\Delta t} \end{pmatrix} \quad (6.6)$$

This approximation is correct to $\mathcal{O}(\epsilon)$ up to an unrelevant renormalization factor. We can now repeatedly apply the matrix product $D \cdot R$ to the wavefunction to obtain its state after a given finite time t by writing

$$\vec{\psi}^{t_0+t} = \left(\prod_{i=1}^{t/\Delta t} D \cdot R \right) \cdot \vec{\psi}^t \quad (6.7)$$

This technique of splitting up the full evolution operator into a product of two or more non-commuting operators that are applied repeatedly to the wavefunction to obtain its state after a finite time is sometimes referred to as *Trotterification* – in reference to the so-called *Lie-Trotter formula* on which it is based – and is widely used in digital quantum simulation [53, 51].

As can be seen in eq. (6.7), the evolution of the wavefunction at infinitesimal times is governed by two processes: The interaction with the potential V and a diffusion process that mixes different spatial parts of the wavefunction with each other. The operator D resembles a Markov diffusion process since each row and column of the matrix sums up to unity, whereas R changes the phase of each element of the wavefunction in accordance with the local potential seen by it. If we apply R to a fully superposed initial state of the form $\psi_i = 1$ (omitting the normalization factor for clarity) and assume that $V_i = 0$ for $i \neq j$ and $V_j\Delta t = \pi/2$ (the potential thus encoding a search function with $C(j) = 1$ and $C(i) = 0$ for $i \neq j$), the element ψ_j will get turned according to $\psi_j \rightarrow i\psi_j$, whereas all other elements ψ_i will remain unchanged. Applying the operator D to the resulting state will transform ψ_j according to $\psi_j \rightarrow \psi_j(i + 2\epsilon(1+i))$ with a corresponding amplitude $\sqrt{1 + 4\epsilon + \mathcal{O}(\epsilon^2)}$ and the adjacent states $\psi_{j\pm 1}$ according to $\psi_{j\pm 1} \rightarrow \psi_{j\pm 1}(1 - \epsilon(1+i))$ with an amplitude $\sqrt{1 - 2\epsilon + \mathcal{O}(\epsilon^2)}$. Hence there is a transfer of amplitude between the state whose phase has been turned and its neighboring states. If we reset the phases of all the ψ_i to zero afterwards, we can iterate the application of $D \cdot R$ until all of the amplitude has been transferred to the element ψ_j which corresponds to a solution to the search problem. This is, in essence, exactly what the Grover algorithm does, the only difference being that it replaces the matrix D with an unitary matrix that maximizes the amplitude transfer to the states solving the search problem, thereby speeding up the algorithm. As stated before, the efficiency with which the algorithm can transfer amplitude between different states is limited by physical constraints, in the next section we will therefore discuss exactly what limits this efficiency and which unitary matrix one should choose to maximize it.

Efficiency of Quantum Searching

It is interesting to ask which is the maximum amount of amplitude that can be transferred in a single step of the Grover search algorithm and which matrix D should be chosen to maximize this transfer. To answer this question and derive the ideal diffusion matrix, we will assume first

that the matrix R which encodes the value of the search function \mathcal{C} in the quantum state of the qubit register can be written in the most general case as

$$R = \sum_{j=0}^{N-1} \exp[i\alpha\mathcal{C}(j)] |j\rangle\langle j| \quad (6.8)$$

Here, α is a factor which we can choose arbitrarily. So, without loss of generality, we can choose $\alpha = \pi$, yielding an Oracle operator of the form

$$R = I - 2 \sum_{j=0}^{N-1} \mathcal{C}(j) |j\rangle\langle j| \quad (6.9)$$

This operator will flip the sign of all states for which $\mathcal{C}(j) = 1$. Now, the next step consists in finding a diffusion or state transfer matrix which will maximize the amplitude transfer to states marked by the Oracle operator above and which will also reset the phases of the quantum register to zero afterwards, such that we might apply the Oracle operator to the resulting state again. In the most general case, such a state transfer matrix will have the form

$$D_c = \begin{pmatrix} b & a & a & \dots & a \\ a & b & a & \dots & a \\ \vdots & \ddots & & & \vdots \\ a & \dots & a & b \end{pmatrix} \quad (6.10)$$

Here, we assume that all non-diagonal elements of the matrix are equal, which is well justified since we have no knowledge of the structure of the search space of the problem and therefore want to treat all basis states equally during the phase-to-amplitude conversion. Furthermore, since both the initial quantum state and the Oracle operator as given by eq. (6.9) contain only real numbers and we demand that the quantum state after applying D_c may contain only positive real numbers as well it is easy to show that a, b must be real numbers. Finally, the unitarity of quantum operators demands that $D_c^\dagger D_c = I$, which for the matrix above is equivalent to the two conditions

$$1 = b^2 + (N-1)a^2 \quad (6.11)$$

$$0 = 2ab + (N-2)a^2 \quad (6.12)$$

Solving these two equations for a, b yields the trivial solution $b = \pm 1, a = 0$ and the more interesting one $b = \pm(1-2/N), a = \mp 2/N$. As can be checked easily, the solution $b = 1-2/N, a = 2/N$ results in a maximum amplitude transfer from states $|i\rangle$ for which $\mathcal{C}(i) = 0$ to states $|j\rangle$

for which $\mathcal{C}(j) = 1$. Thus the ideal diffusion matrix to be used in the Grover algorithm is given as

$$D = \begin{pmatrix} -1 + 2/N & 2/N & 2/N & \dots & 2/N \\ 2/N & -1 + 2/N & 2/N & \dots & 2/N \\ \vdots & & \ddots & & \vdots \\ 2/N & 2/N & 2/N & \dots & -1 + 2/N \end{pmatrix} \quad (6.13)$$

This matrix, together with an Oracle operator R as given by eq. (6.9) will yield the maximum amplitude transfer from states not solving the search problem to states that solve it. Repeating the application of $D \cdot R$ on an initially fully superposed quantum states for $\mathcal{O}(\sqrt{N})$ times will transform the input state to a state containing only the solutions of the search problem, thus solving the problem quadratically faster than possible with any classical algorithm.

6.1.2 Implementation & Comparability to Classical Algorithms

In the following sections we discuss a two-qubit implementation of the Grover search algorithm that we implemented in this work. To be able to compare the Grover algorithm as outlined here to a classical version solving the same search problem, we will now discuss another variant of the algorithm that uses an ancilla qubit to encode the result of the search function. This implementation will make it possible to devise a classical algorithm that can then be compared to the quantum algorithm.

6.1.3 Ancilla-based Implementation of the Algorithm

The implementation of the Grover search algorithm as outlined above encodes the value of the search function \mathcal{C} directly in the phase of the input state supplied to this function. This makes it hard to compare the algorithm to a classical search algorithm which operates on a binary input states and, in general, cannot encode the result of the search function directly in the input state. It is therefore useful to formulate a version of the Grover algorithm where the Oracle function does not directly encode the marked state in the input qubit register but rather uses an ancilla qubit to store the result of calling \mathcal{C} . Such a representation of the algorithm, although of little practical relevance, is very useful since it allows us to directly compare the quantum algorithm to its classical counterpart implemented using reversible logic gates, thus making it possible to benchmark the quantum algorithm and provide an estimation of the quantum speed-up that can be achieved.

Exemplary implementations of ancilla-based search functions \mathcal{C} implemented using reversible (quantum) gates are shown in fig. 6.2 for the two-qubit case. There, a two-qubit Toffoli gate in combination with several single-qubit NOT gates (that can be easily implemented as single-qubit X_π rotations) is used to flip the state of an ancilla-qubit conditionally on the input state of the gate. Using a similar approach, any arbitrary classical search function \mathcal{C} that can be implemented with a set of universal reversible logic gates (e.g. the Toffoli gate and the NOT gate) can be directly

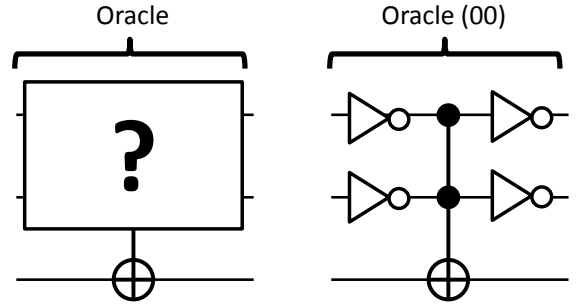


Figure 6.2: a) Two-qubit ancilla-based implementation of the Oracle function C . The state of the third bit get flipped if the search function $C(i) = 1$ for the given input state i . b) An example of an ancilla-based search function that returns a true value for the input state 00.

mapped to a corresponding quantum operator that works on quantum-mechanical input states and implements the classical search function.

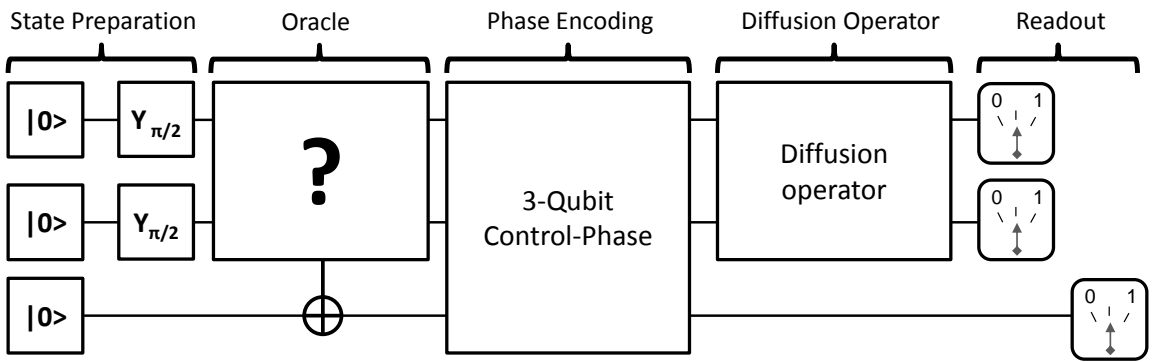


Figure 6.3: A full version of an ancilla-based implementation of the two-qubit Grover search algorithm. The algorithm works on a two-qubit input state and flips the state of a control qubit for one of the four possible input states in accordance to an unknown Oracle function. It then applies a 3-qubit control-phase operation of that maps $|xy1\rangle \rightarrow -|xy1\rangle$, $|xy0\rangle \rightarrow |xy0\rangle$ to encode the state of the control qubit directly in the two input qubits and then uses a diffusion operator to determine the state which has been marked by the Oracle function.

Now, to use the Grover algorithm with such an ancilla-based quantum Oracle, it is necessary to re-encode the result of the Oracle in the qubit input state. Fig. 6.3 shows a version of the two-qubit Grover algorithm that achieves exactly this by using a three-qubit control-not (CNOT) gate C of the form

$$C = I^{n \otimes n} - 2 \sum_{ij} |ij1\rangle \langle ij1| \quad (6.14)$$

to phase-encode the state of the ancilla qubit in the state of the input qubit register. After the re-encoding of the result, the ancilla qubit is not needed during the remainder of the algorithm and must not be read out before the algorithm terminates.

6.2 Comparision to a Classical Algorithm

In order to quantify the speed-up achieved by a quantum algorithm it is necessary to map the problem it solves to an equivalent problem that can be solved by a classical algorithm. For

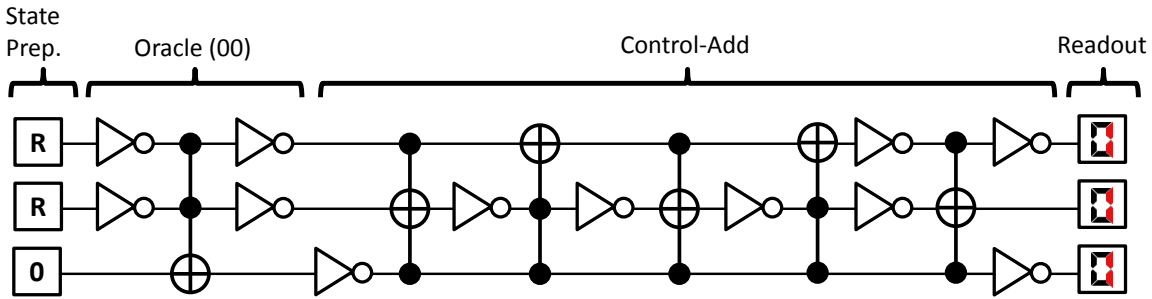


Figure 6.4: Classical reversible implementation of a search algorithm on a two-bit input register. An exemplary Oracle function can be implemented using two single-bit NOT operations and a Toffoli gate. R designates the generation of a random binary value at the beginning of the algorithm. If the Oracle does not yield the correct answer, the test state is incremented. The average success probability of the algorithm is 50 %.

the Grover algorithm, this is the search problem that we discussed in the first section of this chapter. Using the reversible, ancilla-based implementation of the search function that was introduced in the last section we can directly formulate a classical algorithm that solves the same problem as the Grover algorithm and compare the runtime of the two. Since the two-qubit Grover algorithm evaluates the search function \mathcal{C} only once it is interesting to ask what would be the success probability of an equivalent classical algorithm that calls \mathcal{C} once and returns an estimate of the state solving the search problem afterwards. Such an algorithm is shown in fig. 6.4 and it achieves a success probability of 50 % by evaluating once the function \mathcal{C} for a randomly generated two-bit input value r and returning r if it found $\mathcal{C}(r) = 1$ or $r + 1 \pmod 4$ otherwise. The 50 % success rate of this algorithm provides a benchmark against which we will measure the speed-up of our implementation of the Grover algorithm.

Alternatively, we can also compare the success probability of the quantum algorithm with either a simple classical “query” algorithm or a “query-and-guess” algorithm, plotting the success probability of either of them as a function of the number of calls to the Oracle function \mathcal{C} . This makes it possible to compare the performance of the quantum algorithm to the classical ones for an arbitrary number of calls n to \mathcal{C} . Such a comparison will be made later in this chapter when reviewing the experimental data obtained for our implementation of the Grover algorithm.

6.3 Experimental Implementation

We implemented a compiled version of the two-qubit Grover algorithm using our two-qubit quantum processor. The gate sequence of the algorithm is shown in fig. 6.5 and consists in two $i\text{SWAP}$ gates and six single-qubit gates applied to an initial state $|00\rangle$. Here, the first $i\text{SWAP}$ gate together with the two single-qubit $Z_{\pm\pi}$ rotations implements the Oracle function $f(x)$ as given by eq. (6.9), where the signs of the rotation operations determine the state which is marked by the Oracle. This state can be either $|00\rangle$ (corresponding to a $Z_{-\pi/2}^1 \cdot Z_{-\pi/2}^2$ rotation), $|01\rangle$ ($Z_{-\pi/2}^1 \cdot Z_{\pi/2}^2$), $|10\rangle$ ($Z_{\pi/2}^1 \cdot Z_{-\pi/2}^2$) or $|11\rangle$ ($Z_{\pi/2}^1 \cdot Z_{\pi/2}^2$). After the encoding, the second

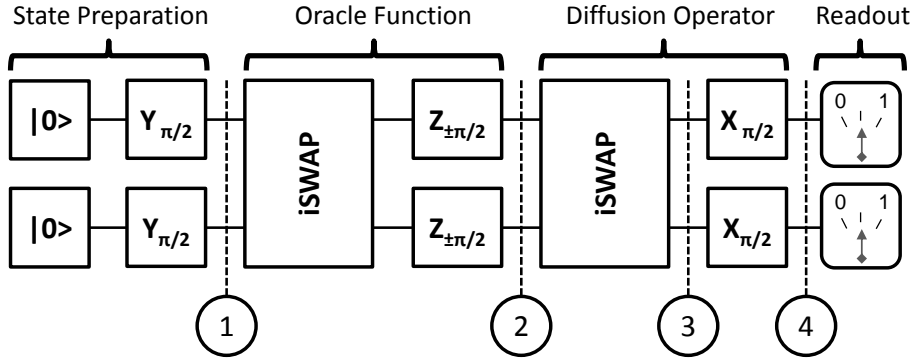


Figure 6.5: Schematic of our implementation of the Grover search algorithm. The algorithm consists in generating a fully superposed input state, applying the Oracle function to it and analyzing the resulting state by applying the Diffusion transform to it and reading out the value of the qubit register afterwards.

*i*SWAP operation together with the following $X_{\pi/2}^1 \cdot X_{\pi/2}^2$ single-qubit operations implement the diffusion operator as given by eq. (6.13). The final step of the algorithm consists in reading out the two-qubit register.

6.3.1 Pulse Sequence

To implement the gate sequence described above we need to realize a sequence of microwave and flux pulses which realize the individual quantum gates of the sequence. To eliminate possible gate errors, we perform a series of calibration measurements before to tune-up the individual single- and two-qubit gates needed for the algorithm. In addition, we run individual parts of the algorithm successively and perform quantum state tomography to characterize the state of the quantum register after each step of the algorithm and correct the gate operations applied to the qubit in order to maximize the fidelity of the measured states in respect to the ideal ones. Fig. 6.6 shows an experimental pulse sequence for the Grover algorithm with an Oracle operator marking the state $|00\rangle$. Shown are the frequencies of the two qubits during the runtime of the algorithm and the microwave drive and readout pulses applied to them.

6.4 Results

Here we discuss the results obtained when running the Grover search algorithm with our two-qubit processor. In the first section we will analyze the quantum state of the qubit register during the algorithm by performing quantum state tomography. In the second section we will present and discuss the single-run results obtained in our experiment.

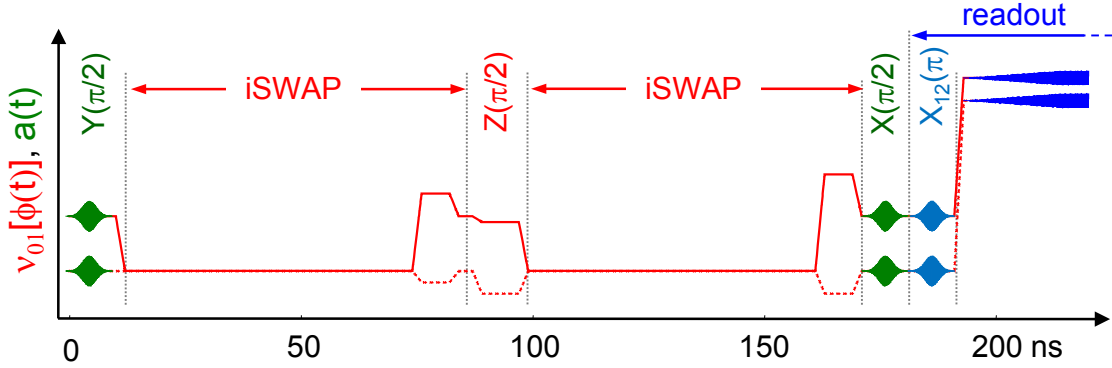


Figure 6.6: The pulse sequence used in realizing Grover’s quantum search algorithm. First, a $Y_{\pi/2}$ pulse is applied to each qubit to produce the fully superposed state $1/2(|00\rangle + |01\rangle + |10\rangle + |11\rangle)$. Then, an $i\text{SWAP}$ gate is applied, followed by a $Z_{\pm\pi/2}$ gate on each qubit, which corresponds to the application of the oracle function. The resulting state is then analyzed using another $i\text{SWAP}$ gate and two $X_{\pi/2}$ gates to extract the state which has been marked by the oracle function. Optionally, a Y_{π}^{12} pulse is used on each qubit to increase the readout fidelity.

6.4.1 State Tomography of the Quantum Register

Fig. 6.7 shows the experimentally measured density matrices of the two-qubit register when running the Grover search algorithm for the four possible Oracle functions. For each of those four cases, density matrices were measured at the steps 1-4 of the Grover algorithm as indicated in fig. 6.5. The black outlined circles in the density matrices represent the ideal theoretical states and the colored solid circles represent the measured states. The trace fidelities of all states with respect to the ideal states are noted above each density matrix. As can be seen, the fidelity diminishes as a function of the runtime of the algorithm due to dephasing and relaxation of the qubit register, as we will discuss later.

6.4.2 Single Run Results

The experimental state tomographies discussed in the last section show that we are able to implement the Grover search algorithm with adequate fidelity using our two-qubit processor. However, the analysis of the two-qubit register by quantum state tomography at the end of the algorithm does not prove that we can achieve real quantum speed-up with our processor. For this, it is necessary to directly read out the state of the qubit register at the end of the algorithm *without* performing any kind of error correction afterwards. By looking at this “raw” outcome data and generating outcome statistics over many single runs of the processor we can then quantify the success rate and the fidelity of the algorithm we implemented. The results of such measurements that we performed for the four possible Oracle functions are shown in fig. 6.8. Besides the single-run probabilities for all four Oracle functions, the diagram shows for comparison the expected outcome probabilities calculated based on the quantum state tomographies discussed above and the readout matrix of the two-qubit processor. As can be seen, the agreement be-

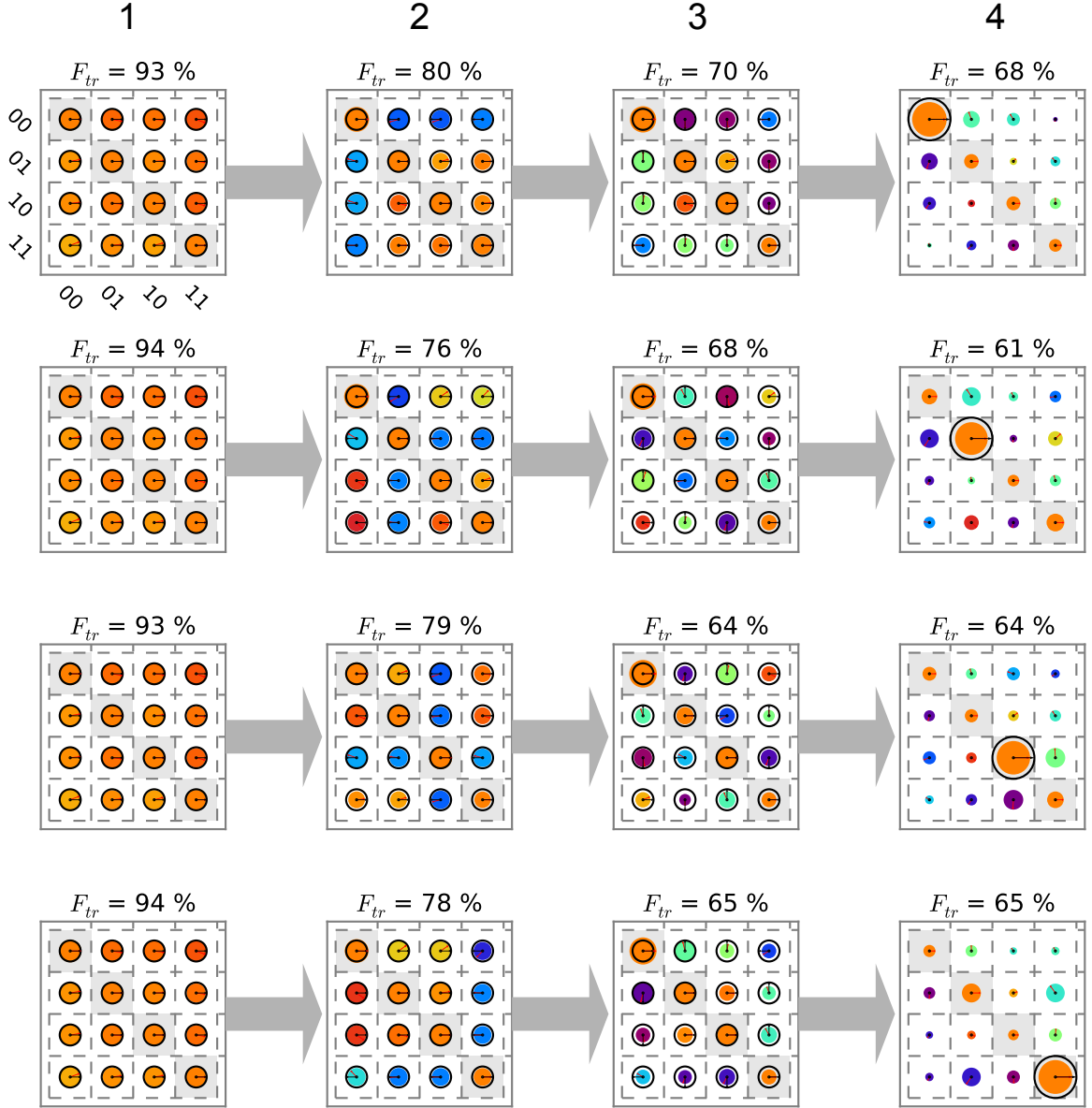


Figure 6.7: Quantum state tomographies at steps 1-4 of the Grover search algorithm, as indicated in fig. 6.6. The density matrices show the experimentally measured states in color and the theoretical states in black. For each state, the trace fidelity $F_{tr}(\rho_A, \rho_B) = \text{Tr}\{\rho_A \cdot \rho_B\}$ is shown above the density matrix.

tween the measured and calculated probabilities is rather good. The dashed line in the diagrams corresponds to the success probability of a classical single-step “query-and-guess” algorithm as described above, which is bound to 50 % and provides the benchmark against which we measure the quantum speed-up in this system. As can be seen, our implementation of the Grover search algorithm outperforms such a classical search algorithm for all four Oracle functions, if only by a small margin.

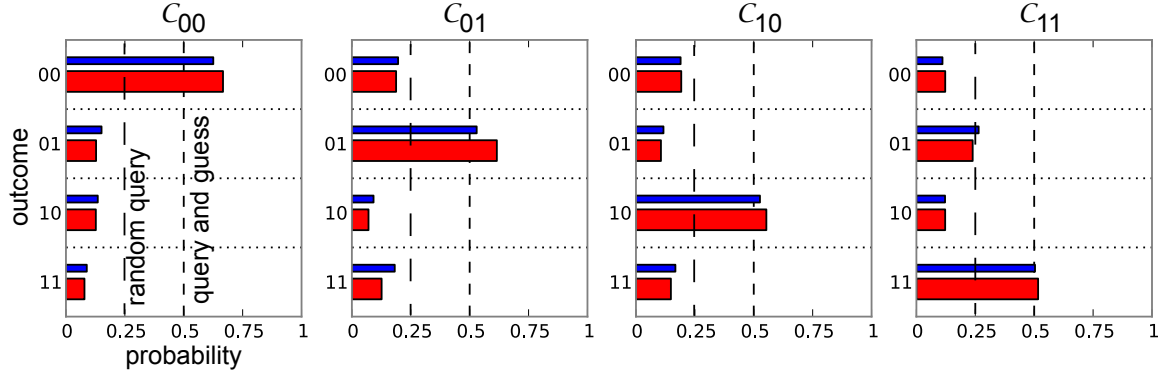


Figure 6.8: The single-run success probabilities of our implementation of the Grover search algorithm. Shown are the averaged probabilities for the four possible Oracle functions. The red bars correspond to measured values, the blue ones to expected probabilities calculated using the reconstructed density matrices after the final step of the algorithm and the measured two-qubit readout matrix. The dashed line indicates the average success probability of a classical query-and-guess algorithm for comparison.

6.5 Algorithm Fidelity

We can define the average fidelity of the algorithm in a single run, which corresponds to the conditional probability of finding the correct state $|i\rangle$ given a certain Oracle function C_i . Table 6.1 shows these single-run probabilities along with the so-called *user fidelities*, which are given as

$$f_{ab} = p(|ab\rangle |ab) = \frac{p(ab| |ab\rangle)}{\sum_{uv} p(uv| |uv\rangle)} \quad (6.15)$$

, where $p(ab| |ab\rangle)$ is the conditional probability of obtaining the search result ab given the Oracle operator $|ab\rangle$. The user fidelity is complementary to the average fidelity and correspond to the conditional probability of having found the correct state given a certain measured state, averaged over all possible Oracle functions. For all four Oracles, both the single-run and user fidelities are $> 50\%$, hence demonstrating quantum speed-up in comparison with a classical query-and-guess algorithm, as will be discussed below.

$ab/ uv\rangle$	$ 00\rangle$	$ 01\rangle$	$ 10\rangle$	$ 11\rangle$	\sum	f_{ab}
00	0.666	0.192	0.188	0.122	1.168	57.0 %
01	0.127	0.554	0.071	0.122	0.874	63.4 %
10	0.128	0.106	0.615	0.239	1.088	56.5 %
11	0.079	0.148	0.126	0.517	0.870	59.4 %

Table 6.1: Conditional probabilities $p_{ab/|uv\rangle}$ and user fidelities f_{ab} for all possible outcomes ab for our implementation of Grover's algorithm.

6.6 Comparision to a Classical Search Algorithm

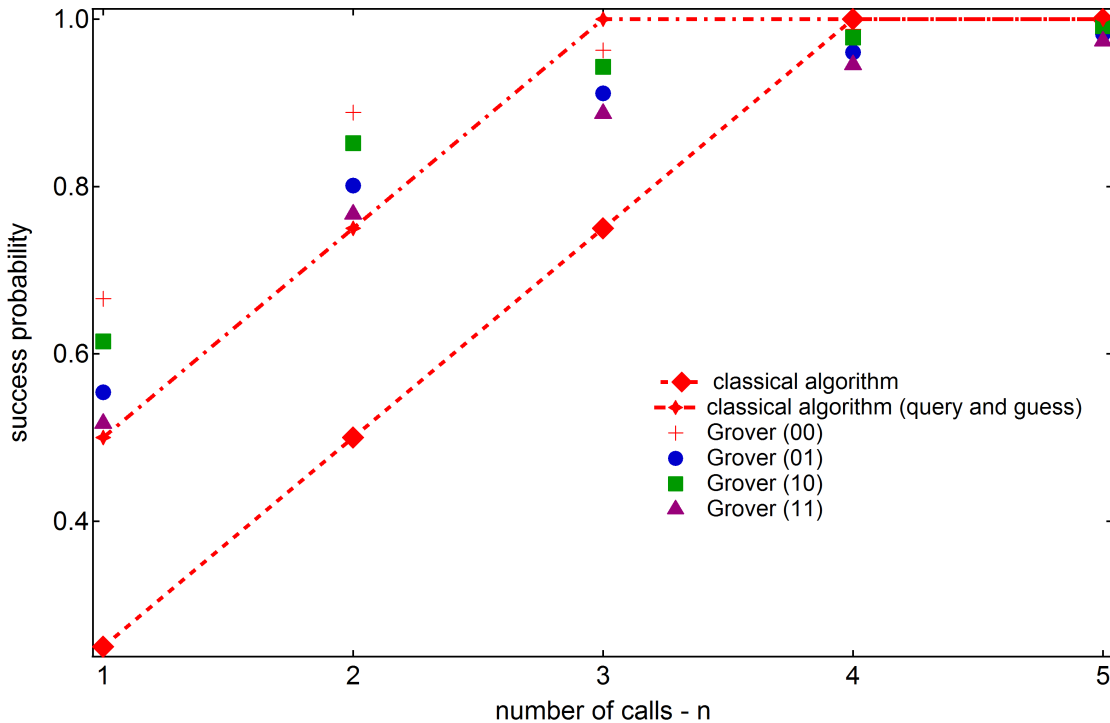


Figure 6.9: Success probability of our implementation of the Grover search algorithm, plotted against the number of single runs of the algorithm n . For comparision we show the success probabilities of a classical query and a classical query-and-guess search algorithm as a function of n .

As discussed above, we can compare the success probability of our implementation of the Grover search algorithm to different classical algorithm in order to quantify the quantum speed-up that we achieve. When repeatedly running the quantum search algorithm we can define the success probability as the probability of obtaining the right answer to the search problems within n single runs, which is given as

$$p_s(n) = \sum_{i=1}^n (1 - p_s)^{i-1} p_s \quad (6.16)$$

Here, p_s is the single-run success probability of the algorithm. We can plot $p_s(n)$ as a function of the runs of the algorithm and compare it with different classical algorithms. Fig. 6.9 shows such a comparisio for our implementation of the Grover search algorithm. For comparision with the quantum algorithm we plot the success probability of a classical query search algorithm and a classical query-and-guess algorithm as a function of Oracle calls n . The difference between the query and the query-and-guess algorithm is that the former doesn't return a result if it does not find the solution to the search problem after a number of n calls, whereas the latter takes an "educated guess" at the right state even if it did not obtain it directly by calling the Oracle function n times. Hence the statistical success probability of the query-and-guess-algorithm is

bigger than that of the simple query algorithm.

As can be seen, our implementation of the Grover search algorithm beats the classical query algorithm for $n < 4$ single runs and the classical query-and-guess algorithm for $n < 3$ single runs. However, unlike the classical algorithms it never converges to 100 % success probability due to always-present unitary and non-unitary errors in our system. We will analyze all such different errors relevant to our experiment in the next section.

6.7 Error Analysis

There are three kind of errors arising in our implementation of the Grover search algorithm that we will analyze in the following section. These errors are:

1. Deterministic, unitary gate errors
2. Stochastic errors introduced due to qubit decoherence during the runtime of the algorithm
3. Readout errors due to qubit relaxation during readout, insufficient readout sensitivity or retrapping of the readout resonator state during measurement.

We analyze the contributions of all these three error sources for the implementation of the algorithm below.

6.7.1 Gate Errors & Decoherence

Gate errors are unitary errors that arise due to misshaped or mistuned gate pulses and qubit frequencies. Usually the effect of these errors is combined with stochastic, non-unitary errors arising due to qubit decoherence during the runtime of the algorithm and therefore has to be analyzed together with the latter. Hence, in order to quantify these errors it is necessary to generate an error model of our algorithm that takes into account both unitary and as non-unitary errors. The parameters of such a model can be obtained by numerically fitting it to our experimental results.

Modeling Decoherence

!1! We could again model decoherence processes in our algorithm by formulating an effective master equation of the two-qubit system that includes relaxation and dephasing processes as we did when analyzing the universal quantum gate that we implemented. For our implementation of the Grover algorithm, however, we chose to rather use a set of discrete decoherence operators that model amplitude (i.e. T_1) and phase damping (i.e. T_ϕ) processes and which we can directly integrate in a more simple, operator-based model of the algorithm. We can then model the decoherence in our algorithm by applying these operators to the calculated quantum states after each individual step of the algorithm. Like this we can generate an error model incorporating the most relevant experimental decoherence processes without the need to numerically integrate an

To Do 1: replace this analytical calculating with a master equation simulation modeling the qubit as a three-level system and capturing all relevant errors

effective master equation, thereby greatly speeding up the process of fitting our experimental data to the formulated error model. In the following paragraphs we introduce the reader to the operators we use to model relaxation and dephasing processes in our error model.

To model qubit relaxation, we can use a pair of single-qubit operators describing amplitude-damaging of the qubit state, which given as [67]

$$E_1^{T_1} = \begin{pmatrix} 1 & 0 \\ 0 & \sqrt{1 - \gamma_{T_1}} \end{pmatrix} \quad E_2^{T_1} = \begin{pmatrix} 0 & \sqrt{\gamma_{T_1}} \\ 0 & 0 \end{pmatrix} \quad (6.17)$$

On the other hand, phase-damaging operators describing qubit dephasing can be written analogously as

$$E_1^{T_{\phi 1}} = \begin{pmatrix} 1 & 0 \\ 0 & \sqrt{1 - \gamma_{\phi}} \end{pmatrix} \quad E_2^{T_{\phi 1}} = \begin{pmatrix} 0 & 0 \\ 0 & \sqrt{\gamma_{\phi}} \end{pmatrix} \quad (6.18)$$

Both operators are applied to a quantum state ρ according to

$$\rho \rightarrow E_1 \rho E_1^\dagger + E_2 \rho E_2^\dagger \quad (6.19)$$

and yield a trace-preserving, non-unitary evolution of the quantum state of ρ . The decoherence fraction γ that is used in the operators can be calculated from the corresponding relaxation and dephasing rates as $\gamma_{T_{1,2}}(t) = 1 - \exp(-t\Gamma_{1,2}^{T_1})$ and $\gamma_{\phi_{1,2}} = 1 - \exp(-t\Gamma_{1,2}^{T_\phi}/2)$, where t is the time during which the state is exposed to the given decoherence process.

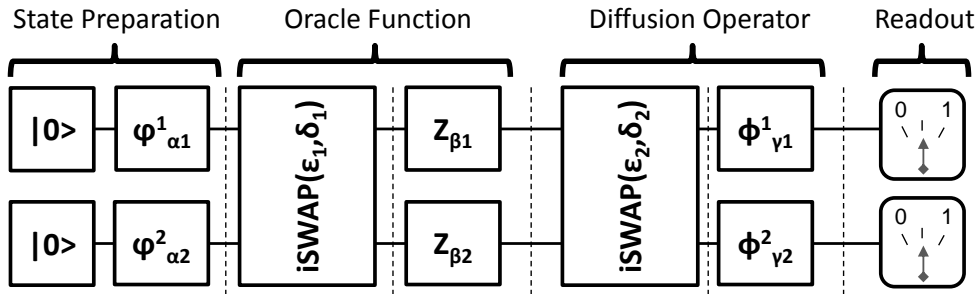


Figure 6.10: The error model we use to analyze the different gate and decoherence errors present when running the Grover search algorithm. The dotted lines indicate the points at which the quantum state has been measured by state tomography.

Using these two operators combined with a set of unitary operators describing the quantum operations performed during the algorithm we formulate a full error model that we use to model our experimental data, as shown in fig. 6.10. This model takes into account the following error sources:

- **Energy relaxation and phase decoherence:** Energy relaxation and dephasing of the qubit is modeled using the processes given in eqs. (6.17) and (6.18), applying these operators with an adapted γ after each unitary operation performed during the algorithm.

- **Single-qubit gate errors:** We model rotation angle and rotation phase errors of our single-qubit X_α and Y_α gates by replacing them with operators of the form $X_\alpha \rightarrow \phi_{\alpha'} = \cos \phi X_{\alpha'} + \sin \phi Y_{\alpha'}$ and $Y_\alpha \rightarrow \varphi_{\alpha'} = \sin \varphi X_{\alpha'} + \cos \varphi Y_{\alpha'}$. For Z -type single-qubit operators we model only rotation angle errors by replacing $Z_\alpha \rightarrow Z_{\alpha'}$
- **Two-qubit gate errors:** We model both detuning and gate-length errors of our $i\text{SWAP}$ 2-qubit gates.

For the two-qubit gates, we model the errors present in the $i\text{SWAP}$ operation by using the representation of the gate

$$i\text{SWAP}(t, \Delta) = \begin{pmatrix} 1 & 0 & 0 & 0 \\ 0 & \cos t g_e - i \frac{\Delta}{g_e} \sin t g_e & i \frac{g}{g_e} \sin t g_e & 0 \\ 0 & i \frac{g}{g_e} \sin t g_e & \cos t g_e + i \frac{\Delta}{g_e} \sin t g_e & 0 \\ 0 & 0 & 0 & 1 \end{pmatrix} \quad (6.20)$$

where $g_e = \sqrt{g^2 + \Delta^2}$ is the effective swap frequency at a qubit frequency detuning $f_{01}^1 - f_{01}^2 = 2\Delta$. Often it is practical to replace t and Δ with $\beta = t g_e$ and $\delta = \Delta/g$. Using this notation of the $i\text{SWAP}$ gate and the definition of the single-qubit gates as discussed before, the full algorithm with only gate errors can be written as (for right-multiplication)

$$\text{Grover} = \phi_{\gamma_1}^1 \otimes \phi_{\gamma_2}^2 \cdot i\text{SWAP}(\epsilon_2, \delta_2) \cdot Z_{\beta_1} \otimes Z_{\beta_2} \cdot i\text{SWAP}(\epsilon_1, \delta_1) \cdot \varphi_{\alpha_1}^1 \otimes \varphi_{\alpha_2}^2 \quad (6.21)$$

In addition, we add dephasing and relaxation error after each step of the algorithm to model the decoherence during the runtime of the algorithm. Numerical optimization is then used to produce a fit of all the gate errors, which is shown in tab. 6.2. Here, the qubit relaxation and dephasing times were measured independently and are not part of the fit.

state	δ_1	δ_2	α_1	α_2	φ_1	φ_2	ϵ_1	β_1	β_2	ϵ_2	γ_1	γ_2	ϕ_1	ϕ_2
$ 00\rangle$	0.06	-0.06	-2.5	2.7	6.1	3.1	-7.3	-3.3	-4.1	7.5	29	9.3	0.66	-1.7
$ 01\rangle$	0.04	-0.3	-0.1	0.1	7.9	3.6	-11	-5.9	2.2	-6.9	28	-19	9	2
$ 10\rangle$	0.09	-0.2	-3.1	1.7	1	-2.5	-6.5	-15	-22	-7.5	-15	32	3.6	5.2
$ 11\rangle$	0.16	0.13	-6	3.9	2.2	0.9	-9.5	-20	-15	17	-12	-32	-7	-8.9

Table 6.2: Fitted error parameters for the measured density matrices, modeled according to the error model given in eq. (6.21). All angles are given in deg.

The resulting fitted error models obtained for our experimental data are shown in tab. 6.2. As can be seen, the phase and gate-time errors for the first gates are comparatively small and grow bigger during the following steps of the algorithm. Curiously, the phase errors are bigger for the states $|10\rangle$ and $|11\rangle$, as are the gate-length errors for the two $i\text{SWAP}$ gates used in the algorithm. This fact might be explained by a drift of the operating point of our microwave setup during the time it took to take the data for the four possible Oracle operators, during which the parameters of individual qubit gates were not recalibrated.

Fig. 6.11 shows again the measured density matrices for our realization of the Grover search algorithm, this time overlaid with the numerically optimized error model according to eq. (6.21).

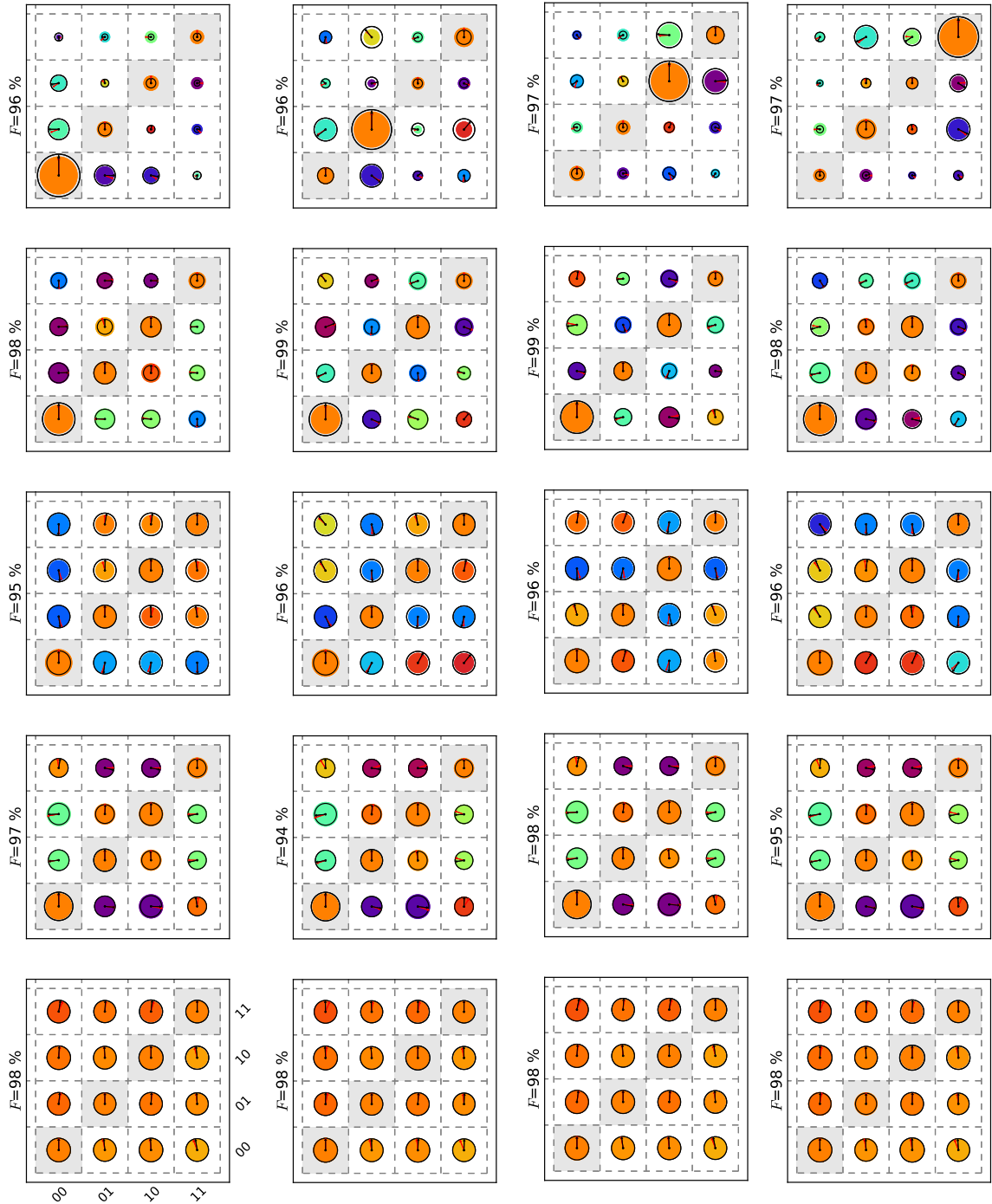


Figure 6.11: Comparison of the fitted error model as given by eq. (6.21) to our experimental data. Experimental data is shown in color, the fitted density matrices as black outlines. As before, we show the state fidelity according to eq. (??) between experimental and fitted states.

As can be seen, our error model is able to capture most of the observed experimental errors and can reproduce to very good accuracy the observed density matrices. The state fidelities according to eq. ?? between the measured density matrices and those of the fitted error model are shown above each density matrix.

Fidelity of the Oracle and diffusion operators

It is interesting to analyze the individual experimental fidelities of the Oracle and diffusion operators that make up the Grover algorithm achieved in our experiment. For this, we compare the action of the ideal operators D' and R' with that of the experimentally implemented versions D'_e and R'_e , taking the measured quantum states before applying each of the operators as input. We take then as the fidelity of each operator the average state fidelity of the measured output states as compared to the calculated ones, i.e.

$$F(D'_e) = F(D'\rho_{in}D'^\dagger, D'_e\rho_{in}D'^\dagger) \quad (6.22)$$

$$F(R'_e) = F(R'\rho_{in}R'^\dagger, R'_e\rho_{in}R'^\dagger) \quad (6.23)$$

where we also make use of the state fidelity according to eq. ?? . By this method, we obtain the following experimental fidelities for the two gate operations:

Operator / State	$ 00\rangle$	$ 01\rangle$	$ 10\rangle$	$ 11\rangle$	Average
D'	92.3	93.4	94.3	91.7	92.9
R'	94.5	93.6	88.5	87.7	91.1

Table 6.3: Measured fidelities of the quantum Oracle and diffusion operators used in the Grover search algorithm according to eqs. (6.22) and (6.23). All fidelities are given in percent.

As can be seen, on average we are able to implement both the diffusion operator and the quantum Oracle with a fidelity $> 90\%$.

6.7.2 Readout Errors

Another source of errors affecting the single-run fidelities of the algorithm arises due to the imperfection of our qubit readout. Here, mostly qubit relaxation during the readout process reduces the visibility of individual qubit states and introduces errors when reading out the qubit register in the final step of the algorithm. We can easily quantify those readout errors by using the readout matrix that was introduced in the last chapter. When running the Grover algorithm we use the $|1\rangle \rightarrow |2\rangle$ shelving method described in the last chapter to increase the readout contrast and thereby the algorithm fidelity. This technique reduces single-qubit readout errors but increases inter-qubit readout crosstalk. To quantify all single-qubit and inter-qubit readout errors, we first model the readout matrix R of the two-qubit system as a product $R = R_v \cdot R_{ct}$, where R_v is the so-called *visibility matrix* and R_{ct} a matrix describing the readout crosstalk. The visibility matrix

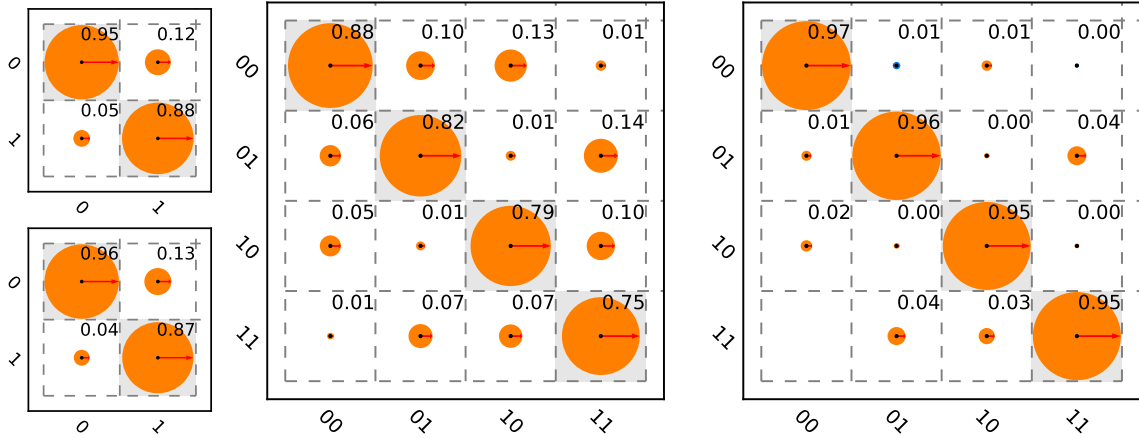


Figure 6.12: a.)The measured single-qubit readout matrices, showing the readout outcome probabilities as a function of the prepared state for both qubits. b.)The measured two-qubit readout matrix, showing again the detector outcome probabilities versus the prepared qubit states. c.) The crosstalk matrix, corresponding to the product of the inverse two-qubit readout matrix and the Kronecker product of the single-qubit readout matrices. Note that the $|1\rangle \rightarrow |2\rangle$ shelving method is used for reading out the qubit state, which increases readout fidelity but also inter-qubit readout crosstalk up to 4 % in the worst case.

can be written as the Kronecker product $R_v = R_v^1 \otimes R_v^2$ of the two single-qubit readout matrices, which have the form

$$R_v^{1,2} = \begin{pmatrix} p_{00}^{1,2} & 1 - p_{11}^{1,2} \\ 1 - p_{00}^{1,2} & p_{11}^{1,2} \end{pmatrix} \quad (6.24)$$

Here, $p_{00}^{1,2}$ ($p_{11}^{1,2}$) corresponds to the probability to measure the value 0 (1) at the readout after having prepared the qubit in state $|0\rangle$ ($|1\rangle$). Usually, the full two-qubit readout matrix R and the single-qubit readout matrices $R_v^{1,2}$ are measured experimentally which allows us then to calculate the crosstalk matrix as $R_{ct} = R_v^{-1} \cdot R$. The three matrices measured in our experiment are shown in fig. 6.12. As can be seen, the single-qubit readout fidelities range between 87 - 96 % and the combined two-qubit readout fidelities between 75 - 85 %. Depending on the qubit state we also observe between 3-5 % inter-qubit readout crosstalk in our system.

Fig. 6.8 shows the single-run probabilities when running the Grover algorithm for the four different Oracle functions. In blue, the expected readout outcome probabilities, as calculated using the state tomography of the final states given in fig. 6.7d and the measured readout matrix of our system are shown along the measured readout outcome probabilities. The readout error model shows good quantitative agreement with the measured data, with deviations most probably due to parameter drifts occurred between the measurement of the quantum state tomography and the single-run experiment.

6.8 Conclusions

To summarize, we have shown that we can implement the Grover search algorithm with our quantum processor and achieve a single-run fidelity that is sufficient to demonstrate simple probabilistic quantum speed-up as compared to a classical, reversible search algorithm. The error model formulated in this chapter is able to account for most of the observed imperfections and can explain the data we observed. Unfortunately, the coherence times of our qubits does not permit the realization of more complex algorithm with this system, but nevertheless it provides a proof-of-principle of our approach to build a superconducting quantum computer with individual-qubit single shot readout.

In the following chapter, we will discuss the extension of this approach to a system of four qubits and explain different strategies for scaling up such system to an even larger number of qubits.

Chapter 7

Designing a Scalable Architecture for Quantum Bits

7.1 Definition & Requirements

7.2 Qubit Design

7.2.1 Qubit Parameters

7.2.2 Qubit-Qubit Coupling

7.3 Readout Design

7.3.1 Readout Parameters

7.3.2 Qubit-Readout Coupling

7.4 Single-Qubit Manipulation

7.4.1 Error Analysis

7.5 Multi-Qubit Manipulation

7.5.1 Error Analysis

7.6 Implementing a Universal Set of Quantum Gates

7.7 Realizing A Four-Qubit Architecture

7.8 Scaling Up

Chapter 8

Conclusions & Perspective

8.1 Future Directions in Superconducting QC

8.1.1 3D Circuit Quantum Electrodynamics

8.1.2 Hybrid Quantum Systems

8.1.3 Quantum Error Correction & Feedback

Appendix A

Modeling of Multi-Qubit Systems

A.1 Analytical Approach

A.1.1 Multi-Qubit Hamiltonian

A.1.2 Energies and Eigenstates

A.2 Master Equation Approach

$$\hat{H} = \begin{pmatrix} e_0^I + e_0^{II} & & & & & \\ & e_0^I + e_1^{II} & & & & \\ & & e_0^I + e_2^{II} & & & \\ & & & e_1^I + e_0^{II} & & \\ & & & & e_1^I + e_1^{II} & \\ & & & & & e_1^I + e_2^{II} \\ & & & & & & e_2^I + e_0^{II} \\ & & & & & & & e_2^I + e_1^{II} \\ & & & & & & & & e_2^I + e_2^{II} \end{pmatrix} \quad (\text{A.1})$$

Without loss of generality we can assume $e_0^I = 0$, $e_0^{II} = 0$. We define $\omega_{01}^I = e_1^I$, $\omega_{01}^{II} = e_1^{II}$, $\Delta_{01} = \omega_{01}^{II} - \omega_{01}^I$ and $\alpha^I = e_2^I - 2e_1^I$ and $\alpha^{II} = e_2^{II} - 2e_1^{II}$. The interaction Hamiltonian is given

as

$$\hat{H}_i = \begin{pmatrix} 0 & 0 & 0 & g & 0 & 0 & 0 & 0 & 0 \\ 0 & 0 & 0 & 0 & 0 & 0 & 0 & 0 & 0 \\ 0 & 0 & 0 & 0 & \sqrt{2}g & 0 & 0 & 0 & 0 \\ 0 & g & 0 & 0 & 0 & 0 & 0 & 0 & 0 \\ 0 & 0 & \sqrt{2}g & 0 & 0 & 0 & \sqrt{2}g & 0 & 0 \\ 0 & 0 & 0 & 0 & 0 & 0 & 0 & 2g & 0 \\ 0 & 0 & 0 & 0 & \sqrt{2}g & 0 & 0 & 0 & 0 \\ 0 & 0 & 0 & 0 & 0 & 2g & 0 & 0 & 0 \\ 0 & 0 & 0 & 0 & 0 & 0 & 0 & 0 & 0 \end{pmatrix} \quad (\text{A.2})$$

Going to the interaction picture with $\hat{H}_0 = \hat{H}$ the interaction Hamiltonian \hat{H}_i becomes

$$\hat{H}_i = \begin{pmatrix} 0 & \dots & & & & & & & \\ 0 & 0 & \dots & & & & & & \\ 0 & 0 & 0 & \dots & & & & & \\ 0 & ge^{-i\Delta t} & 0 & & 0 & \dots & & & \\ 0 & 0 & \sqrt{2}ge^{-i(\Delta-\alpha^{II})t} & 0 & 0 & & \dots & & \\ 0 & 0 & 0 & 0 & 0 & 0 & \dots & & \\ 0 & 0 & 0 & 0 & \sqrt{2}ge^{-i(\Delta+\alpha^I)t} & 0 & 0 & \dots & \\ 0 & 0 & 0 & 0 & 0 & 2ge^{-i(\Delta+\alpha^I-\alpha^{II})t} & 0 & 0 & \dots \\ 0 & 0 & 0 & 0 & 0 & 0 & 0 & 0 & 0 \end{pmatrix} \quad (\text{A.3})$$

Relaxation and Dephasing

We can model relaxation and dephasing of the three-level system using a set of 6 Lindblad operators. The relaxation operators are based on the three matrices

$$\sigma_{01}^- = \begin{pmatrix} 0 & 1 & 0 \\ 0 & 0 & 0 \\ 0 & 0 & 0 \end{pmatrix} \quad \sigma_{12}^- = \begin{pmatrix} 0 & 0 & 0 \\ 0 & 0 & 1 \\ 0 & 0 & 0 \end{pmatrix} \quad \sigma_{02}^- = \begin{pmatrix} 0 & 0 & 1 \\ 0 & 0 & 0 \\ 0 & 0 & 0 \end{pmatrix} \quad (\text{A.4})$$

and the dephasing operators on

$$\sigma_{01}^z = \begin{pmatrix} 1 & 0 & 0 \\ 0 & -1 & 0 \\ 0 & 0 & 0 \end{pmatrix} \quad \sigma_{12}^z = \begin{pmatrix} 0 & 0 & 0 \\ 0 & 1 & 0 \\ 0 & 0 & -1 \end{pmatrix} \quad \sigma_{02}^z = \begin{pmatrix} 1 & 0 & 0 \\ 0 & 0 & 0 \\ 0 & 0 & -1 \end{pmatrix} \quad (\text{A.5})$$

Using these matrices, we define a set of three relaxation operators $L_{01}^r = \sqrt{\Gamma_{10}^r} \sigma_{01}^-$, $L_{12}^r = \sqrt{\Gamma_{12}^r} \sigma_{12}^-$ and $L_{02}^r = \sqrt{\Gamma_{02}^r} \sigma_{02}^-$ as well as a set of dephasing operators $L_{01}^\phi = \sqrt{\Gamma_{01}^\phi / 2} \sigma_{01}^z$, $L_{12}^\phi = \sqrt{\Gamma_{12}^\phi / 2} \sigma_{12}^z$, $L_{02}^\phi = \sqrt{\Gamma_{02}^\phi / 2} \sigma_{02}^z$.

A.2.1 Direct Integration

We can use the Hamiltonian and the Lindblad operators discussed above to directly integrate the master equation of the two-qubit system, which is given as

$$\frac{d\rho}{dt} = -\frac{i}{\hbar}[H, \rho] + \sum_j [2L_j \rho L_j^\dagger - \{L_j^\dagger L_j, \rho\}] \quad (\text{A.6})$$

Here $-i/\hbar [H, \rho]$ corresponds to the unitary evolution of the state of the system and the part right to it to the non-unitary part, i.e. relaxation and dephasing. For numerical analysis it is usually convenient to rewrite this equation in the form

$$\frac{d\vec{\rho}}{dt} = \mathcal{L}(t)\vec{\rho}(t) \quad (\text{A.7})$$

where $\vec{\rho}$ is a column vector containing all elements of ρ and \mathcal{L} is the so-called “superoperator” which acts on the vectorized density matrix. For a density matrix with dimension $N \times N$, the superoperator has dimensions $N^2 \times N^2$, which makes the numerical solution of eq. (A.7) computationally expensive for large N . An alternative method which avoids this inefficiency is the so-called “quantum monte carlo” method which we will discuss in the next section.

From these matrices, the corresponding two-qubit operator can be obtained as $L_i^I = L_i \otimes \mathcal{I}$ and $L_i^{II} = L_i \otimes \mathcal{I}$.

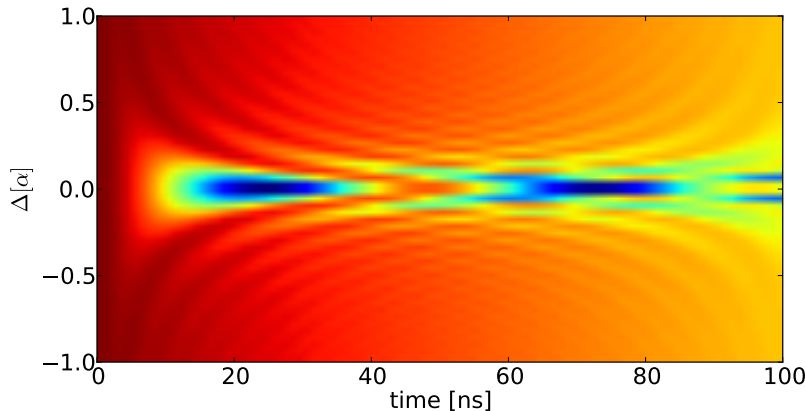


Figure A.1: ...

A.2.2 Monte Carlo Simulation

A.2.3 Speeding Up Simulations

```
from helpnet import *

def foo(x,y):
    print "Hello, world. This is quite a long line which should
    be wrapped I guess. The sum x + y = %g" % (x,y)
```

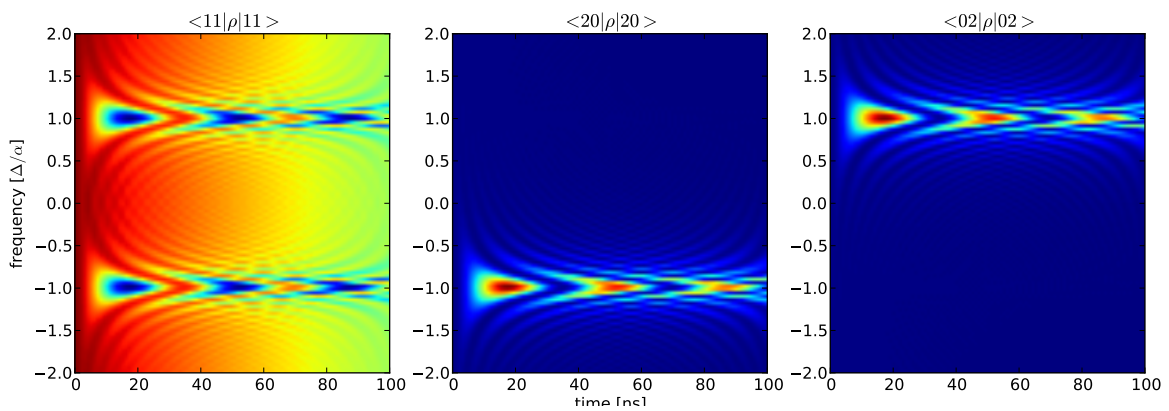


Figure A.2: ...

Appendix B

Data Acquisition & Management

B.1 Data Acquisition Infrastructure

B.2 Data Management Requirements

B.3 PyView

B.3.1 Overview

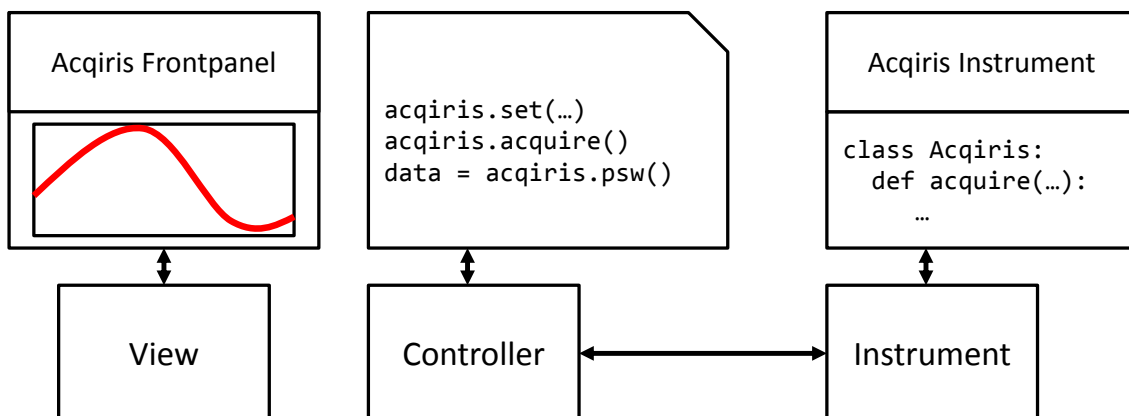


Figure B.1

B.3.2 Instrument Management**B.3.3 Data Acquisition****B.3.4 Data Management****B.3.5 Data Analysis**

Appendix C

Design & Fabrication

C.1 Mask Design

C.2 Optical Lithography

C.3 Electron Beam Lithography

Bibliography

- [1] J. B. Altepeter, D. Branning, E. Jeffrey, T. C. Wei, P. G. Kwiat, R. T. Thew, J. L. O'Brien, M. A. Nielsen, and A. G. White. Ancilla-assisted quantum process tomography. *Physical Review Letters*, 90(19):193601, May 2003.
- [2] M. Ansmann, H. Wang, R. C. Bialczak, M. Hofheinz, E. Lucero, M. Neeley, A. D. O'Connell, D. Sank, M. Weides, J. Wenner, A. N. Cleland, and J. M. Martinis. Violation of bell's inequality in josephson phase qubits. *Nature*, 461(7263):504–506, 2009.
- [3] A. Aspect, P. Grangier, and G. Roger. Experimental realization of einstein-podolsky-rosen-bohm gedankenexperiment: A new violation of bell's inequalities. *Physical Review Letters*, 49(2):91–94, July 1982.
- [4] A. Barenco, C. H. Bennett, R. Cleve, D. P. DiVincenzo, N. Margolus, P. Shor, T. Sleator, J. A. Smolin, and H. Weinfurter. Elementary gates for quantum computation. *Physical Review A*, 52(5):3457–3467, Nov. 1995.
- [5] J. T. Barreiro, M. Müller, P. Schindler, D. Nigg, T. Monz, M. Chwalla, M. Hennrich, C. F. Roos, P. Zoller, and R. Blatt. An open-system quantum simulator with trapped ions. *Nature*, 470(7335):486–491, Feb. 2011.
- [6] J. Bell. On the einstein podolsky rosen paradox. *Physics*, pages 195–200, 1964.
- [7] P. Bertet, I. Chiorescu, G. Burkard, K. Semba, C. J. P. M. Harmans, D. P. DiVincenzo, and J. E. Mooij. Dephasing of a superconducting qubit induced by photon noise. *Physical Review Letters*, 95(25):257002, Dec. 2005.
- [8] P. Bertet, I. Chiorescu, C. J. P. M. Harmans, and J. E. Mooij. Dephasing of a flux-qubit coupled to a harmonic oscillator. *arXiv:cond-mat/0507290*, July 2005.
- [9] A. Blais, J. Gambetta, A. Wallraff, D. I. Schuster, S. M. Girvin, M. H. Devoret, and R. J. Schoelkopf. Quantum-information processing with circuit quantum electrodynamics. *Physical Review A*, 75(3):032329, Mar. 2007.
- [10] A. Blais, R.-S. Huang, A. Wallraff, S. M. Girvin, and R. J. Schoelkopf. Cavity quantum electrodynamics for superconducting electrical circuits: An architecture for quantum computation. *Physical Review A*, 69(6):062320, June 2004.

- [11] V. Bouchiat, D. Vion, P. Joyez, D. Esteve, and M. H. Devoret. Quantum coherence with a single cooper pair. *Physica Scripta*, T76(1):165, 1998.
- [12] H.-J. Briegel, T. Calarco, D. Jaksch, J. I. Cirac, and P. Zoller. Quantum computing with neutral atoms. *Journal of Modern Optics*, 47(2-3):415–451, 2000.
- [13] G. Burkard, R. H. Koch, and D. P. DiVincenzo. Multilevel quantum description of decoherence in superconducting qubits. *Physical Review B*, 69(6):064503, Feb. 2004.
- [14] I. Chiorescu, Y. Nakamura, C. J. P. M. Harmans, and J. E. Mooij. Coherent quantum dynamics of a superconducting flux qubit. *Science*, 299(5614):1869 –1871, Mar. 2003.
- [15] J. M. Chow, L. DiCarlo, J. M. Gambetta, F. Motzoi, L. Frunzio, S. M. Girvin, and R. J. Schoelkopf. Optimized driving of superconducting artificial atoms for improved single-qubit gates. *Physical Review A*, 82(4):040305, Oct. 2010.
- [16] J. I. Cirac and P. Zoller. Quantum computations with cold trapped ions. *Physical Review Letters*, 74(20):4091–4094, May 1995.
- [17] J. Clarke. *The SQUID Handbook: Fundamentals and Technology of SQUIDs and SQUID Systems*, volume 1. Wiley-VCH, 2005.
- [18] J. Clarke, A. N. Cleland, M. H. Devoret, D. Esteve, and J. M. Martinis. Quantum mechanics of a macroscopic variable: The phase difference of a josephson junction. *Science*, 239(4843):992–997, Feb. 1988.
- [19] J. F. Clauser, M. A. Horne, A. Shimony, and R. A. Holt. Proposed experiment to test local hidden-variable theories. *Physical Review Letters*, 23(15):880–884, Oct. 1969.
- [20] E. Collin, G. Ithier, A. Aassime, P. Joyez, D. Vion, and D. Esteve. NMR-like control of a quantum bit superconducting circuit. *Physical Review Letters*, 93(15):157005, Oct. 2004.
- [21] A. Cottet. *Implementation of a quantum bit in a superconducting circuit*. PhD thesis, Université Paris VI, Paris, 2002.
- [22] G. M. D'Ariano and P. Lo Presti. Quantum tomography for measuring experimentally the matrix elements of an arbitrary quantum operation. *Physical Review Letters*, 86(19):4195–4198, May 2001.
- [23] C. M. Dawson and M. A. Nielsen. The solovay-kitaev algorithm. *arXiv:quant-ph/0505030*, May 2005.
- [24] D. Deutsch. Quantum theory, the church-turing principle and the universal quantum computer. *Proceedings of the Royal Society of London. A. Mathematical and Physical Sciences*, 400(1818):97 –117, July 1985.

- [25] M. Devoret. Quantum fluctuations in electrical circuits. In *Les Houches Session on Quantum Fluctuations*, volume LXIII, pages 351–386. 1995.
- [26] M. H. Devoret, J. M. Martinis, and J. Clarke. Measurements of macroscopic quantum tunneling out of the zero-voltage state of a current-biased josephson junction. *Physical Review Letters*, 55(18):1908–1911, Oct. 1985.
- [27] L. DiCarlo, J. M. Chow, J. M. Gambetta, L. S. Bishop, B. R. Johnson, D. I. Schuster, J. Majer, A. Blais, L. Frunzio, S. M. Girvin, and R. J. Schoelkopf. Demonstration of two-qubit algorithms with a superconducting quantum processor. *Nature*, 460(7252):240–244, July 2009.
- [28] L. DiCarlo, M. D. Reed, L. Sun, B. R. Johnson, J. M. Chow, J. M. Gambetta, L. Frunzio, S. M. Girvin, M. H. Devoret, and R. J. Schoelkopf. Preparation and measurement of three-qubit entanglement in a superconducting circuit. *Nature*, 467(7315):574–578, 2010.
- [29] D. P. DiVincenzo. The physical implementation of quantum computation. *Fortschritte der Physik*, 48(9-11):771–783, Sept. 2000.
- [30] D. P. DiVincenzo. Fault-tolerant architectures for superconducting qubits. *Physica Scripta*, T137:014020, Dec. 2009.
- [31] W. Dür and J. I. Cirac. Nonlocal operations: Purification, storage, compression, tomography, and probabilistic implementation. *Physical Review A*, 64(1):012317, June 2001.
- [32] A. Einstein, B. Podolsky, and N. Rosen. Can quantum-mechanical description of physical reality be considered complete? *Physical Review*, 47(10):777–780, May 1935.
- [33] E. Farhi, J. Goldstone, S. Gutmann, and M. Sipser. Quantum computation by adiabatic evolution. *arXiv:quant-ph/001106*, Jan. 2000.
- [34] A. Fedorov, L. Steffen, M. Baur, and A. Wallraff. Implementation of a toffoli gate with superconducting circuits. *arXiv:1108.3966*, Aug. 2011.
- [35] R. Feynman. Simulating physics with computers. *International Journal of Theoretical Physics*, 21(6):467–488, 1982.
- [36] M. H. Freedman, A. Kitaev, and Z. Wang. Simulation of topological field theories by quantum computers. *Communications in Mathematical Physics*, 227(3):587–603, 2002.
- [37] A. Galiautdinov, A. N. Korotkov, and J. M. Martinis. Resonator–zero-qubit architecture for superconducting qubits. *Physical Review A*, 85(4):042321, Apr. 2012.
- [38] R. Gerritsma, G. Kirchmair, F. Zähringer, E. Solano, R. Blatt, and C. F. Roos. Quantum simulation of the dirac equation. *Nature*, 463(7277):68–71, Jan. 2010.

- [39] L. K. Grover. A fast quantum mechanical algorithm for database search. In *Proceedings of the twenty-eighth annual ACM symposium on Theory of computing*, STOC '96, page 212–219, New York, NY, USA, 1996. ACM.
- [40] L. K. Grover. Quantum mechanics helps in searching for a needle in a haystack. *Physical Review Letters*, 79(2):325–328, July 1997.
- [41] L. K. Grover. From schrödinger's equation to the quantum search algorithm. *American Journal of Physics*, 69(7):769–777, 2001.
- [42] S. Haroche and J.-M. Raimond. *Exploring the Quantum: Atoms, Cavities and Photons*. Oxford University Press, 2006.
- [43] M. Hofheinz, H. Wang, M. Ansmann, R. C. Bialczak, E. Lucero, M. Neeley, A. D. O'Connell, D. Sank, J. Wenner, J. M. Martinis, and A. N. Cleland. Synthesizing arbitrary quantum states in a superconducting resonator. *Nature*, 459(7246):546–549, May 2009.
- [44] J. Jones. NMR quantum computation. *Progress in Nuclear Magnetic Resonance Spectroscopy*, 38(4):325–360, June 2001.
- [45] B. Josephson. Possible new effects in superconductive tunnelling. *Physics Letters*, 1(7):251–253, July 1962.
- [46] A. Kitaev. Fault-tolerant quantum computation by anyons. *Annals of Physics*, 303(1):2–30, Jan. 2003.
- [47] E. Knill, R. Laflamme, and G. J. Milburn. A scheme for efficient quantum computation with linear optics. *Nature*, 409(6816):46–52, Jan. 2001.
- [48] J. Koch, T. M. Yu, J. Gambetta, A. A. Houck, D. I. Schuster, J. Majer, A. Blais, M. H. Devoret, S. M. Girvin, and R. J. Schoelkopf. Charge-insensitive qubit design derived from the cooper pair box. *Physical Review A*, 76(4):042319, Oct. 2007.
- [49] K. Kraus, A. Böhm, J. D. Dollard, and W. H. Wootters, editors. *States, Effects, and Operations Fundamental Notions of Quantum Theory Lectures in Mathematical Physics at the University of Texas at Austin*. Lecture Notes in Physics. Springer, 1983. DOI: 10.1007/3-540-12732-1.
- [50] G. d. Lange, Z. H. Wang, D. Ristè, V. V. Dobrovitski, and R. Hanson. Universal dynamical decoupling of a single solid-state spin from a spin bath. *Science*, 330(6000):60–63, Jan. 2010.
- [51] B. P. Lanyon, C. Hempel, D. Nigg, M. Müller, R. Gerritsma, F. Zähringer, P. Schindler, J. T. Barreiro, M. Rambach, G. Kirchmair, M. Hennrich, P. Zoller, R. Blatt, and C. F. Roos. Universal digital quantum simulation with trapped ions. *Science*, 334(6052):57–61, July 2011.

- [52] M. T. Levinsen, R. Y. Chiao, M. J. Feldman, and B. A. Tucker. An inverse ac josephson effect voltage standard. *Applied Physics Letters*, 31(11):776–778, Dec. 1977.
- [53] S. Lloyd. Universal quantum simulators. *Science*, 273(5278):1073–1078, Aug. 1996.
- [54] D. Loss and D. P. DiVincenzo. Quantum computation with quantum dots. *Physical Review A*, 57(1):120–126, Jan. 1998.
- [55] E. Lucero, J. Kelly, R. C. Bialczak, M. Lenander, M. Mariantoni, M. Neeley, A. D. O’Connell, D. Sank, H. Wang, M. Weides, J. Wenner, T. Yamamoto, A. N. Cleland, and J. M. Martinis. Reduced phase error through optimized control of a superconducting qubit. *Physical Review A*, 82(4):042339, Oct. 2010.
- [56] F. Mallet, F. R. Ong, A. Palacios-Laloy, F. Nguyen, P. Bertet, D. Vion, and D. Esteve. Single-shot qubit readout in circuit quantum electrodynamics. *Nat Phys*, 5(11):791–795, Nov. 2009.
- [57] M. Mariantoni, H. Wang, T. Yamamoto, M. Neeley, R. C. Bialczak, Y. Chen, M. Lenander, E. Lucero, A. D. O’Connell, D. Sank, M. Weides, J. Wenner, Y. Yin, J. Zhao, A. N. Korotkov, A. N. Cleland, and J. M. Martinis. Implementing the quantum von neumann architecture with superconducting circuits. *Science*, 334(6052):61–65, Oct. 2011.
- [58] J. M. Martinis, K. B. Cooper, R. McDermott, M. Steffen, M. Ansmann, K. D. Osborn, K. Cicak, S. Oh, D. P. Pappas, R. W. Simmonds, and C. C. Yu. Decoherence in josephson qubits from dielectric loss. *Physical Review Letters*, 95(21):210503, Nov. 2005.
- [59] J. M. Martinis, M. H. Devoret, and J. Clarke. Energy-level quantization in the zero-voltage state of a current-biased josephson junction. *Physical Review Letters*, 55(15):1543–1546, Oct. 1985.
- [60] J. M. Martinis, M. H. Devoret, and J. Clarke. Experimental tests for the quantum behavior of a macroscopic degree of freedom: The phase difference across a josephson junction. *Physical Review B*, 35(10):4682–4698, Apr. 1987.
- [61] J. M. Martinis, S. Nam, J. Aumentado, and C. Urbina. Rabi oscillations in a large josephson-junction qubit. *Physical Review Letters*, 89(11):117901, 2002.
- [62] C. Monroe, D. M. Meekhof, B. E. King, W. M. Itano, and D. J. Wineland. Demonstration of a fundamental quantum logic gate. *Physical Review Letters*, 75(25):4714–4717, Dec. 1995.
- [63] J. E. Mooij, T. P. Orlando, L. Levitov, L. Tian, C. H. van der Wal, and S. Lloyd. Josephson persistent-current qubit. *Science*, 285(5430):1036–1039, 1999.
- [64] F. Motzoi, J. M. Gambetta, P. Rebentrost, and F. K. Wilhelm. Simple pulses for elimination of leakage in weakly nonlinear qubits. *Physical Review Letters*, 103(11):110501, 2009.

- [65] Y. Nakamura, Y. A. Pashkin, and J. S. Tsai. Coherent control of macroscopic quantum states in a single-cooper-pair box. *Nature*, 398(6730):786–788, Apr. 1999.
- [66] F. Nguyen. *Cooper Pair Box Circuits: Two-Qubit Gate, Single-Shot Readout, and Current to Frequency Conversion*. PhD thesis, Université Paris VI, Saclay, 2008.
- [67] M. A. Nielsen and I. L. Chuang. *Quantum Computation and Quantum Information*. Cambridge University Press, 2000.
- [68] L. Ozyuzer, A. E. Koshelev, C. Kurter, N. Gopalsami, Q. Li, M. Tachiki, K. Kadowaki, T. Yamamoto, H. Minami, H. Yamaguchi, T. Tachiki, K. E. Gray, W.-K. Kwok, and U. Welp. Emission of coherent THz radiation from superconductors. *Science*, 318(5854):1291–1293, Nov. 2007.
- [69] H. Paik, D. I. Schuster, L. S. Bishop, G. Kirchmair, G. Catelani, A. P. Sears, B. R. Johnson, M. J. Reagor, L. Frunzio, L. I. Glazman, S. M. Girvin, M. H. Devoret, and R. J. Schoelkopf. Observation of high coherence in josephson junction qubits measured in a three-dimensional circuit QED architecture. *Physical Review Letters*, 107(24):240501, Dec. 2011.
- [70] A. Palacios-Laloy. *Superconducting Qubit in a Resonator: Test of the Leggett-Garg Inequality and Single-Shot Readout*. PhD thesis, Commissariat à l'Energie Atomique, Saclay, 2010.
- [71] J. F. Poyatos, J. I. Cirac, and P. Zoller. Complete characterization of a quantum process: The two-bit quantum gate. *Physical Review Letters*, 78(2):390–393, Jan. 1997.
- [72] D. M. Pozar. *Microwave Engineering*. Wiley, 4 edition, Nov. 2011.
- [73] E. Purcell. Spontaneous emission probabilities at radio frequencies. In *Physical Review*, volume 69, page 681, 1946.
- [74] R. Raussendorf and H. J. Briegel. A one-way quantum computer. *Physical Review Letters*, 86(22):5188–5191, May 2001.
- [75] M. D. Reed, L. DiCarlo, S. E. Nigg, L. Sun, L. Frunzio, S. M. Girvin, and R. J. Schoelkopf. Realization of three-qubit quantum error correction with superconducting circuits. *arXiv:1109.4948*, Sept. 2011.
- [76] C. Rigetti, S. Poletto, J. M. Gambetta, B. L. T. Plourde, J. M. Chow, A. D. Corcoles, J. A. Smolin, S. T. Merkel, J. R. Rozen, G. A. Keefe, M. B. Rothwell, M. B. Ketchen, and M. Steffen. Superconducting qubit in waveguide cavity with coherence time approaching 0.1ms. *arXiv:1202.5533*, Feb. 2012.
- [77] D. I. Schuster. *Circuit Quantum Electrodynamics*. PhD thesis, Yale University, New Haven, 2007.

- [78] N. Shenvi, J. Kempe, and K. B. Whaley. Quantum random-walk search algorithm. *Physical Review A*, 67(5):052307, May 2003.
- [79] P. Shor. Algorithms for quantum computation: discrete logarithms and factoring. In *Foundations of Computer Science, 1994 Proceedings., 35th Annual Symposium on*, pages 124–134, Nov. 1994.
- [80] P. W. Shor. Polynomial-time algorithms for prime factorization and discrete logarithms on a quantum computer. *arXiv:quant-ph/9508027*, Aug. 1995. SIAM J.Sci.Statist.Comput. 26 (1997) 1484.
- [81] I. Siddiqi, R. Vijay, M. Metcalfe, E. Boaknin, L. Frunzio, R. J. Schoelkopf, and M. H. Devoret. Dispersive measurements of superconducting qubit coherence with a fast latching readout. *Physical Review B*, 73(5):054510, Feb. 2006.
- [82] I. Siddiqi, R. Vijay, F. Pierre, C. M. Wilson, M. Metcalfe, C. Rigetti, L. Frunzio, and M. H. Devoret. RF-Driven josephson bifurcation amplifier for quantum measurement. *Physical Review Letters*, 93(20):207002, Nov. 2004.
- [83] R. W. Simmonds, K. M. Lang, D. A. Hite, S. Nam, D. P. Pappas, and J. M. Martinis. Decoherence in josephson phase qubits from junction resonators. *Physical Review Letters*, 93(7):077003, Aug. 2004.
- [84] J. Simon, W. S. Bakr, R. Ma, M. E. Tai, P. M. Preiss, and M. Greiner. Quantum simulation of antiferromagnetic spin chains in an optical lattice. *Nature*, 472(7343):307–312, Apr. 2011.
- [85] S. J. Srinivasan, A. J. Hoffman, J. M. Gambetta, and A. A. Houck. Tunable coupling in circuit quantum electrodynamics using a superconducting charge qubit with a v-shaped energy level diagram. *Physical Review Letters*, 106(8):083601, Feb. 2011.
- [86] D. J. Van Harlingen, T. L. Robertson, B. L. T. Plourde, P. A. Reichardt, T. A. Crane, and J. Clarke. Decoherence in josephson-junction qubits due to critical-current fluctuations. *Physical Review B*, 70(6):064517, Aug. 2004.
- [87] L. M. K. Vandersypen, M. Steffen, G. Breyta, C. S. Yannoni, M. H. Sherwood, and I. L. Chuang. Experimental realization of shor’s quantum factoring algorithm using nuclear magnetic resonance. *Nature*, 414(6866):883–887, Dec. 2001.
- [88] R. Vijay, M. H. Devoret, and I. Siddiqi. Invited review article: The josephson bifurcation amplifier. *Review of Scientific Instruments*, 80(11):111101–111101–17, Nov. 2009.
- [89] R. Vijay, C. Macklin, D. H. Slichter, S. J. Weber, K. W. Murch, R. Naik, A. N. Korotkov, and I. Siddiqi. Quantum feedback control of a superconducting qubit: Persistent rabi oscillations. *arXiv:1205.5591*, May 2012.

- [90] D. Vion, A. Aassime, A. Cottet, P. Joyez, H. Pothier, C. Urbina, D. Esteve, and M. H. Devoret. Manipulating the quantum state of an electrical circuit. *Science*, 296(5569):886 –889, May 2002.
- [91] A. Wallraff, D. I. Schuster, A. Blais, L. Frunzio, R.-S. Huang, J. Majer, S. Kumar, S. M. Girvin, and R. J. Schoelkopf. Strong coupling of a single photon to a superconducting qubit using circuit quantum electrodynamics. *Nature*, 431(7005):162–167, 2004.
- [92] T. Yamamoto, M. Neeley, E. Lucero, R. C. Bialczak, J. Kelly, M. Lenander, M. Mariantoni, A. D. O’Connell, D. Sank, H. Wang, M. Weides, J. Wenner, Y. Yin, A. N. Cleland, and J. M. Martinis. Quantum process tomography of two-qubit controlled-z and controlled-NOT gates using superconducting phase qubits. *Physical Review B*, 82(18):184515, Nov. 2010.
- [93] B. Yurke and J. S. Denker. Quantum network theory. *Physical Review A*, 29(3):1419–1437, Mar. 1984.